Transpiration Cooling for Double-Walled Jet Engine Turbine Blades



Matthew Courtis

New College
University of Oxford

A thesis submitted for the degree of

Doctor of Philosophy

Trinity 2023

Acknowledgements

I would like to thank my supervisor Professor Peter Ireland for his enthusiasm and expertise which has been fundamental in guiding me throughout my research. It has been a fantastic journey sparked during my undergrad and I will certainly miss the weekly catch-up meetings, where I learnt a tremendous amount. My sincere gratitude goes to Rolls-Royce PLC and the Engineering and Physical Sciences Research Council (EPSRC), grant number EP/P000878/1, for their financial support. Thanks to all the technicians and staff at the OTI for the immense work from which I have benefited.

This thesis would not be possible without the support and love from my parents who have been there before and throughout these many years of being a student. While my brother can take no credit for the content here, trying to beat him in our Math class must have spurred me on to where I am today.

Dom, Gaby and Koji thank you so much for being incredible friends and being there for me whenever I needed it. Special mention must go to my lockdown buddy Tommy who kept me surfing, running and exploring, while only breaking me on Dartmoor once. My love for OUSC and the friendships made in and out of the pool are just as valuable as the expertise I have gained in pursuit of an academic title. To all my friends from Oxford and beyond, thank you.

Abstract

Increasing thermal loads on turbine blades has led to the need for more advanced cooling systems. Transpiration cooling techniques are of renewed interest, partly because of more advanced manufacturing methods, and are characterised by small film-cooling hole sizes, with a high coverage density, to achieve a suitable cooling performance for small coolant mass flow requirements. The timely implementation of such systems could provide the aerospace industry with significant benefits of increased engine efficiency and reduced costs. This thesis provides a framework for experimental and numerical testing and consequences of moving towards transpiration-like cooling. The use of a numerically efficient method was successfully implemented to predict the overall thermal performance of highly-dense film-arrays in a double-wall configuration which utilised both impingement jet cooling as well as external film protection. Three main benefits were found. More uniform and elevated film effectiveness protection on the external blade surface. Reduction in the maximum and mean temperature on the external surfaces as well as enhanced overall cooling performance throughout the double wall structure. And reduction in the thermal gradient between outer and inner skins. Challenges remain for implementation of transpiration double-wall configurations on more complex blade geometries. But there is a lot of promise to realise the potential for superior thermal protection, which could vastly improve the life of turbine blades in harsh environments and normal operation.

Contents

1 Introduction **1**
- 1.1 Background . . . 1
- 1.2 Research Aims . . . 4
- 1.3 Publications . . . 5
- 1.4 Achievements . . . 6
- 1.5 Thesis Outline . . . 7

2 Literature Review **8**
- 2.1 Cooling System Overview . . . 8
- 2.2 Film Cooling . . . 10
- 2.3 Effusion Cooling . . . 16
  - 2.3.1 Overview . . . 16
  - 2.3.2 Double-Walled Systems . . . 17
- 2.4 Transpiration Cooling . . . 21
  - 2.4.1 Main Principles . . . 21
  - 2.4.2 Historical Development . . . 22
  - 2.4.3 Application to Nozzle Guide Vanes . . . 24
  - 2.4.4 Hole Blockage . . . 25
- 2.5 Experimental Methods . . . 28
  - 2.5.1 Aerodynamic Measurement Techniques . . . 28
  - 2.5.2 Heat Transfer Measurements . . . 29
- 2.6 Numerical Methods . . . 30
  - 2.6.1 Review of Methods . . . 30
  - 2.6.2 Conjugate Heat Transfer Methods . . . 31
- 2.7 Summary . . . 34

3 Experimental Facility **35**
- 3.1 Overview . . . 35
- 3.2 Infrared Methodology . . . 38
  - 3.2.1 Blackbody calibration . . . 39
  - 3.2.2 Greybody Calibration . . . 40
- 3.3 Double-Walled Test Piece Design . . . 41

4 Numerical Methods **46**
- 4.1 Introduction . . . 46
- 4.2 Decoupled Unit-Cell Conjugate Method . . . 46
  - 4.2.1 Internal Model . . . 47
  - 4.2.2 Film Effectiveness . . . 48
  - 4.2.3 Integration of Internal and External Cooling . . . 50

4.2.4 Limitations of unit-cell method . . . 52
4.3 Semi-coupled Unit-Cell Method . . . 52
4.4 Semi-coupled streamwise domain . . . 53
4.5 Low Order Model . . . 53

5 Film Effectiveness 58
5.1 Overview . . . 58
5.2 Preliminary Investigation . . . 59
5.3 Journal Paper . . . 62
5.3.1 Introduction . . . 63
5.3.2 Materials and Methods . . . 65
5.3.2.1 Research Object . . . 65
5.3.2.2 Numerical Method . . . 67
5.3.2.3 Experimental Method . . . 68
5.3.3 Results and Discussion . . . 69
5.3.3.1 Numerical Results . . . 69
5.3.3.2 TD2 Results . . . 72
5.3.3.3 Experimental Results . . . 74
5.3.3.4 Numerical and Experimental Comparison . . . 81
5.3.4 Conclusions . . . 85
5.4 Further High Porosity Results . . . 86
5.5 Compound Angle . . . 91
5.6 Adiabatic Assumption . . . 100
5.7 Material Selection . . . 104
5.8 Turbine Blade Application . . . 105
5.9 Summary . . . 107

6 Internal Component Study 109
6.1 Overview . . . 109
6.2 Journal of Applied Thermal Engineering . . . 110
6.2.1 Introduction . . . 111
6.2.2 Aerothermal Analysis . . . 113
6.2.2.1 Aerothermal Model . . . 113
6.2.2.2 Full thermal Solution . . . 117
6.2.2.3 Wall spacing and inner wall thickness effects on internal aerothermal field . . . 118
6.2.3 Link between aerothermal and mechanical analysis . . . 124
6.2.3.1 Overall strategy . . . 124
6.2.3.2 Using the aerothermal output . . . 125
6.2.4 Mechanical analysis . . . 126
6.2.4.1 Material Model for CMSX-4 alloy . . . 126
6.2.4.2 Thermal stresses in a double wall turbine blade . . . 127
6.2.4.3 Thermal stress in flat double plates . . . 129
6.2.4.4 Thermal and centrifugal stresses in a DWTC system . . . 132
6.2.5 Evaluation of results . . . 139
6.2.6 Conclusions . . . 144
6.3 Further Investigation . . . 152
6.3.1 Domain . . . 152
6.3.2 Results . . . 153
6.4 Summary . . . 156

7 Evaluation of Numerical Methods **158**
7.1 Overview . . . 158
7.2 Preliminary Numerical Study . . . 158
7.2.1 Unit-Block Results . . . 158
7.2.2 Full Solution . . . 160
7.2.3 Full Test Piece Considerations . . . 162
7.3 Hole Inclination . . . 163
7.4 Model comparison . . . 165
7.5 Pressure gradient . . . 168
7.6 Experimental comparison . . . 172
7.7 Summary . . . 174

8 Evaluation of Outerskin Porosity **175**
8.1 Overview . . . 175
8.2 ASME 2022 paper . . . 176
8.2.1 Introduction . . . 177
8.2.2 Geometric Domain . . . 180
8.2.3 Numerical Model . . . 181
8.2.4 Results . . . 186
8.2.5 Summary . . . 197
8.2.6 Tabulated Results . . . 198
8.3 Experimental Results . . . 199
8.4 Summary . . . 210

9 Concluding Remarks **211**
9.1 Summary of the film effectiveness work . . . 211
9.2 Summary of the double-wall work . . . 211
9.3 Summary of the numerical evaluations work . . . 212
9.4 Summary of outerskin porosity in a double-wall configuration . . . 212
9.5 Suggestions for Further Work . . . 213

List of Figures

1.1 Rollys-Royce UltraFan® . . . 1

2.1 Schematic of turbine blade cooling techniques . . . 9
2.2 Schematic of an inclined film hole with compound angle . . . 12
2.3 Jet in cross flow . . . 13
2.4 Matrix Cooling Method Concept . . . 14
2.5 Double-skinned effusion cooled blade . . . 18
2.6 DWEC flow migration . . . 18
2.7 Cooling performance with increasing porosity . . . 21
2.8 Schematic of a transpiration-cooled surface . . . 21
2.9 Secondary flows around a nozzle guide vane as presented by Langston [1]. . . . 24
2.10 Deposition of ash on high pressure turbine nozzle guide vanes . . . 26
2.11 Schematic of a de-coupled CHT procedure . . . 32

3.1 Experimental Facility Section View . . . 35
3.2 Test section view . . . 36
3.3 Rohacell magnified view of a 2 mm film hole . . . 37
3.4 Instrumentation of test pieces . . . 41
3.5 TD1 Geometry Schematic . . . 42
3.6 D6 Geometry Schematic . . . 42
3.7 TD2 film side rendering . . . 43
3.8 D6 film-side rendering . . . 43
3.9 Plenum-side rendering for TD2/D6 . . . 44
3.10 Picture of the internal cavity features . . . 44

4.1 CFD domain and boundary conditions - symmetric unitblock. . . . 48
4.2 CFD domain and boundary conditions - periodic unitblock. . . . 48
4.3 Stream-wise development of cooling films, using Sellers Method . . . 50
4.4 Decoupled unit-cell method schematic . . . 51
4.5 Schematic of the semi-decoupled unit-cell method . . . 53
4.6 Circuit diagram of the thermal resistance model . . . 57

5.1 Film effectiveness method comparison - Moderate Pitch . . . 60

5.2 Film effectiveness method comparison - Low Pitch 61
5.3 Schematic of geometric experimental setup for the film effectiveness studies . . 66
5.4 Visualisation of Sellers' superposition method 67
5.5 Annotated schematic of the OTI experimental facility 69
5.6 Comparison area for film span variation study - constant blowing ratio 70
5.7 Comparison area for film span variation study - constant coolant mass flow . . 70
5.8 Effect of film spacing (S_x,S_y) on mean film effectiveness, for $M = 0.5$ 71
5.9 Effect of film spacing (S_x,S_y) on mean film effectiveness - constant mass flow . 71
5.10 TD2 film span variation vs film effectiveness 73
5.11 TD2 film span variation eta_f contours 73
5.12 $m*$ vs eta_f for film span variations 74
5.13 Experimental film effectiveness contours for $m^* \approx 1.8$ 75
5.14 Experimental film effectiveness contours for $m^* \approx 3.2$ 76
5.15 Spanwise-average film effectiveness for $m^* \approx 1.8$ 79
5.16 Spanwise-average film effectiveness for $m^* \approx 3.2$ 79
5.17 Streamwise-average film effectiveness for $m^* \approx 1.8$ 80
5.18 Streamwise-average film effectiveness for $m^* \approx 3.2$ 80
5.19 Comparison of numerical and experimental spanwise-averaged film effectiveness 82
5.20 Comparison of numerical and experimental streamwise-averaged film effectiveness 83
5.21 Comparison of film effectiveness contours between Experiments and Goldstein-Sellers 84
5.22 Highly Porous Plate: η_f contours 1 87
5.23 Highly Porous Plate: η_f contours 2 88
5.24 Highly Porous Plate: spanwise-average η_f 89
5.25 Schematic of film plate for compound angle study 92
5.26 Film effectiveness contours: $m^* \sim 1.8$ 96
5.27 Film effectiveness contours: $m^* \sim 3.7$ 97
5.28 Film effectiveness contours: mass flow $m^* \sim 6.4$ 98
5.29 Compound angles: Spanwise-averaged film effectiveness 99
5.30 Area-averaged η_f and pressure ratio vs m^* for compound angle study 99
5.31 Spanwise-averaged film effectiveness comparison between a Rohacell and perfectly adiabatic material 101
5.32 Contours of the difference in cooling effectiveness on the film-side wall for rohacell and perfectly adiabatic material. 101
5.33 Rohacell impact on mean film effectiveness for film arrays 102
5.34 A) Original 'uncorrected' mean film effectiveness results in [2]. B) Adiabatic correction applied. 103
5.35 TD2 and D6 area-averaged film effectiveness for the IR view area 105

5.36 Film effectiveness contours for TD2 geometry for open compared to closed cell ROHACELL as well as D6 film effectiveness. 105

6.1 Double-wall turbine blade finite element model 114
6.2 Conjugate aerothermal model schematic 115
6.3 Internal convection contribution and overall cooling parameters for a double-wall effusion configuration 116
6.4 Impingement target-surface Nusselt number and mass flow distribution for varying pedestal heights 119
6.5 The impact of pedestal height on the impingement jet structure and the resulting flow and heat transfer characteristics 120
6.6 Minimum film hole mass flow rates and cooling performance for varying pedestal height and inner wall thickness 123
6.7 Thermoelastic properties of the CMSX-4 alloy 127
6.8 Thermal stress fields at the cross-section of the turbine blade model 130
6.9 Variation of the magnitude of the nominal compressive thermal stres 133
6.10 Mechanical analysis results for the double-wall model 135
6.11 Variation of stress quantities for the double-wall model 136
6.12 Annotated schematic of HS2 (T1) 153
6.13 Visualisation of the variation in pedestal height for the HS2 (T1) unit-cell. . . . 153
6.14 Influence of pedestal height and inner-wall thickness on minimum outlet mass . 154
6.15 Impingement Nusselt number for varying pedestal heights and inner-wall thickness 154
6.16 Velocity vectors and pressure for varying pedestal height and inner-wall thickness 155

7.1 Blowing Ratio Variation in TD1 158
7.2 Unit-block Example CFD 159
7.3 Overall Cooling Effectiveness Contours for D6 and TD1 161
7.4 Average Cooling Effectiveness for the External Skin of TD1 vs D6 161
7.5 Influence of Model Domain 162
7.6 Impact of inclination angle on internal cooling CFD 164
7.7 External cooling parameter comparison between numerical methods 167
7.8 Cumulative outlet mass fraction - E2 170
7.9 Cumulative outlet mass fraction - T1 170
7.10 Impact of variable pressure on film effectiveness 171
7.11 Numerical compared to experimental external cooling effectiveness 173

8.1 Visualisation of flow through a typical DWEC system 178
8.2 Renderings of the four unit-cell domains. 180
8.3 Schematic demonstrating implementation of decoupled method 182
8.4 CFD boundary conditions 183

8.5 Stream-wise development of cooling films, using Sellers Method 185
8.6 Proportion of heat flux for each component 187
8.7 Film outlet distribution for T1 and T2 188
8.8 Velocity vectors for two film holes in close proximity to the impingement jet . . 188
8.9 Blackflow pressure margin 189
8.10 Film effectiveness contours for $m^* = 1.7$ 190
8.11 Film effectiveness contours for $m^* = 5.0$. 191
8.12 Span-averaged film effectiveness for $m^* = 5.0$ 192
8.13 Cooling effectiveness contours at $m^* = 1.7$ 193
8.14 Cooling effectiveness contours at $m^* = 5.0$ 194
8.15 Inner and outer mean overall-effectiveness 195
8.16 Experimental cooling effectiveness contours - T2 outerskin-outer 201
8.17 Experimental cooling effectiveness contours - T1 outerskin-outer 202
8.18 Experimental cooling effectiveness contours - E2 outerskin-outer 203
8.19 Experimental cooling effectiveness contours - T2 innerskin-outer 204
8.20 Experimental cooling effectiveness contours - T1 innerskin-outer 205
8.21 Experimental cooling effectiveness contours - E2 innerskin-outer 206
8.22 Experimental area-averaged cooling effectiveness - outerskin-outer 208
8.23 Experimental area-averaged cooling effectiveness - innerskin-outer 208
8.24 Thermal gradient between inner- and outer- surfaces 209

List of Tables

3.1 Typical experimental conditions 37
3.2 Comparison of TD2, TD1 and HS2 designs to Murray's D6 Design 42

4.1 Typical conditions used in conjugate study 47

5.1 Properties for TD2 film spacing variation study 66
5.2 Approximate experimental conditions 68
5.3 Geometric properties of the two high-porosity plates 86
5.4 Approximate aerothermal conditions 86

6.1 Fixed parameters used in the study. 113
6.2 Aerothermal output variables 117
6.3 Geometric parameters 152

7.1 Numerical Method Cost Comparison 165
7.2 Film effectiveness comparison between modelling methods 166
7.3 Cooling effectiveness comparison between modelling methods 166

8.1 Geometric parameters for the repeating unti-cell domains. 180
8.2 Boundary conditions applied to CFD domain. 182
8.3 Overall effectiveness difference between the outer and inner exterior surfaces . 194
8.4 Transpiration Factor for the outerskin external surface 196
8.5 Film Effectiveness: area-averaged and maximum results 198
8.6 Cooling effectiveness on the outerskin outer surface: area-averaged and minimum results 198

Nomenclature

Acronyms

CAD	Computer-Aided Design
CFD	Computational Fluid Dynamics
CMC	Ceramic Matrix Compounds
DNS	Direct Numerical Simulation
DUC	De-coupled Unit-Cell
FEM	Finite Element Method
LES	Large Eddy Simulation
PSP	Pressure Sensitive Paint
RANS	Reynolds-Averaged Navier-Stokes
SSD	Semi-Coupled Streamwise Domain
SUC	Semi-Coupled Unit-Cell
TBC	Thermal Barrier Coating
TLC	Thermochromic Liquid Crystal

Non-Dimensional Numbers

ε_o	Overall effectiveness
η_f	Film effectiveness
ϕ	Porosity
Bi	Biot number
DR	Density ratio
I	Momentum flux ratio
M	Blowing ratio
m^*	Non-dimensional mass flow rate
Nu	Nusselt Number
PR	Pressure ratio
Re	Reynolds number
TF	Transpiration factor
VR	Velocity ratio

Properties

α	Inclination angle	deg
$\dot{m}$	Mass flow rate	kg/s
γ	Compound angle	deg
λ	Thermal conductivity	W/(m K)
ν	Kinematic viscosity	m^2/s
ρ	Density	kg/m^3
σ	Stefan Boltzmann constant	$W/(m^2\ K^4)$
τ	Transmissivity	
ξ	Emissivity	
c_1	Spanwise distance constant	
c_2	Spanwise shaping constant	
c_p	Specific heat	J/(kg K)
D	Diameter	m
H	Height of pedestal	m
h	Heat transfer coefficient	$W/(m^2K)$
P	Pressure	Pa
q	Heat transfer rate	W
R	Thermal resistance	K/W
S_x	Streamwise spacing	m
S_y	Spanmwise spacing	m

T	Temperature	K	x	Streamwise direction	m
t	Time	s	x_{decay}	Film decay variable	
v	Velocity	m/s	y	Spanwise direction	m

Subscripts

aw	adiabatic wall
c	coolant
e	external
f	film
∞	free stream
h	hot gas (main flow)
i	internal
imp	impingement
m	metal
p	pedestal
s	solid
w	wall

1 Introduction

This introductory chapter will outline the background to the problem, highlight the gaps in existing knowledge and finish with an overview of the content contained in the following chapters.

1.1 Background

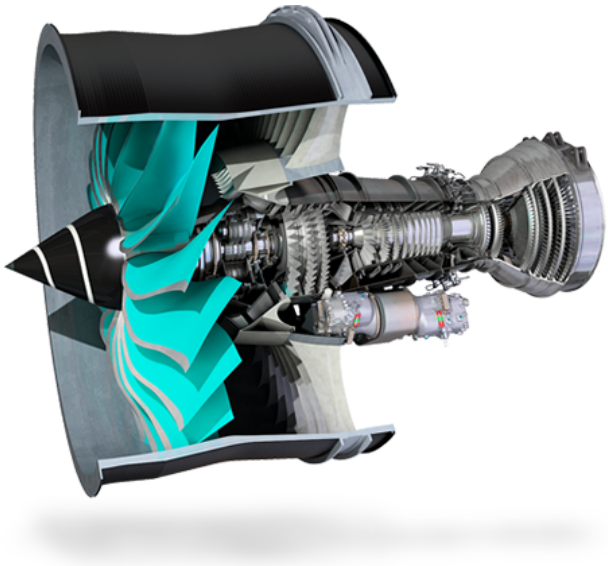


Figure 1.1: Rollys-Royce UltraFan® [3]

Over the last several decades the operating temperature of gas turbines continues to increase, at about 10 K per year. This is largely driven by the 2nd law of thermodynamics, which ensures that an increase in temperature leads to an increase in overall engine efficiency. Consequently, high inlet temperatures are experienced by the turbine, imposing high thermal stresses, especially on the guide vanes and first several blade rows. In addition the blades are subject to high centrifugal loads, high pressures and vibration, leading to turbine blades being the most rejected engine parts during maintenance inspection, whilst also being the most expensive [4]. In order

to reduce the imposed thermal stresses and thus limit replacement frequency and maintain suitable dependability of engines (i.e avoid blade failure), there is a need for turbine blade cooling systems. These can be broadly grouped as: internal cooling, external cooling and thermal barrier coating. The first two techniques require coolant flow to be bled from upstream compressor stages and exhaust from the turbine blade via a mixture of internal passages, pedestals, ribs, impingement jets or film holes. However, the use of any coolant comes with an associated cycle efficiency penalty and potential for aerodynamic losses. Consequently, reducing the amount of mass flow used while maintaining suitable metal temperatures requires further advancement in turbine cooling systems.

Developments in turbine cooling were summarised by Krewinkel [5] and indicate the move from discrete film hole cooling toward effusion and transpiration-like cooling, which is driven by increased efficiency with porosity [6]. Effusion cooling is established by many rows of film holes, while transpiration cooling is associated with the use of porous materials. While manufacturing constraints have kept the latter from being realised, the evolution of additive manufacturing enables the design of novel and small-scale internal structures [7]. Despite this, further research is required to address associated problems, such as blockage [8, 9], risk of hot-gas ingestion [10] and high computational demand [11].

The main schemes investigated in this thesis is that of transpiration and effusion cooling, which both have potential for significant benefits to the aerospace industry. Increased engine efficiency will reduce fuel costs and in turn has the capability to reduce CO_2 emissions by over 180,000 kg per engine per year (2018) [12]. And application to hypersonic vehicles has potential for reduced flight costs and performance.

Transpiration cooling takes advantage of porous walls and injects coolant into the flow, creating a protective film between the surface wall and hot gas. Two main processes are involved to produce cooling:

1. Convective cooling - between the cooling fluid and porous wall, and any other internal features.

2. Film cooling - a layer of coolant air on the external blade surface which reduces the convective heat flux from the hot-gas cross-flow.

While transpiration cooling has been intensively researched for many years, such as early work produced in 1951 by NASA [13], successful application in engines has remained unattainable due to limitations of the porous materials available. Until recently, the strength and oxidation resistance have not favourably compared to cast structures and the porous blades have been susceptible to particle clogging [14]. Difficulties also arose from the control of local permeability which, if not properly implemented, results in local areas of excess coolant - increasing the associated aerodynamic losses. Additionally, accurately modelling the aerothermal and mechanical stress fields remains a challenge as coupling is required between the aerodynamic, thermal and stress fields.

A distinction between transpiration and effusion cooling is worth being made here, as the difference between the two is not always clear. Transpiration cooling theoretically occurs when the coolant and solid are in a thermal equilibrium, which occurs without the effects of radiation. Transpiration cooling is additionally associated with porous media, while effusion cooling generally utilises a number of discrete holes. Krewinkel [5] pointed out that earlier studies have not always fully regarded these fundamental differences.

For implementation on turbine blades, a possible configuration is that of a double-walled structure. Consisting of two walls connected by a thermal tie, the inner and outer wall porosity can be altered to control the level of coolant flow and take advantage of both internal convective cooling and external film cooling. Additionally, the use of more conventional manufacturing materials and methods may be utilised while still meeting the required porosity for effusion and transpiration cooling. The consequences on cooling and aerodynamic performance of transpiration cooling in double-walled configurations must be understood if implementation into engine design is to be realised.

1.2 Research Aims

This thesis documents an investigation into the transition from discrete and full coverage effusion system to that of transpiration cooling by exploring configurations with higher outerwall porosity than previously studied in detail. The following features of double-wall configurations will be assessed:

- Film coverage and effectiveness levels
- Overall cooling performance
- Consequences of internal feature design
- Application for turbine blades

The primary aims of this thesis were as follows:

- Modification and validation of a predictive method for assessment of film cooling and its application to densely packed film arrays.
- Implications of densely packed film arrays on the film protection.
- Comparison of numerical methods which can be used to assess different double-wall cooling designs.
- Assess the impact of increased outerskin porosity on cooling of a double-wall configuration using both numerical and experimental techniques.
- Understand the implications of the innnerskin thickness and pedestal height (spacing between intneral and outer walls) on the aerothermal performance.

1.3 Publications

Journal Papers

Courtis M., Murray A., Coulton B., Ireland P., Mayo I. "*Influence of Spanwise and Streamwise Film Hole Spacing on Adiabatic Film Effectiveness for Effusion-Cooled Gas Turbine Blades*". International Journal of Turbomachinery, Propulsion and Power. 2021; 6(3):37.
https://doi.org/10.3390/ijtpp6030037

Skamniotis, Christos and Courtis, Matthew and Cocks, Alan, "*Multiscale Analysis of Thermo-mechanical Stresses in Double Wall Transpiration Cooling Systems for Gas Turbine Blades*", International Journal of Mechanical Sciences, Volume 207, 2021,106657, ISSN 0020-7403.
https://doi.org/10.1016/j.ijmecsci.2021.106657

Courtis, Matthew and Skamniotis, Christos and Cocks, Alan and Ireland, Peter, "*Coupled Aerothermal-Mechanical Analysis in Single Crystal Double Wall Transpiration Cooled Gas Turbine Blades with a Large Film Hole Density.*", Applied Thermal Engineering, 2022, 119329, ISSN 1359-4311.
https://dx.doi.org/10.2139/ssrn.4102556

Conference Papers

M. Courtis, A. V. Murray, P. Ireland, and I. Mayo, "*Influence of Spanwise- and Streamwise-Film Hole Spacing on Adiabatic Film Effectiveness for Gas Turbine Blades*," Proceedings of 14th European Conference on Turbomachinery Fluid dynamics & Thermodynamics, pp. 1–14, 2021.

Courtis M. and Ireland P. T. "*Influence of Porosity on Double-Walled Effusion-Cooled Systems for Gas Turbine Blades*". ASME Turbo Expo 2022, Turbomachinery Technical Conference & Exposition, June 2022, Rotterdam, The Netherlands. GT2022-80377.

1.4 Achievements

- Validation of a superposition method for film effectiveness, which is a modified version used in [6], for application on densely packed film arrays.
- In comparison to conventional film cooling arrays, the application of densely packed arrays, can promote more uniform film coverage and elevated film effectiveness to protect the turbine blade from the external hot gases. In this way, more effective film cooling may provide the opportunity for reduced coolant mass flow and therefore a more efficient jet engine.
- Co-authored journal paper which showed the stress benefits associated with highly porous outerskin for a double-wall turbine blade [15]. This may result in added reliability and in-service life of turbine blades.
- Validation of a decoupled conjugate CFD technique for porous double wall designs, and a demonstration of its validty in comparison to using a coupled conjugate CFD method.
- Numerical and experimental demonstration of the cooling performance benefits of densely packed film arrays in a double-walled cooling system, over less porous designs. These being: reduced maximum and mean temperatures, reduced thermal gradient between inner and outer walls and potential for reduced coolant mass flow. All of which may result in better in-service life of turbine blades and increased engine efficiency.

1.5 Thesis Outline

The structure of this document is as follows:

- Chapter 2: Literature review of the current state of turbine cooling as well as a review of the various experimental and numerical methods.
- Chapter 3: Description of the experimental facility and methods used.
- Chapter 4: Numerical methods for modelling of internal and exteternal aerothemal characteristics.
- Chapter 5: An assessment of film effectiveness both numerically and experimentally for a range of configurations and parameters.
- Chapter 6: Investigation of internal features, pedestal height and innerwall thickness, on double-wall cooling.
- Chapter 7: Assessment of the numerical methods to one another and experimental results.
- Chapter 8: The impact of external wall porosity on the overall cooling performance.
- Chapter 9: A summary of the findings documented in this thesis and areas for further work.

2 Literature Review

A review of the current and historical developments for turbine cooling shall be provided in this chapter. An overview of typical turbine cooling systems is presented and the progression of three cooling systems from one to another is presented:

1. Film cooling
2. Effusion cooling
3. Transpiration

Focus will be made on double-walled configurations and the opportunity, but also challenges, of transpiration cooling. Finally, a review of relevant experimental and numerical methods is given.

2.1 Cooling System Overview

Gas turbine blades are cooled both internally and externally, as shown in the schematic of the cooling system in Figure 2.1. Internal cooling can be achieved by a range of methods, with current designs using a complement of impingement holes, ribs, pedestals and multi-pass systems (see Figure 2.1). The aim is to enhance heat transfer between the blade and the coolant without sustaining a pressure drop which is too large. Such methods promote fluid mixing as well as an increased wetted area to achieve the designed cooling performance. An additional benefit of some internal cooling methods, such as pedestals, is that they can offer structural advantages. In the case of pedestals they act as a mechanical tie, resisting bursting loads, and a thermal tie, reducing temperature gradients between walls. Conversely, while impingement jets offer an efficient method for cooling performance, they can degrade the structural strength of a turbine

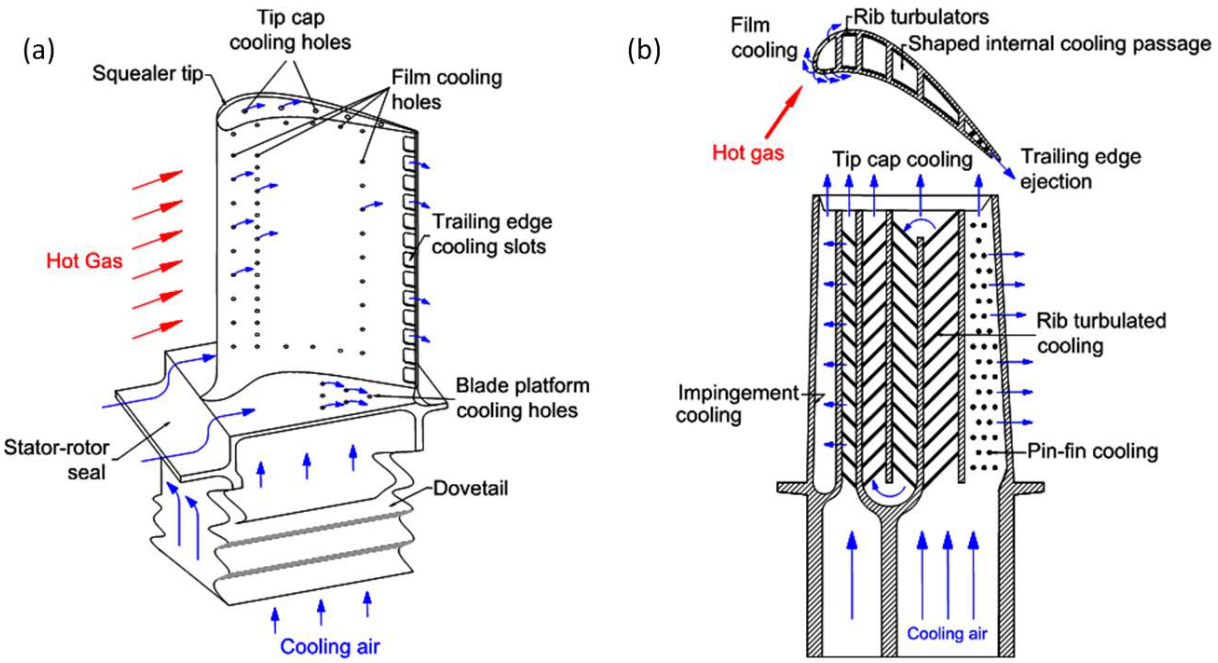


Figure 2.1: Schematic of a turbine blade with common cooling techniques a) External cooling b) Internal cooling [16]

blade [17].

For external cooling, film cooling is the predominate method used and is illustrated in Figure 2.1 a. This is discussed in more detail in Section 2.2. In addition to this, thermal barrier coating (TBC) is often applied on the surface of combustion liners and turbine blades to protect components. TBC is a ceramic material applied to the outer surface of the aerofoil with a complex structure allowing compliance for expansion. Principally it adds an insulating layer which can be treated analytically as equivalent to a reduction in the external heat transfer coefficient. However, TBCs are sensitive to ash and sand deposition, which can cause TBC cracking and reduce the life of the component.

To assess the performance of any cooling system a non-dimensional temperature ratio, often referred to as the overall cooling effectiveness, may be used:

$$\varepsilon_o = \frac{T_{w,0} - T_w}{T_{w,0} - T_{c,i}} \tag{2.1}$$

where $T_{w,0}$ is the wall temperature without any cooling. Consequently, if the coolant mass flow is 0 then $\eta = 0$, and if it is 1 complete cooling is achieved.

The designers usually target a particular effectiveness level to achieve component life, but their design needs to take into account the stage efficiency, the component mass, cost and manufacturing capability.

While turbine temperatures have increased, Horlock et al. [18] demonstrated that the benefits could be marginal once accounting for two important factors. 1) A reduction in inlet turbine temperature due to the increased coolant mass requirements. 2) The pressure drop associated with mixing of the coolant and hot-gas flow. Such findings provide further motivation for more efficient cooling systems which can reduce the required coolant mass fraction.

2.2 Film Cooling

External protection of metal components, both combustor liners and turbine blades, can be achieved by creating a barrier from the hot-gas flow with a layer of coolant flow. However, the amount of coolant should be limited as aerodynamic losses need to be considered due to the associated total pressure loss from the mixing of the coolant with the mainstream flow. Additionally, limiting the coolant mass flow required will reduce any temperature distortions to the mainstream flow. The prevailing technology used to externally cool turbine blades is the inclusion of rows of film cooling through discrete holes. The level of film protection generally increases with the blowing ratio, M, which is the ratio of density (ρ) multiplied by velocity (v) of coolant (c) to that of the mainstream flow (h).

$$M = \frac{(\rho v)_c}{(\rho v)_h} \tag{2.2}$$

However, at a critical M, a phenomenon called coolant lift-off can occur, and as a consequence film cooling protection is hindered. It is also important to try and avoid this film separation to avoid subsequent vortex generation which will induce additional aerodynamic losses without any further film protection benefits. Additionally, suitable levels of film protection are relatively short-lived as the film mixes with the mainstream. Subsequent rows are therefore required to provide further protection. From equation 2.2, one can see that M is a combination of two

important scaling parameters: density ratio (DR) and velocity ratio (VR), defined as:

$$DR = \frac{\rho_c}{\rho_h} \tag{2.3}$$

$$VR = \frac{v_c}{v_h} = \frac{M}{DR} \tag{2.4}$$

An alternative to the blowing ratio for scaling from engine to laboratory conditions is the momentum flux ratio (I), which is defined as:

$$I = \frac{\rho_c v_c^2}{\rho_h v_h^2} = \frac{M^2}{DR} \tag{2.5}$$

This parameter captures the ratio of momentum flux between the coolant and hot gas, and thus the ability of the mainstream to turn the coolant jet towards the wall. At low momentum flux ratios, the coolant remains close to the surface, while at higher flow rates the momentum of the jet results in the coolant moving away from the wall.

Many experiments performed in laboratory studies result in density ratios which differ from engine conditions, as matching density ratio may involve more complex and expensive setups. As a consequence the question of which of the three scaling factors between M, VR and I are the most appropriate to match arises. This question has been considered by many research groups, but most notably at the University of Texas at Austin led by David Bogard. Sinha et al. [19] investigated the effect of varying density ratio (DR = 1.2, 1.6 and 2.0) for cylindrical holes inclined at $\alpha = 35^\circ$ and a pitch of $S_x/D_f = 3$, with M = 0.25 to 1.00. It was demonstrated that the density ratio had a significant impact, and while the centreline effectiveness could be scaled with velocity ratio, the lateral spreading could not be conclusively scaled by any of the remaining parameters. This was again found in [20] where in both cylindrical and shaped holes, both M and I didn't provide cooling performance which was fully independent of the density ratio. Additionally, research at the University of Oxford [21] demonstrated that for calculation of the aerodynamic losses of a film cooled aerofoil, the momentum flux ratio was more appropriate than the blowing ratio.

$$\eta_f = \frac{T_{\infty,0} - T_{aw}}{T_{\infty,0} - T_{c,e}} \tag{2.6}$$

An important parameter used to express the performance of a film cooling system is the film effectiveness η_f, defined by equation 2.6. $T_{\infty,0}$ is the total mainstream temperature, $T_{c,e}$ is the exit total temperature of the coolant and T_{aw} is the adiabatic wall temperature on the external blade surface. Given this definition, a value of 1 would indicate complete protection from the external hot-gas and a value of 0 means there is no film cooling effect present. One must consider the total temperature as the transfer of energy is influenced not just by the heat energy (represented by static temperature) but also by the kinetic energy of the gas (accounted for in the total temperature), and therefore the total temperature provides a more accurate assessment of the thermal load a blade must withstand. In high speed flows the difference between total and static temperature becomes more pronounced and therefore it is an important distinction which is often neglected.

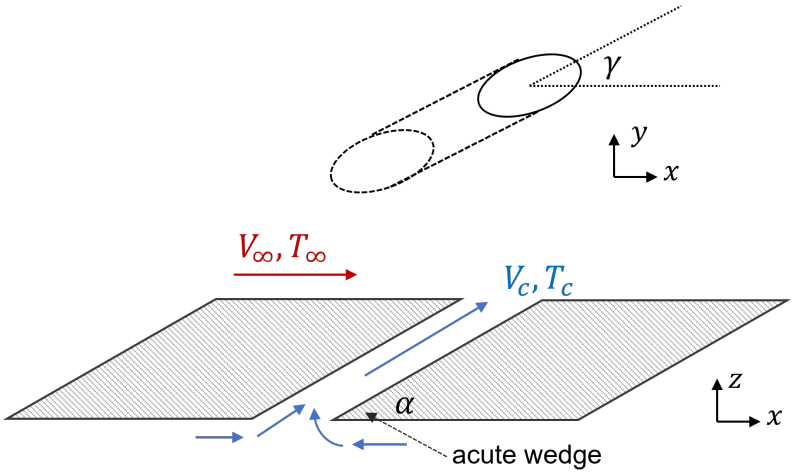


Figure 2.2: Schematic of film cooling hole with inclination angle, α, and compound angle, γ.

The flow from the film cooling hole is similar to a jet in cross-flow and the interaction between coolant and external hot-gas flow is fundamental to its behaviour. A visualisation of the typical flow structure is shown in Figure 2.3. Inside the film hole itself a vortex system is established from the separation of the flow as it travels around the sharp edged intake, known as the acute

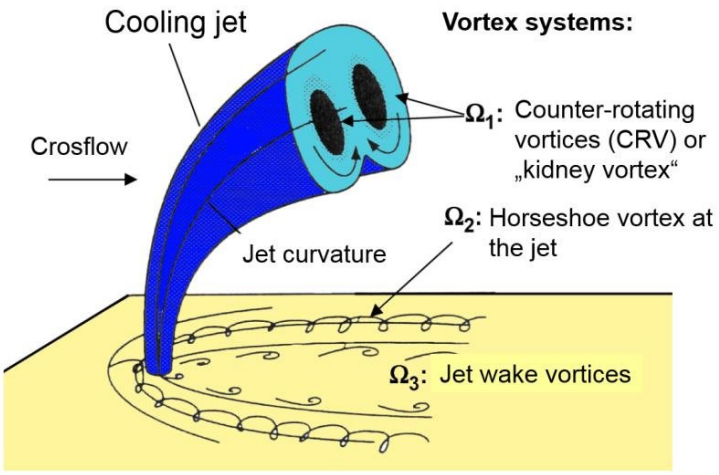


Figure 2.3: Visualisation of a jet in cross-flow and induced vortical structures, reproduced from [22].

wedge illustrated in Figure 2.2 which creates a re-circulation region and a jetting effect on the opposing side. The result of this is a counter-rotating vortex pair and its strength will mainly be determined by the Reynolds number of the film hole. As the flow emerges into the mainstream a counter-rotating (kidney) vortex pair develops (Ω_1). The exact nature of the pairs formation is dependent on the density ratio, hairpin vortices for low density ratio and the jet shear-layer vortices for high density ratio [23]. Ultimately the induced vortex pair is the primary contribution to entrainment of the hot-gas as one moves further downstream [24]. The behaviour results in the degradation of the film protection with streamwise distance. The horeshoe vortex, Ω_2 is much smaller in scale and in turbulent cases is not present as the boundary layer does not separate at the leading edge [23].

The design of film holes differ between manufactures and engine designs. The hole shape has been extensively studied [25, 26, 27] with recent focus on optimisation of hole shape [28] and the use of slots at the trailing edge [29]. General features for current hole designs include hole inclination angle, compound angle, length-to-diameter ratio and shaped holes. Inclination of the hole can increase the cooling effect, for a given wall thickness, due to the increased surface area [30]. As an additional benefit, the coolant jet exits at an angle close to the wall direction, and consequently is more likely to follow the blade surface. The use of compound angle, the orientation of the film hole centreline to the streamwise direction, was shown to benefit the overall film protection [31, 32, 33], by increasing the lateral coverage and delay of jet lift-off.



Figure 2.4: Matrix cooling method concept on an experimental setup for a nozzle guide vane [35].

Moreover, compound angle can be particularly useful in areas where an aligned film hole would be difficult to manufacture, such as the turbine leading edge. Shaped or combined-hole strategies can be used to elevate the film effectiveness, but at some manufacturing cost and difficulty. Holes with a diffuser exit shape have been shown to increase film effectiveness [34], especially at high blowing ratios. Deceleration of the flow in the diffuser section results in the coolant film more closely following the blade surface, thus the coolant can spread more laterally.

Combined-hole designs include: sister holes or combined triple-jet holes [36] where two smaller holes are placed in close proximity laterally to the main cooling hole; anti-vortex holes [37] where two side holes are drilled to intersect with the main cooling hole; and double-jet holes [38], where two cylindrical holes of opposite compound angles are used. For all the combined hole schemes, the aim is to reduce the impact of the kidney vortex and its interactions with the mainstream flow. Additionally, the increased internal surface area promotes higher convective cooling inside the film holes. Another scheme for use in regions of high thermal loads is that of Matrix Cooling Method where multiple intersecting holes are closely packed resulting in high internal surface area. This concept is visualised in Figure 2.4 and shown to provide efficient cooling for leading edges of nozzle guide vanes and turbine blades [35]. Despite the benefits of more complex hole shapes, in thin aerofoils or when requiring small film hole diameter, manufacture limitation may prohibit their application. In this way, either simple inclination and/or compound film angled holes may be more suitable.

The application of films on turbine aerofoils is further complicated by the surface curvature. The blade shape has convex curvature at the leading edge and suction side, and concave curvature on the pressure side. This curvature results in external normal pressure gradients to the blade surface which can be either beneficial or detrimental to film cooling. For convex curvature, if the momentum of the jet tangentially to the wall is low, then the external normal pressure gradient will drive the flow towards the wall. For a concave surface an increase in tangential momentum will push the jet into the wall, however this can work in opposition to the normal momentum which works to promote jet lift-off, further highlighting the importance of shallow inclination angles. In general, at low blowing ratios, convex curvature benefits film effectiveness compared to a flat plate, while concave curvature is detrimental [39].

At the start of the blade's service life the surfaces will be smooth, however with added time-in-service the blade will wear, experience deposits of solid and face oxidation damage, increasing the surface roughness. Goldstein et al. [40] investigated the impact of surface roughness on film effectiveness for one- and two- row film cooling using a flat plate facility. They showed roughness was responsible for a reduction in the average film effectiveness for low blowing ratios, but an increase for higher blowing ratios. Schmidth et al. [41] compared smooth and two roughness surfaces for a single film hole row and found reduced film effectiveness along the centre-line downstream of the hole, but some improvement on the lateral spreading further downstream of the film hole. They concluded that despite the small improvement in film effectiveness, increased hot-gas heat transfer rates would result in a reduction in the overall cooling performance. It appears roughness will raise the turbulence levels in the near-wall region, but the significance of this on cooling performance is dependent not only on the levels of roughness but the mainstream turbulence. Turbulence levels are high from the combustor, and vanes experience turbulence in the range of 7% to 20% [42]. For low momentum jets, turbulence reduces film effectiveness as increased mixing of the mainstream occurs. However, at high momentum flux ($I > 1$) the turbulence can reduce the impact of jet lift-off by returning some coolant to the blade surface [43].

The use of multiples film rows arranged in arrays increases the cooling coverage over a blade, while also providing additional surface area between the hole and internal coolant which promotes convective cooling. Additionally, Foster and Lampard [44] observed that a reduction in spanwise hole pitching decreased jet lift-off, due to a reduced blowing ratio, and a formation of a near continuous film. The increase in cooling effectiveness has also been attributed to a reduction in mixing in the boundary layer [45]. Moreover, Jiang et al. [46] showed that an adjacent film pair would complement the film effectiveness through entrainmemt of the adjacent coolant by vortex interaction. One outcome of this work at Oxford was an enthusiasm to research full-coverage discrete-hole film cooling, now referred to as effusion cooling.

2.3 Effusion Cooling

2.3.1 Overview

Advancements in cooling systems have led to larger and more complex array systems of cooling holes with smaller diameters, resulting in effusion cooled systems. Initially, this transition to effusion was made for combustion liners, with two main technologies emerging: Lamilloy® and Transply. The former was developed by the Allison Engine Company and consists of laminated, photo-etched metal sheets which form a porous medium [47]. This technology was used by GE/Rolls-Royce for the combustion chamber of the F136 aircraft engine [48]. Transply is a Rolls-Royce technology produced by brazing together several laminates of a high-temperature alloy containing a multiplicity of interconnecting flow passages [49]. Fundamentally, the two have the same limitations: high manufacturing costs, poor repeatability, and lack of mechanical strength limiting the practicality of application to turbine blades. Oxidation resistance is another concern as it can reduce the porosity over time. Hickel et al. [47] demonstrated that, for Lamilloy and wire-wound porous material, coolant flow decreased with time. During a test programme, the Lamilloy specimen was found to be completely clogged after about 440 hours at 1094°C. However, it was noted that the results were probably pessimistic, as the airflow through the material during high temperature exposure was not accounted for. Despite these limitations, early work [45, 50] to understand the perceived advantages and limitations of quasi-transpiration and transpiration cooling are founded on such schemes.

Effusion cooling for a turbine blade application was considered in a study by Battisti et al. [14] who reported the benefits of an effusion cooled system formed by an electro-forming process called Poroform®. There authors stated that this method provides a reasonably easy manufacturing process which integrates construction of the component with the cooling system, while having strict tolerances and high repeatability. The coolant injection speed was inherently limited by the natural divergence of the holes and by adjusting the diameter and distribution of the holes the required cooling capacity could be realised. Experiments demonstrated the production of a uniform temperature distribution and withstanding of blade temperatures up to 1200 K, while maintaining a low coolant mass flow (0.02% of the main flow). However, acceptable mechanical strength and fatigue endurance at high temperatures were not demonstrated.

An excellent review of effusion cooling studies was made by Krewinkel in 2013 [5]. This includes a comparison between film and effusion cooling, the effects of parameters such as hole spacing, and example designs applied to gas turbine blades. It was shown that an arrangement of effusion holes staggered with respect to the injection holes, for impingement cooling, by half the effusion hole pitch gives higher heat transfer in comparison to a shifted or an in-line arrangement. This is a consequence of the large primary vortex and counter-rotating vortices which are generated by the staggered arrangement [51]. Surface roughness in the effusion holes can enhance the cooling effectiveness, η, and consequently the way in which the aerofoils are manufactured has an influence on performance [50]. The overall cooling effectiveness of blades depends on the convective cooling in both the cooling holes and internal structure, as well as the thermal conductivity of the base material; hence the need for coupled Finite Element Modelling and Computational Fluid Dynamics (FEM/CFD) solvers or fully conjugate calculations [52].

2.3.2 Double-Walled Systems

Recent developments at the University of Oxford Thermofluids Institute have focused on Double Walled Effusion Cooling (DWEC) systems [6, 53, 54]. Principally, consisting of an inner skin with impingement holes through which coolant enters an intricate chamber, and impinges

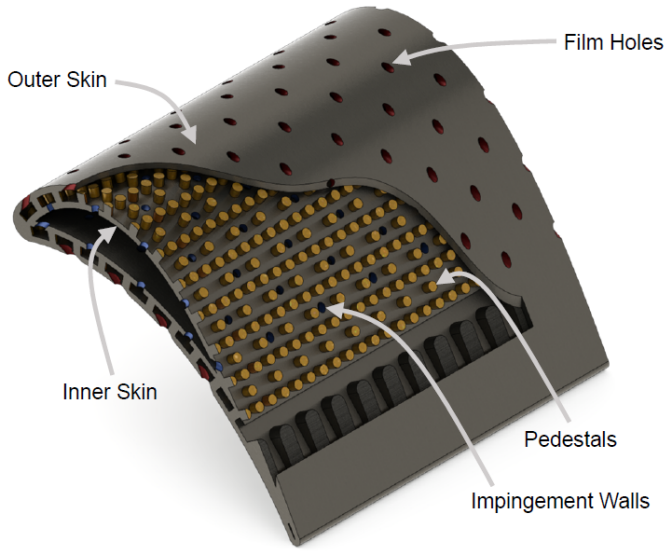


Figure 2.5: Double-Skinned Effusion-Cooled Turbine Blade, Murray et al. [6]

on inner surface of the outer skin with film holes in a regular array, which the coolant exits through. This is illustrated in Figure 2.5. The two walls are mechanically and thermally connected by pedestals, which provide an increase in wetted surface area and enhanced flow mixing, and thus increased heat transfer. Both studies successfully used a de-coupled conjugate heat transfer approach, developed by Murray et al. [10], this method is discussed in more detail in Section 2.6.2. It was shown [6, 54] that the overall cooling effectiveness was dominated by internal convective heat transfer, a consequence of impingement cooling and a large array of pedestals.

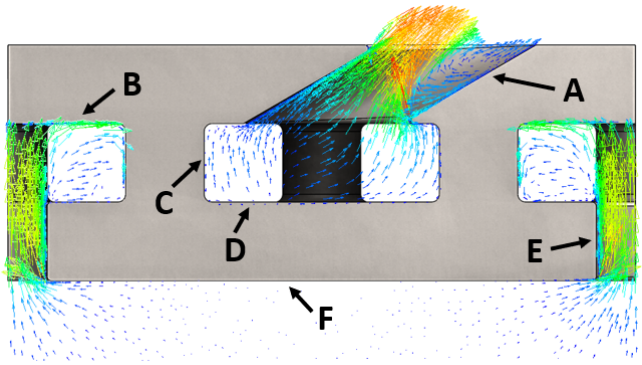


Figure 2.6: Visualisation of flow migration through a typical DWEC system. Labelled components are as follows: A) Film Hole B) Outerskin-inner surface C) Pedestal D) Innerskin-inner surface E)Impingement Hole F) Innerskin-outer surface.

An overview of a typical DWEC system is provided here and a visualisation of such a system is shown in Figure 2.6. Coolant enters the system through the impingement holes and picks up an

amount of heat along the outer-surface of the inner wall (denoted as F in Figure 2.6) as well as along the surfaces of the impingement holes (denoted as E in Fig 2.6). In such a configuration, walls F will have the lowest metal temperatures as they are located above the internal cooling feed. The outer wall where the inclined film holes are located experiences high heat loads from the external mainstream flow, thus the peak metal temperatures are observed here. Given that low metal temperatures occur in the above regions, only a small fraction of convection cooling takes place at F and E. As flow is restricted through the impingement hole, the coolant velocity increases and an impingement jet is formed which travels across the inner cavity and stagnates on the inner hot wall surface (denoted as B in Figure 2.6).

The impingement jets have two main purposes: they act to enhance the heat transfer coefficient with high values realised near the jet stagnation region on the target surface. They are also responsible for a significant fraction of the pressure loss, so can be used in the design to set the the flow rate. Impingement jets often contribute the major share of overall cooling enhancement for double-wall effusion/impingement configurations but this is dependent, among other factors, on the outer-wall thickness. For a thin wall, the impingement contribution dominates, while for a thicker wall the effusion holes may contribute a similar or greater share [55]. This split will also be strongly determined by the outer-wall porosity of a turbine aerofoil. As the porosity increases the internal wetted-area will increase which provides additional surface and for the same internal heat transfer coefficient, this will result in elevated cooling performance. For the outer wall as the porosity increases the share of the cooling performance by the effusion holes will rise, and can begin to dominate the overall cooling performance. Porosity will also strongly influence the pressure drop of a double-wall configuration. For low porosity, the pressure drop will be high, but as it is increased the pressure drop will be reduced for a given mass flow rate. The nature of where the main pressure drop occurs is determined by the difference in porosity between the inner and outer walls. For effusion configurations, the inner wall has a lower porosity than the outer wall and consequentially will dominate the overall pressure drop.

The coolant flows radially out from the stagnation point as a wall jet parallel to the wall surface moving radially outwards until either obstructed by the pedestal surfaces (denoted as C in Fig-

ure 2.6) or migrating towards the film holes or moving downwards as a fountain jet toward the innerskin. A convective cooling benefit within the film hole will occur as well as a reduction in external heat flux associated with film cooling. It should be acknowledged that the acute wedge of the internal film hole rim may cause a separation bubble to form as the coolant turns to enter the film holes and is expelled to the outer surface. Depending on the aspect ratio and the operating condition, the flow may not reattach to the film hole surfaces. Consequently, the effective outlet area would decrease, and a relatively high film jet velocity can be observed. This condition implies that jet-lift off occurs at relatively lower blowing ratios than expected and that the film jet detaches from the outer hot wall surface, causing a reduction in film protection.

Miller et al. [56] investigated the use of a coupled impingement-effusion cooling system and the influence of the target spacing, defined as the height of the cavity between the inner and outer walls, H. For low target spacings ($H/D_{imp} < 6$) there was significant variation of the Nusselt number on the target surface, while for large spacings ($H/D_{imp} > 10$) this was relatively uniform. It was also observed that a staggered arrangement for the film holes in relation to impingement jets promoted a stronger and more even coverage provided by the radial jet which emerges from the stagnation point. For film holes closer to the impingement stagnation region, flow was redirected away from the target surface, reducing the effectiveness of the impingement jet. Cho et al. [51] also demonstrated that staggered spacing had the best thermal performance, compared to inline or shifted arrangements ($3000 < Re_{imp} < 14{,}000$), and double wall configuration was superior to either solely impingement (50% increase) or effusion cooling (3-4 times more).

Motivation for an increase in the number of film holes is shown in Figure 2.7 [6]. A larger effective porosity ($\phi_{eff} = C_d \times \phi$) led to an increase in overall- and film- effectiveness, for the same pressure ratio across the double-wall. Additionally, the same trend was observed as the pressure ratio increased, but with less benefit at increased pressure ratio. As previously mentioned, the impingement holes act as an important flow rate controller through a double-wall system, and as the outerskin porosity increases the overall discharge coefficient will be mostly determined by the innerskin. As a result, increased outerskin porosity may be considered

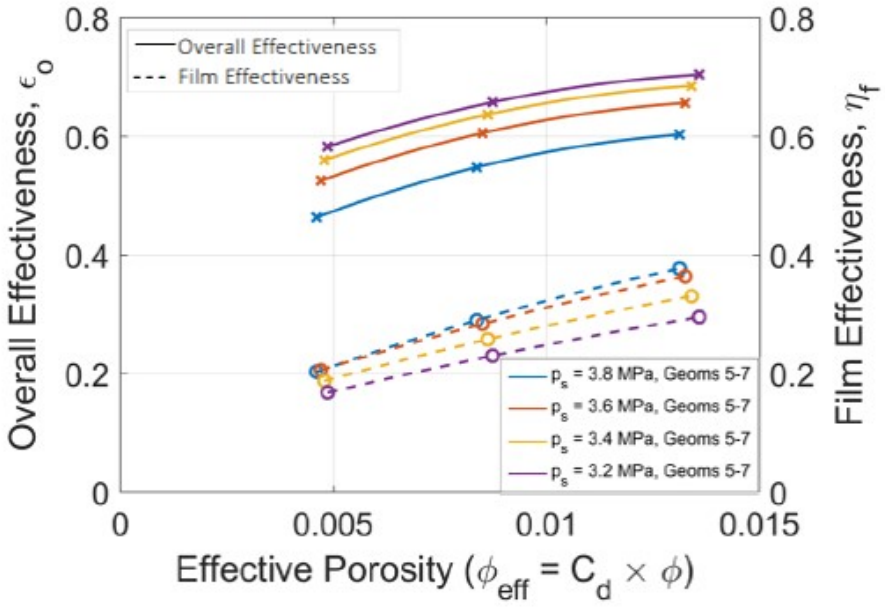


Figure 2.7: Benefit to cooling performance with increased effective porosity [6]

without the need to change the feed pressure. This fact is important to enable novel blade designs to be incorporated into the current engine architecture. Consequently, more porous geometries are of interest, naturally leading to the consideration of transpiration cooling.

2.4 Transpiration Cooling

2.4.1 Main Principles

Transpiration cooling is the use of porous media with the aim to achieve thermal equilibrium between coolant and solid. A basic overview of transpiration cooling principles will be presented here. For a more detailed explanation of transpiration cooling Langener's 2011 PhD thesis [57] is recommended, as well as a review of transpiration studies by Polezhaev [58].

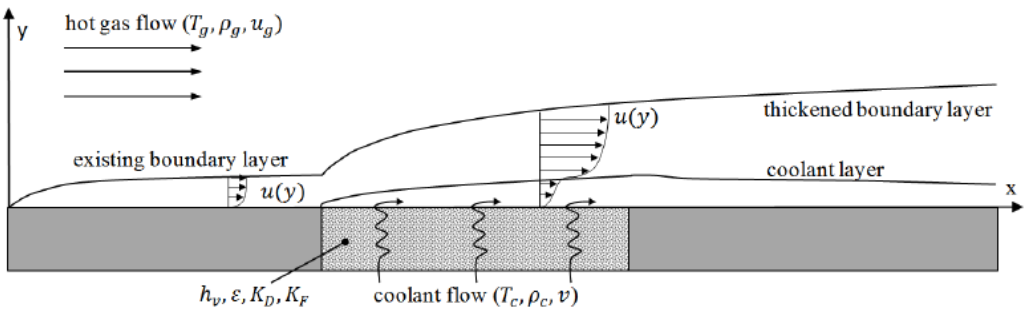


Figure 2.8: Schematic of a transpiration-cooled surface [59]

Application of a transpiration scheme can be achieved in several ways: fine laser drilling, single or multi-layered perforated metal, or a more advanced approach using multi-layered porous media. Regardless of the manufacturing method, the aim is to create a good layer of protection using a coolant layer which develops over the surface and will thicken due to the injected coolant (illustrated in Figure 2.8). Reducing velocity and thermal gradients near the wall - the principle here is the same as a full-coverage film cooling technique.

2.4.2 Historical Development

In the early 1950s, Eckert and Livingood [25] made, to the author's knowledge, the first study to compare transpiration cooling to convective and film cooling techniques. A flat plate with uniform freestream velocity and temperature was modelled analytically for the three methods. The authors found that transpiration cooling achieves the same cooling effectiveness as the other cooling technologies but with lower coolant mass flow, and was therefore judged the superior technique. They noted that the benefit of transpiration cooling was reduced when radiation was included, but the radiative heat load is often negligible in high pressure turbine applications. It was also demonstrated that, as the number of slots for film cooling is increased, the effectiveness approaches that of transpiration. However, it was pointed out that film cooling can be superior for cooling a specific location. The benefits of transpiration cooling over traditional film cooling were also reported in 1970 by Langanelli [60].

A later study, conducted in 1986, by Andrews et al. [45] investigated the contribution of film cooling to the overall cooling effectiveness in geometries relevant to combustor wall cooling. A porous stainless steel material was used to simulate a transpiration wall which was subject to a mainstream flow with a Mach number of 0.047 at approximately 750 K and coolant at 292 K. It was found that the thermal boundary layer thickness increased with axial distance, and that the data approached an asymptote. Film cooling made a major contribution to overall cooling over all coolant flow rates. At higher coolant flow rates, there was no observed promotion of turbulent mixing as the coolant film remained attached - unlike effusion cooling. This is likely a consequence of the possible absence of film hole separation and/or negligible disturbance to the boundary layer due to blowing ratios which contrasted to the higher local flow rates for film

cooling with discrete holes. Additionally, a large pressure drop across the porous wall results in low injection velocities of coolant, and therefore reduced disturbance to the mainstream flow. Transpiration cooling was compared to a full-coverage discrete-hole film cooling system and, at low flow rates of coolant, the film cooling performance was comparable. Again transpiration cooling had a higher overall performance compared to discrete film hole cooling due to increased internal wall heat transfer.

Despite the theoretical benefits of transpiration cooling, there are several challenges beyond the manufacturing capability for the implementation of a transpiration cooling system. The distribution of coolant must be controlled to avoid excessive quantities of cooling air issuing to regions of low external static pressure, resulting in regions of over-cooling, which can induce high temperature gradients in the vicinity of coolant release [58]. In practice, the distribution of flow rate may be controlled through predicting the pressure difference required for a given coolant flow rate and controlling local permeability by adjusting the effective discharge coefficient and porosity of the blade. While, the cooling benefit of transpiration cooling was seen for much of the blade profile, Wang et al. [61] suggested that a more traditional method, such as a film cooling slot at the trailing edge may be advantageous. Additionally, the authors noted the ability to manufacture a porous skin for a thin trailing edge may limit transpiration cooling's application in this location.

Any external cooling which introduces coolant to the mainstream flow results in an aerodynamic loss. This is due to mixing of the mainstream and injected flows, possible increase in the effective wall roughness, sub-standard design of the porous blade profile, flow separation and vortex generation [58]. Bayley [62] found that the introduction of coolant reduced the skin friction drag, and coolant flow rates had negligible effects on velocity distribution, but had only a small effect on the profile loss coefficient.

$$Y_p - Y_{po} = \frac{\gamma Ma^2 \dot{m}_c / \dot{m}_\infty}{(1 - P/P_t)} \tag{2.7}$$

Where γ is the ratio of specific heats, Ma is the Mach number and P and P_t are the static and

total pressure.

2.4.3 Application to Nozzle Guide Vanes

Nozzle guide vanes are located immediately downstream of the combustion chamber with the primary role of turning the hot gases toward the turbine blades for optimal alignment. The vanes must be aerodynamically efficient to reduce any energy losses which could impact engine efficiency and ensure that the turbine receives a relatively uniform flow. Given the location of the nozzle guide vanes, they are exposed to some of the highest temperatures and heat loads of the entire engine. As such, any improvements in cooling system technology are most critically applied to the nozzle guide vanes. Additionally, exposure to high pressures result in the need to balance the high cooling demands with maintaining suitable pressure margins in order to avoid hot-gas ingestion.

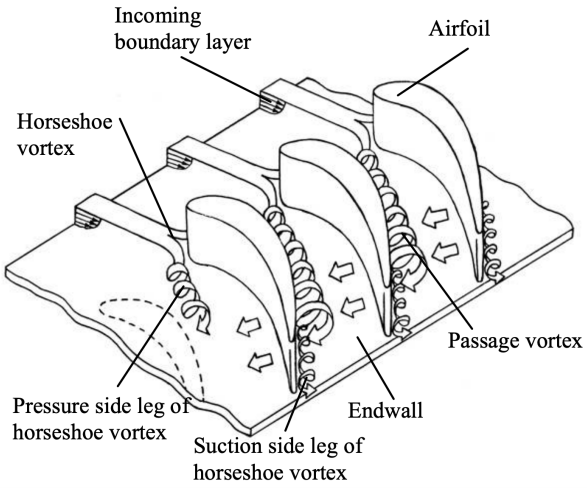


Figure 2.9: Secondary flows around a nozzle guide vane as presented by Langston [1].

The leading edge faces the most significant thermal challenge and application of highly efficient cooling systems is critical but requires careful design to maintain the sufficient coolant pressure margin and prevent films from jet lift-off. Compared to the leading edge, the pressure side has a more favourable environment for transpiration cooling, with a relatively lower risk of film jet lift-off and better coolant pressure margin. For the suction side, lower heat fluxes are present but higher risk of flow separation characterise this region. A benefit of transpiration cooling is that the film layer inherently has low tangential momentum and therefore film adherence to

the turbine surface is more likely compared to conventional discrete-film cooling. Toward the trailing edge the pressure gradient can affect cooling effectiveness [63] and there are increased challenges due to vortex shedding. Moreover, the presence of the horseshoe vortices present further complications.

The incoming boundary layer at region of the end-wall and the nozzle guide rolls up into a horseshoe vortex which splits around the pressure and suction surfaces, illustrated in Figure 2.9. The pressure side will develop into a passage vortex and move toward the suction surface. The risk to the suction surface is that the vortical structures can sweep away coolant and exposing susceptible areas to increased heat transfer coefficients. Further research and development is required to understand the feasibility of transpiration systems given the existence of complex flow patterns.

2.4.4 Hole Blockage

The problems associated with volcanic ash ingestion into aeroengines came to a head with the eruption of the Icelandic volcano Eyjafjallajökull in 2010. This event grounded 1000s of flights causing enormous disruption to flights across Europe. Wylie et al. [64] demonstrated the importance of metal temperature, particle diameter and film cooling hole angle on the rates on ash deposition in cooling hole passages. Most notably the authors found that higher metal temperatures resulted in further deposition causing a positive feedback loop as deposition increased temperature are therefore the likelihood of blockage. While volcanic ash clouds are rare events for aviation operation, particle-laden environments are more common with added aviation demand in Asia and the Middle East. A visual in Figure 2.10 shows the potential impact when turbine engines come in contact with volcanic ash clouds.

Similar to volcanic ash studies, high metal temperatures raising the risk of blockage was observed for other fine particles (sand), by Varney et al. [9], and raised coolant temperatures shown to have a stronger effect. Additionally, the dependence of the coolant hole angle in relation to the coolant flow direction on blockage was determined, with high inclination angle promoting

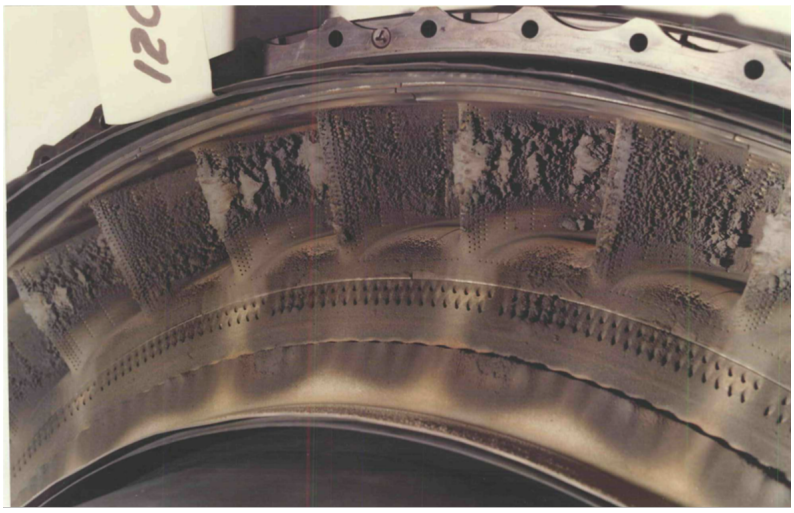


Figure 2.10: Deposition of volcanic ash on high pressure turbine nozzle guide vanes of a Rolls-Royce RB211-524C engine [65].

added deposition as the particles fail to make the turn through the film hole and deposit inside.

As cooling systems move toward transpiration cooling, the susceptibility of clogging may be even more significant. Consequently, current issues of sand and ash deposition experienced by state of the art engines may be aggravated. Huang et al. [66] investigated the effects of blockage as a consequence of introducing partition walls used to enable an increase in ultimate tensile strength for sintered porous plates. The porosity was close to 30%, and the resultant blockage to holes only had a minimal influence to the film protection. Even with 60% of holes blocked the performance was comparable, indicating this method may be suitable to tailor coolant for specific blade regions. Similar studies by Yang et al. [8, 67] found that the blockage ratio was a dominating parameter for cooling effectiveness, and that the impact on upstream regions was more sensitive to higher blockage. High temperatures could degrade performance as permeability can be a function of temperature, often decreasing with increasing temperature [68]. In addition to this, oxidation can increase due to the high surface area to volume ratio of porous materials.

Hole blockage is a problem faced by current turbine blades, and given the operating fleet in the Middle East is projected to double in the next 20 years [69], understanding and mitigating the impact on future engine design will provide a key competitive advantage. However, further research is required to assess how the risk of hole blockage changes as porous wall designs

replace conventional cooling systems. While the likelihood of a single hole blockage event may increase, the nature of large film hole arrays provides a larger level of redundancy.

2.5 Experimental Methods

For turbine engine design, both aerodynamic and heat transfer measurements are required to assess the performance of transpiration cooling systems. The importance of the former is that understanding here enable the designer to assess flow interactions and fluid properties, which will have consequences on the thermal field, as well as the overall engine performance.

2.5.1 Aerodynamic Measurement Techniques

Understanding the aerodynamic behaviour of a cooling system is important to enhance cooling efficiency as well as minimise aerodynamic losses. Therefore, velocity and pressure measurements are required to understand flow characteristics.

Velocity measurements can be made using methods such as thermal anemometry, laser anemometry or pressure measurements. Thermal anemometry offers high spacial resolution of the instantaneous fluid velocity and can be used for boundary layer measurements. Laser anemometry methods, such as Particle Image Velocimetry (PIV), are now widely used in the turbomachinery field and a study by Basley et al. [70] used a large-scale close-loop wind tunnel at Imperial College to investigate the boundary layer and mechanisms of mixing in effusion films. A major benefit is that they are non-intrusive so as not to disturb the flow field. However, seeding of the flow, access and expense are challenges not to be under-estimated. As in the case of the Imperial College experimental setup where the wind tunnel cross-section was 10x5m and over 15m in length.

Pressures can be determined from static pressure tappings along a surface or the use of probes placed in the flow. Pneumatic probes are robust, can be small in size and can measure both static and stagnation pressures. Consequently, they are the most commonly used. If a high response is required, high frequency pressure transducers can be utilised, although they tend to be slightly larger in size.

2.5.2 Heat Transfer Measurements

Direct thermal measurements can be performed using thermocouples, infrared (IR) thermography, temperature sensitive paints or thermochromatic liquid crystals (TLCs). All such methods involve creating a temperature difference between the mainstream flow and the coolant, and for reliable measurements, the measurement surface is usually made of low conductivity material to ensure a wall surface temperature that responds in a well conditioned way to the thermal property (heat transfer coefficient or film effectiveness) being measured.

Infrared thermography provides a non-invasive means of measuring the heat transfer distribution over a solid surface with only a single transient test. Despite the relatively high cost of an IR camera and IR-spectrum transmission window, detailed, spatially resolved heat transfer measurements can be measured. The main advantages of this method are minimal surface preparation, less restricting temperature limits compared to TLCs (as long as the material has low conductivity) and that an initial temperature distribution is obtained. This method has been used in both effusion [10] and transpiration [57] cooling studies with great success.

TLCs can be used in both steady state and transient experiments. They are organic compounds which reflect different colours based on local temperature resulting in detailed surface temperature measurements. A review of their use within the field of heat transfer and aerodynamics is given by Ireland and Jones [71]. An advantage is that they can cover the complete surface giving global temperature and shear stress measurements. Drawbacks to using TLCs include a limited temperature range ($\approx 20^{\circ}$) and sensitivity to the illumination source, as well as camera position. A limitation which may be critical in a high porosity medium is that the post-processing model may not correct the temperature distributions with sufficient accuracy [72].

Despite the use of low conductivity materials, conduction issues can still occur. However, this problem can be mitigated using the heat-mass transfer analogy, first developed by Schmidt [73] and Nusselt [74]. This method relates the energy and diffusion equations which, with the correct assumptions and validation, can produce identical solutions for the same boundary conditions.

Experimentally this method can be achieved through either the ammonia-diazo technique or the Pressure Sensitive Paint (PSP) technique, which is well described by Caciolli et al [72]. PSP uses luminescent molecules sensitive to oxygen concentration which emit light depending on the oxygen concentration - a consequence of oxygen quenching. Film cooling effectiveness can thus be expressed by equation 2.8, using measurements of the mass fraction of oxygen, C.

$$\eta_f = \frac{T_h - T_{aw}}{T_h - T_{c,e}} = \frac{C_h - C_w}{C_h} \tag{2.8}$$

As an example, air could be used as the main flow gas and nitrogen as the coolant flow, and thus the light intensity would be representative of the coolant flow. A drawback is that PSP is temperature dependent and thus the coolant and mainstream flows should be maintained at the same temperature. Additionally, optical access is required, although this is also true for alternative methods, such as TLC. It has also been argued by Caciolli et al. [72] that PSP is a superior steady-state method, without the need for correction in data post-processing.

2.6 Numerical Methods

2.6.1 Review of Methods

Directly solving Navier-Stokes can be achieved by Direct Numerical Simulations (DNS), or partly using Large Eddy Simulations (LES), but incur high computational demand, limiting their application. LES has produced promising results for film cooling rows [75], which was validated against experimental results [76] using a PIV method. For turbine blades, the use of Reynolds-Averaged Navier-Stokes Simulations (RANS) has been the predominant method for computing the aerodynamic impacts of a cooling system. However, lower fidelity occurs from the use of a turbulence model, which will is inherently based on empiricism. Although, even RANS simulations can become numerically taxing and a study by Jiang et al. [77] indicated that large computational mesh sizes (51 million elements for a 40 hole geometry) were required to adequately capture films for effusion cooling. Consequently, lower fidelity methods may be used, and film effectiveness calculations for single to multiple holes may be performed using an analytical method, or RANS for a single hole and the use of a superposition method [78] -

see Section 4.2.2 for more details. However, for both RANS methods, CFD [10, 54, 77] produced narrower films with a slightly higher peak film effectiveness compared to experiments. An alternative method is to use heat sinks at cooling hole locations, however this hasn't lead to satisfactory results for an effusion cooled blade [5].

Another complication is the difficulty in accurately capturing the behaviour of impingement jets. Modelling of turbulence and the interaction with the target wall has been a notorious problem resulting in fine resolution grids required to capture the correct behaviour. However, this doesn't inherently guarantee success as the region where there largest heat transfer occurs, the viscous sublayer, is the place most difficult for RANS solvers to predict the flow. A review of impingement jets and modelling approaches was made by Zuckerman and Lior [17] in which the general trends of computational time and impingement jet transfer coefficient are presented for a range of turbulence models. What becomes clear is that RANS models can introduce errors in the impingement heat transfer in the range of 15-30%. While improvement may be made using DNS or LES models, the previously mentioned computational cost limit application.

For the case of turbine blades, the aerodynamic and thermal fields need to be adequately assessed, and as a result, conjugate heat transfer (CHT) studies are of interest. And for effusion cooling this method has shown good agreement with experiments [5] in some instances.

2.6.2 Conjugate Heat Transfer Methods

CHT methods allow evaluation of the temperature and thermal stress field in the solid material alongside aerodynamic performance. There are two main strategies: coupled and de-coupled. The former only needs one solver and solves all equations in the fluid and solid domain in a single system. This offers the advantage of temperature continuity and the heat flux at interfaces being implicitly guaranteed.

Another challenge is modelling of small-diameter holes, inadequate discretization and turbulence modelling in CFD. This can lead to difficulty in convergence [79]. Consequently, de-coupled CHT solvers were developed as a trade-off between accuracy and cost. The de-coupled

method calculates the fluid flow and solid thermal field separately, and exchanges information via boundary conditions at the interface between the two. The fluid phase is solved using conventional Navier-Stokes solvers while the solid phase uses a Finite Element Analysis solver, which is computationally efficient. However, an iterative approach must be used to transfer data between the two phases and solvers, as both the internal and external heat transfer depend on the solid surface temperature.

Amaral et al. [80] used a de-coupled CHT approach to model an internally cooled gas turbine blade, a Navier-Stokes solver for external non-adiabatic flow and heat transfer, a finite element solver for the heat and stress solution in the solid, and a 1D aerothermal model for cooling channels. Similar methodology has been used for film-cooled blades (Bonini et al. [81] and Andreini et al. [82]) and effusion cooling [54].

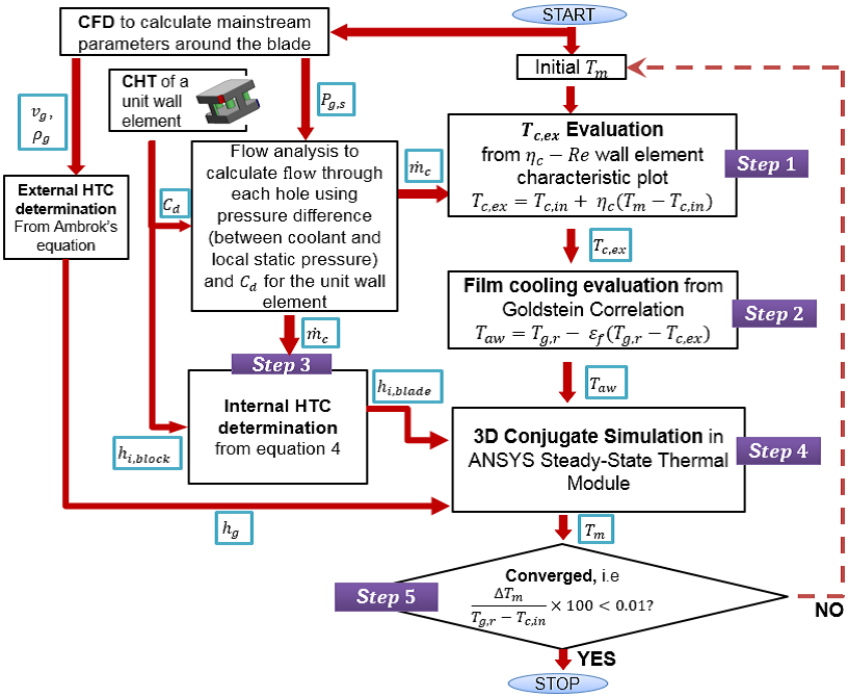


Figure 2.11: Iterative Procedure For A De-coupled CHT. Image courtesy of Ngetich et al. [54]

Ngetich et al. [54] used a de-coupled CHT flow solver that depends on an implicit finite volume method in conjunction with multi-block approach. This is based on a method proposed by Murray et al. [6] and validated against experimental results in the most recent publication [10], using a simple flat plate geometry with double-walled cooling. The results provided rela-

tively minute discrepancies, but the CFD simulations over-predicted the effect of impingement on cooling performance. The following procedure is adopted. The Goldstein correlation [26] was employed for film cooling effectiveness of a single hole. The 2D distribution of film cooling effectiveness of an array of cooling holes was represented by film superposition, using a correlation by Sellers [78]. The iterative procedure used an initial guess of the metal temperature T_m for the CFD, CHT of a unit wall element and Goldstein correlation. With the correct exchange of information a new guess of T_m is made until a desired convergence criteria is met. This process is illustrated in Figure 2.11. Compared to results in open literature, the film and metal effectiveness and the coolant mass flow closely matched.

2.7 Summary

In this chapter the historical and current state of turbine cooling systems was explored, highlighting the challenges involved in both internal and external cooling methods. The transition from film- to effusion- and ultimately to transpiration-cooling was described and particular attention was paid towards double-walled configurations. The opportunity of transpiration cooling was highlighted with the high cooling potential available from increased internal convective area as well as a more protective external film coolant layer. Several challenges of this technology were discussed such as location of applicability on nozzle guide vanes and susceptibility to blockage. An increasing amount of research is being conducted through the use of high fidelity numerical simulations. However, given the computational expense in using a fully 3D CFD simulation to model the cooling performance of a blade, and the accuracy of such simulations for complex flows, the use of semi-empirical methods will be heavily relied upon in both academia and industry for advancements in cooling technology. The development and integration of transpiration systems for turbine blade cooling is a balance between cooling effectiveness, structural integrity, and aerodynamic performance.

3 Experimental Facility

The features of the facility in which all experimental results included here will be described in Section 3.1 and the measurement technique in Section 3.2. Finally detailed descriptions of the double-walled configurations is given in Section 3.3.

3.1 Overview

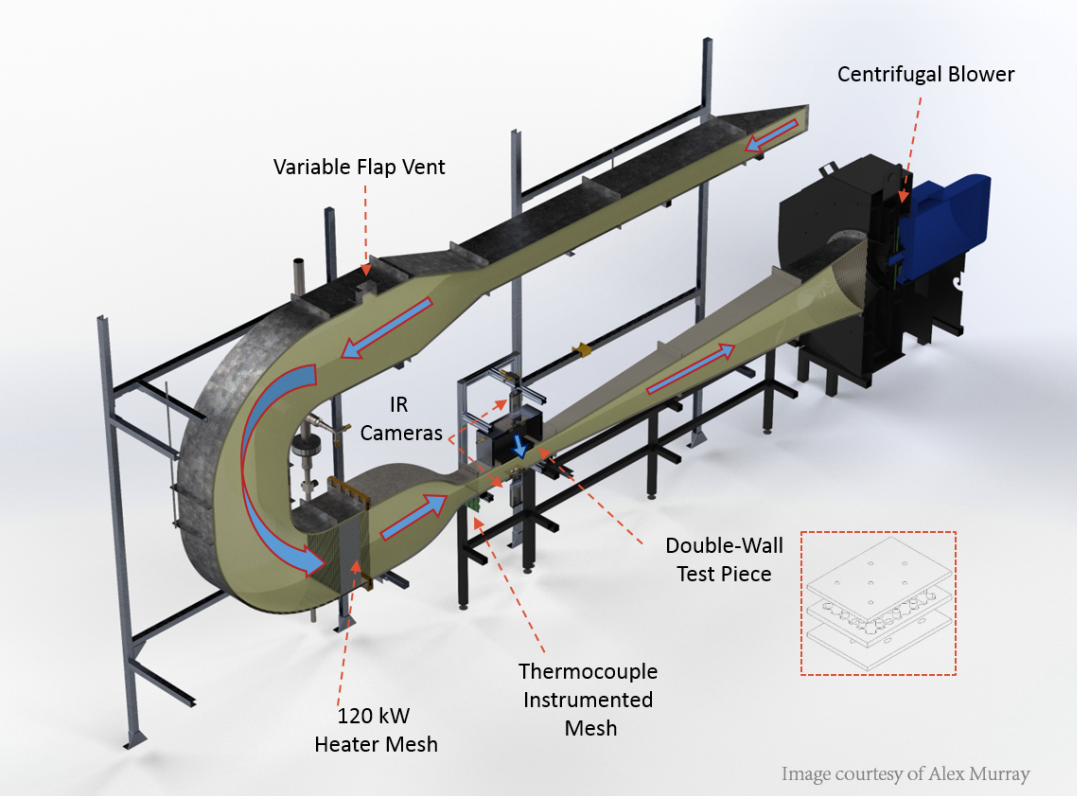


Figure 3.1: Section view of the Re-circulatory Double-Walled Effusion Cooling Facility

Experimental measurements were conducted using a re-circulatory wind tunnel facility at the Oxford Thermo-fluids Institute, University of Oxford. Figure 3.1 illustrates a section view of the facility and a more detailed view of the test section is provided in Figure 3.2. Designed and

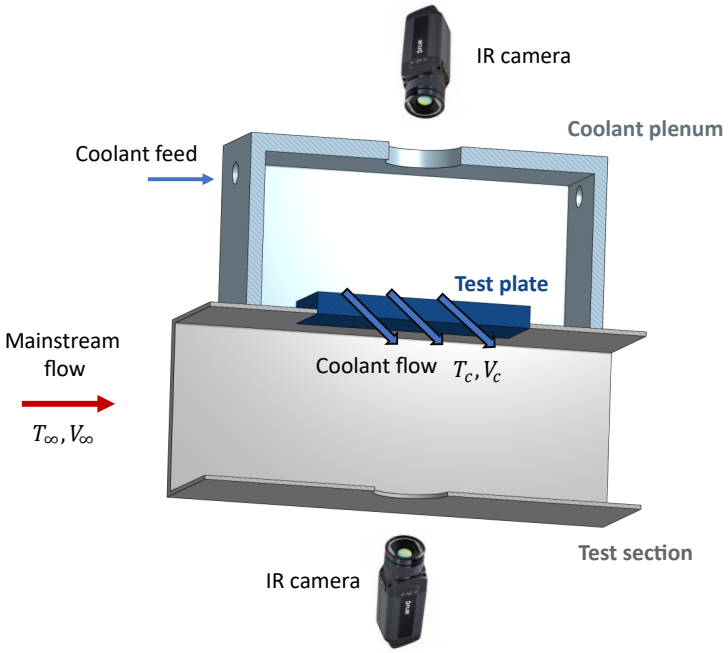


Figure 3.2: Test section schematic showing the location of the test piece and the IR cameras monitoring the internal and external surface.

constructed by Alex Murray (Univeristy of Oxford), the facility provides conditions for scaled tests of flat plate double-walled cooling geometries and is described and tested in Murray et al. [53].

Test pieces for the double-walled cooling-configurations were placed inside an aluminium coolant plenum which was fed by ambient temperature air supplied by a 30PSI feed. The coolant flow rate was controlled by a pneumatic regulator and measured using a convergent-divergent nozzle. The test piece was placed so that the film wall was flush with the inner surface of the wind tunnel. The tunnel flow was controlled by a 55 kW centrifugal blower and the temperature elevated by a heater mesh, which could provide approximately 120kW of power. The heater mesh was comprised of a fine metal mesh across which a current is passed causing a rise in the temperature of the metal strands. The heater mesh was located in the low velocity section so that as the mainstream flow passes through the apertures in the mesh the result was a near uniform increase in the mainstream temperature.

The facility provides both Reynolds and Biot number similarity (10% for Re and 25% for Bi) to engine conditions and has been specified for high temperature capabilities. The Biot number

(see equation 3.1) is important for aerothermal measurements as it influences the importance of internal thermal gradients and for a Biot larger than 0.1, transient heat transfer becomes significant. For similarity between real engine and experimental facility measurements, similarity in the Biot number is desired.

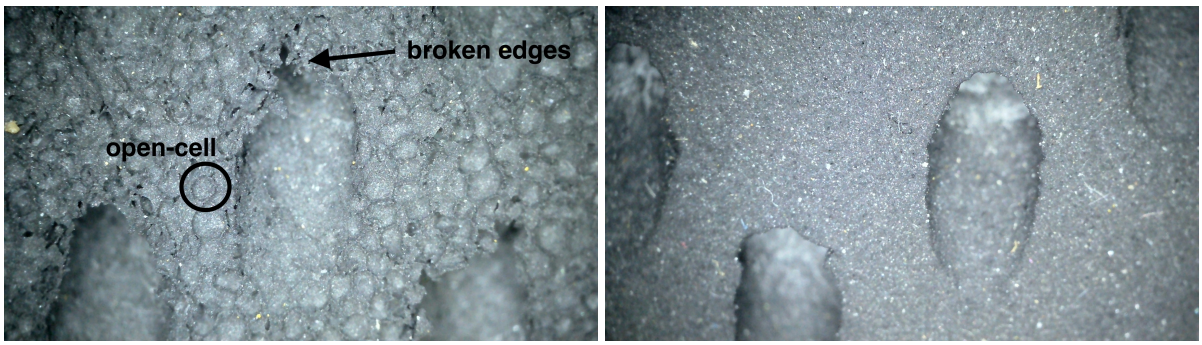
$$Bi = \frac{hL}{k_b} \tag{3.1}$$

The density ratio was not perfectly matched with an experimental value of ≈ 1.2 compared to engine values of around 2. However, at larger temperature differences (hot gas to coolant) this could be reduced and introducing a mechanism for cooling of the coolant, rather than relying on the ambient temperature, as well as raising the hot gas temperature, this difference could be reduced. The range of operating conditions used in this document is provided in Table 3.1.

v_∞	Ma	T_∞	T_c	T_c/T_∞	ρ_c/ρ_∞	External h
60 m/s	0.182	373 K	290 - 298 K	0.76 - 0.8	0.75 - 0.85	140 W/(m^{2}K)

Table 3.1: Typical experimental conditions

One key feature of the facility is the lining of the internal surfaces with a high performance insulating material that has a smooth, non-porous surface. During the experimental runs, temperatures on the external surfaces of the tunnel were not elevated more than 1.5 K above the ambient air temperature. Resulting in lower time required to reach a steady-state mainstream temperature. It should also be noted that the hot gas thermal conditions differs from those of real engine conditions - exhaust gas from combustor compared to air used in the experimental facility.



a) Open-cell b) 71 Hero (Closed-Cell)

Figure 3.3: Rohacell magnified view of a 2 mm film hole

Rohacell was used for test geometries to investigate film effectiveness, assuming an adiabatic surface. Rohacell was chosen due to its low thermal conductivity ($\lambda \sim 0.030$ W/m-K), and effort was made to reduce the impact that the roughness of the material would have on results, due to small features inherent in transpiration-like geometries. This is investigated further in the use of a high grade with closed-cell structure (*EVONIK 71 HERO*), and the difference to a open-cell structure is shown in Figure 3.3. In these two pictures the magnified view of a 2 mm film hole is shown and it can be observed that the closed-cell structure offers a more distinct film hole outline. Additionally, using the 71 HERO grade enabled film holes in much closer proximity without breakthrough between adjacent film holes. Therefore, this grade was used to provide more realistic film effectiveness results as well as machinability.

3.2 Infrared Methodology

Temperatures of the two external surfaces were monitored by two *FLIR A655sc* infrared cameras, with optical access provided by Zinc Selenide windows. This permitted simultaneous monitoring of the two surfaces and data was recorded using *FLIR ResearchIR* software. The cameras were both equipped with wide angle, 13 mm, 45° field of view (FoV) lenses. The maximum camera resolution was 640×480 pixels at a frame rate of 50 Hz, with a maximum frame rate of 200 Hz for smaller window sizes of 640×120. The frame rate of the camera was set at 25 Hz for film effectiveness measurements to allow assessment of flow unsteadiness, and data is averaged over 10 seconds (250 frames) to provide a mean steady-state temperature. For metal effectiveness measurements, mainstream and coolant flow fluctuations have only a minute impact on the surface temperature. As a consequence, a frame rate of 6.25 Hz was used to minimise data file sizes. Data was averaged over 10 seconds (63 frames) for the steady state temperature. Thin wire thermocouples were attached to both the hot-gas and coolant plenum external surfaces of the test geometry, within the IR camera field of view, permitting an in-situ calibration. External surfaces were painted matt black to minimise IR reflections from the surroundings. The calibration must calculate the blackbody temperature based on the detected incident heat radiation; account for transmissivity variations due to the optical pathway between the IR de-

tector and target surface; account for the effect of thermal reflections from the surroundings; account for the emissivity of the surface being observed. The calibration method is highlighted below, and based upon Kirollos and Povey [83], Holgate [84] and Murray [85].

The IR camera uses an array of microbolometers which have an electrical resistance dependent upon temperature. This temperature is dependent on the incident electromagnetic radiation within a spectral range. For the cameras in this study the spectral range is 7.5 - 14 μm [86]. Voltage measured across each microbolometer is a function of the electrical resistance, which can be converted to a 16-bit digital signal. Subsequently the software can record the raw count dependent on pixel voltage. A calibration procedure is necessary to account for influences mentioned above, and this can be done in two parts: the calculation of ideal blackbody parameters and the calculation of greybody parameter. Once the parameters are calculated the total radiance is given by equation 3.2 where σ_b is the Stefan-Boltzmann constant, ξ is the emissivity of the observable surface, τ is the transmissivity of the optical pathway, T_w is the temperature of the surface of interest and temperatures T_{bb}, T_{amb} and T_{opt} are the blackbody, ambient and optical pathway temperatures respectively.

$$\sigma_b T_{bb}^4 = \sigma_b \xi \tau T_w^4 + \sigma_b (1-\xi) \tau T_{amb}^4 + \sigma_b (1-\tau) T_{opt}^4 \tag{3.2}$$

3.2.1 Blackbody calibration

The raw count (C_R) output of the camera is approximately a linear function of the incident radiation (q_{cam}), and hence the camera radiance can be expressed in terms of the ideal blackbody temperature by equation 3.3

$$q_{cam} = \sigma_b T_{bb}^4 = aC_R + b \tag{3.3}$$

Calculation of constants a and b was done by an isothermal cavity calibration. Further information of this procedure is provided in [85], with the constants for each camera described below:

Cam Film (24487)
$$\sigma_b T_{bb}^4 = 0.0394 C_R - 102.72 \tag{3.4}$$

Cam Film (25959)
$$\sigma_b T_{bb}^4 = 0.0414 C_R - 122.60 \tag{3.5}$$

3.2.2 Greybody Calibration

The test surface can not be described as a pefect blackbody as a consequence of a less than unity emissivity, reductions in IR transmittance through the optical pathways and radiance arising from refelction of the surroundings. The right hand side of equation 3.2 can be split into two parts: the contribution of the surface temperature (the first term), and those from the surroundings (the last two terms). These final two terms can be combined into one radiance term (q^*) given by equation 3.6

$$q^* = \frac{\sigma_b \left\{ \tau(1-\xi) T_{amb}^4 + (1-\xi) T_{opt}^4 \right\}}{1 - \tau\xi} \tag{3.6}$$

Equation 3.2 can be rearranged in the form of equation 3.7

$$T_w = \sqrt[4]{\frac{\sigma_b T_{bb}^4 - (1-\tau\xi) q^*}{\sigma_b \tau \xi}} \tag{3.7}$$

T_{bb} is from from the raw counts signal and blackbody calibration, but ξ,τ and q^* are still to be determined. The first two are found via an in-situ calibration procedure, where the product of these two terms ($\xi\tau$) was found to be 0.961 for the film wall and 0.953 for the impingement wall.

The surrounding radiance term (q^*) depends on the conditions during the experiment. Thermocouples were instrumented on both external wall within view of the IR cameras (see Figure 3.4) and attached by a high conductivity paste and sprayed with matt black paint, in order for the readings to be representative of the wall temperature. Equation 3.7 can be rearranged in in the form of equation 3.8, where $T_{w,thermo}$ denotes the thermocouple temperature and $T_{bv,thermo}$ denotes the IR camera blackbody temperature measured at the pixels in proximity to the ther-

mocouple.

$$q^* = \frac{\sigma_b \left(T^4_{bb,thermo} + \tau\xi T^4_{w,thermo} \right)}{1 - \tau\xi} \tag{3.8}$$

The procedure detailed above is the method used for all surface temperature measurements for both the film wall and impingement across all experimental runs.

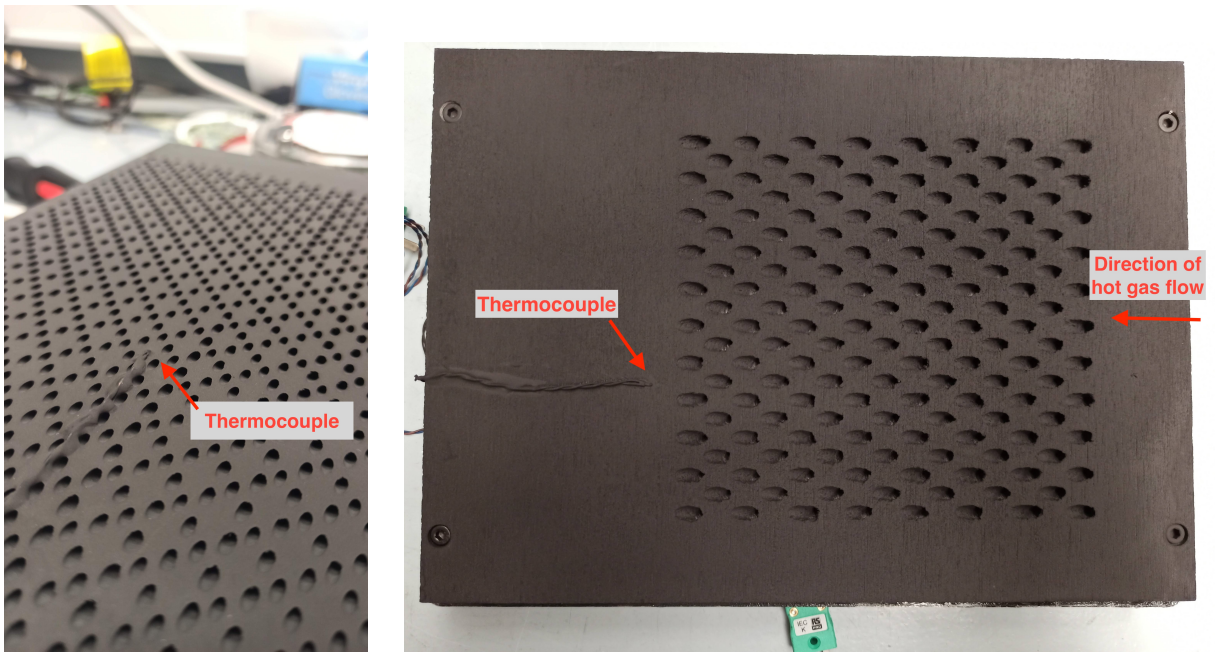


Figure 3.4: Instrumentation of test pieces

3.3 Double-Walled Test Piece Design

To evaluate the consequence of transpiration-like geometries, a base-line for double-skinned effusion cooling was selected. Alex Murray's D6 design was selected as it had a large bank of numerical and experimental data for comparison [85, 87], and was relatively simple in construction. This consisted of 24 film holes on the outer wall of 10 mm diameter in a staggered arrangement. The primary spacing of film holes were equal at $S_x = S_y = 5.64D_f$. The inner-wall consisted of 24 impingement holes located between the film holes with a diameter of 5 mm. The outer wall included square pedestals with 5 mm sides which were orientated at 45° to the streamwise flow direction, and called 'diamond' shape due to this construction. In a similar

fashion, two geometries were designed (TD2 and TD1) with reduced film hole sizes and spacing resulting in a more porous double-wall assembly. A comparison of properties is shown in Table 3.2 with a visualisation of the difference between TD1 and D6 in Figures 3.5 and 3.6. A CAD rendering of the full domain for TD2 and D6 is illustrated by Figure 3.7 and 3.8 with the location of the IR view area shown for the film-side wall. Figure 3.9 illustrates the IR view area for the impingement-side wall, and Figure 3.10 is a picture of the internals for the TD2 metal plate.

	TD2	TD1	HS2	D6
D_f	2.0 mm	1.75 mm	4.0 mm	10 mm
D_i	3.50 mm	3.50 mm	5.0 mm	5.0 mm
S_f/D_f	3.5	4.0	3.5	5.64
S_p/D_i	2.8	4.0	2.8	2.8
L_p	5.0 mm	5.0 mm	5.0 mm	5.0 mm
H_i/D_i	3.0	4.39	3.0	3.0
$\phi\|_{30°}$	19.2%	14.7%	19.2%	9.9%

Table 3.2: Comparison of TD2, TD1 and HS2 designs to Murray's D6 Design

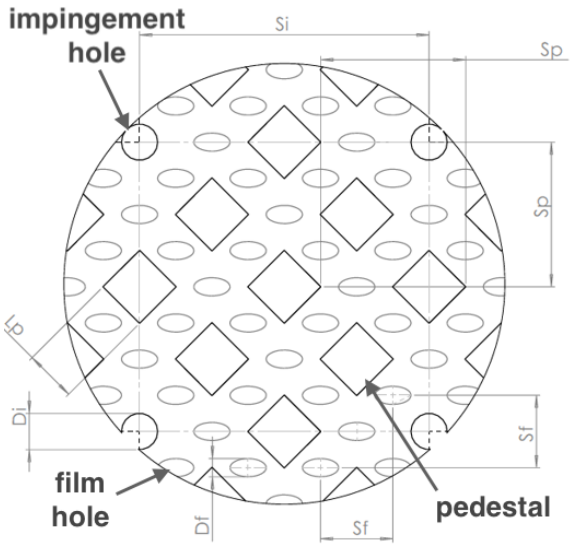


Figure 3.5: TD1 Geometry Schematic

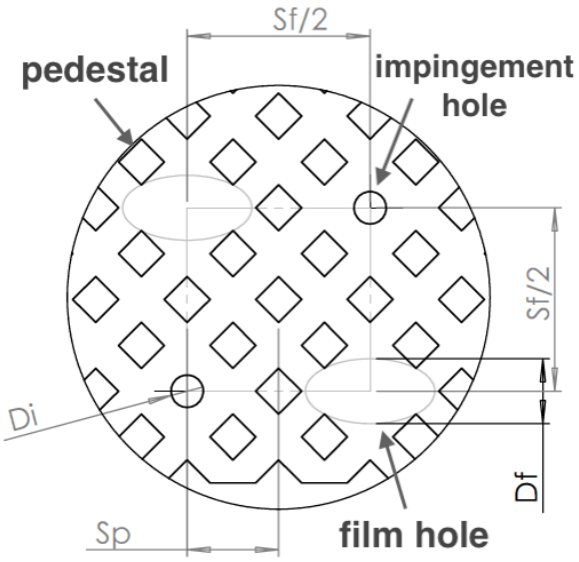


Figure 3.6: D6 Geometry Schematic

The first step was to consider a more porous geometry, while decreasing the hole diameter. To isolate this change, the internals were largely maintained, with no altercation to the pedestal location, orientation or size. However, for T1, the impingement holes were doubled in number, with additional impingement holes at the locations where D6 film holes are projected from the

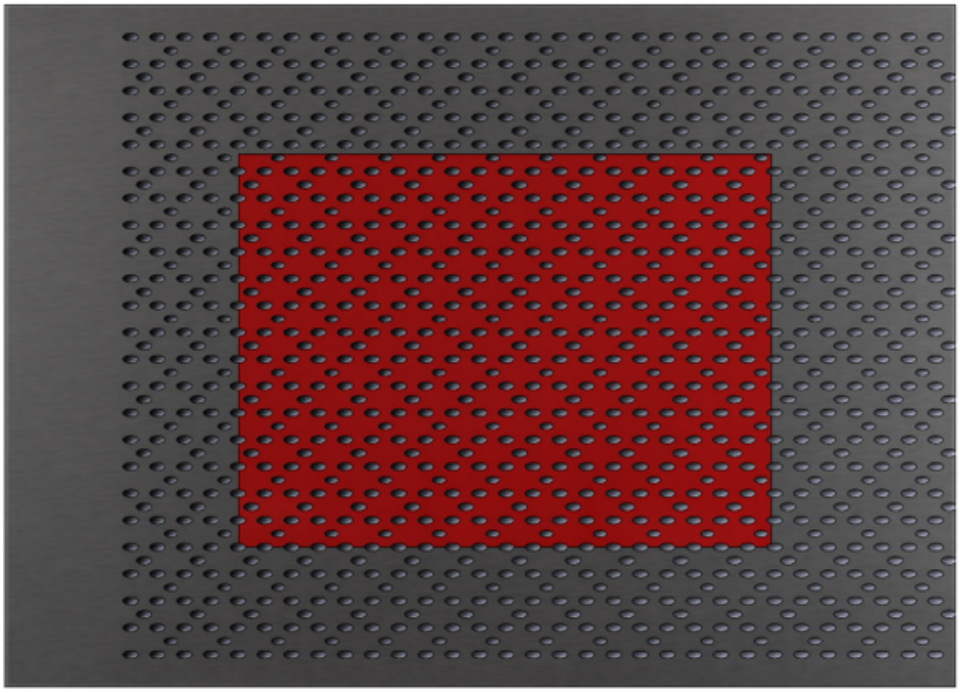


Figure 3.7: CAD rending of the film surface and IR view area for TD2.

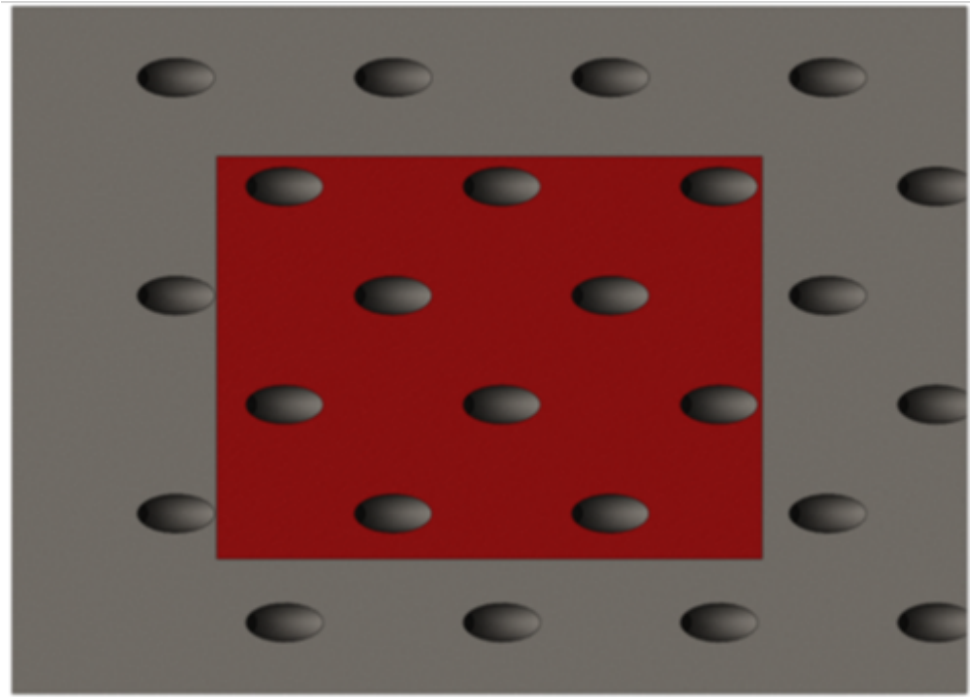


Figure 3.8: CAD rending of the film surface and IR view area for D6.

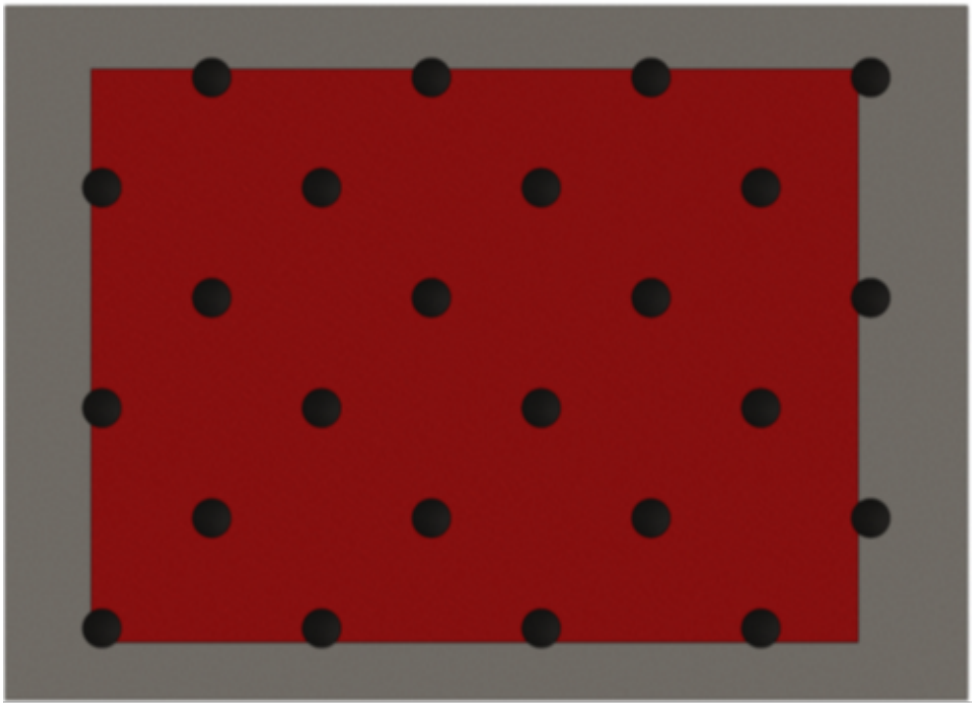


Figure 3.9: CAD rending of the plenum-side surface and IR view area, common to both TD2 and D6.

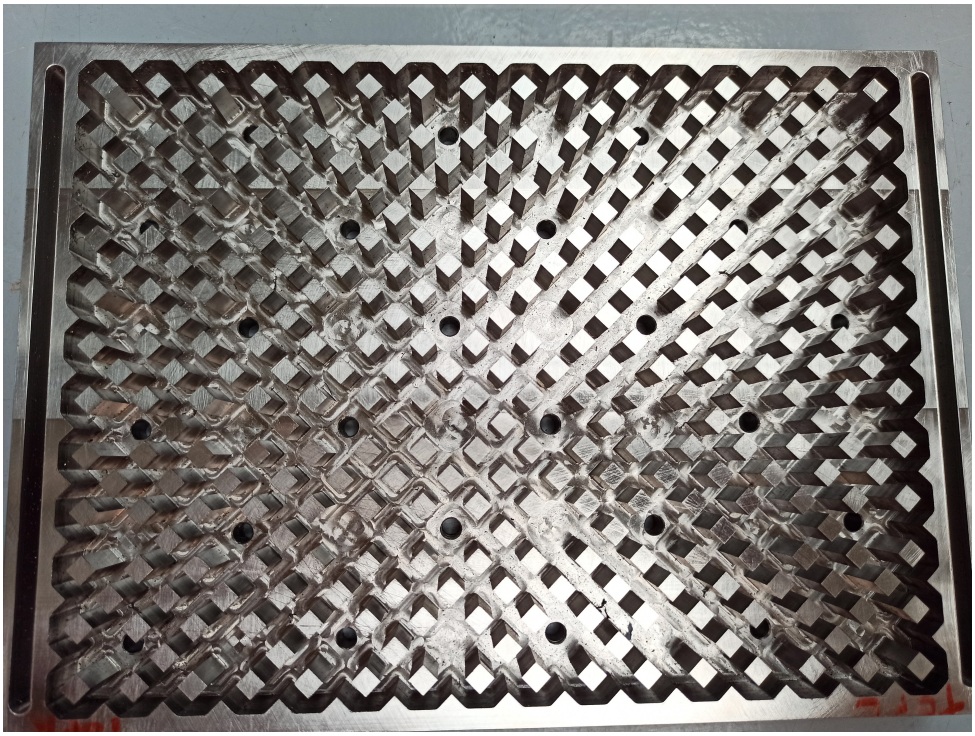


Figure 3.10: Internal cavity features of the double-wall design.

bottom of the external skin to the internal skin. To maintain the impingement jet velocity, the diameter was scaled by $1/\sqrt{2}$. This change was also made in attempt to avoid an impingement jet being degraded by being in too close proximity to a film hole, which may result in uneven mass flow distribution between film holes.

The film holes followed a similar staggered arrangement observed in D6, where a set of primary film-holes were placed at a span- and stream-wise spacing (S_y and S_x) from each other, with a secondary array offset by half a pitch in both directions. However, this would result in holes falling at pedestal locations, hence these film holes were removed. The consequence of this can be thought of as a blockage of a similar staggered array. The resultant first geometry was TD1, however it was noted that a hole diameter of 1.75 mm at an inclination of 30 degrees could be difficult for manufacture. As a result a second geometry TD2 was designed, which had the simple change of a larger hole diameter - 1.75 mm to 2.0 mm. As a consequence of maintaining the same film hole spacing, in absolute terms, the non-dimensional spacing was reduced and hence a larger porosity for TD2.

4 Numerical Methods

A range of numerical methods were investigated to determine the level of computational complexity required to achieve satisfactory results for double-walled cooling systems. The main principle was to use an empirical correlation for the external cooling and utilise CFD for the internal cooling performance. These two results could be coupled together in several different ways, providing the resultant cooling performance. All four methods are compared to one another, alongside experimental results in Chapter 7. All other numerical work used the method outlined in Section 4.2.

4.1 Introduction

Four methods were used for numerical calculations and starting from the least computationally expensive to the most.

1. LOM - low order model
2. DUC - de-coupled unit-cell
3. SUC - semi-coupled unit-cell
4. SSD - semi-coupled streamwise (internal) domain

4.2 Decoupled Unit-Cell Conjugate Method

To investigate the aerothermal performance a decoupled conjugate technique was used, denoted as DUC. This was based on a method developed by Murray et al. [6], and shown to adequately capture heat transfer properties for double-walled effusion-cooled geometries, without incurring

too large of a computational demand since the internal and external heat transfer are evaluated separately and used to determine the resulting aerothermal performance.

	Engine Conditions	Rig Conditions
Ma_∞	0.3	0.182
T_∞	1870 K	375 K
T_c	1000 K	293 K
ρ_∞/ρ_c	0.5 - 0.6	0.75 - 0.85
P_∞	3.4 MPa	-2000 Pa (gauge)
External h_{conv}	7500 W/m^2/K	140 W/m^2/K
Solid Material	CMSX4	Stainless Steel 303

Table 4.1: Typical conditions used in conjugate study

4.2.1 Internal Model

Internal heat transfer is modelled using a commercial solver (*ANSYS Fluent v16.2*) for a unit block as illustrated in Figure 4.1 with typical boundary conditions in Table 4.1, which involve a hot gas mainstream flow temperature, T_∞, and velocity, v_∞, an external heat transfer coefficient, h_∞, and pressure, $p_{s,outlet}$, as well as an original coolant temperature, T_c, and mass flow, $\dot{m}_c$. A significant difference between the numerical simulation and geometry in reality is the inclination of film holes. Numerically the holes were perpendicular to the plate surface, while the physical geometry had an angle of 30 degrees to the surface. However, this provided the benefit of being able implement symmetry boundary conditions for the CFD solver, although Byerley [88] showed that this changed the discharge coefficient between 0-30 % depending on pressure drop. An update to this method was provided in the course of the study by modelling inclined holes with the use of periodic boundary conditions. A visualisation of the boundary conditions and difference in hole inclination domains are illustrated in Figures 4.1 and 4.2, and a comparison of the two methods is provided in Section 7.3.

A mesh dependency study was conducted using area-averaged inlet pressure and area-averaged heat flux for the impingement target-surface as metrics to determine a suitable mesh resolution. An unstructured mesh from *ANSYS Mesher* was used with fifteen prism layers along fluid-solid interfaces with an overall height of 0.1 mm and a growth rate of 1.2, to keep non-dimensional wall height, $y^+ \leq 1$. The solver method was pressure-based and uses the $k-\varepsilon$ turbulence model,

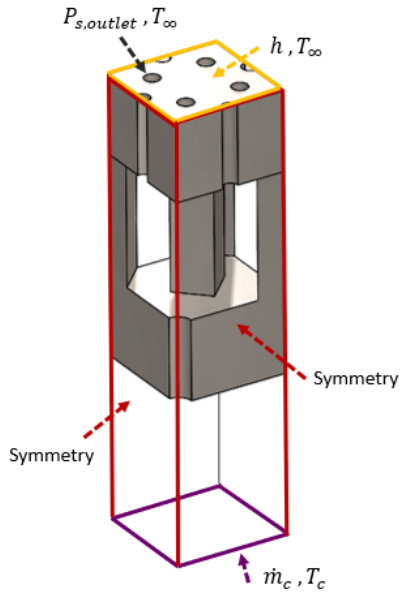


Figure 4.1: CFD domain and boundary conditions - symmetric unitblock.

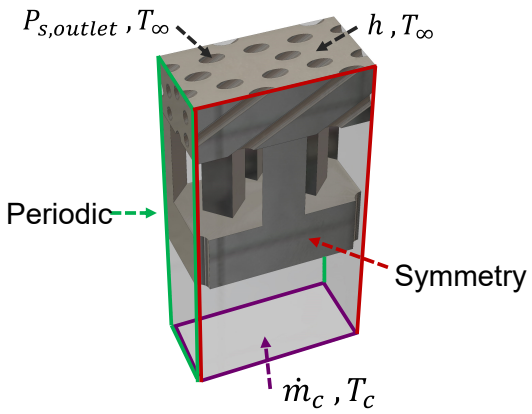


Figure 4.2: CFD domain and boundary conditions - periodic unitblock.

with enhanced wall function and thermal effects enabled. Air was treated as an ideal gas for the fluid domain with thermal conductivity and viscosity evaluated by kinetic theory and the Sutherland method, respectively. The outputs from the CFD analysis are in two parts. Firstly, the coolant velocity and temperature at film hole exit, v_f and T_f respectively, are feed into an empirical correlation as described in Section 4.2.2. Secondly, internal heat fluxes and wall temperature of fluid-solid boundaries are exported to be used for internal and external thermal coupling.

4.2.2 Film Effectiveness

Rather than solving the external flow, coolant films can be modelled using an empirical correlation. One such correlation was first proposed by Goldstein [26] to model the decay of a film in both the streamwise and spanwise directions:

$$\eta_f(x,y) = \frac{MV_\infty D}{8\alpha_t\,(x/D+0.5)} \exp\left(-0.693\left(\frac{y}{y_{1/2}}\right)^2\right) \tag{4.1}$$

Where α_t is the turbulent thermal diffusivity and $y_{1/2}$ describes the spanwise distance at which the film effectiveness is half the centreline value. A further modification to introduce an addi-

tional variable x_{decay} in place of a constant was made and shown to be appropriate by Murray et al. [6]. This was done to enable further control over the streamwise film decay and takes the form:

$$\eta_f(x,y) = \frac{MV_\infty D}{8\alpha_t\left(x/D + x_{decay}\right)} \exp\left(-0.693\left(\frac{y}{y_{1/2}}\right)^2\right) \tag{4.2}$$

Experimental data of the film effectiveness for a single hole at a range of blowing ratios was used to find data the constants turbulent thermal diffusivity α_t, x_{decay} and $y_{1/2}$, based on M. In this study a similar approach is used, however, to further account for the change in the spanwise shape with downstream distance a modification conceptualised and studied by Coulton et al. [89] is used.

$$\hat{\eta}_{f,i}(x,y) = \frac{M_i V_\infty D}{8\alpha_t\left(x/D + x_{decay}\right)} \exp\left(-\left(\frac{y}{c_1}\right)^{c_2}\right) \tag{4.3}$$

The spanwise distance constant, c_1 and spanwise shaping constant, c_2, are variables dependent on M and x. c_2 enables the transition of the film as it first emerges from the film hole, to form a Gaussian shaped distribution downstream, and c_1 captures the width of this distribution. This is the correlation used throughout this thesis.

Each film hole is subject to the modified Goldstein equation independently to find $\hat{\eta}_f$, and together with T_f used in the definition:

$$\eta_{f,i}(x,y) = \hat{\eta}_{f,i}(x,y)\frac{T_\infty - T_f}{T_\infty - T_c} \tag{4.4}$$

to compute the film effectiveness accounting for differences in T_f between film holes.

A superposition method proposed by Sellers [78] was used to capture the streamwise interaction between films. This represents an important aspect for the geometries seen here due to the proximity of adjacent holes compared to typical cooling arrangements. Each film is taken

to be independent, where downstream layers can be considered to operate with a free-stream temperature as influenced by the preceding film, and can be described by equation 4.5 and demonstrated by Figure 4.3.

$$\eta_f(x,y) = 1 - \prod_{i=1}^{n} \left(1 - \eta_{f,i}(x,y)\right) \tag{4.5}$$

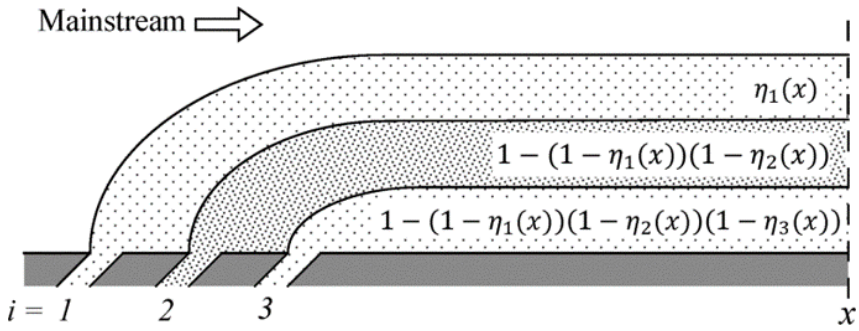


Figure 4.3: Illustration of the streamwise development of films using Sellers [90]

A similar approach was used by Murray, however, the temperature of the preceding film was taken as remaining constant once it reached the new film. Consequently, this infers that upstream films would no longer decay once reaching the next row, and an overestimation of the film effectiveness was observed [6, 10]. In this study, the film effectiveness and therefore adiabatic wall temperature for each film was calculated across the entire domain, and then used for a local point (x,y) with Sellers. The consequence is that the degradation of films will be accounted for across the entire domain and thus the adiabatic temperature can be determined at any point by:

$$\eta_f(x,y) = \frac{T_\infty - T_{aw}(x,y)}{T_\infty - T_c} \tag{4.6}$$

4.2.3 Integration of Internal and External Cooling

A full thermal solution was calculated using outputs from the internal CFD model and empirical film effectiveness method. A schematic of the procedure is illustrated in Figure 4.4, and further

explanation presented here.

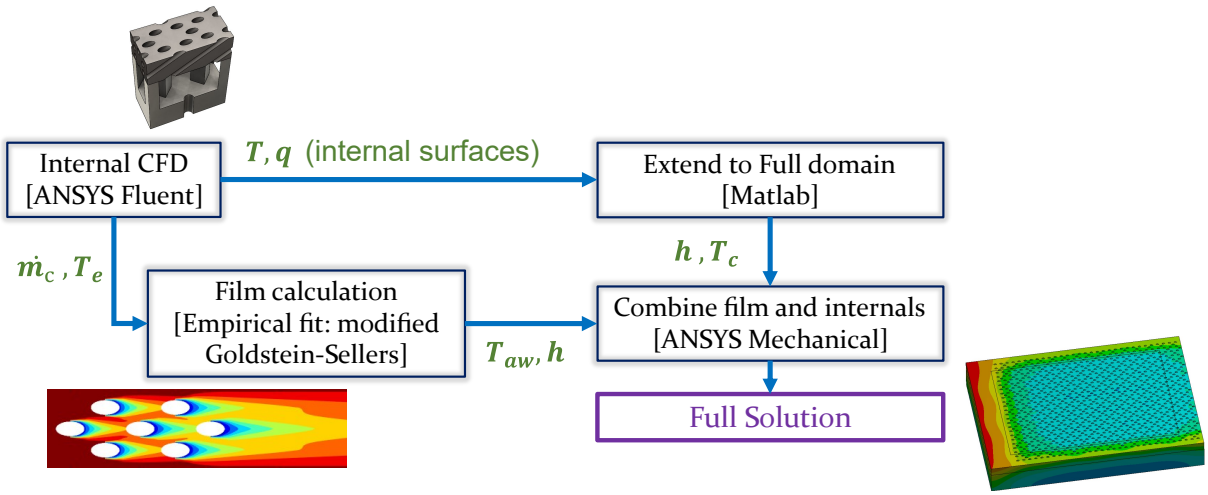


Figure 4.4: Decoupled unit-cell conjugate method schematic. This chart indicates the implementation and coupling of external and internal cooling characteristics.

An internal CFD analysis was made for the unit-cell of the DWEC system. Mass flow rate and temperature at the outlets are used in the modified Goldstein-Sellers. Wall temperature and heat fluxes are exported to a Matlab program which finds the heat transfer coefficient based upon wall temperature and inlet coolant temperature as defined here:

$$h = \frac{q}{(T_w - T_c)} \tag{4.7}$$

These values are extended to capture the full unit-cell repeating area and exported as boundary conditions into *ANSYS Mechanical v16.2* alongside T_{aw} and h for the hot-side surface calculated by the film effectiveness methodology. The side boundary walls at the plate extents are assumed to be perfectly insulated, and internal walls outside the repeating blocks are assumed to be the area-average of that component feature. As an example, the pedestals would take the area-averaged heat transfer coefficient observed in the unit-cell as calculated in equation 4.7. The FEA solver calculates the temperature throughout the domain, which was exported for analysis and comparison between geometric variants and operating conditions.

4.2.4 Limitations of unit-cell method

While the decoupled method provides a low computationally expensive way to find aerothermal solutions to complex double-wall systems, several key features may be overly simplified. Firstly, the film effectiveness calculation utilises the film hole temperature without considering the influence of the film layer itself. In reality, the film protection will lower the external wall temperature and consequently internal heat fluxes will be reduced. As a result, the exhausting fluid at the film outlets will have a lower temperature than calculated in the DUC CFD. As a consequence the film effectiveness using DUC will underestimate the film effectiveness of each film hole, given the definition of film effectiveness: $\eta_f = (T_\infty - T_{c,ex})/(T_\infty - T_c)$. In addition to this, the mass flow was equally distributed between unit-blocks with no streamwise differences, and this implies an assumption of constant external static pressure between unit-blocks. Contrary to this, an external streamwise pressure gradient exists and therefore mass flow will be skewed toward the trailing edge at the detriment to the leading-edge film holes.

Internally the DUC CFD will have higher than expected heat fluxes, q, and wall temperatures, T_w. However, the impact of this is limited given that the implementation in ANSYS Mechanical is through the heat transfer coefficient, h. As the wall temperature will be lower once film protection is applied, the calculated heat flux must drop for a prescribed h.

4.3 Semi-coupled Unit-Cell Method

The Semi-coupled Unit-cell method (SUC) method attempts to address some of the issues mentioned above, without the need for a domain size capturing the full streamwise extent. A schematic showing the implementation of the scheme is in Figure 4.5 and a further explaination here. Results from the DUB method are used as the starting point and labelled as unit block 0. The calculated film effectiveness from unit-block 0 is used as the external wall boundary condition, and the previous aerothermal calculation used for initialisation. As there are only minute changes in the aerodynamic patterns and mostly a correction applied for the thermal solution, this modification can be made with relatively few (500-750) further iterations. Film hole exit mass flow and temperature are exported and used to find the new film effectiveness which can

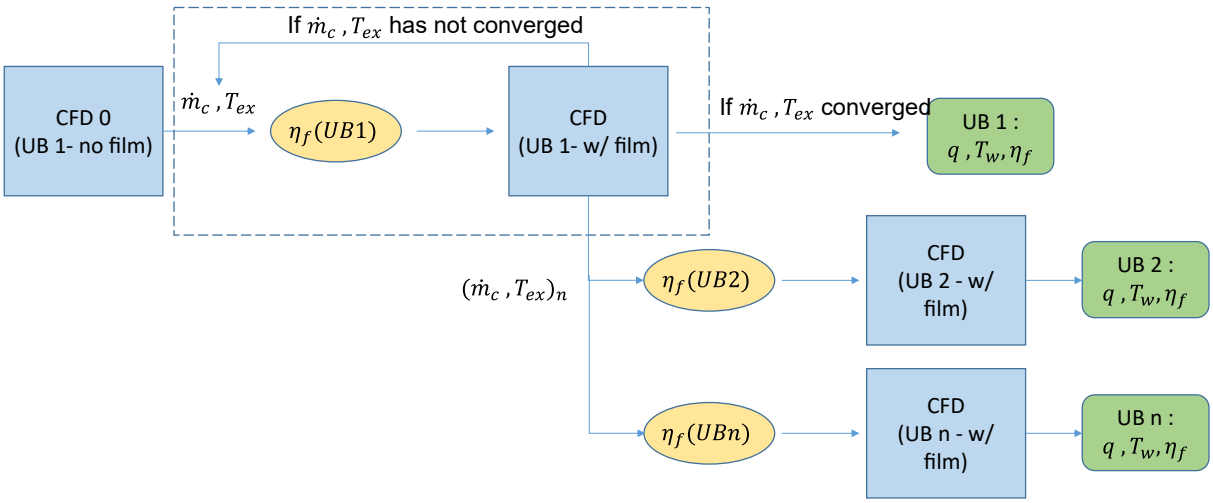


Figure 4.5: Schematic of the semi-decoupled unit-cell method

be reapplied in the same manner, creating an iterative process which will converge to a more realistic solution. This can be done for any number of unit-blocks, providing the expected film effectiveness at any location in the streamwise direction. Once all unit-blocks are found, the corresponding film hole mass flows and temperatures are used to find a multi-block film effectiveness and likewise the internal heat fluxes and wall temperatures used to find the multi-block heat transfer coefficients.

4.4 Semi-coupled streamwise domain

The SSD method simulated the entire streamwise domain with the width of one unit-block. Given the larger domain size any calculations are more computationally expensive, but a full streamwise film effectiveness can be easily calculated and applied to the entire domain. In addition to this, an external pressure gradient can be applied and provide valuable insight into variation in mass flow between unit-blocks. Both simulations with and without an external pressure gradient were made. Pressure gradient was implemented by taking an interpolated pressure gradient from experimental results.

4.5 Low Order Model

A low-order model for double-wall cooling systems was proposed and experimentally validated by Murray et al. [91]. These types of low level models can act as good tools for assessing the

feasibility of new designs or conditions for thermal engineers, and act as a screening process against designs which do no meet certain thermal criteria. The reduction in computational demand results in the ability to test a much greater number of design options. However, the lower fidelity does result in the loss of some important features (i.e flow features, spatial resolution) and the potential for error in modelling assumptions. Nevertheless, a low-order model was compared to the previously mentioned studies to understand how useful these types of models can be for preliminary assessment.

Thermal problems can be treated to the analogy of an electrical circuit where heat flow is represented by current, temperatures by voltages, heat sources by current sources and thermal resistances by resistors. Here a double-wall thermal resistance model inspired by [92] was constructed for a double-wall unit-cell with thermal resistance and heat flows acting added for each surface component. A cross-sectional cut of a typical double-wall unit-cell and the associated circuit diagram are displayed in Figure 4.6. The components modelled here are as follows: innerskin outer and inner surfaces, impingement hole walls, outerskin-inner surface (impingement target surface), film hole walls, outerskin-outer wall (external hot wall) and the internal resistance associated with the innerskin, pedestals and outerskin. A first guess film hole coolant exit temperature, $T_{c,e}$, is estimated at 10% increase of the coolant to mainstream temperature and the mid-pedestal temperature, $T_{p,mid}$, is taken as half way between the coolant and mainstream temperature. Using these initialised values the heat transfer rates and surface temperatures may be found and iterated to update the pedestal temperature.

$$NTU = \frac{\sum hA}{\dot{m}_c c_p} \tag{4.8}$$

$$\eta_c = 1 - e^{NTU} = \frac{T_{ce} - T_c}{T_{p,mid} - T_c} \tag{4.9}$$

The cooling efficiency, η_c, can be related to the internal cooling using the number of transfer units (NTU) method, where the NTU is the ratio of the internal heat transfer coefficient to the cooling capacity potential. Additionally the convective efficiency can be related to both the pedestal temperature and coolant exit temperature. A step-by-step breakdown of each iteration is provided by equations 4.10 to 4.17, where the initialised value of T_{aw} was used during itera-

tion 1 and updated for each iterative step, until convergence of less than 0.5% is satisfied. After, the outer- and inner- external surface temperatures was calculated by equations 4.18 and 4.19 respectively.

Iterative procedure:

$$\dot{Q}_1 = \frac{T_{aw}(i) - T_c}{R_{os} + R_{o,in}} \tag{4.10}$$

$$T_{o,mid}(i) = T_{aw}(i) - \dot{Q}_1(i)(R_{os} + R_{o,in}) \tag{4.11}$$

$$\dot{Q}_2(i) = \frac{T_{oi}(i) - T_c}{R_{oi} + R_{o,out} + R_4} \tag{4.12}$$

$$T_{oi}(i) = T_{o,mid}(i) - \dot{Q}_2(i)R_{ow,out} \tag{4.13}$$

$$\dot{Q}_3(i) = \frac{T_{oi}(i) - T_c}{R_{p,in} + R_3} \tag{4.14}$$

$$T_{p,mid}(i) = T_{oi}(i) - \dot{Q}_3(i)R_{p,in} \tag{4.15}$$

$$T_{c,e}(i) = T_c + (T_{p,mid}(i) - T_c)\eta_c \tag{4.16}$$

$$T_{aw}(ii+1) = T_\infty + \eta_f(T_{c,e}(i) - T_\infty) \tag{4.17}$$

Calculation of overall parameters:

$$T_{ow} = T_{aw} - \dot{Q}_1 R_{os} \tag{4.18}$$

$$T_{io} = T_{i,mid} - \dot{Q}_6 R_{i,out} \tag{4.19}$$

In this thermal circuit, the thermal resistance associated by conduction term can be found from the distance though which the heat conducts, L, the thermal conductivity of the material, k, and the cross-sectional area perpendicular to the thermal flux A.

$$R_{cond} = \frac{L}{kA} \tag{4.20}$$

Similarly, the convective thermal resistance if found from the heat transfer coefficient, h, and the area subject to convective heat transfer A.

$$R_{conv} = \frac{1}{hA} \tag{4.21}$$

Each component of the DWEC system will have varying convection loads. Correlations for the Nusselt number, Nu, can be found in literature from which the heat transfer coefficient can be derived. For the impingement and film holes internal convection the Dittus-Boelter correlation

is used:

$$\overline{Nu} = 0.023 Re_D^{0.8} Pr^0.4 \tag{4.22}$$

While there exists many correlations for round-jet impingement heat transfer a correlation [93] was shown to be appropriate for double-wall configurations in a low-order model [92].

$$\overline{Nu}_{jet} = \frac{(24 - |H_p/D_i - 7.75|)\, Re_i^{0.76}}{533 + 44\,(x/D_i)^{1.285}} \tag{4.23}$$

For the innerwall-inner, initially a correlation from Gillespie's 1996 thesis [94] was used,

$$\overline{Nu}_{ii} = A\overline{Nu}_{oi} \tag{4.24}$$

Where $A = 0.423$, however this returned much higher heat transfer compared to the internal CFD, and resulted in an overestimation of the overall cooling compared to experimental results. Therefore this was revised to be $A = 0.16$ for all geometries, which more accurately represented the results in this study. For all other surfaces, the pedestals and innerskin-outer wall, results from CFD solutions were applied as appropriate empirical data was not found for the geometries of interest.

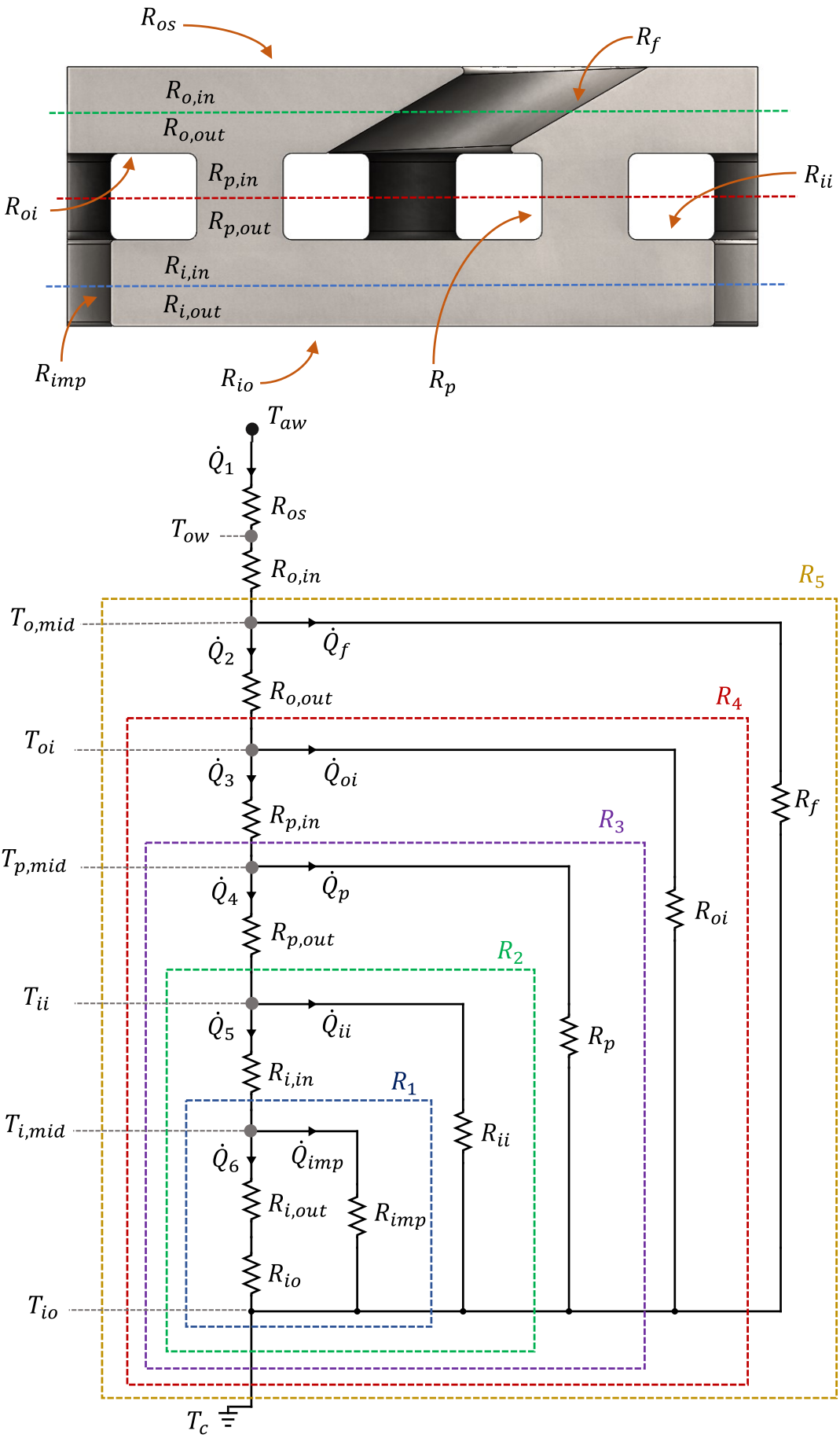


Figure 4.6: Circuit diagram of the thermal resistance model

5 Film Effectiveness

5.1 Overview

Film superposition is a powerful phenomenon which effusion and transpiration cooling devices attempt to take advantage of. While increasing the number of film holes may provide added opportunity to take advantage of the superposition of films, this comes with an associated cost. Either the system must be provided with increased coolant mass flow, or the blowing ratio must be reduced. For the latter this may come with a detriment to the individual film hole performance, although depending on the operating conditions, it may benefit from avoiding the critical blowing ratio value for jet lift-off. In addition to this, the increase in film holes can be achieved by reducing film hole spacing in the streamwise and/or spanwise directions. While reducing these spacings in equal measure has been investigated, any attempts to distinguish the merits for prioritising one direction over the other are limited. A preliminary study to understand the impact of film superposition and assessment of the numerical technique is made in Section 5.2. This chapter then addresses the issue of film jet directional preference as well as the consequences of superposition of dense-array spacing in Section 5.3. The work here includes that presented at the European Turbomachinery 2021 conference and published in the International Journal of Propulsion and Power [2]. Subsequent studies evaluate a further high porosity configuration, Section 5.4, and the impact of compound angle, Section 5.5. The influence of the adiabatic assumption and the material used in experimental tests is evaluated in Sections 5.6 and 5.7 and application of these findings to a turbine blade is considered in Section 5.8. Finally a summary of the findings in this chapter is provided in Section 5.9.

5.2 Preliminary Investigation

Evaluation and a direct comparison of the update to application of Sellers superposition, where the modification is discussed in more detail in Section 4.2.2 is made here. Contours of the film effectiveness for experimental results using the PSP method, a multi-hole CFD domain and the 'Murray' superposition method presented in [10] are compared to the superposition method used in this study, and illustrated in Figure 5.1 and 5.2.

For a pitch of 5.75D, the superposition method used in this study more accurately captured the films compared to the method used by Murray. In contrast to a large over-estimation of downstream films, there was in fact a small under-estimation of the film effectiveness, similar to the multi-hole result. The centre-line of the film had lower peak values in comparison to both the experimental and multi-hole results. However, in contrast to the multi-hole, an overestimation of the lateral spread of film effectiveness was made. For larger blowing ratios (BR = 0.96), where lift-off is a dominant influence, the film effectiveness was over-estimated.

For films in closer proximity, a comparison between experimental and multi-hole results by Murray and the film superposition method was done using a pitch of 3.0D and blowing ratios of 0.48 and 0.96. Contour of the results are shown in Figure 5.2. Here the Goldstein-Sellers method adequately captures the build-up and lateral mixing of films. However, at the blowing ratios and spacing shown here it is difficult to assess how well this is captures given that the film effectiveness saturates. Even so, this empirical method provides a numerically more efficient mechanism of capturing representative film effectiveness profiles compared to the multi-hole CFD method. Furthermore, these results demonstrate the high potential of closely-packed film arrays and the quick saturation in the streamwise direction. Consequently further insight is required to understand how changes to the film hole spacing impact the film protection as well as how well the modified Goldstein-Sellers method can capture such behaviour.

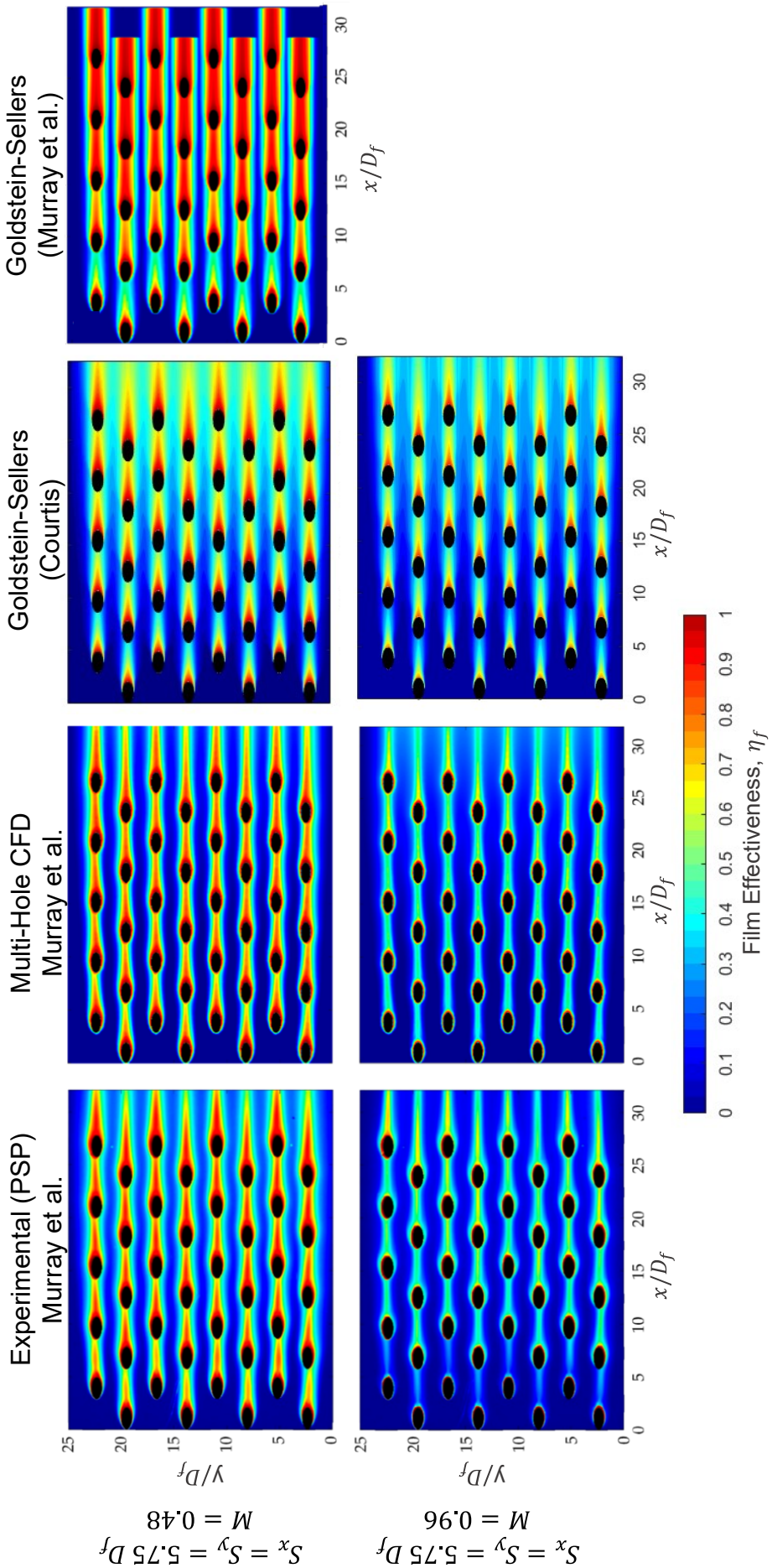


Figure 5.1: Comparison of Goldstein-Sellers superposition in this thesis compared to experimental, CFD and Goldstein-Sellers in [10]. For a staggered array with film spacing of 5.75 D_f and blowing ratios of 0.48 and 0.96.

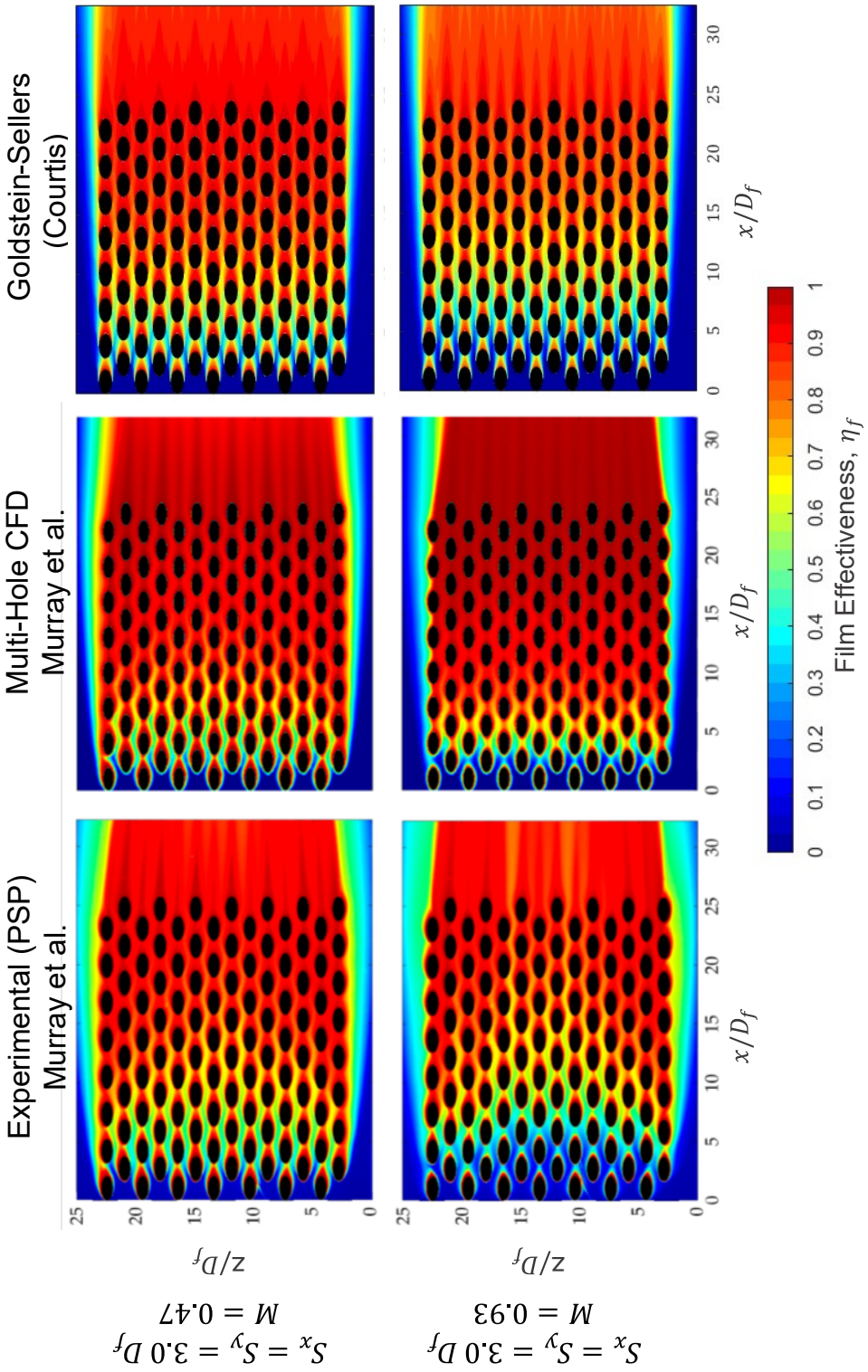


Figure 5.2: Comparison of Goldstein-Sellers superposition in this thesis compared to experimental, CFD and Goldstein-Sellers in [10]. For a staggered array with film spacing of 3.0 D_f and blowing ratios of 0.47 and 0.93.

5.3 Journal Paper

International Journal of Turbomachinery, Propulsion and Power
2021

Vol. 6, Page 37

Influence of Spanwise and Streamwise Film Hole Spacing on Adiabatic Film Effectiveness for Effusion-Cooled Gas Turbine Blades

Matthew Courtis[1*], Alexander Murray[1], Ben Coulton[1], Peter Ireland[1] and Ignacio Mayo[2]

1. Oxford Thermofluids Institute, University of Oxford, Oxford OX2 0ES, UK;

alexander.murray@eng.ox.ac.uk (A.M.); ben.coulton@eng.ox.ac.uk (B.C.);

peter.ireland@eng.ox.ac.uk (P.I.)

2. Rolls-Royce PLC, Derby DE24 8BJ, UK; mayo@rolls-royce.com

* Correspondence: matthew.courtis@eng.ox.ac.uk or matthew.courtis.10@gmail.com

Abstract

To meet the challenges of increased thermal loads and performance demands on aero-engine turbine blades, more advanced cooling techniques are required. This study used a modification of the well-known Goldstein equation to predict film effectiveness for an individual film cooling hole, and applied the Sellers' superposition method to apply these films across effusion cooled configurations. In doing so, it tackles a relatively unchallenged problem of film holes in close spanwise proximity. An experimental set-up utilised infrared cameras to assess the film effectiveness of nine geometries of varying spanwise- and streamwise- spacings. Higher porosity led to increased thermal protection, and the spanwise spacing had the most profound impact, with film effectiveness approaching 0.9. Additionally, greater uniformity in the spanwise direction was observed. The modified Goldstein-Sellers method showed good agreement with experimental results although lateral mixing was underestimated. This method represents a tool which could be easily implemented in industry for rapid assessment of novel cooling geometries.

5.3.1 Introduction

Over the last several decades the operating temperature of gas turbines has continued to increase, at about 10 K per year. As a result of the second law of thermodynamics, an increase in temperature leads to an increase in overall engine efficiency. The consequence is high inlet temperatures seen by the turbine, imposing high thermal stresses, especially on the guide vanes and first several blade rows. To resolve such issues and maintain suitable dependability of engines there is a need for turbine blade cooling systems. Major milestones, such as internal cooling and film cooling, have enabled inlet temperatures of up to 2000 K. Coolant flow rate should be minimised to limit aerodynamic losses and consequently as temperatures continue to move beyond 2000 K more advanced cooling methods are required. Increased engine efficiency will reduce fuel costs and in turn has the capability to reduce CO_2 emissions by over 180,000 kg per engine per year [12].

Transpiration cooling takes advantage of porous walls and injects coolant into the flow, creating a protective film between the surface wall and hot gas. Two main processes are involved to produce cooling:

1. Convective cooling - between the cooling fluid and porous wall
2. Film cooling - a layer of coolant air over the blade reduces the convective heat flux from the hot gas cross flow

Consequently, the study of turbine cooling performance generally takes two distinct forms: film effectiveness and metal effectiveness. The former represents the performance of only the films and is measured by how closely the adiabatic wall temperature can be kept to to the coolant temperature, shown in equation 5.1. Metal effectiveness combines both the film cooling and internal convective cooling, providing a representation of the overall cooling performance.

$$\eta_f = \frac{T_\infty - T_{aw}}{T_\infty - T_c} \tag{5.1}$$

While transpiration cooling has been intensively researched for many years, such as early work

produced in 1951 by NASA [13] or more recently in [58], successful application in engines has remained unattainable due to limitations of the porous materials available. Additionally, accurately modelling the aerothermal and mechanical stress fields remains a challenge as coupling is required between the flow, thermal and stress fields. These are made even more complex, given the shear number of film holes present in highly porous cooling schemes.

Despite this, there is a move from traditional film cooling methods to effusion cooling. Krewinkel [5] highlighted that the difference between transpiration and effusion cooling is not always clear, although the former tends to be associated with porous media and the latter with discrete film holes. Nevertheless, effusion cooling represents a path on the way to transpiration cooling which theoretically occurs when the solid and coolant reach thermal equilibrium. A significant number of studies on effusion cooling have been performed in recent years [14, 95, 77, 54, 96], which is unsurprising given the major benefits of film superposition. This occurs with reduced film hole spacing as a result of film jet interaction with the consequence of augmented film protection offered by each subsequent downstream film hole.

Superposition was first proposed by Sellers [78], which found that summation of films from a single hole could be used to replicate multiple rows of films. This takes the form of equation 5.2.

$$\eta_f(x,y) = 1 - \prod_{i=1}^{n} \left(1 - \eta_{f,i}(x,y)\right) \tag{5.2}$$

Experiments by Muska et al. [97] and more recently Murray et al. [10] reaffirm the superposition method, and its usefulness in predicting multi-row film cooling. The latter used a modified Goldstein equation [26] (described later, but in the form of equation 5.3) to predict the film distribution of an individual hole and when combined with Sellers' superposition found the additive effect of multiple film hole rows. Jiang et al. [46] found that even one additional staggered row (offset by half the primary spacing in both streamwise and spanwise directions, x and y) produced much higher film effectiveness. Even at high injection velocities, where the coolant flow detached from the metal surface, the vortex pairs of the first cooling row acted to

push the second row films toward the surface resulting in quick reattachment and enhanced film protection.

Murray et al. [6] used the Sellers method as part of a decoupled solver (separately solving the internal and external thermal fields) and showed good agreement between experimental and numerical results, as well as an exhibit for efficient numerical studies for complex double-walled effusion systems. Despite these successes, no account was made for the proximity of adjacent holes (spanwise consideration), and as such were deemed to be independent. This causes an issue for more porous geometries, and most studies have focused on film cooling with relatively large spanwise distances. This study builds upon this work to incorporate the method to more porous geometries which are required to move from effusion towards transpiration-like cooling.

The present study investigates the influence of streamwise and spanwise spacing on film effectiveness using a modified Goldstein-Sellers approach, which is explained in the next section. An infrared methodology measures the cooling performance for nine geometries at six coolant flow rates. Numerical results for varying film spacing are presented and a more advanced cooling layout explored. Experimental results are presented before a comparison between the two result sets are evaluated. The work represents a preliminary step in understanding the importance of film hole proximity and extensions to the Goldstein-Sellers method.

5.3.2 Materials and Methods

5.3.2.1 Research Object

Film cooling performance was assessed using flat plate geometries, all of which had a staggered configuration of film holes inclined at 30° to the plate surface, as illustrated in Figure 5.3. The hole diameter in all cases was 4.0 mm, with additional dimensions also stated. Spacing between film holes was varied in both the streamwise- and spanwise- direction for S_x/D = 3.0, 4.5 and 6.0, and similarly for S_y/D, to produce a test matrix of nine geometries. The area of coverage of film holes was based on a 6×6 array for $S_y/D = S_x/D = 6.0$, and the other spacings had more rows and columns in order to meet the same coverage area.

Geometric Properties	
D	4.0 mm
H	10 mm
S_x/D	3.0 , 4.5 , 6.0
S_y/D	3.0 , 4.5 , 6.0
Rows	11 , 8 , 6
Columns	11 , 8 , 6
L/D	5.0
l_1	248 mm
l_2	178 mm
l_3	20 mm
l_4	29 mm
l_i,x	140 mm
l_i,y	100 mm
γ	30°

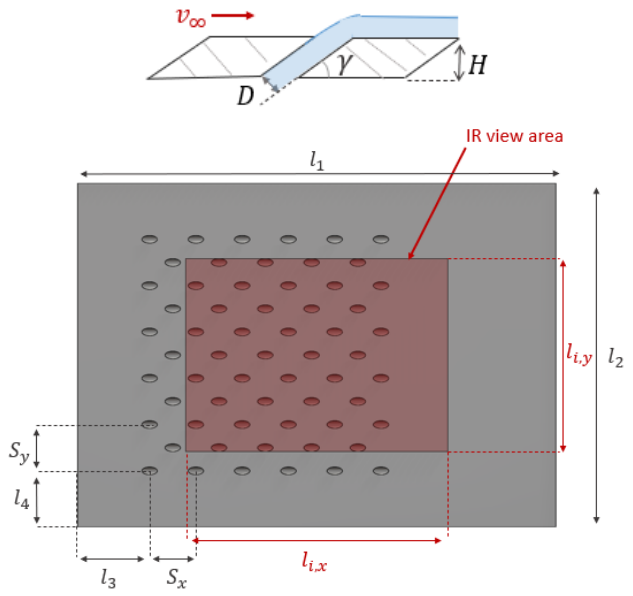


Figure 5.3: Schematic showing the dimensions of the flat plate geometry, where the red section highlights the visible portion for the IR camera. The illustration here shows the $S_x/D = S_y/D = 6.0$ geometry.

A more advanced film cooling system was also numerically investigated. A base-line design (TD2) was used, and represents a transpiration-like cooling system with porosity of 19%. This design was originally modelled on a double-wall effusion system [53] at the Oxford Thermofluids Institute (OTI), but with an increase in the number of film holes. The film hole diameter was also reduced to be 1/5 the size of conventional holes. The hole spacing was $S_x/D = S_y/D = 3.5$ with a hole diameter of 2 mm, and a 'hole blockage' of 25%. The latter is defined as the ratio of film holes removed due to proximity to internal design features (pedestals and impingement jets). For direct comparison the spanwise spacing was varied and the streamwise spacing altered to maintain porosity, as tabulated in Table 5.1. Films effectiveness was found using the modified Goldstein-Sellers approach for each configuration at four blowing ratios ($M = 0.20, 0.25, 0.30, 0.35$), across the extent of the domain.

TD2 Study Geometric Properties					
D	2.0 mm				
S_x/D	4.9	4.1	3.5	3.1	2.7
S_y/D	2.5	3.0	3.5	4.0	4.5

Table 5.1: Properties for TD2 film spacing variation study

5.3.2.2 Numerical Method

An in-house MATLAB code was used to predict the film effectiveness of any given film using a modified Goldstein correlation. This method attempts to model the decay of films in both the streamwise and spanwise directions, and is defined in equation 5.3. M is the blowing ratio of the film, specified as the product of the ratios of density and velocity between the coolant and free-stream fluid, $M = (\rho_c v_c)/(\rho_\infty v_\infty)$. This parameter influences the following constants: turbulent thermal diffusivity α_t and x_{decay} which captures changes in the streamwise direction. The spanwise distance constant (c_1) and the spanwise shaping constant (c_2), which influence the spanwise film decay, are variables dependent on both the blowing ratio M and distance downstream of the film hole x. Values for these are based on experimental and correlation data - which can be found in [10] and [98].

$$\eta_f(x,y) = M\frac{V_\infty D}{8\alpha_t\left(x/D + x_{decay}\right)}\exp\left\{-\left(\frac{y}{c_1}\right)^{c_2}\right\} \tag{5.3}$$

Films were placed individually on a global grid, and subject to the Sellers' superposition as illustrated in Figure 5.4. This method could take into account variable blowing ratios, and any form of spatial configuration. It is worth noting that the empirical data used had a hole aspect ratio (L/D) of 2.0, compared to $L/D = 5.0$ for geometries investigated in this study. Lutum and Johnson [99] demonstrated that a lower aspect ratio reduced film effectiveness, and consequently the film effectiveness calculated here may represent a conservative estimate of the actual value.

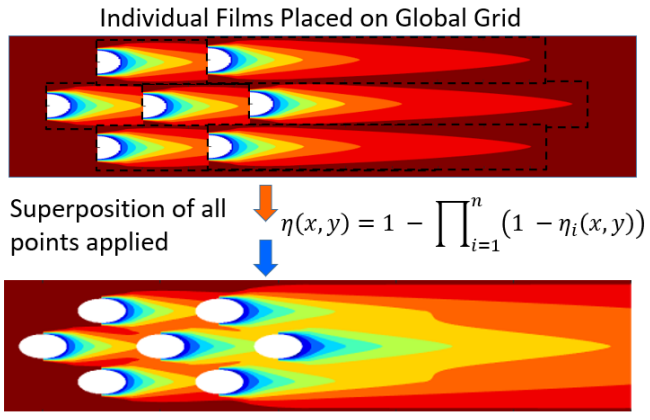


Figure 5.4: Visualisation of Sellers' superposition method

5.3.2.3 Experimental Method

Experimental Facility

The **D**ouble-Walled **E**ffusion **C**ooling **A**erothermal **F**acility (DECAF) at the Oxford Thermofluids Institute was used for the experimental study - see Figure 5.5. The facility provides conditions for scaled tests of flat plate cooling geometries. A more detailed description of the facility and measurement procedure can be found in [87], although a brief summary is also provided here.

The facility provides Reynolds number similarity to engine conditions and has been specified for high temperature capabilities. Rohacell was used for test geometries to investigate film effectiveness, assuming an adiabatic surface. This material was chosen due to its low thermal conductivity ($\lambda \sim 0.030$ W/m-K), and a high grade with a closed cell structure was selected (71 HERO) for improved machining and reduction of the impact roughness would have on film holes with small diameters. Film effectiveness is calculated by measuring surface temperature through an infrared camera, and the back-side surface temperature is also monitored. A range of mass flows between 0.01 kg/s and 0.035 kg/s were investigated for each geometry. This was achieved by varying the coolant mass flow into the plenum, while keeping the mainstream velocity constant. The typical experimental mainstream Reynolds number based on film hole diameter, mainstream temperature, coolant-mainstream temperature ratio and density ratio, as well as other parameters are tabulated in Table 5.2.

Re_{∞,D_f}	T_∞	T_c/T_∞	ρ_c/ρ_∞	Bi_{Roha}
1.12×10^4	373 K	0.8	1.2	47

Table 5.2: Approximate experimental conditions

Infrared Methodology

Temperatures of the external surface were made through the use of two *FLIR A655sc* infrared cameras, with optical access provided by Zinc Selenide windows. Thin wire thermocouples were attached to both the hot-gas and coolant plenum external surfaces of the test geometry. These are within the IR camera field of view, permitting an in-situ calibration. External sur-

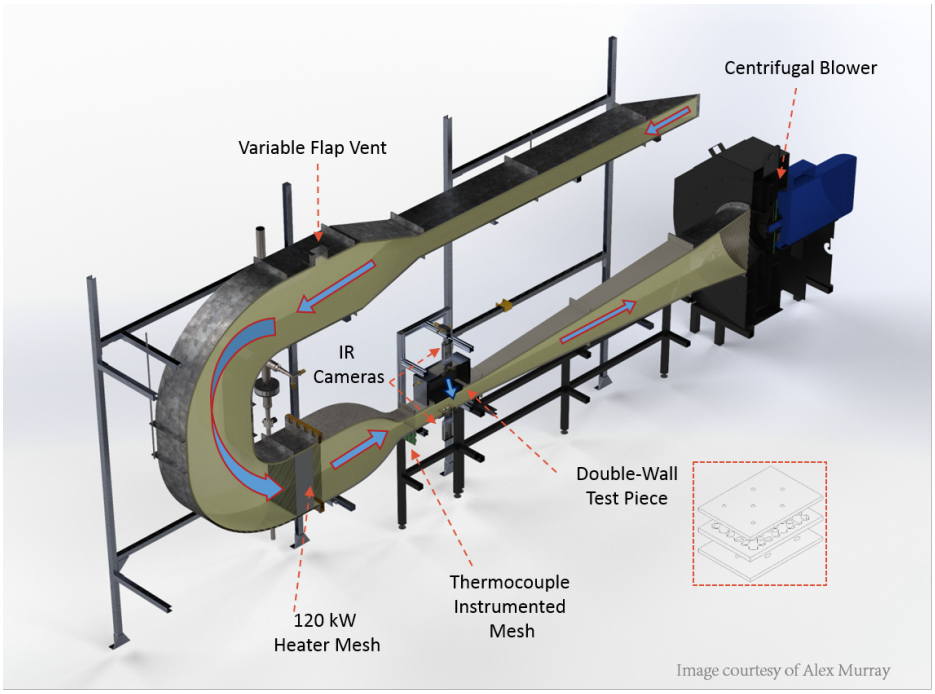


Figure 5.5: Annotated schematic of the OTI experimental facility

faces were painted matt black to minimise IR reflections from the surroundings. The calibration method is described in detail in [87], in which both the blackbody and greybody calibration were used to calculate temperatures from the raw data output of the cameras. The former finds the ideal blackbody parameters, and the latter finds parameters due to non-ideal surface IR emission. The frame rate of the camera was set at 25 Hz to allow assessment of flow unsteadiness, and data is averaged over 10 seconds (250 frames) to provide a mean steady-state temperature. Using these temperatures, the film effectiveness was calculated using equation 5.1.

5.3.3 Results and Discussion

5.3.3.1 Numerical Results

To determine the affect of changing streamwise (S_x) and spanwise (S_y) spacing on the film effectiveness, the modified Goldstein method with Sellers superposition was implemented across a standardised geometry. The first study focused on maintaining a constant blowing ratio with 3 rows and 3 columns for a staggered array, which were varied as $3.0 \leq S_y/D \leq 5.0$ and $3.0 \leq S_x/D \leq 8.0$. A visualisation of this along with the comparison area can be seen in Figure 5.6. Another set of calculations were based on the assumption of constant mass flow between geometries. To achieve this, each geometry was made to cover the same surface area, and the

coolant mass flow kept constant, as illustrated in Figure 5.7.

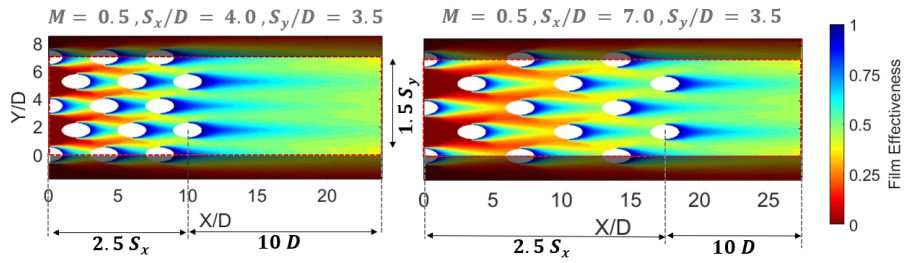


Figure 5.6: Comparison area for mean film effectiveness with varying S_x/D and S_y/D, using a constant blowing ratio

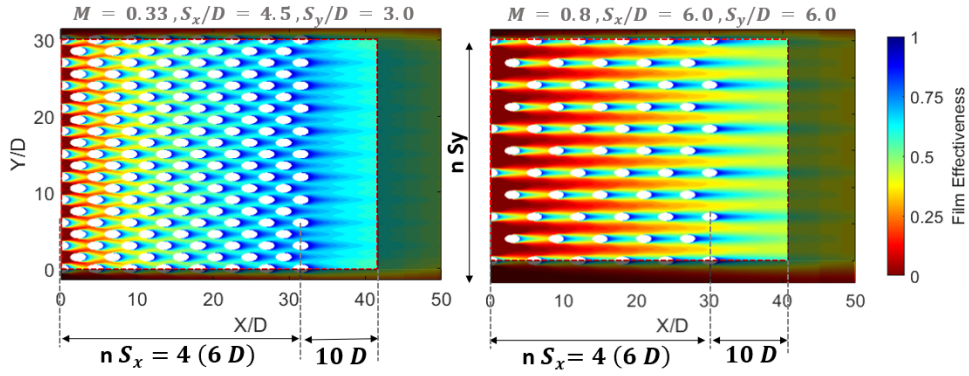


Figure 5.7: Comparison area for mean film effectiveness with varying S_x/D and S_y/D, with a constant coolant mass of $\dot{m}_c = 2.56\,\text{kg/s/m}^2$

For a fixed mass flow rate, increasing porosity reduces the blowing ratio. While this reduces the performance of any individual film, the proximity of neighbouring holes may compensate for this detriment. Figure 5.7 illustrates that as spanwise distance increases the films become more isolated, and distinct hot-streaks can be observed between film columns. As S_y decreases the extent of the hot streaks is reduced given the adjacency of a staggered film and less of the exterior wall is subject to the mainstream temperature, a benefit even without accounting for film interaction. Additionally, the lower spanwise distance resulted in merging of adjacent films. Film effectiveness is enhanced by reducing S_x as would be predicted by Sellers superposition, but since films propagate with the mainstream flow, proximity in the streamwise direction is less influential than that for the spanwise direction.

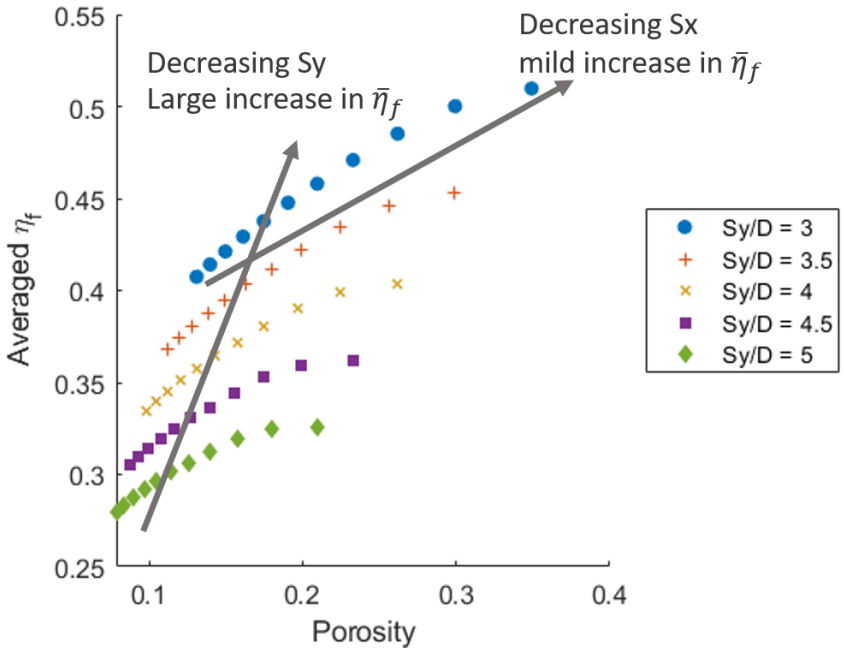


Figure 5.8: Effect of film spacing (S_x,S_y) on mean film effectiveness, for $M = 0.5$

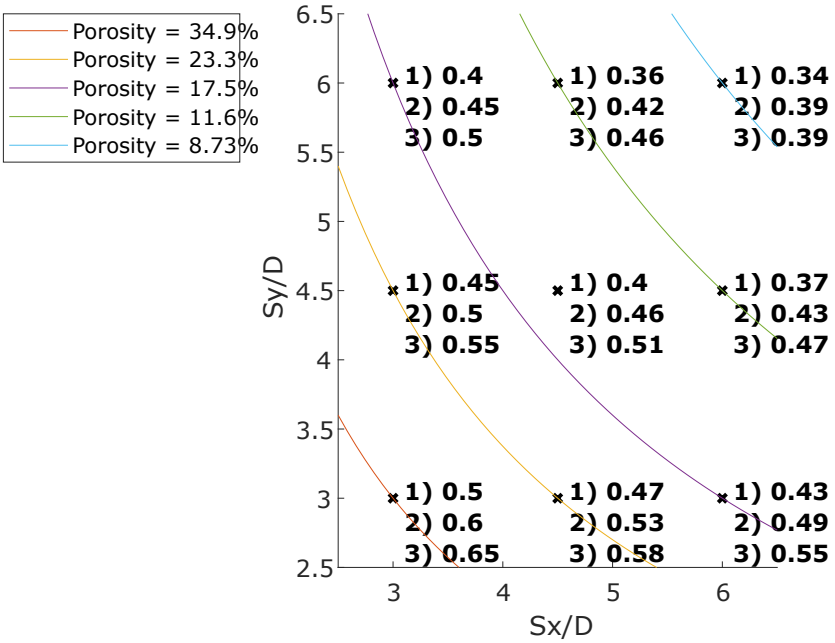


Figure 5.9: Effect of film spacing (S_x,S_y) on mean film effectiveness, for three coolant mass flows. Isobars of constant porosity are displayed.

The averaged film effectiveness for the first study is compared to porosity in Figure 5.8, where the symbols correspond to a constant S_y. Here porosity is defined as the geometric porosity, the surface area of the film holes (A_h) compared to the area these holes cover (A_s), and is defined in equation 5.4.

$$\phi = \frac{A_h}{A_s} = \frac{\pi}{2(S_x/D)(S_y/D)\sin(\gamma)} \tag{5.4}$$

As spanwise spacing was reduced, the area-averaged film effectiveness increased at a greater rate than the influence of streamwise spacing. This is made clear on the figure by two arrows indicating the general trend of film effectiveness for a reduction in S_y and S_x respectively. Consequently, for an increase in porosity, and to reduce the added mass flow required, having films with a lower S_y was advantageous.

To investigate constant mass flow across all geometries the area-averaged film effectiveness is shown in Figure 5.9, alongside isobars of constant porosity. As one moves along a constant porosity curve, the film effectiveness benefits from decreasing S_y and increasing S_x. This was true for all three mass flow rates, confirming that increasing porosity will enhance overall film effectiveness.

5.3.3.2 TD2 Results

High film effectiveness was demonstrated by TD2, as well as the design variants. Figure 5.10 plots the area-averaged film effectiveness of each variant characterised by the ratio of streamwise- to spanwise- spacing (S_x/S_y), for four blowing ratios. The same trend of increased film effectiveness with a reduction in S_y is observed. Increasing the blowing ratio increased the film effectiveness throughout, although with diminishing returns for each blowing ratio increment. Film effectiveness contours for two TD2 variants and the base geometry are shown in Figure 5.11 at $M = 0.3$. It can be seen that the leftmost plot (smallest S_y) has increased spanwise uniformity and reduction of hot spots observed at the location where film holes were removed. The increased lateral spread acts to compensate for a missing film hole and maintain uniformity

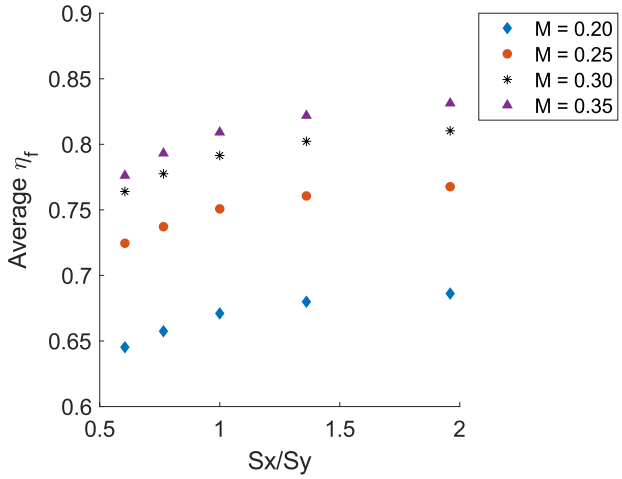


Figure 5.10: Averaged film effectiveness compared to ratio of spanwise- and streamwise- spacing for TD2-base geometry for four blowing ratios.

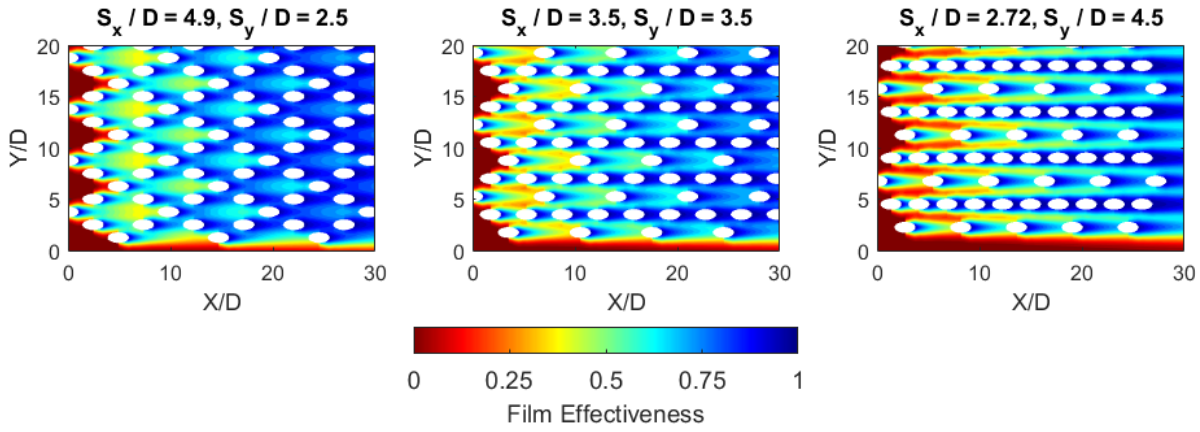


Figure 5.11: Film effectiveness contours for TD2 and two film spacing variations, for $M = 0.30$. TD2 is the central plot.

of film coverage. This is consistent with results by [8] which demonstrated that while blockage ratio was an important parameter affecting film effectiveness for a porous metal plate, ratios of up to 30% had only a small influence.

For streamwise columns without hole removal (the second column from the bottom and for figures as we move left to right at $Y/D = 2.5$, $Y/D = 3.5$ and $Y/D = 4.5$) the increased streamwise spacing reduced the superposition effect, but given these are well protected areas and reach saturation after several rows, one would expect this not to be a concern for overall blade design. These results suggest that further double-walled effusion designs should consider implementing low spanwise spacing if feasible.

5.3.3.3 Experimental Results

To account for differences in tunnel velocity and fluid properties between experimental runs, a non-dimensional mass flow was used for comparison, defined in equation 5.5. Where $\bar{h}$ is the mean heat transfer coefficient (W/m^2/K) and A is the surface area of the flat plate.

$$m^* = \frac{\dot{m}_c c_p}{\bar{h} A} \tag{5.5}$$

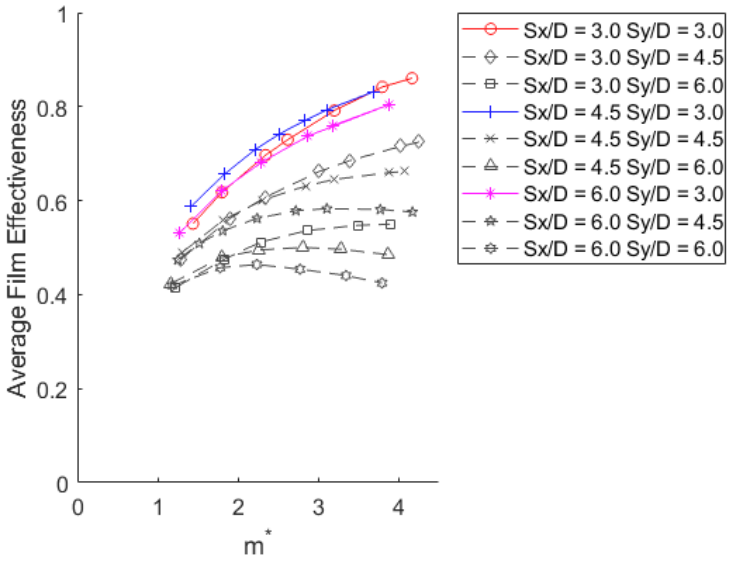


Figure 5.12: Experimental overall film effectiveness against non-dimensional mass flow (m^*). Geometries with $S_y/D = 3.0$ are highlighted, and have the highest averaged film protection illustrating the benefits associated with low spanwise film spacing.

The averaged film-effectiveness, for the visible camera area, was calculated for each condition and is displayed in Figure 5.12. At m^* near 1 there are three distinct groupings of film effectiveness, each with constant S_y. Between the three groups, as S_y decreases the film effectiveness increases. For larger values of m^* these lines diverge and the porosity (ie S_x) determines the film effectiveness range. For clarity the lowest spanwise spacing results ($S_y/D = 3.0$) are highlighted and exhibited the best performance, across the entire range of m^*. This indicates that S_y is more crucial to film protection than S_x. And can be seen when comparing two geometries with the same porosity, the line plotted with triangles ($S_x/D = 4.5$, $S_y/D = 6.0$) and stars ($S_x/D = 6.0$, $S_y/D = 4.5$). Across the entire range of m^* the latter geometry, with lower S_y, has a higher average film-effectiveness.

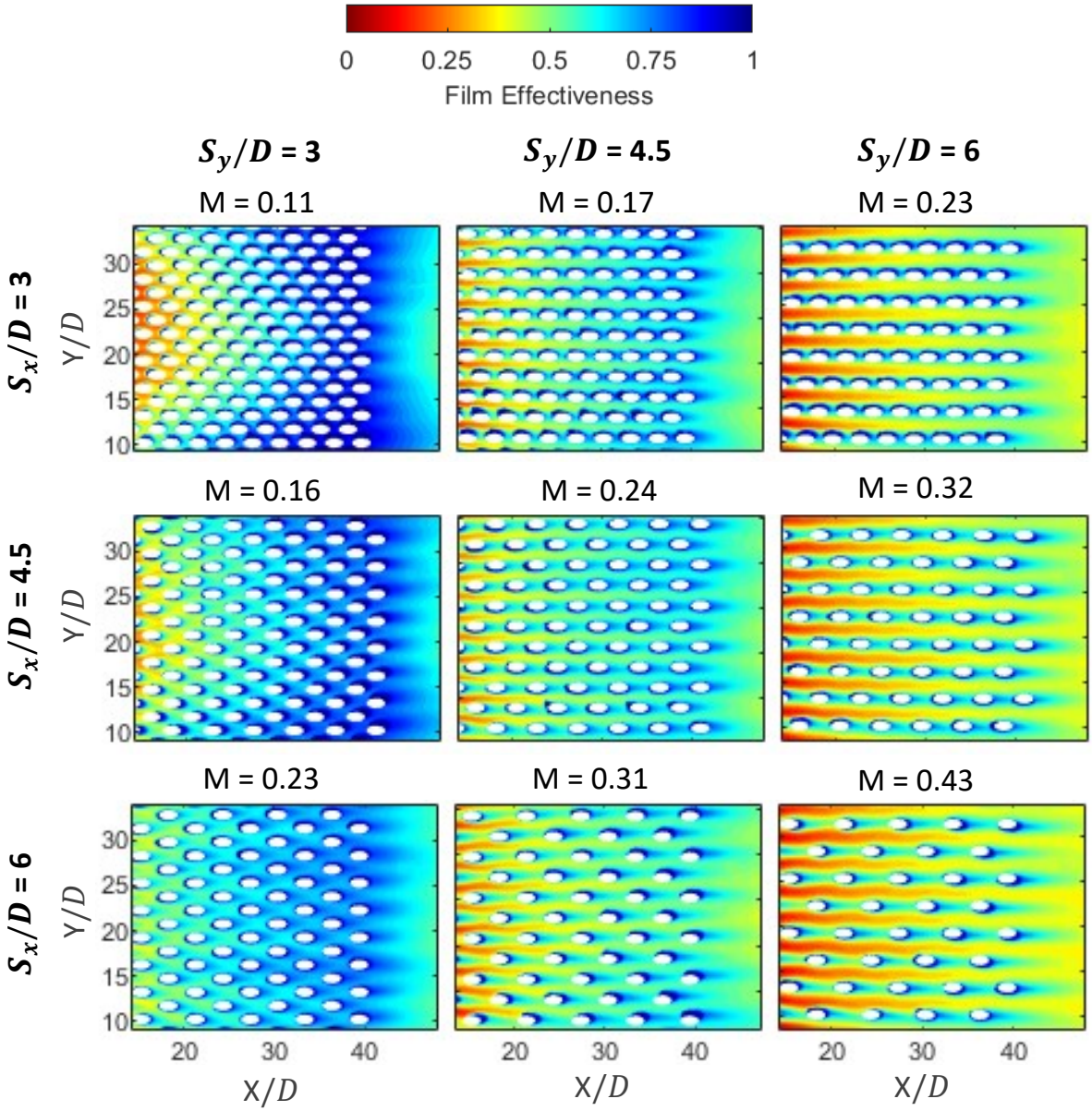


Figure 5.13: Experimental film effectiveness contours for $m^* \approx 1.8$. The blowing ratio,M is displayed above each geometry. In general increased porosity results in a more uniform film coverage.

The general characteristic of these curves is an increase in film protection with coolant flow which plateaus as coolant saturates, and for $S_y = 3.0$ geometries they approach a film effectiveness of 0.9. For lower porosity cases, not only is a plateau reached but film effectiveness reduces. This is a consequence of high blowing ratios, and the occurrence of jet lift-off. An unexpected observation was a higher average film effectiveness for $S_x/D = 4.5, S_y/D = 3.0$ compared to the most porous geometry ($S_x/D = S_y/D = 3.0$) for all but the highest mass flow, discussed in more detail below.

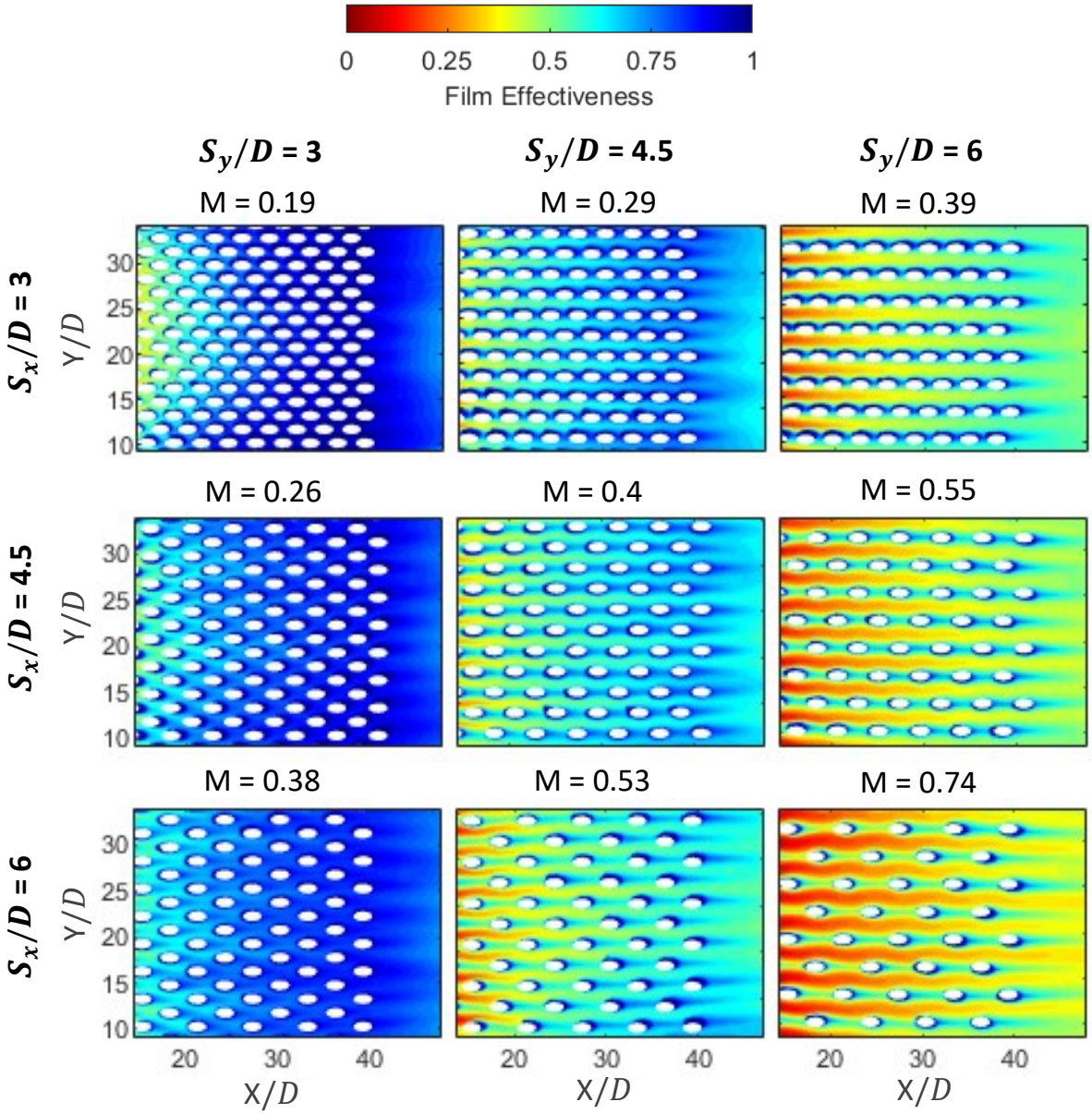


Figure 5.14: Experimental film effectiveness contours for $m^* \approx 3.2$. The blowing ratio,M is displayed above each geometry. High porosity geometries form saturated films leading to uniform and almost complete protection.

Contours of film effectiveness for two mass flows, approximately $m^* = 1.8$ and $m^* = 3.2$ are illustrated in Figures 5.13 and 5.14 respectively. Enhanced film protection is evident for the most porous geometries, as well as the benefit of low spanwise spacing. The most striking feature is that film hole proximity to adjacent ('staggered') rows enhances the superposition of films. This is still present at $S_y/D = 4.5$, albeit to a lower extent. However for $S_y/D = 6.0$ it is almost absent.

At the two highest porosities with $S_y/D = 3.0$ (S_x/D of 3.0 and 4.5) there is a variation in film effectiveness across the spanwise direction. A similar feature was observed by [10], where a flat plate with hole spacings of $S_x/D = S_y/D = 3.0$ was investigated using pressure-sensitive paint for a range of blowing ratios. It was suggested to be a result of variations in the blowing ratio between film holes across the span, and a product of the side-wall boundary layer reducing the mainstream flow velocity in the vicinity of the side film holes. In this study, given the distance between the side walls and test piece, another explanation for the variation in blowing ratio is provided here. At large spanwise spacings, the mainstream flow can migrate around individual film holes, evidenced by hot streaks. However, as S_y decreases the mainstream flow must also divert around the nearby staggered holes. Consequently, increased upwards curvature of the mainstream flow imposes an increased static pressure on the film hole outlet. Given the finite lateral boundary of the cooling array, film holes at the edge do not pose as large of a obstacle for the mainstream flow, as it can curve both upwards and laterally, thus the static pressure is lower at the edge of the cooling array compared to the middle. This explains the higher averaged film effectiveness for $S_x/D = 4.5, S_y/D = 3.0$ compared to $S_x/D = S_y/D = 3.0$, as coolant deviates to the periphery holes rather than those which are central. Additionally, the upstream central holes for the latter geometry may struggle due to the lower blowing ratio, which may lead to hot-gas ingestion at the leading central film holes. Despite this feature, geometries with $Sy = 3.0$ still exhibit a high film effectiveness throughout the visible domain, even along the centreline.

The streamwise-averaged film effectiveness is introduced here, and shown in Figure 5.17 and 5.18, with constant S_y for each plot. This metric is an indication of how uniform the protection

is perpendicular to the mainstream flow. For film holes spaced with $S_y/D = 6.0$, the difference between the peak and trough streamwise-average film effectiveness is approximately 0.4, compared to 0.2 for $S_y/D = 4.5$ and 0.15 for $S_y/D = 3.0$. This highlights that a reduction in S_y increases the mean film effectiveness as well as reducing the variance. Hence one can conclude that if a uniform protection is desired, the spanwise film spacing is crucial to this aim. On the contrary streamwise spacing has only a small influence on this, but acts to increase the mean film effectiveness.

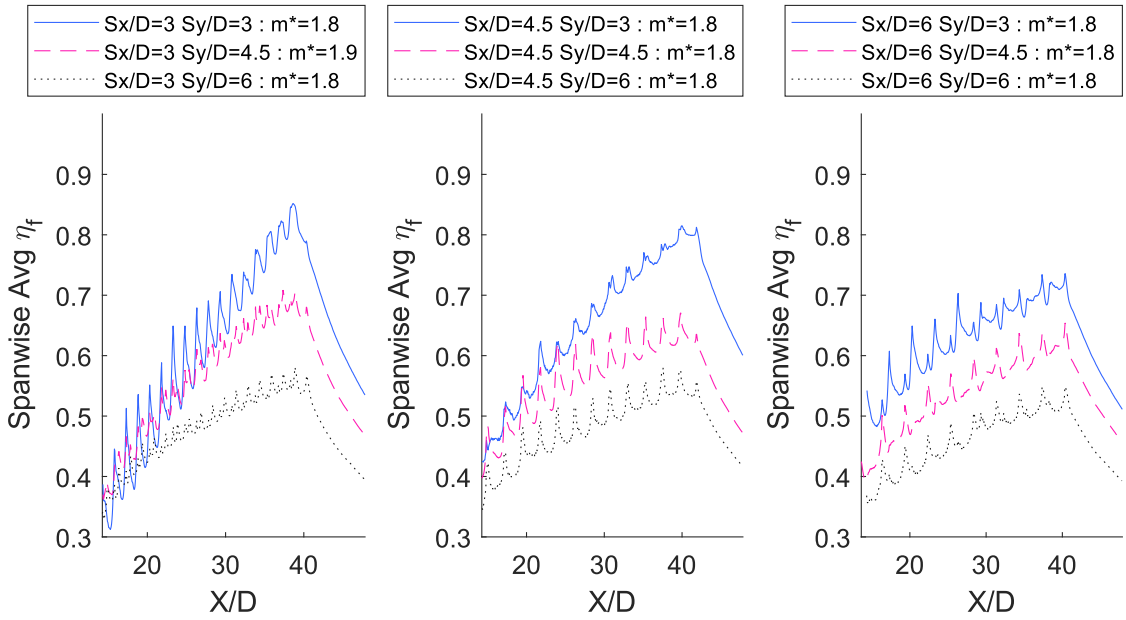


Figure 5.15: Spanwise-average film effectiveness for $m^* \approx 1.8$. In each individual plot geometries with constant S_x are shown

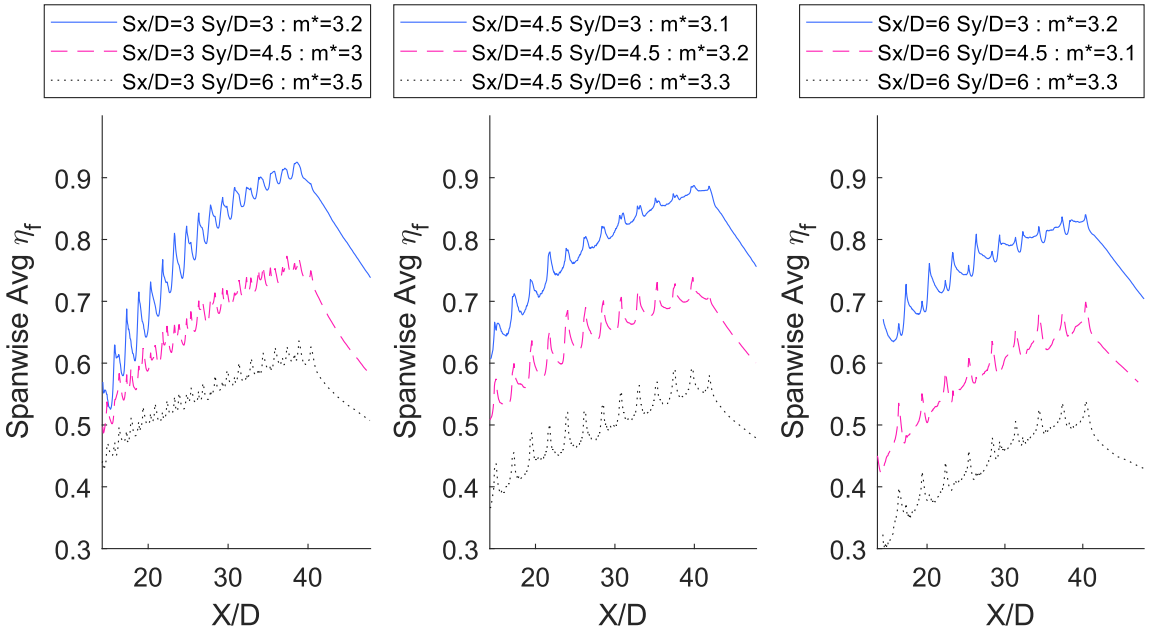


Figure 5.16: Spanwise-average film effectiveness for $m^* \approx 3.2$. In each individual plot geometries with constant S_x are shown

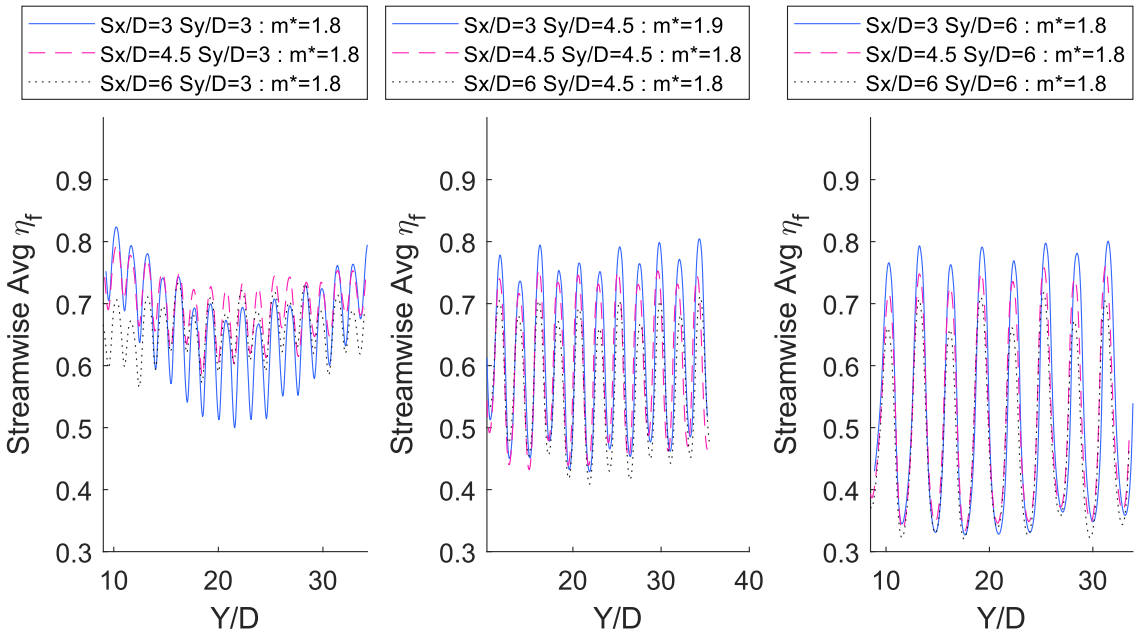


Figure 5.17: Streamwise-average film effectiveness for $m^* \approx 1.8$. In each individual plot geometries with constant S_y are shown

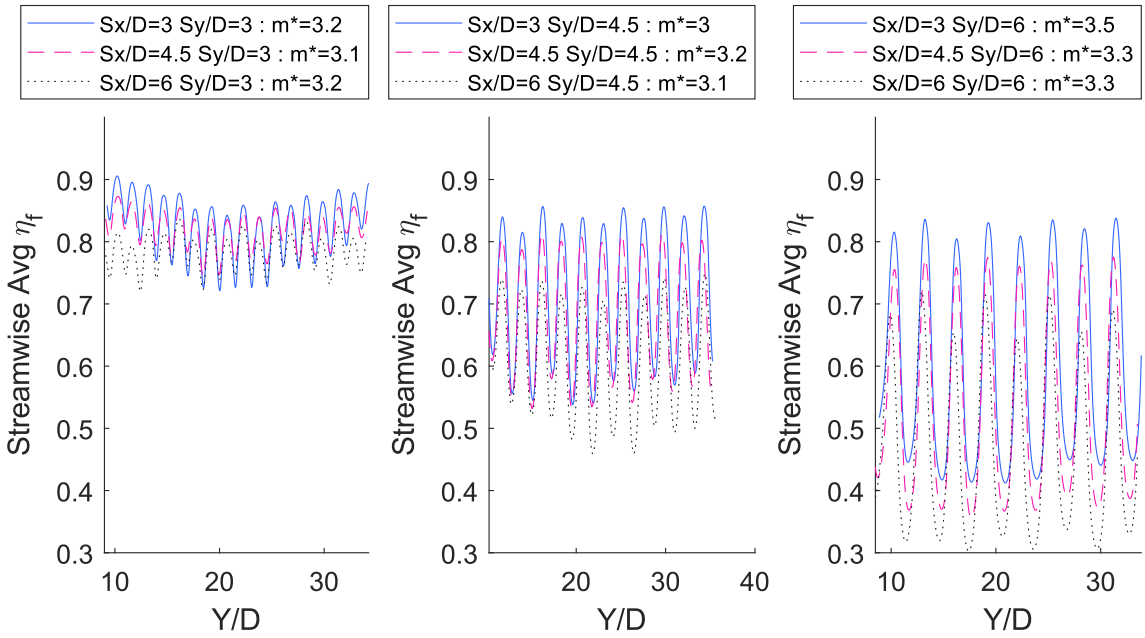


Figure 5.18: Streamwise-average film effectiveness for $m^* \approx 3.2$. In each individual plot geometries with constant S_y are shown.

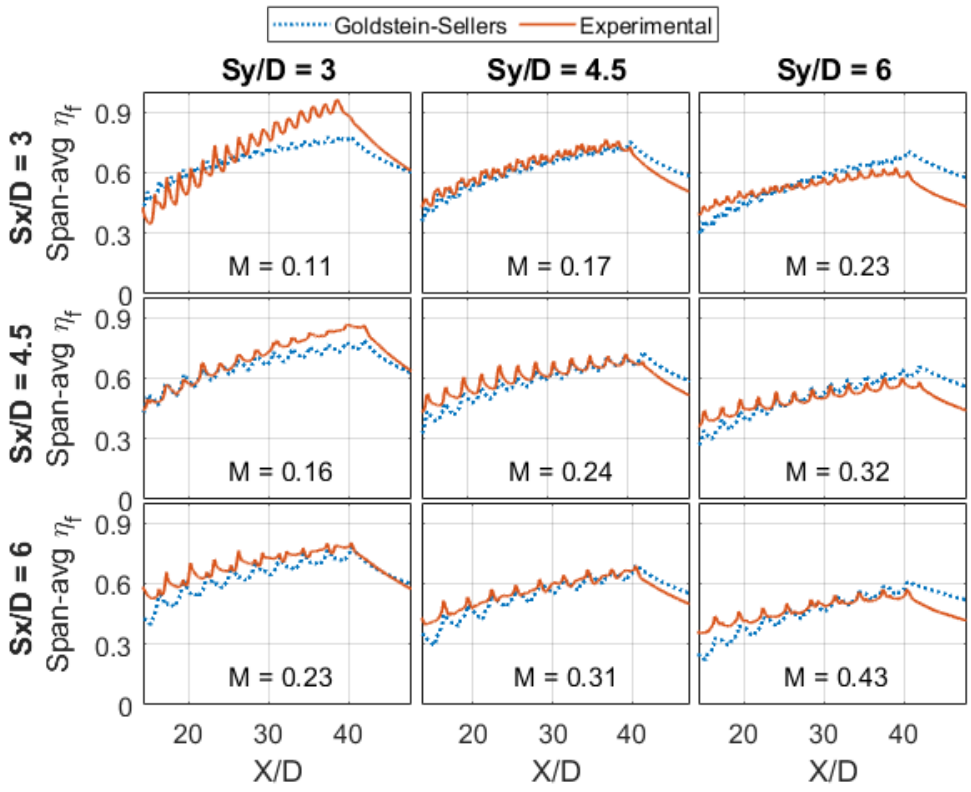
5.3.3.4 Numerical and Experimental Comparison

Spanwise- and streamwise- averaged film effectiveness were calculated using the modified Goldstein-Sellers across the same area as the infrared camera: $14D < x < 48D$ and $9D < y < 34D$. Spanwise-averged results are shown in Figure 5.19 A and B and the streamwise-averaged results in Figure 5.20 A and B, with the solid and dashed line representing experimental and numerical results respectively.

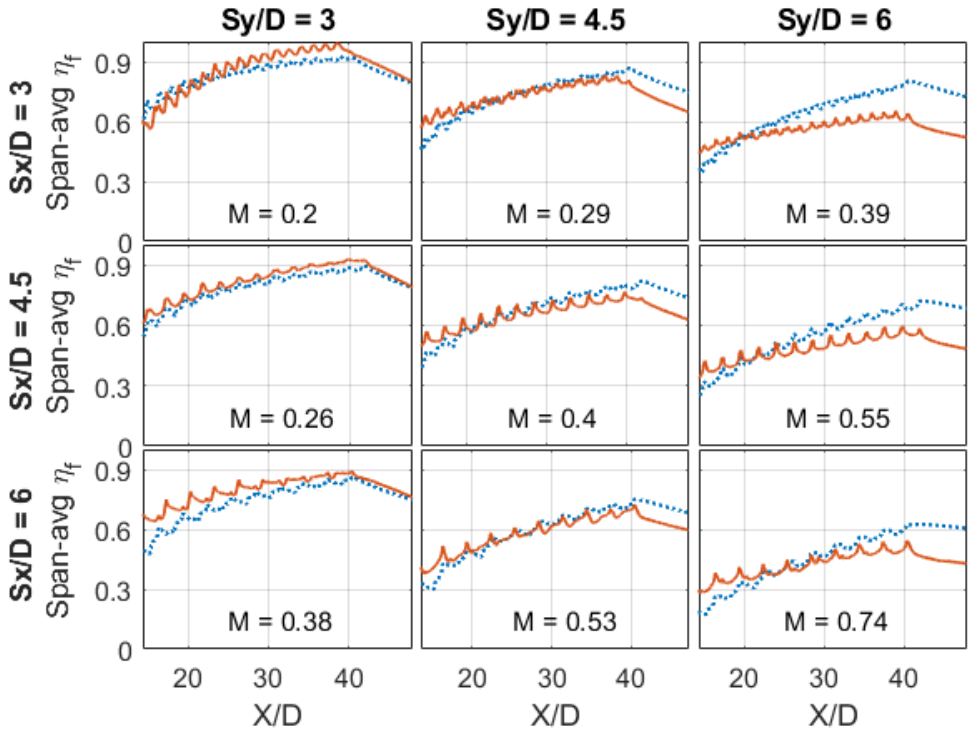
The modified Goldstein-Sellers captures the general trend of spanwise-average film effectiveness across all geometries. For the largest spanwise spacing ($S_y = 6D$) the spanwise-averaged η_f is under-predicted for the leading film holes up to $X/D = 20$ but over-predicted beyond $x/D = 40$, indicating that while the initial film protection was underestimated, the effect of superposition was overly optimistic. The same trend can be observed for $S_y = 4.5D$, but to a lesser extent. For the lowest spanwise spacing ($S_y = 3D$) spanwise-averaged η_f was well captured despite a small under-prediction throughout the domain, with a deviation for $S_x = 3D$, $S_y = 3D$ due to suspected variable mass flow distribution, as previously discussed.

The streamwise-average film effectiveness indicates that films are well-matched for $S_y = 6D$ and $S_y = 4.5D$, with numerical results having higher film effectiveness directly downstream of the film holes, and a lower film effectiveness in the gaps between film hole columns. This would suggest a lack of lateral spread in film coverage was predicted numerically. For $S_y = 3D$ the numerical model under-predicts throughout the plate, however the level of variation between film rows was similar.

Spanwise- and streamwise- averaged film effectiveness indicate the modified Goldstein-Sellers method can predict the superposition of staggered film arrays for both densely packed and moderately spaced film holes. This is further examined by the film effectiveness contours for both experiments and numerical method in Figures 5.21 **(a)** and **(b)**. Three geometries with evenly spaced film holes ($S_x = S_y$) are shown at two mass flows, with blowing ratios indicated above each plot. For the lowest film spacing ($S_x = S_y = 3D$) the two mass flows paint a contrasting

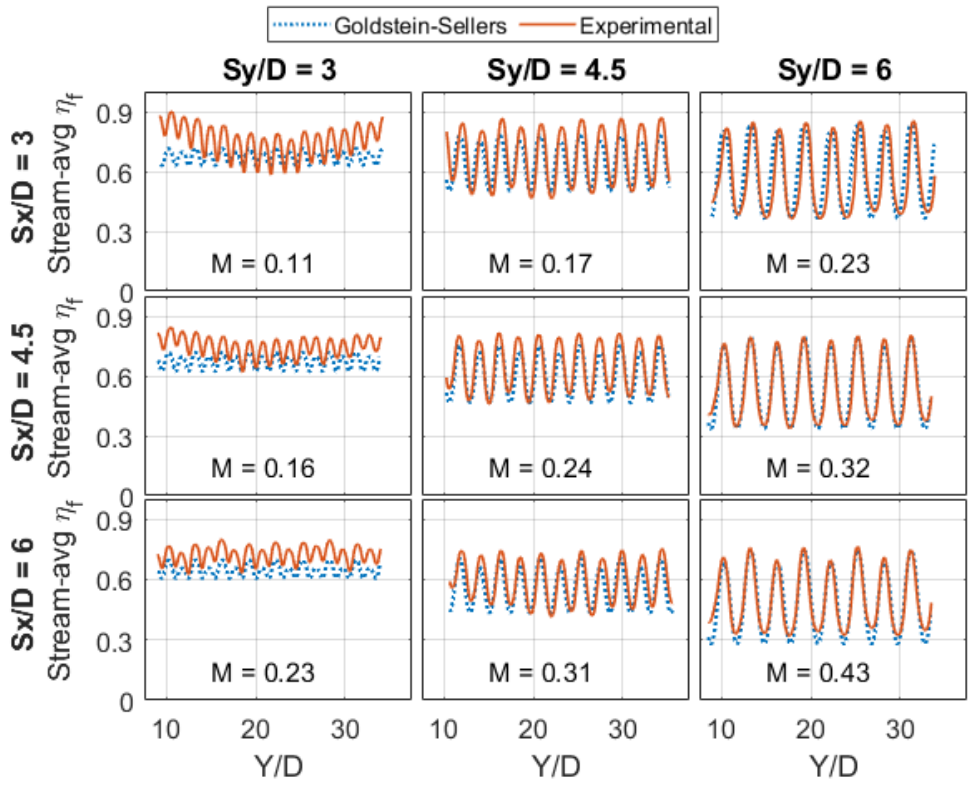


(A) $m^* = 1.8$

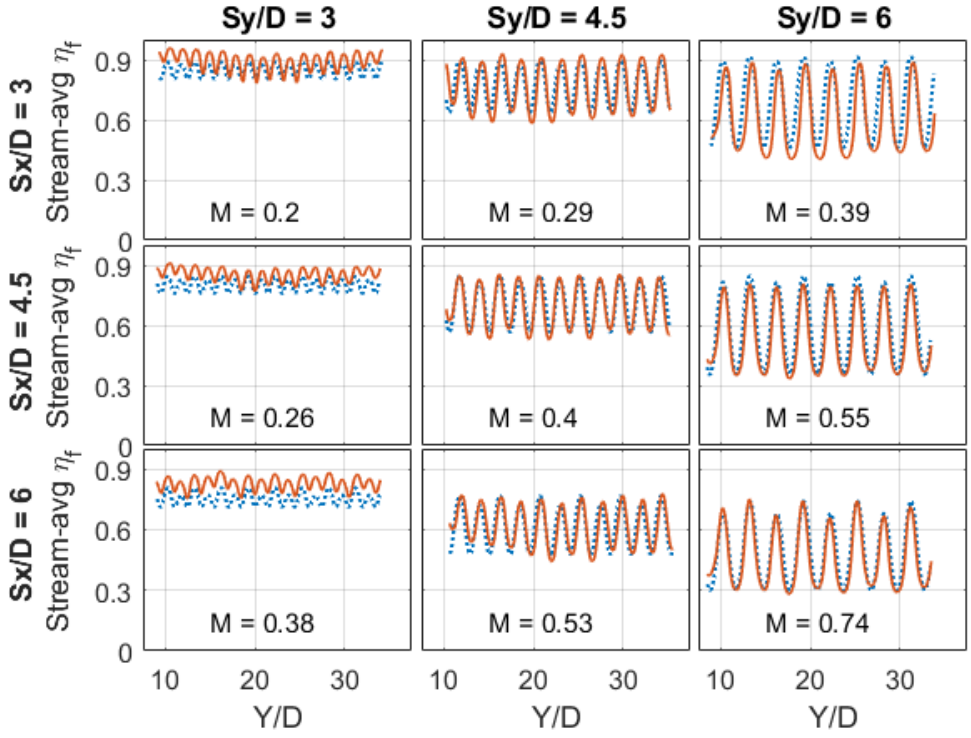


(B) $m^* = 3.2$

Figure 5.19: Comparison of numerical and experimental spanwise-averaged film effectiveness



(A) $m^* = 1.8$



(B) $m^* = 3.2$

Figure 5.20: Comparison of numerical and experimental streamwise-averaged film effectiveness

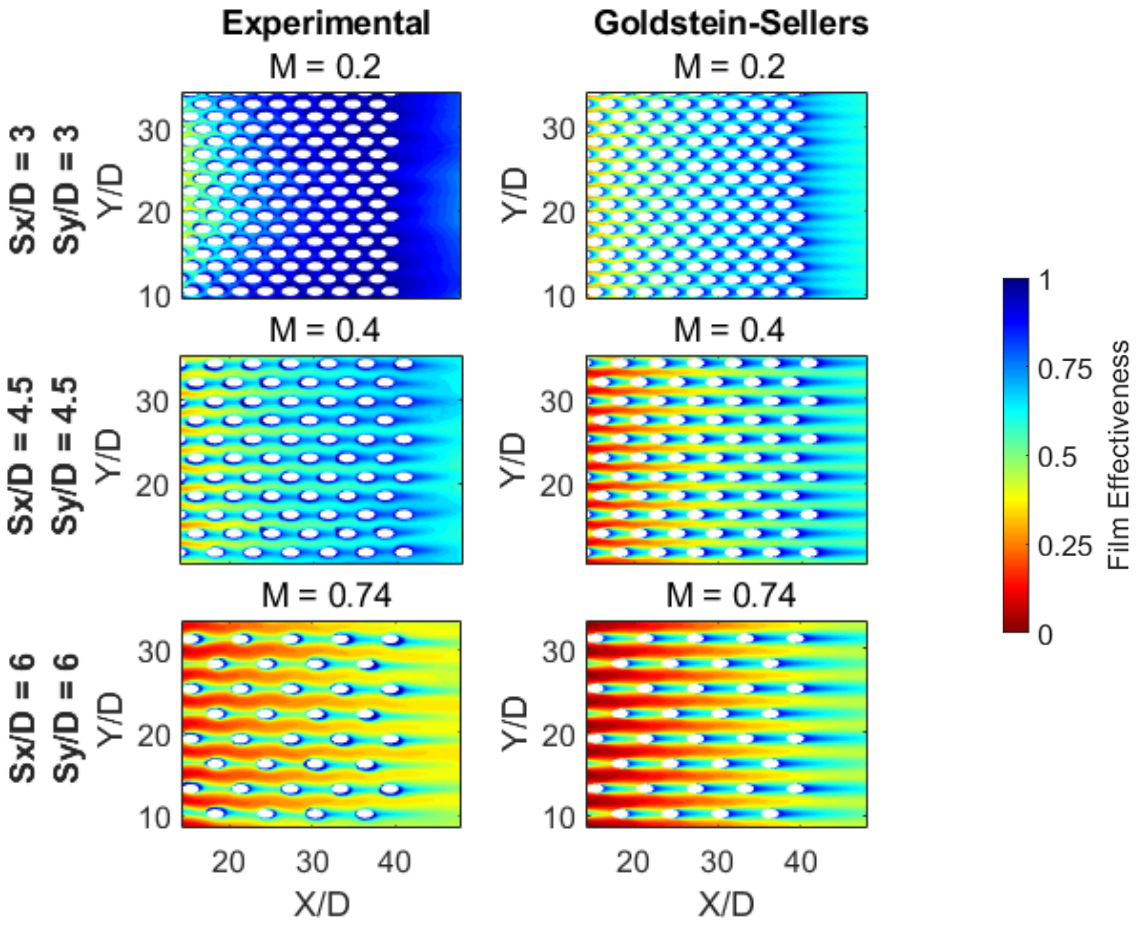


Figure 5.21: Comparison of film effectiveness contours between Experiments and Goldstein-Sellers for $m^* \approx 3.8$, and the corresponding blowing ratio is displayed.

picture. At $m^* = 1.8$ the experiments had lower film effectiveness at upstream film rows, and this was more pronounced at the centre-line of the array. Conversely, film effectiveness builds up more as you move downstream compared to Goldstein-Sellers. This was largely due to the variable mass flow distribution observed for highly porous geometries. As mass flow increases to $m^* = 3.8$ this phenomenon was less pronounced, and may be due to earlier saturation of film effectiveness and thus differences are constrained to upstream rows outside the IR camera view. The authors suggest that investigation of the upstream rows for densely packed film arrays should be made in future work.

For the two other geometries shown in Figure 5.21 ($S_x = S_y = 4.5D$ and $S_x = S_y = 6D$) film effectiveness was over-predicted for film hole centre-lines, however this appears to be at the expense of hot streaks between film holes. This is an indication of increased mixing in the experimental study that is not accounted for by the Sellers approach. Some of the discrepancy

may be due to manufacturing differences between the experimental pieces in this study compared to that used by [10] and [98] in the formulation of the modified Goldstein equation. In this study the flat plates were made from ROHACELL and consequently the hole boundaries had significant deviations which may enhance the lateral spread of films and increase the turbulence of the film jets.

5.3.4 Conclusions

The effect of variable span-wise and stream-wise film hole spacing was investigated for staggered hole arrays. While a decrease in both spacings enhances the film effectiveness, the span-wise spacing is more effective and jet lift off at higher mass flows can be avoided. Additionally, the range of streamwise-averaged film effectiveness is reduced by half when moving from S_y = 6.0 to S_y = 4.5, indicating a more uniform coverage. It is thus worth considering moving away from equal spanwise- and streamwise- spacing for effusion designs, despite this being common practice in industry. This could be important in designs looking to increase film hole porosity, as manufacturing realities may introduce the need for missed rows for structural purposes. Further work needs to address variable mass flow distribution between film holes for geometries with porosity in excess of 20%.

Highly porous film-hole coverage represents an efficient cooling method with film effectiveness approaching 0.9. However, metal effectiveness and mechanical stresses should be considered for a better understanding of the overall consequences on more engine-like designs. This is an area of research investigated by [92], and something which the authors of this study look to expand upon.

A modified Goldstein-Sellers film superposition method was compared to experimental results for a range of staggered film hole spacings. This method was shown to predict the behaviour of film superposition relatively well, but did not completely account for lateral mixing. Consequently, this method could be a useful tool for preliminary evaluations, and use in de-coupled and coupled conjugate studies.

5.4 Further High Porosity Results

D	S_x	S_y	N_x	N_y	L/D	α
2.2 mm	2.4 D	2.4 D	9	35	4.55	30°

Table 5.3: Geometric properties of the two high-porosity plates

T_∞/T_c	$DR = \rho_c$ / ρ_∞	$M = DR\frac{v_c}{v_\infty}$	$I = \frac{\rho_c}{\rho_\infty}(\frac{v_c}{v_\infty})^2$	T_∞	v_∞
1.24	0.8	0.06 - 0.25	0.005 - 0.08	373 K	60 m/s

Table 5.4: Approximate aerothermal conditions

Highly porous panels were tested on a scaled turbine blade by Wambersie et al. [100] in which high levels over effectiveness were shown at low coolant flow rates. However, ingestion at leading edge holes was observed on the suction surface because of the stream-wise negative pressure gradient and low internal cavity pressures giving rise to coolant favouring downstream coolant holes which starved the upstream holes. This issue was not observed for the pressure surface. Another challenge with the experiments was an internal pressure gradient resulting in coolant favouring one side of the blade over the other. To further understand these issues, a flat plate geometry with a staggered film hole arrangement was designed by the author and manufactured for experiments in the DECAF facility, with two distinct objectives:

1. Investigation of the upstream region- where film formation could be observed.

2. Experiments focused on the downstream region - where the films downstream of the array could be observed to allow evaluation of film degradation.

The rig setup stayed the same as the journal paper presented here [101] but the plates were manufactured with the film holes to be nearer or further from the leading edge to achieve the two variants. These panels were tested for a range of mass flow rates. The geometric parameters are presented in Table 5.3 and aerothermal conditions in Table 5.4.

Film effectiveness contours for both the upstream and downstream configurations are displayed for a range of blowing ratios in Figures 5.22 and 5.23. A consistent finding through this work is that a highly porous film-array promotes a good coverage and high values of film effectiveness.

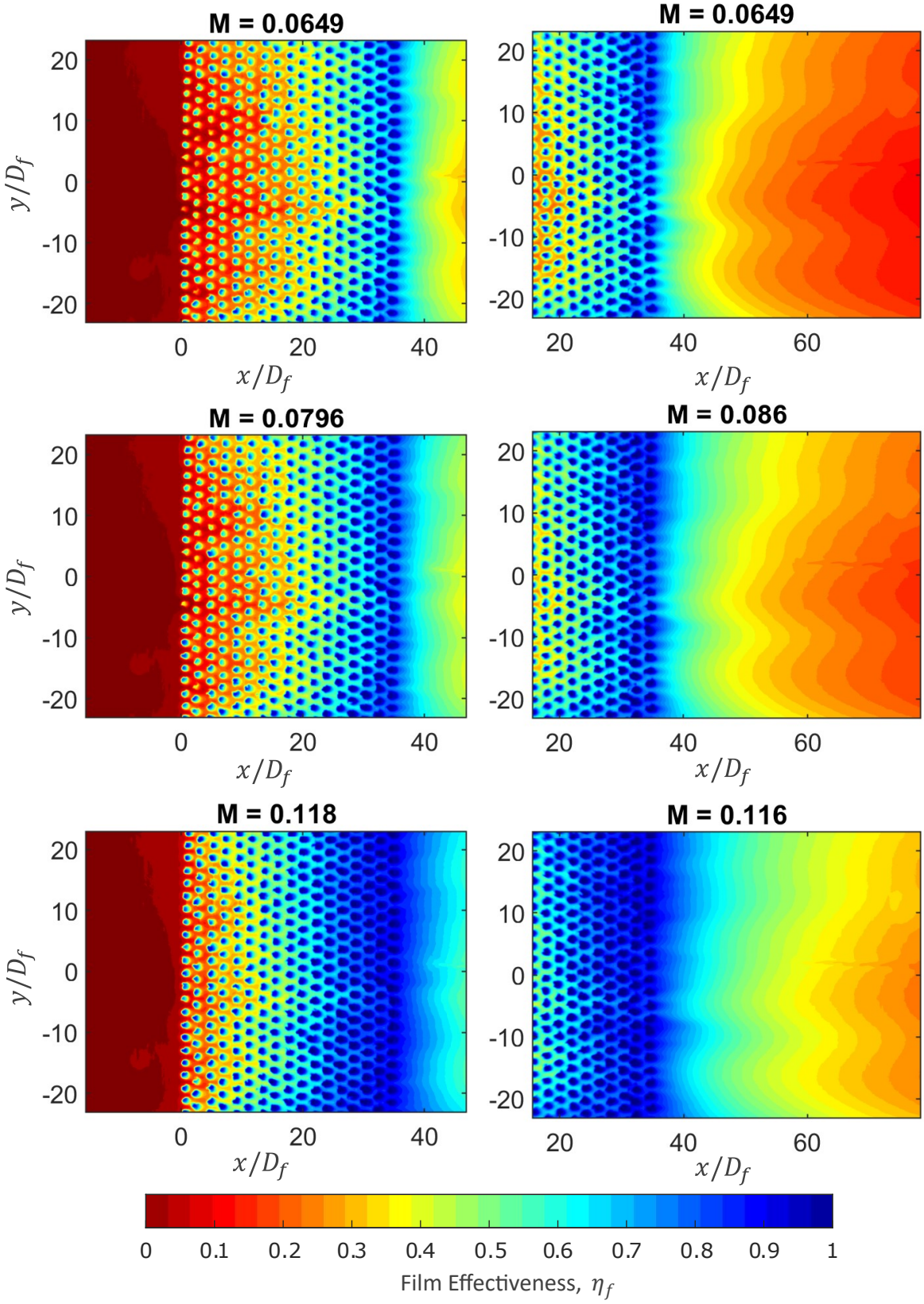


Figure 5.22: Film effectiveness contours for a) upstream and b) downstream experimental configurations for a highly porous film array.

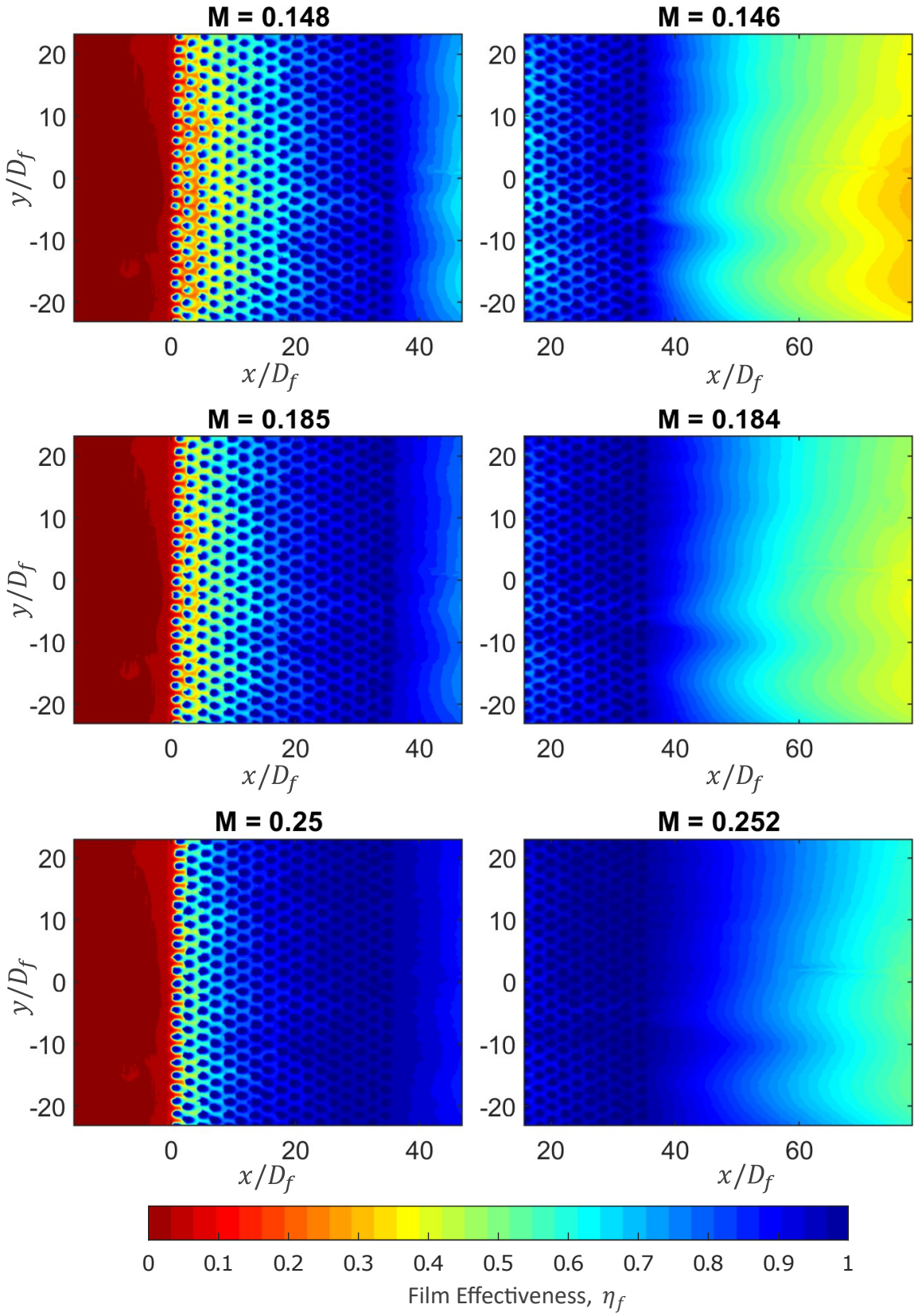


Figure 5.23: Film effectiveness contours for a) upstream and b) downstream experimental configurations for a highly porous film array.

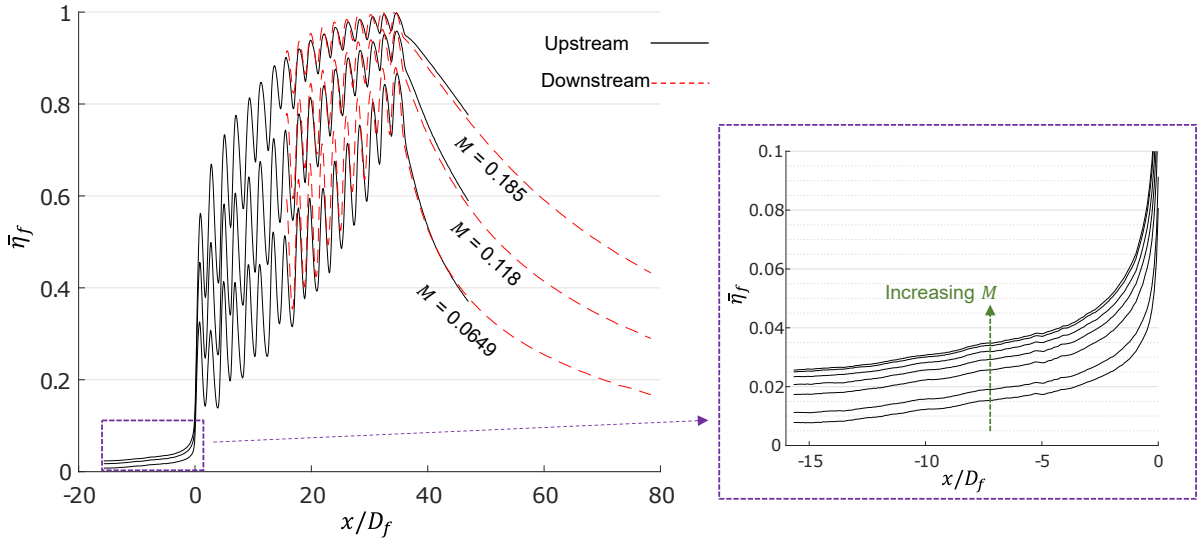


Figure 5.24: Spanwise averaged film effectiveness for both the upstream and downstream configurations. Values of over 0.9 $\bar{\eta}_f$ was observed with near linear degradation of the downstream film at the highest blowing ratios. Upstream $\bar{\eta}_f$ is highlighted here to demonstrate the impact of the non-ideal adiabatic material used in the experiments, and the impact of internal cooling, which increases with blowing ratio.

Even at low blowing ratios, at each film row the film merges with subsequent rows, developing protection across the spanwise direction and the impact of superposition can be observed by continuing protection downstream of the final row. As the blowing ratio increases, the protection of the film layer is promoted and film effectiveness with uniform high levels observed with only several film hole rows as M approaches 0.25. The film effectiveness level starts to saturate which means that there is only a marginal benefit to array, but the added film thickness and coolant mass propagates further downstream, elongating the region of high film effectiveness. In the case where $M = 0.25$ the film effectiveness was approximately 0.5, even as far as 40 diameters downstream of the final film hole row. Whereas for low blowing ratios, the decay to levels below 0.5 occured within a distance, from the most downstream row, of only several diameters.

These results also confirm the finding seen before where variable mass flow to the film holes was observed. The contours for the lower blowing ratios (Figure 5.22) show that the first few rows struggle to establish a film, this is likely in part to the local M being lower than the average M, which is already a low value. Additionally, the 'v-shape', where the centre-line experiences a suppression in film effectiveness, is observed. As previously discussed this is suspected to be a blockage effect of the film hole array. Figures 5.22 and 5.23 also indicate that a consequence

of this feature is a reduction of the film effectiveness downstream of the film array, $x/D_f > 40$, approximately along the centre-line.

The growth and decay of the film layers can be further understood by spanwise-averaged film-effectiveness ($\bar{\eta}_f$) plots, shown in Figure 5.24. $\bar{\eta}_f$ is plotted against streamwise distance from the leading edge film row ($x/D_f = 0$), where the solid and dashed lines are the upstream and downstream configurations respectively. Three blowing ratios are presented to illustrate the change in behaviour over the range investigated. As blowing ratio increases, the step change in film protection at the upstream row increases, and elevated protection is continued throughout the film array.

The general increase in film effectiveness at the lowest blowing ratio ($M = 0.065$) is approximately linear whereas, for the highest blowing ratio, this behaviour is closer to logarithmic behaviour with an asymptote of 1. For the latter this is a result of the nature of film superposition. While for the lower blowing ratios the author believes that this difference in behaviour is a result of uneven coolant distribution between the film rows. And the lower blowing ratio conditions experience proportionally a larger impact.

An explanation of the above behaviour is as follows. For all conditions, the pressure gradient along the flat plate results in more coolant, and therefore higher blowing ratios for each downstream cooling row, however at the lowest blowing ratio the pressure gradient between the coolant and mainstream is lower. If we consider the 'local' pressure ratios where $P_{\infty,1}/P_c$ is the leading film hole pressure ratio and $P_{\infty,n}/P_c$ is the most downstream film pressure ratio, for constant external conditions ($P_{\infty,1}$ and $P_{\infty,n}$ are independent of the applied coolant condition), the difference in these two ratios will be more pronounced for a lower P_c and therefore lower blowing ratio condition. As an example, for the lowest blowing ratio condition, M = 0.065, the plenum pressure is 0.6% higher than the mainstream pressure, whereas for the highest blowing ratio condition, M = 0.25, this difference is 0.8%. As a consequence the impact on the maldistribution of coolant to film holes will be proportionally higher for the lowest blowing ratio condition.

An additional feature of Figure 5.24 is the clear comparison of downstream film effectiveness between M conditions. After the last film row, the film effectiveness experiences an exponential decay, $\eta_f = A \exp -B\left(x/D_f\right)$, where A approaches 1 as the films saturate and the blowing ratio reduces the decay rate, B. Therefore, the impact of M is crucial for highly porous film arrays to ensure an adequate level of film protection across a turbine blade, and full film hole coverage may not be required.

Lastly, it was observed that the film effectiveness upstream of the leading edge film hole was not 0, and it increased with M. This is not indicative of any film forming upstream of the film holes, but rather the impact of using a material which is not perfectly adiabatic. Inside film holes there will be some convective heat transfer along the internal wall surface and given the high porosity and resulting internal area, this heat transfer may become significant. As a result of the non-ideal adiabatic condition some conduction is possible and therefore the plate may be cooled in close proximity to the film holes. As M increases the flow velocity and therefore heat transfer coefficient associated with internal convective cooling increases, resulting in the observed additional cooling. Further investigation of this phenomena is provided in Section 5.6.

5.5 Compound Angle

For discrete film cooling, compound angle has been shown to be advantageous in promoting higher lateral film effectiveness [31, 32, 33]. Given the lower levels of porosity studied in literature, focus has been on blowing ratios much larger ($[0.5 \leq M \leq 1.0]$, $[1.0 \leq M \leq 4.0]$, $[0.5 \leq M \leq 1.5]$) than those presented in this thesis, as well as larger hole spacing. As such, it is of interest to understand the impact of compound angle on the film jets for film arrays with greater numbers and lower blowing ratios.

Six tests plates were constructed with staggered film-arrays coinciding with the IR visible area, ensuring the leading edge row was in view. Two compound angles of 15° and 30° were investigated over a range of equal film holes spacing, $S/D_f = S_x/D_f = S_y/D_f$. The inclination

	D_f [mm]	$S_x = S_y$ [D_f]	γ [°]
A	4.0	3.0	15
B	3.5	3.4	30
C	4.0	4.5	15
D	4.0	4.5	30
E	4.0	6.0	15
F	4.0	6.0	30

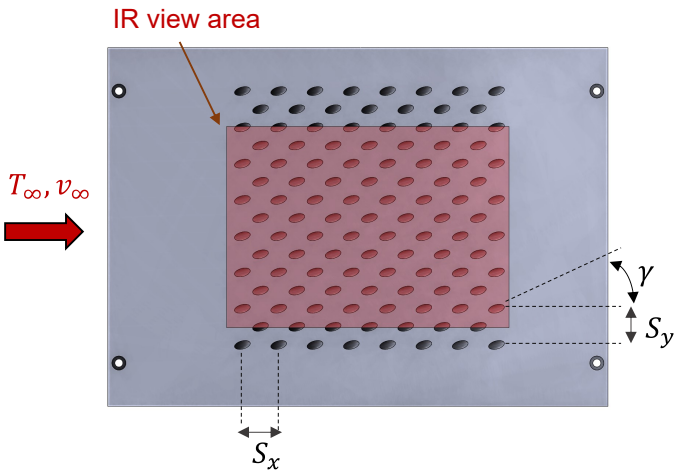


Figure 5.25: Schematic showing the dimensions of the flat plate geometry, where the red section highlights the visible portion for the IR camera. The illustration is the variation with $S_x/D = S_y/D = 4.5$ and a compound angle of $\gamma = 30°$.

angle of $\alpha = 30°$ remained the same as the previous film studies. Geometric values are tabulated alongside a visual schematic of the test plates in Figure 5.25. Three film hole spacings of 3.0, 4.5 and 6.0 D_f were to be investigated at constant D_f, however during the manufacture of geometry B some of the material between adjacent film holes broke through due to close proximity from low spacing and larger compound angle and the low Rohacell strength. Therefore, to avoid breakthrough, the same absolute spacing was maintained and the film hole diameter reduced from 4.0 mm to 3.5 mm. While this will change the film hole aspect ratio from $L/D_f = 5$ to $L/D_f = 5.7$, it was shown by [99] that the film effectiveness is particularly unchanged beyond an aspect ratio of 5. Each geometry was subject to a range of mass flow rates ($1.35 \leq m^* \leq 6.8$) and monitored by the IR camera to determine the film effectiveness over the visible region. Results of all six geometries at three different flow rates are presented as film effectiveness contours in Figures 5.26, 5.27 and 5.28, where in each figure the closest m^* for each geometry were selected and these three figures represent a low, middle and high mass flow rate within the range investigated.

For the lowest spaced geometry it is not clear the immediate impact of a change in compound angle, however, this is made more difficult due to the difference in film hole diameter and therefore film hole spacing, $S/D_f = 3.0$ and $S/D_f = 3.4$. The impact of this change is that for the same coolant flow rate, the latter geometry (B) will have a higher blowing ratio, but of course

at the compromise of reduced proximity of adjacent films. The film effectiveness coverage and strength was similar between the two, hinting that the compound angle may help in reduce the perceived spacing between films in the span-wise direction. The same phenomenon of suppressed coolant flow to the central leading edge films was observed for geometry A, but much less evident for geometry B. However, it is again not clear whether this was due to the hole spacing or the compound angle. Regardless, as coolant mass flow increased the films start to approach saturation and near-saturation is observed after 7 primary film columns for $m^* \sim 6.4$ in Figure 5.28. While it was not obvious that this point is further upstream for geometry B, the first three film columns at least experience a promoted lateral coverage, reducing the prevalence of hot-streaks between film rows.

As the hole spacing was increased to $S/D = 4.5$ the larger compound angle promoted lateral mixing of films as well as the superposition resulting in increased film effectiveness in the first several film columns. Here the space between film rows was large enough for the compound angle to have a significant impact, but also close enough for a reasonable amount of adjacent film interaction. It therefore can be said that the increase in compound angle had a positive impact on film coverage, and was observed across the range of mass flow rates investigated. In particular the degree to which the hot-streaks extend into the film array was reduced. A good example of this is in Figure 5.27 where, for geometry C, a film effectiveness of 0.35 in the centre-line of film rows is reached by approximately $3S$. Whereas this same level is achieved by $2S$ for geometry D. For geometries E and F, $S/D = 6.0$, increased compound angle provides enhanced lateral coverage, albeit to a lesser extent compared to the lower film spacing. Two benefits were enhanced film protection immediately downstream of each individual hole and a marginal reduction in hot-streak propagation.

To further understand how the film coverage is altered with compound angle Figure 5.29 plots the spanwise-averaged film effectiveness, $\overline{\eta_f}$, in relation to the distance from the upstream film hole, x/D_f. This is done for each configuration and the three mass flow rates shown in the previous contour plots. Firstly the confirmation of porosity benefits are clearly seen in B and C, $m^* \sim 3.7$ and $m^* \sim 6.4$. However, in the lowest mass flow case, plot A, it could be argued that

the benefits from $x/D_f > 20$ for geometries A and B come at the cost of lower initial film protection. For geometries A and B, the compound angle has only a marginal benefit in which there was an elevation of $\overline{\eta_f}$ at $x/D_f < 10$. For the moderate film spacing of $S/D_f = 4.5$ compound angle was a more important role, and throughout the mass flow range and streamwise extent, $\overline{\eta_f}$ is enhanced. This occurs to the extent that for $m^* \sim 1.8$ and ~ 3.7 geometry D is comparable to the two higher porosity plates (geometry A and B). The benefit of compound angle was most keenly felt at the first several film holes were the gradient of the film effectiveness is much greater for $\gamma = 30^\circ$ than $\gamma = 15^\circ$. As the films build further downstream the film effectiveness increase mirrors one another, but the upstream elevation is retained. One may expect that for a large enough film-array these two lines to meet again at some saturation asymptote, but further work would be required to confirm this. And for the film array in the present study it would be expected for the elevated film effectiveness to be retained downstream. As film spacing increases further to $S/D_f = 6$, the compound angle again becomes less consequential, although it did provide some enhancement throughout.

The macro effects of the above can be summarised by the area-averaged film effectiveness, $\overline{\overline{\eta_f}}$, plotted in Figure 5.30 a for each configuration and all coolant mass flow rates. The region used for area-averaging was the start of the film hole array and the endpoint being the minimum furthest point downstream between all configurations. This was done to reduce any impact on the exact starting point of the film array within the IR window. For geometries A and B there is little difference between them, but given the increase in film spacing between A and B, the compound angle may play some role in minimising any expected reduction. For $S/D_f = 4.5$ the benefits of increased compound angle was evident. The enhancement of $\overline{\overline{\eta_f}}$ increased with coolant flow rate until around $m^* < 4$ at which point the gap between the two narrows. Furthermore for $m^* < 4$ geometry D ($\gamma = 30^\circ$) provides a similar coverage compared to A and B. As previously mentioned the largest film spacing, $S/D_f = 6.0$ only had a marginal benefit for an increase in compound angle, but it did outperform geometry C for $m^* \leq 2.5$.

While elevated film effectiveness may be achieved through reduced film spacing and increased compound angle, for the same mass flow rate, it is worth considering the impact of the pres-

sure margin across these configurations. And the pressure ratios between coolant plenum and free-stream $PR = P_c/P_\infty$ are plotted against the mass flow rate in Figure 5.30 b. As expected the pressure ratio reduces with increased film-hole spacing (increased porosity) and increases for increased mass flow. Pressure margins of above 5% were observed for $S/D_f = 6.0$ and $S/D_f = 4.5$, but for the latter only once m^* approached a value of 4. For $S/D_f = 4.5$ the pressure angle was insensitive to an increase in the compound angle, the geometry pairs of A and B and E and F experienced some difference in behaviour. The discharge coefficient may have changed with increase in compound angle therefore impacting the mass flow - pressure relationship.

To summarise, compound angle provided benefits for full-coverage film arrays, but the largest benefit was observed for $S/D_f = 4.5$. This benefit acted to elevated film effectiveness in the region of the more porous configurations, but retained the benefit of a larger pressure margin, which could help to reduce sensitivity of the mass flow rate, and consequentially the film and cooling performance, to variations in feed or external pressure. Further research could focus on the downstream area of film arrays with compound angles to assess changes to the film degradation.

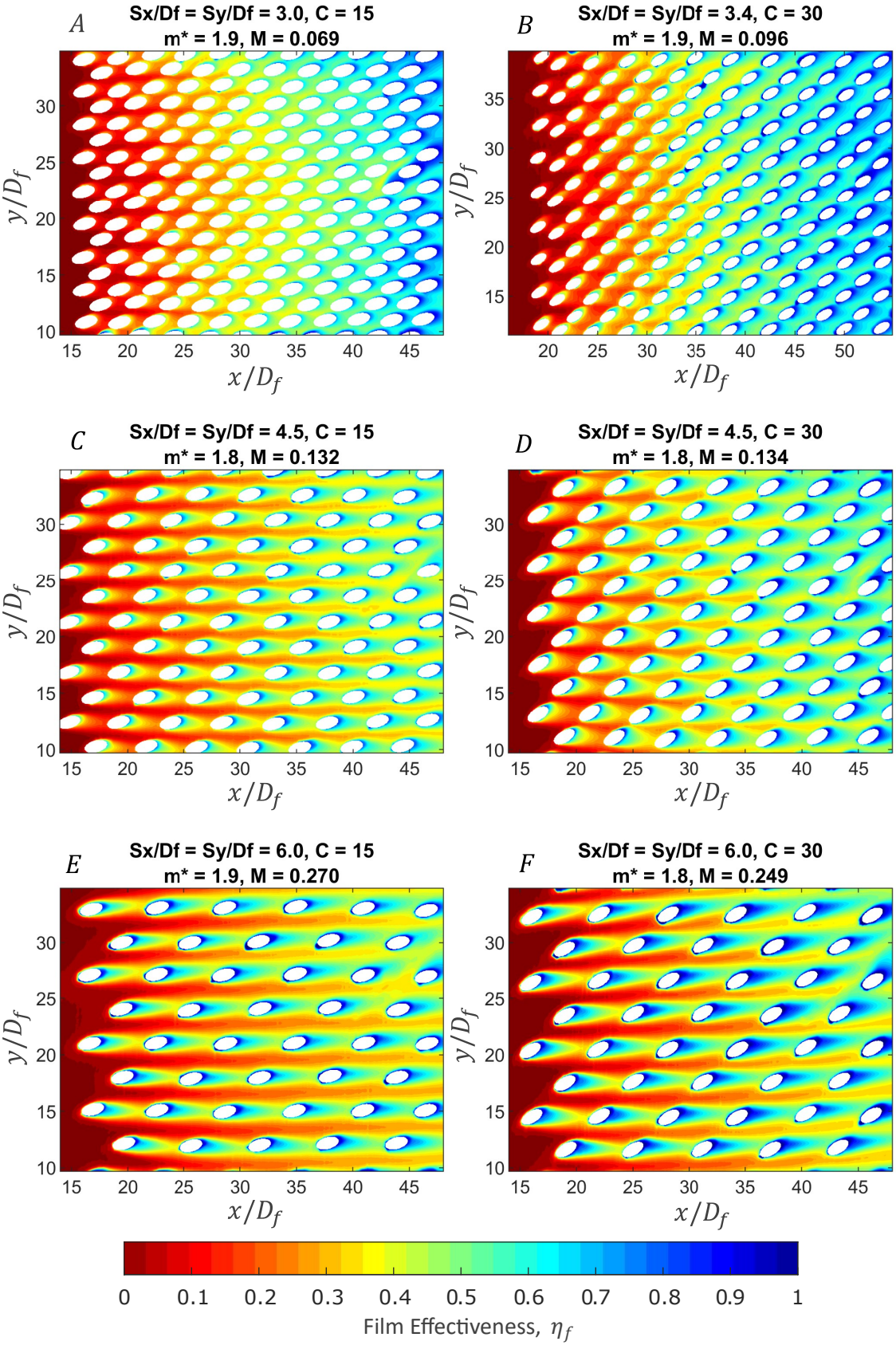


Figure 5.26: Film effectiveness contours for compound angle study geometries at m^* nearest to 1.8

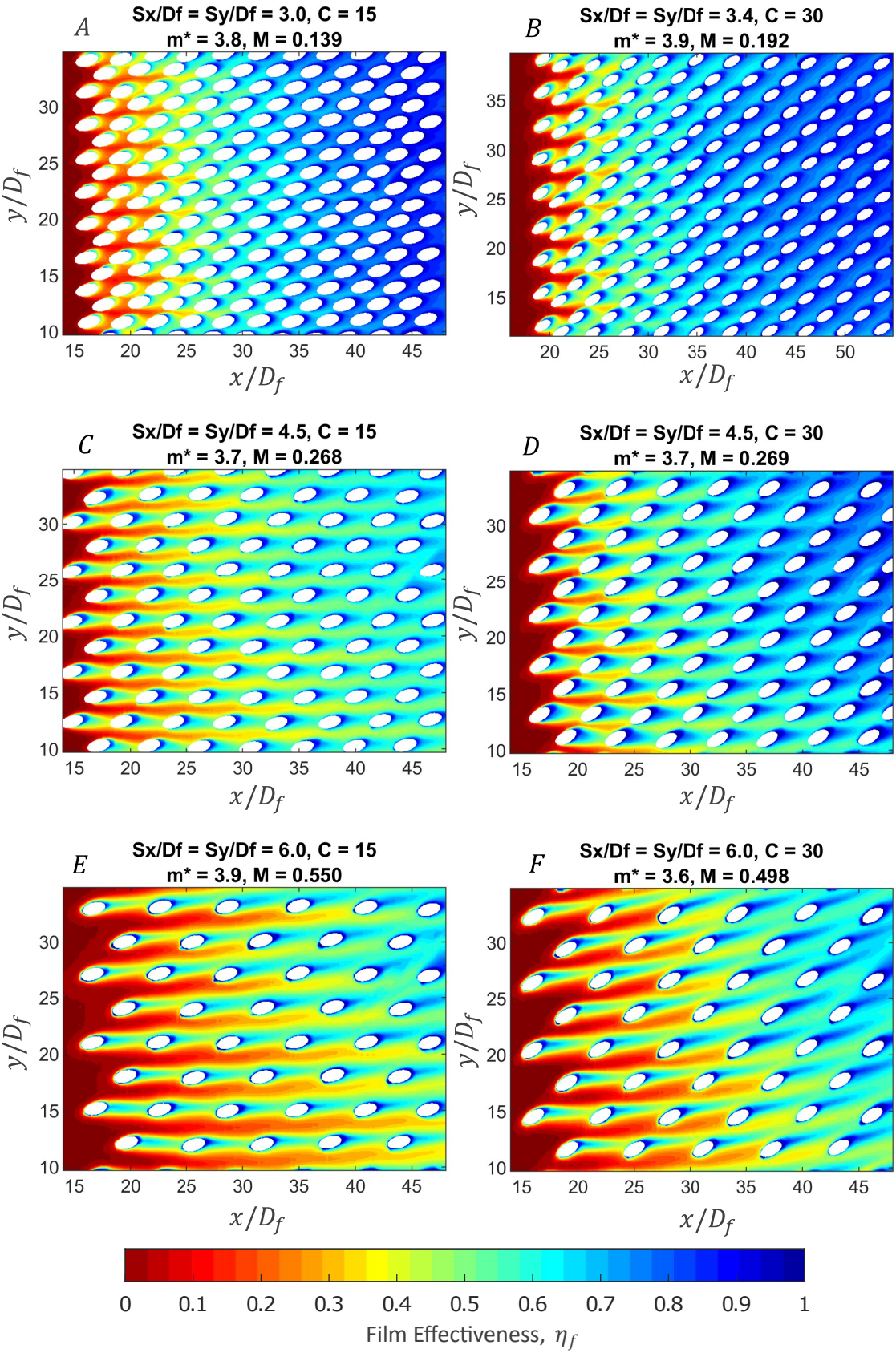


Figure 5.27: Film effectiveness contours for compound angle study geometries at m^* nearest to 3.7

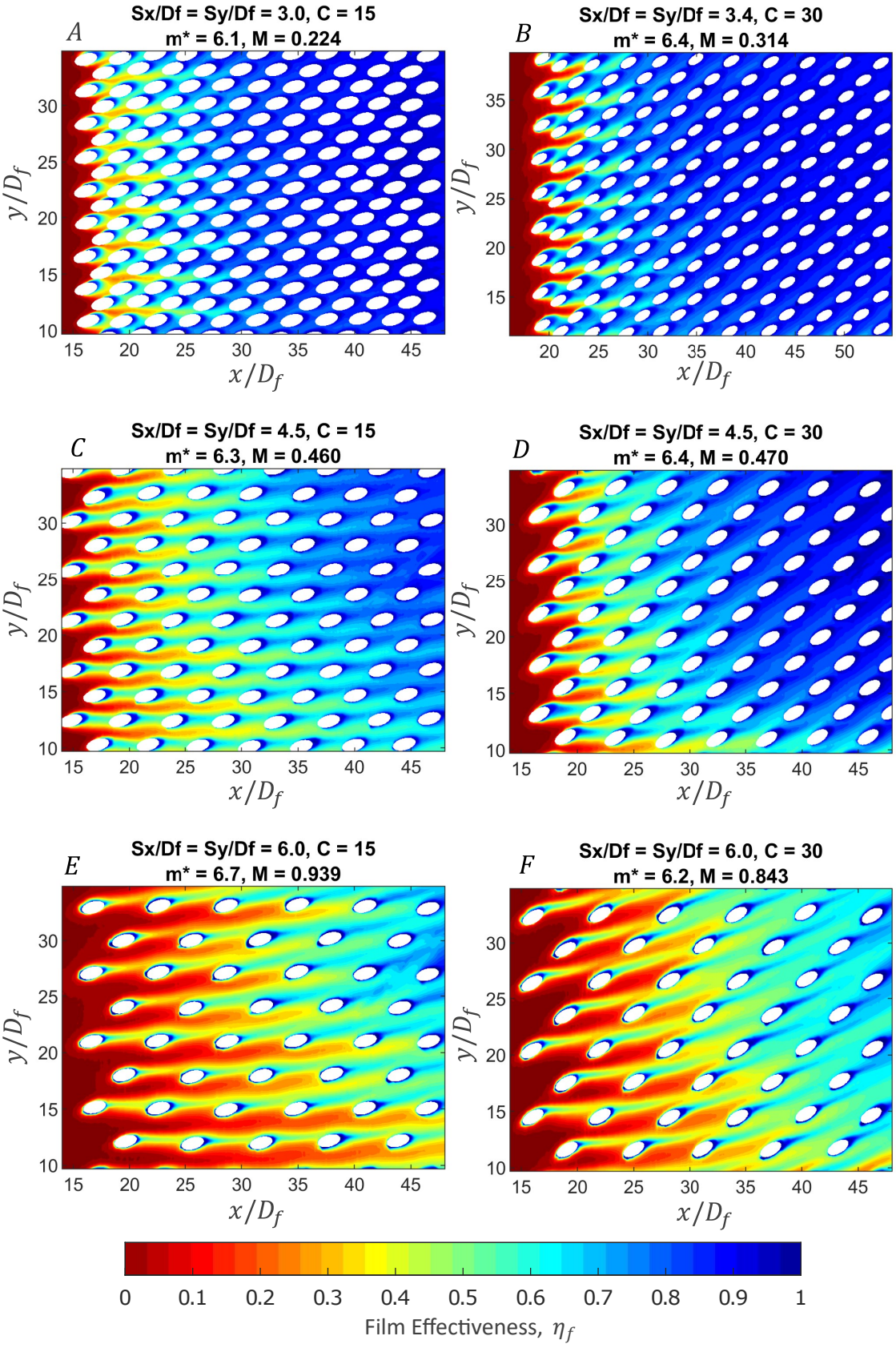


Figure 5.28: Film effectiveness contours for compound angle study geometries at m^* nearest to 6.4

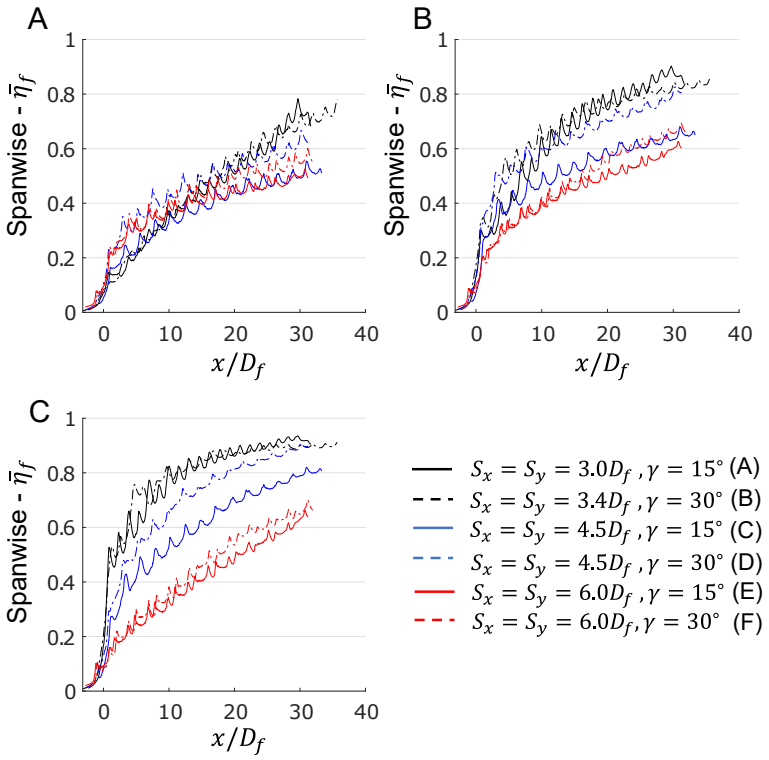


Figure 5.29: Geometry comparison of spanwise-averaged film effectiveness for three coolant mass flow rate: A) $m^* \sim 1.8$ B) $m^* \sim 3.7$ C) $m^* \sim 6.4$. Porosity and compound angle are beneficial for film coverage, especially at high flow rates. However, for low coolant flow rates there is some penalty for the first several film rows.

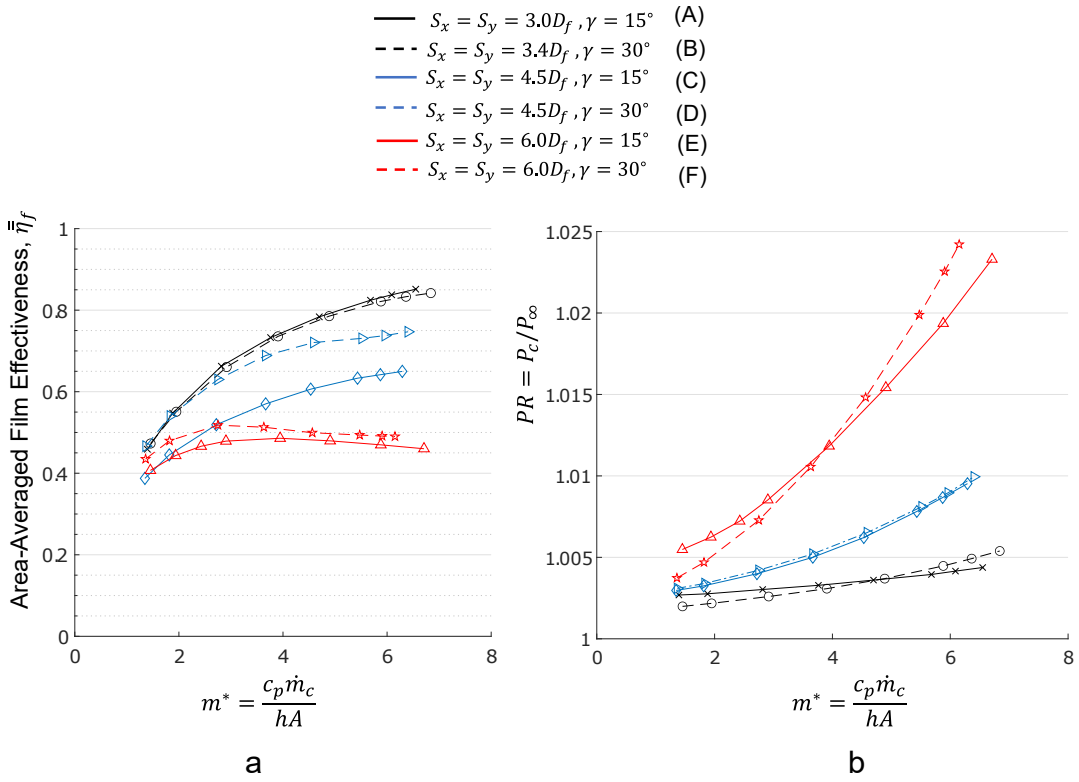


Figure 5.30: A) Spanwise-averaged film effectiveness across the range of coolant mass flow rates. Porosity and compound angle both provide benefits to the film effectiveness. B) Pressure ratio across the wall for each configuration.

5.6 Adiabatic Assumption

Despite efforts to isolate film effectiveness, the test pieces were not fully adiabatic. The Rohacell plates used were the 71 HERO grade supplied by Evonik with quoted thermal conductivity of 0.028 - 0.024 W/m^2/K at 20°C and 0.035 - 0.041 W/m^2/K at 80°C. Consequently conduction was present through the thickness of the plate from the external hot surface to the internal cavity, and toward any film holes. As highlighted in Figure 5.24 in Section 5.4, increased coolant flow rates resulted in lower hot wall temperatures upstream of the film-hole array. To further understand the differences caused by the non-adiabatic behaviour, the application of external films and internal cooling was applied to a geometry which will be studied further in Chapter 8. Here a geometry with porosity of 20% is considered with film hole diameter of 4mm and hole spacing of $S_x/D_f = S_y/D_f = 3.5$ in a staggered arrangement, a cooling condition of $m^* = 7.1$, and for representative experimental conditions of $T_\infty = 373\,\text{K}$, $T_c = 302\,\text{K}$ and $v_\infty = 60\,\text{m/s}$. Two simulations were conducted in ANSYS Steay-State Thermal, the first setting the material to be Rohacell and the second assuming a perfectly adiabatic material, i.e $\lambda = 0\,\text{W/m}^2\text{/K}$.

Figure 5.31 plots the span-wise averaged film effectiveness in the streamwise direction for both conditions. The behaviour previously described upstream of the cooling array was observed here as an offset in wall temperature is present, where the Rohacell had a temperature lower than the mainstream, before any films are applied. This difference increased from the leading edge to the first film holes. Once reaching the film hole array an increase in span-averaged film effectiveness is present throughout the length of the plate.

Contours of the difference in 'film effectiveness' or what can be deemed to be reduced wall temperature by conduction is show in Figure 5.32. The difference was most prevalent at the leading edge of the upstream film holes and was a consequence of the convective cooling effect on the inner edge of the cooling holes where the solid and film hole leading edge form an acute angle. Given that the upstream solid will be at a higher temperature than that which was protected by the resulting films, the temperature gradient was larger, resulting in a more pronounced cooling effect. Overall the mean difference over the full plate is 3.9% of the driving

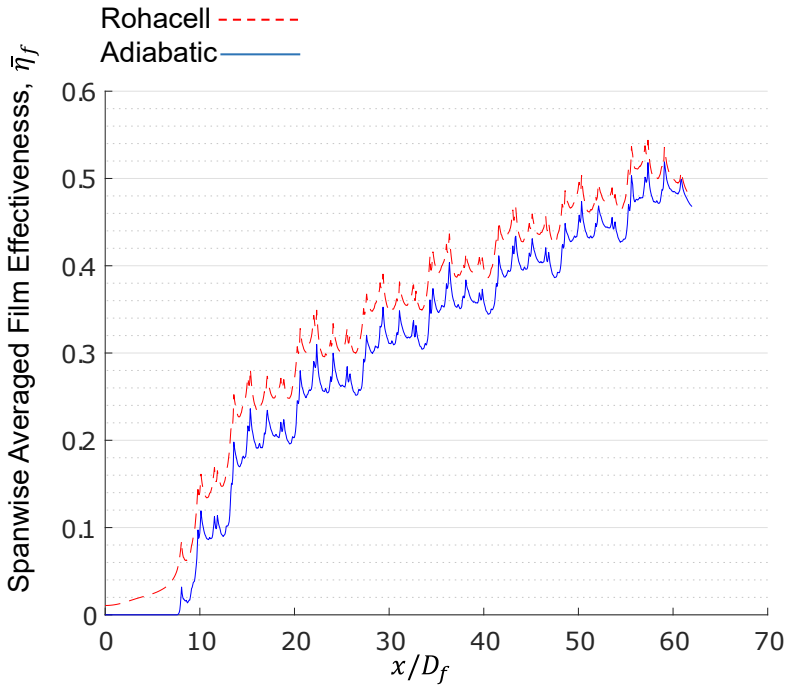


Figure 5.31: Spanwise-averaged film effectiveness comparison between a Rohacell and perfectly adiabatic material. HS2 geometry at $m^* = 7.1$.

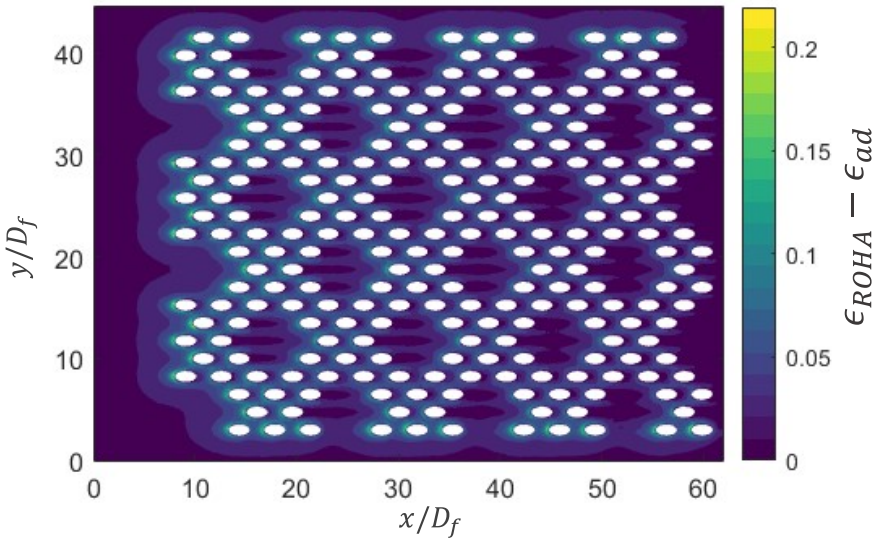


Figure 5.32: Contours of the difference in cooling effectiveness on the film-side wall for rohacell and perfectly adiabatic material.

temperature, $T_\infty - T_c$, with film hole proximity being the main determinate over the uncertainty in results.

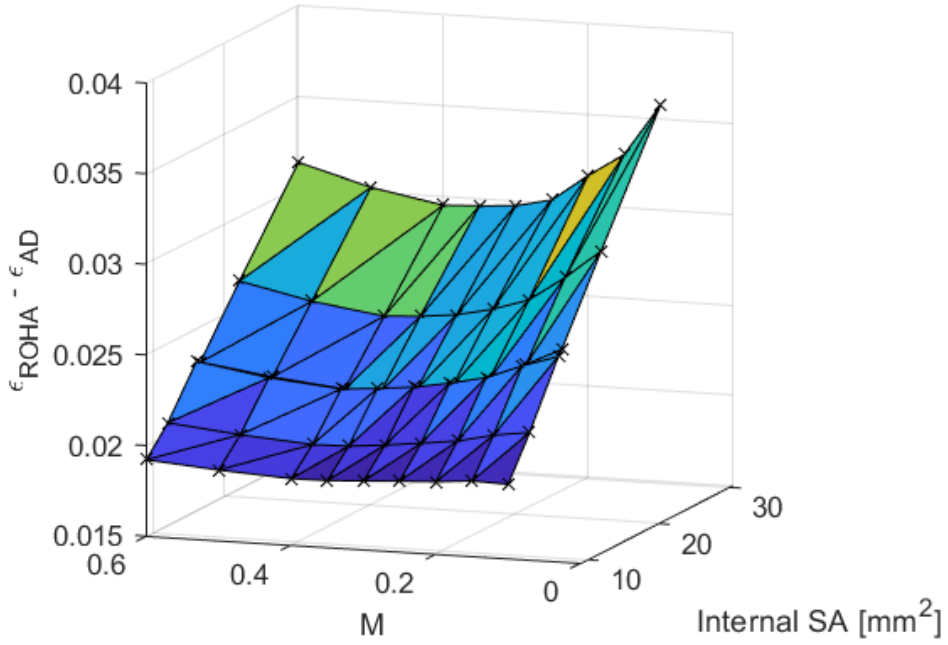


Figure 5.33: Difference in cooling effectiveness associated with the non-perfect adiabatic behaviour of Rohacell as applied to several of the film arrays studied in [2]. The difference in film effectiveness is shown to be impacted by both the internal surface area of the film holes (porosity) and the blowing ratio, M.

For the results presented in Section 5.3 the impact of rohacell on the film effectiveness measurements was considered with results on the mean film effectiveness overestimation for several geometries shown in Figure 5.33. The following six geometries were considered:

	1	2	3	4	5	6
S_x	3.0	3.0	3.0	4.5	4.5	6.0
S_y	3.0	4.5	6.0	4.5	6.0	6.0

And at the following blowing ratios: 0.1, 0.15, 0.2, 0.25, 0.3, 0.35, 0.4, 0.5, 0.6. It was observed that the internal film surface area (i.e. porosity) has a strong impact on the departure from adiabatic behaviour. While the blowing ratio did have an influence on this, this effect was secondary. For blowing ratios above 0.25 there was only a small influence, however below 0.2, there was a stronger impact. This is best explained by the films being weaker and therefore the temperature gradient between the external wall and internal surface being larger. Despite

these findings, given the moderate levels seen for a sample with 20% porosity and relatively high cooling, this represents only a small addition of uncertainty within the film effectiveness results presented in this thesis, and the results presented are expected to be a good indication of the overall trends.

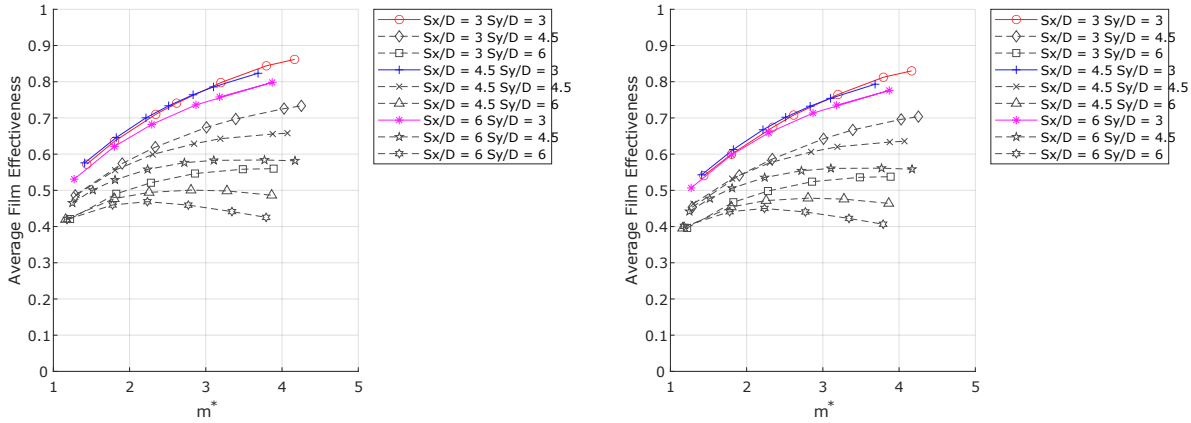


Figure 5.34: A) Original 'uncorrected' mean film effectiveness results in [2]. B) Adiabatic correction applied.

As further evidence of this the mean film effectiveness of the experimental results shown previously in Section 5.3 have been corrected using this correction factor and the original results and updated ones are displayed in Figure 5.34 a and b respectively. Here we can see that while the results make a difference in the overall mean film effectiveness values, the geometric trends are consistent.

An additional feature to consider is the film jet temperature. For rohacell tests the semi-adiabatic behaviour gives coolant temperature which remains mostly unchanged in temperature throughout the test piece, as only a small amount of heat will be transferred from the internal surfaces. Therefore the films will have a lower hole exit temperature than in a non-adiabatic case (such as a metal blade), further overestimating the film effect compared to non-adiabatic tests. Further studies may address these discrepancies in behaviour and apply some compensation to experimental results to determine appropriate values for consideration in the case of a turbine blade.

5.7 Material Selection

Film effectiveness measurements for both TD2 and D6 are compared in Figure 5.35 where the former has measurements for both grades of Rohacell used as well as predicted values using the modified Goldstein-Sellers method. TD2 exhibited a significant increase in film effectiveness compared to D6, approximately doubling this value. This represents an incredibly enhanced film protection which could be vital in protecting advanced systems. For the TD2 results, the modified Goldstein-Sellers method captured the average film effectiveness relatively well across the range of mass flows rates.

The change in Rohacell had only a small influence on the averaged film effectiveness, but in general the closed-cell Rohacell had higher values at lower mass flow rates, while the open-cell had high film effectiveness as the mass flow increased ($m^* \geq 3$). The latter experienced poorly defined hole exits due to the small film hole sizes in comparison to typical film holes, 2 mm vs 10 mm at 10 times engine scale. The closed-cell Rohacell (71HF) in comparison had well defined holes, in similarity to 10 mm holes in open-cell. The consequence of the manufacturing is exhibited in Figure 5.36, where film effectiveness contours of both grades is displayed. More distinct film streaks were observed for the closed-cell, whereas there is more lateral spread for the open-cell. Given that manufacturing in metal will provide more distinct hole shapes, the closed-cell results should be more representative of the film effectiveness expected for engine application.

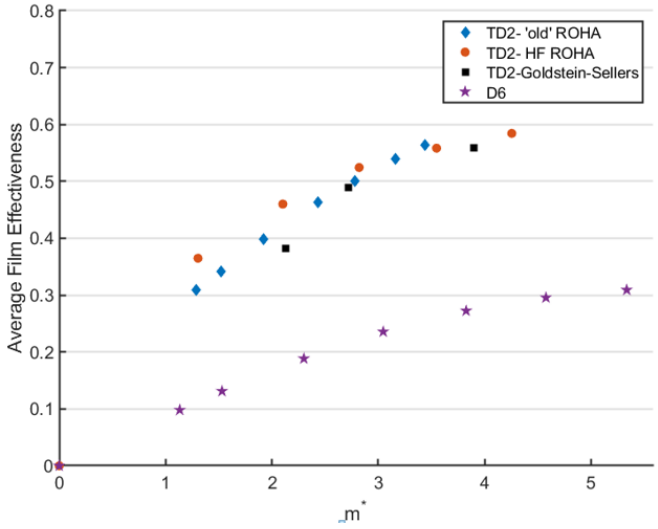


Figure 5.35: TD2 and D6 area-averaged film effectiveness for the IR view area. A comparison of the two ROHACELL types has been included as well as a Goldstein-Sellers prediction.

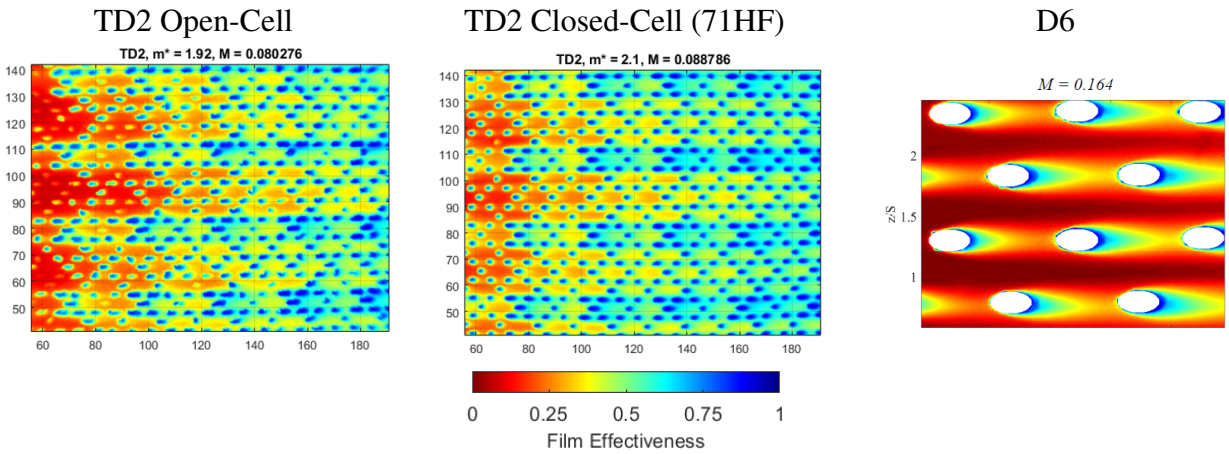


Figure 5.36: Film effectiveness contours for TD2 geometry for open compared to closed cell ROHACELL as well as D6 film effectiveness.

5.8 Turbine Blade Application

Application of the findings here must also be considered carefully with respect to a real turbine blade design. A key feature in the flat plate studies is the impact of the external pressure gradient on the film distribution. The translation to the suction surface will be even more consequential given the large pressure gradient from the blades' curvature. Therefore control of mass flow to specific rows on the turbine blade must be considered as a important feature for successful implementation of porous designs. While there are many ways to achieve this, a general suggestion is provided here.

If a multitude of rows is required on the suction surface, isolation of several rows from one another will be crucial to avoid adverse flow migration towards the downstream rows. This could be achieved using internal baffles to isolate specific cavities from one another. For example a leading edge SS section, middle SS section and downstream SS section could be established. Further to this, the need for different internal resistances for each portion may be established to encourage flow toward the leading edge. One method may be a higher outerskin porosity nearer the leading edge, and reduced porosity in subsequent section. This could be achieved using lower spanwise spacing to take advantage of the film-cooling benefits previously described with reducing this parameter. One a film is established further rows in the downstream cavities can be used to reduce the film degradation, but not unnecessarily draw away upstream coolant from the leading edge film rows.

An alternate method would be to use variable impingement hole diameters or frequency in each cavity. One disadvantage of this method is that as the upstream cavity throat area increases the impingement velocity and therefore stagnation Nusselt will be reduced in the most highly thermally loaded region. Therefore consideration of film cooling, internal convection between the film wall and coolant, and the impingement jet enhancement is required to find a suitable configuration.

While the pressure surface has a more favourable pressure gradient, the turbine blade shape plays an equally important role. The concave shape is not favourable for film cooling attachment, as the normal pressure gradient curves the jet away the wall, so while the films will be well distributed, they are expected to decay much more quickly than on the suction surface. It is also argued by El-Hady and Verma [102] that the secondary flows play a significant role in increasing the film to mainstream mixing. For the suction surface the opposite is true, where films may propagate for large streamwise distances as the films are pushed closer to the blade surface. As a consequence careful consideration must be made to where dense film arrays are located as well as the need for variable streamwise distancing between films depending on the blade shape.

5.9 Summary

Assessment of flat-plate film effectiveness was made for a range of geometric configurations under varying coolant flow rates. Variable spanwise and streamwise spacing were considered for a staggered film-array and it was shown that the spanwise direction was fundamental to achieve full lateral coverage as well as enhanced film protection. While the streamwise spacing was required to be sufficiently low to promote superposition, this is secondary in comparison. Variable mass distribution to film holes was observed for highly-packed film-arrays with the leading edge holes being more susceptible to low flow or even hot-gas ingestion. Consideration of such risks must be further explored if this promising technology is to be used on engine blades. The benefits of compound angle to the film effectiveness, especially in the first several film rows was also shown. And this may enable the feasibility of more moderately spaced film-arrays while maintaining high film effectiveness. While these results are encouraging, the experimental method may provide some overestimation of the true film effectiveness due to the non-ideal adiabatic behaviour, although the overall difference for an appropriate material (Rohacell) can be below 5%. Lastly, implementation on turbine blade design was discussed and further research should focus on applying these findings to representative curvature to clarify the extent of film effectiveness enhancement and explore flow management techniques.

Statement of Authorship for joint/multi-authored papers for PGR thesis

To appear at the end of each thesis chapter submitted as an article/paper

The statement shall describe the candidate's and co-authors' independent research contributions in the thesis publications. For each publication there should exist a complete statement that is to be filled out and signed by the candidate and supervisor **(only required where there isn't already a statement of contribution within the paper itself).**

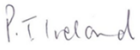
Title of Paper	Influence of Spanwise and Streamwise Film Hole Spacing on Adiabatic Film Effectiveness for Effusion-Cooled Gas Turbine Blades
Publication Status	□**Published** □ ~~Accepted for Publication~~ □~~Submitted for Publication~~ □~~Unpublished and unsubmitted work written in a manuscript style~~
Publication Details	Courtis M., Murray A., Coulton B., Ireland P., Mayo I. "*Influence of Spanwise and Streamwise Film Hole Spacing on Adiabatic Film Effectiveness for Effusion-Cooled Gas Turbine Blades*". International Journal of Turbomachinery, Propulsion and Power. 2021; 6(3):37

Student Confirmation

Student Name:	Matthew Courtis		
Contribution to the Paper	Research and conceptualisation, methodology, performing of all experimental and numerical work and writing of manuscript.		
Signature 		Date	07/07/23

Supervisor Confirmation

By signing the Statement of Authorship, you are certifying that the candidate made a substantial contribution to the publication, and that the description described above is accurate.

Supervisor name and title: Peter Ireland, Head of the Oxford Thermofluids Institute		
Supervisor comments		
Signature: 	Date	24/07/2023

This completed form should be included in the thesis, at the end of the relevant chapter.

6 Internal Component Study

6.1 Overview

As mentioned previously a DWEC system consists of an inner- and outer- skin connected by a thermal tie, i.e. pedestals. Each component offers the potential for aerothermal benefits, however mechanical considerations must also be accounted for. An analysis of thermal stresses in a DWEC system was made by Elmukashfit et al.[92], in which a thermal model was developed through a combination of empirical correlations and CFD to evaluate the thermal field as inputs into a FEA model for evaluation of the stress state of several geometric features. They found that stresses could be reduced by reducing pedestal height. Additionally, an increase in film hole number was observed to limit stresses to the external surface of the outer skin. Skamniotis and Cocks [103] found that the inner skin thickness was critical to the compressive stresses on the outer wall. However, the study did not model the effect of film cooling hole disposition and geometry on the DWTC temperature - rather a temperature field independent of feature variation was used. Consequently, the present author has eliminated the simplification from the assumped temperature field and determined the impact of geometric feature changes on the resulting stress field. The following study was presented in the Journal for Applied Thermal Engineering [104], in collaboration with Christos Skamniotis and Alan Cocks. Presented below is the paper in full where the present author undertook the aerothermal analysis in Section 6.2.2 and work by Christos Skamniotis is given in Section 6.2.4. An evaluation of the full set of results is given in Section 6.2.5, and finally the conclusions of this study are provided in Section 6.2.6.

6.2 Journal of Applied Thermal Engineering

Coupled aerothermal-mechanical analysis in single crystal double wall transpiration cooled gas turbine blades with a large film hole density

Mathew Courtis*, Christos Skamniotis*, Alan Cocks, Peter Ireland

Department of Engineering Science, University of Oxford, OX2 OES, UK

*contributed equally

Correspondence: c.skamniotis13@ic.ac.uk, peter.ireland@eng.ox.ac.uk

Journal of Applied Thermal Engineering

Volume 219, Part A, 25 January 2023, 119329

https://doi.org/10.1016/j.applthermaleng.2022.119329

Abstract

The ambition for increasing gas turbine efficiency beyond current levels through the elevation of gas temperatures demands substantial progress in turbine blade cooling technology. Double wall transpiration cooling (DWTC) is an emerging technology which offers enhanced thermal protection at only modest coolant flows, thanks to a combination of impingement jets and densely packed arrays of film cooling holes. This paper presents a coupled aerothermal-mechanical investigation of a transpiration cooled double wall turbine blade design, by employing Computational Fluid Dynamics (CFD), heat transfer theory as well as stress analysis based on plate theory and Finite Element (FE) analysis. In comparison to previously explored systems with modest outer wall porosity, a system with high porosity is found to display enhanced cooling effectiveness and to reduce the temperature difference across the two walls that drives thermal stresses. This difference can be decreased further by reducing the wall spacing, H, or the inner-outer wall thickness ratio, t_c/t_h, at the cost of higher overall metal temperatures. A lower bound for H should be used to avoid undesirable poor coolant flow distribution and hot gas ingestion effects; while the t_c/t_h ratio does not impose any aerothermal constraints. Thermal stresses associated with a fixed temperature field are invariant with H but they vary drastically with t_c/t_h. From a design perspective, the above suggest that H is primarily determined by aerothermal requirements, whereas t_c/t_h by the mechanical performance. The single

crystal orientation and elastic anisotropy of Nickel alloys are shown to have a profound impact on the stress concentration around cooling holes, with secondary crystallographic directions, such as $\langle 110 \rangle$ and $\langle 111 \rangle$, playing a prominent role in the local stress state. Our study provides a framework for optimising the aerothermal and mechanical performance in a range of high temperature components and highlights key areas where more elaborate analysis is needed.

6.2.1 Introduction

Gas turbine efficiency depends on the level of thermomechanical loading that can be withstood by critical hot stage components, such as high-pressure turbine blades [105]. To address the increasing efficiency demands and environmental concerns, future cooling systems must continue to protect these components against even more aggressive heat fluxes, by using the minimum possible coolant mass flow [10]. To achieve this, effusion and transpiration type systems [106, 5] with arrays of film cooling holes are being considered, which offer the benefits of higher internal surface area and elevated external film protection [101, 107]. Recently, the double wall transpiration cooling (DWTC) system has been proposed to enhance the cooling capability through a combination of film and impingement cooling [55].

The repeating unit of one such system is depicted in Fig 1d with a high outer wall porosity of 19.2% associated with inclined film holes through which the coolant escapes to protect the metal against the external heat flux (Fig 1e); prior to this, the coolant is impinged on the interior of the outer wall with the aid of transverse holes in an inner wall. The wall-connecting pedestals resist bursting loads and facilitate thermal conduction between the hotter outer wall and cooler inner wall. The outstanding cooling effectiveness of DWTC systems has been demonstrated through Computational Fluid Dynamics (CFD) analysis and empirical correlations by a number of authors, including Li et al. [55], Murray et al. [87] and Ngetich et al. [54]. The beneficial effect of film hole density, i.e. outer wall porosity, on film effectiveness has been demonstrated by Murray et al. [10] as well as Courtis et al. [101], who varied film hole spacing on a flat plate in a re-circulatory experimental facility, with results indicating that low film hole spacing increases mean film effectiveness, provides more uniform protection and reduces hot streaks. [100] explored the impact of high porosity panels on the suction and pressure surfaces of a

turbine blade; a high film effectiveness was achieved with low mass flow rates, especially on the suction surface. Despite the wealth of recent studies on DWTCs, full thermal solutions for outer wall porosities as high as 20% have not been obtained. One of the key objectives of this study is to generate relevant solutions.

The relationship between the film hole density and the structural integrity of DWTCs has received even less attention. Relevant work has only been presented by the authors in terms of elastic theoretical and Finite Element (FE) analysis [108] and studies which consider local inelastic deformation [109] in systems of relatively low outer wall porosity, of the order of 10%. The repeating unit of one such system is shown in Fig 6.2 a2 and can be visually compared against the one studied here in 6.2 a1. It was shown that since the walls are connected by rigid pedestals and experience different temperatures, they must extend equally in plane, causing membrane thermal stresses [103]. Additionally, a thermal gradient exists across the hot wall thickness but the wall rotations are self-constrained by the blade geometry, superimposing bending thermal stresses in the outer hot wall [103]. Mechanical stresses associated with centrifugal loading are also superimposed on the thermal stress field [110, 111]. Locally, at holes and pedestals the stresses are magnified beyond yield, leading to reversed plastic straining and eventually localised cracking due to low cycle fatigue (LCF) [110]. Such inelastic effects were shown to be critical at external features, i.e. film holes, where the metal experiences its peak temperature and therefore can exhibit high creep rates and low yield strength [109]. It was suggested that geometric features should be modified towards minimising film hole stresses: by tailoring the film hole characteristics (inclination, ellipticity) to attenuate stress concentration effects, and simultaneously reducing the inner wall thickness to reduce the nominal thermal stresses in the outer wall [109].

None of these design recommendations have taken into account the role of material anisotropy. Moreover, no study reports on the effect of internal features, i.e. inner to outer wall thickness ratio and wall spacing/pedestal height, on the cooling performance and resulting temperature field. These knowledge gaps highlight the need for a more comprehensive investigation of the aerothermal performance and stress fields, particularly when the design concerns highly porous

single crystal turbine blade components. This need is addressed in the present paper through a combination of aerothermal and mechanical analyses via theoretical and numerical means. In particular, the following questions will be addressed:

1. what are the implications of using a high outer wall porosity on the aerothermal and mechanical performance?

2. how does the wall spacing/pedestal height and the inner wall thickness influence the aerothermal performance and temperature field?

3. how does anisotropy and crystal orientation influence nominal wall stresses and stress concentrations at features?

4. does a thinner cool wall result in a better overall mechanical performance in both isotropic and anisotropic systems?

Unit-cell geometry		Aerothermal		Thermal load		Centrifugal load	
D_{film}	0.2 mm	T_c	1000 K	T_{max}	1100 °C	ρ	8.7e-9 tn/mm^3
D_{imp}	0.35 mm	m^*	1, 3, 5	T_{mid}	1050 °C	R_{tip}	400 mm
D_{ped}	0.5 mm	$\dot{m}_c/A_{in}$ [kg/s/m^2]	5.1, 15.2, 25.3	T_{min}	100 °C	L	60 mm
s	2.8 mm	T_∞	1870 K				
w	1.4 mm	h	7500 W/m^2/K				
t_h	1 mm	$P_\infty = P_{s,out}$	3.4 MPa				
γ	60 °	k	22 W/m/K				
ρ_{ped}	30 μm	c_p	1006 J/kg/K				
ρ_{hole}	10 μm						

Table 6.1: Fixed parameters used in the study.

6.2.2 Aerothermal Analysis

6.2.2.1 Aerothermal Model

We consider a low curvature (and low pressure) region of a double wall turbine blade, as denoted in Fig 6.1b. This enables us to assume a flat unit cell geometry for our FE-mechanical model 6.2 d and CFD-aerothermal model (Fig 6.2 a1). The effect of inner wall thickness, t_c, and wall spacing/pedestal height, H, on the internal aerothermal fields is studied by varying H for a fixed t_c= 1 mm (t_c/D_{imp}= 2.86 for fixed impingement hole diameter D_{imp}= 0.35 mm), as well

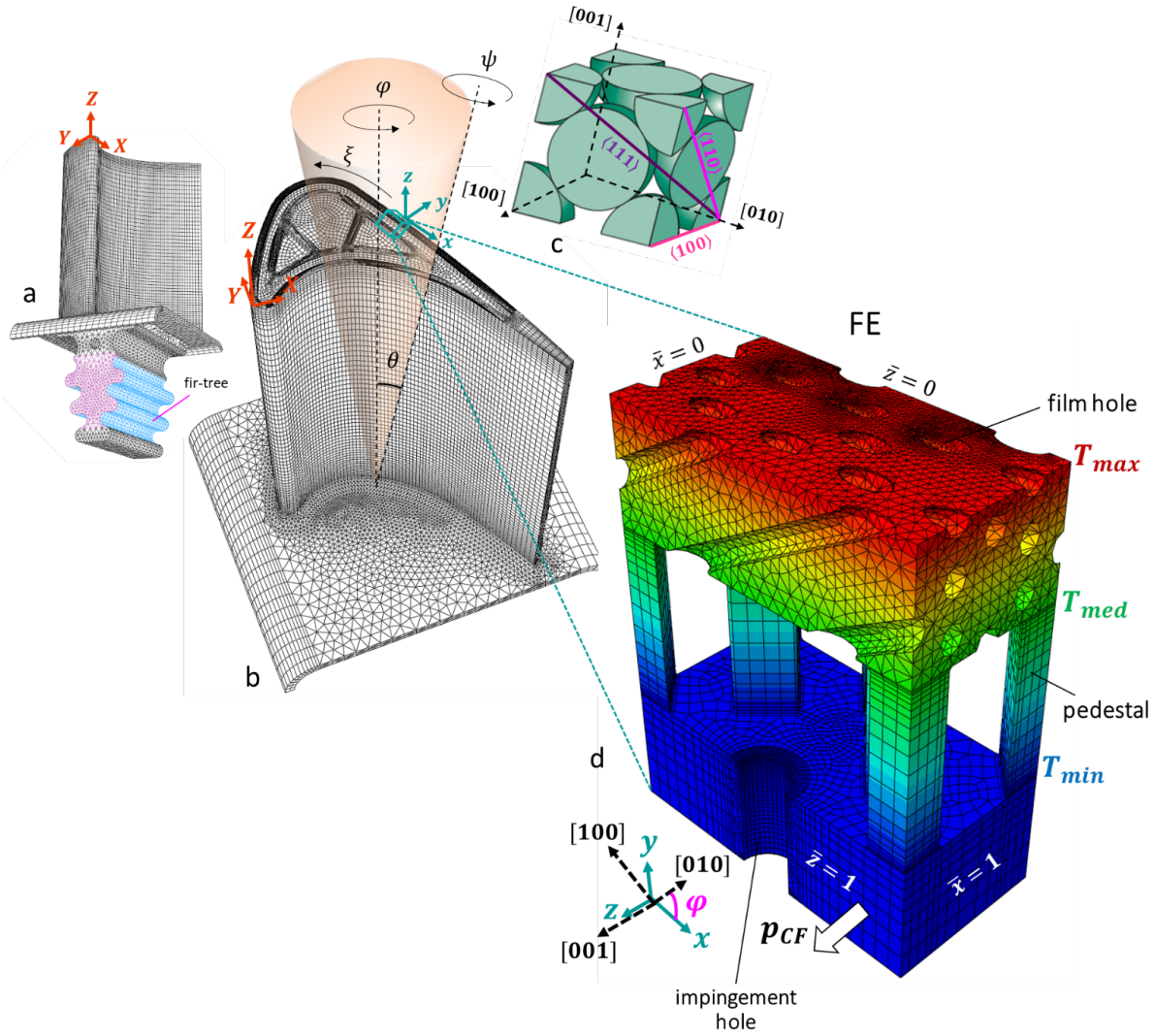


Figure 6.1: (a-b) Double wall turbine blade FE model reproduced from [108]; 4×10^5 8-node hexahedral elements (ABAQUS code: C3D8T) are used to mesh the walls (25 elements across the wall thicknesses) and 10^5 4-node tetrahedral elements (C3D4T) are used to mesh the platform and fir-tree regions. (c) FCC crystal rotated by Euler angles ϕ, π, ψ in Fig 3b with respect to the global blade system XYZ. (d) Flat unit cell with discrete pedestals and holes, corresponding to the low curvature region in Fig 3b and the local blade system xyz; contours show the idealised temperature field; 3×10^4 C3D8T elements are used to mesh the inner wall and pedestals and 105 C3D4T are used in the hot wall.

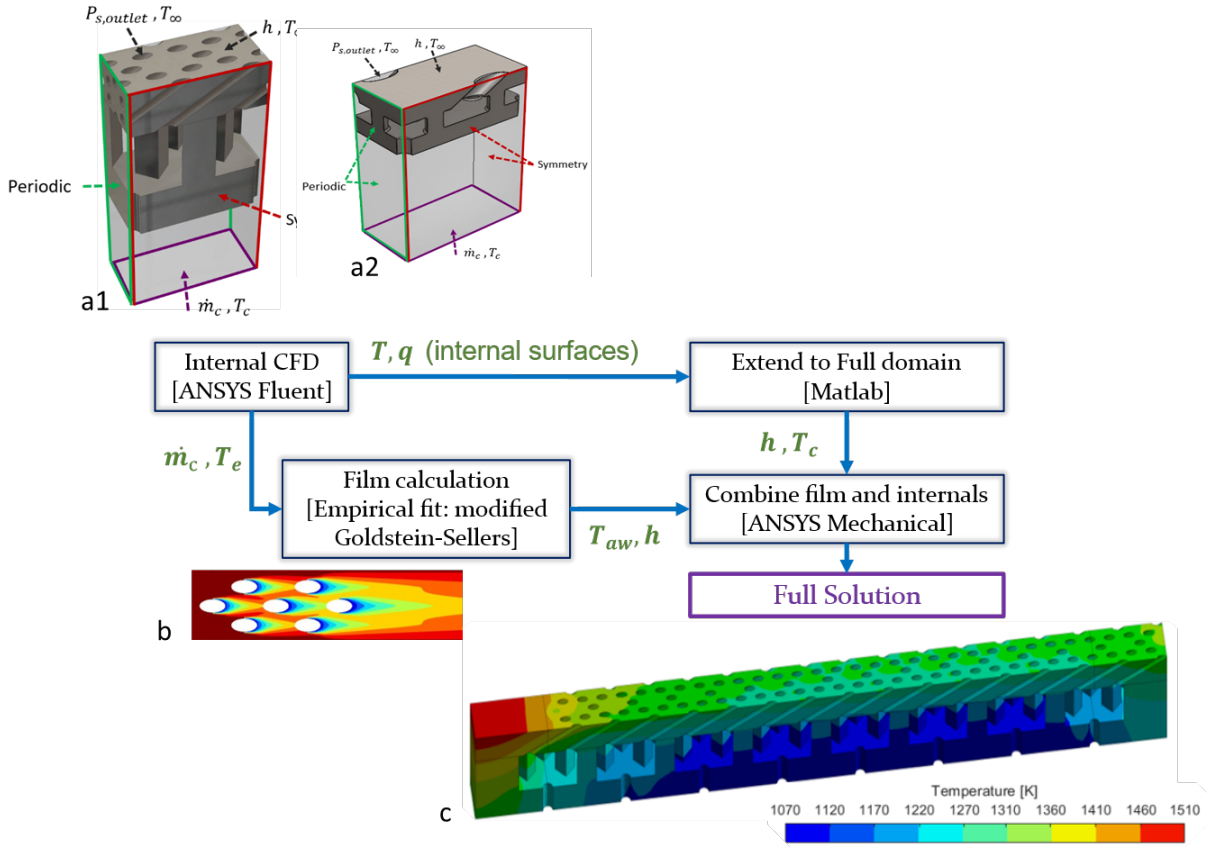


Figure 6.2: Schematic of the conjugate aerothermal analysis method developed by Murray et al [87]. (a1) CFD model used in present study, corresponding to the repeating unit cell of the DWTC system with high outer wall porosity of 19.2%. (a2) CFD model used previosuly in [108] for a DWTC system with low outer wall porosity of 10%. (b) Illustration of cooling effectiveness calculated by the modified Goldstein-Sellers method. (c) Temperature field of the full streamwise domain for a non-dimensional coolant flow rate, $m^* = 3$, and the typical geometric ratios of t_c/D_{imp}= 2.86 and H/D_{imp} = 4.29.

as by varying t_c for H= 1.5 mm (H/D_{imp}= 4.29). The remaining geometric ratios are fixed and reported in Table 1. A full thermal solution is obtained by utilising the conjugate method developed by Murray et al. [87] and later used by the authors [108, 2]]. As shown by the schematic in Fig 6.2 the method involves the following steps:

1. CFD analysis of internal coolant flow using the unit cell model in Fig 6.2 a1.
2. Empirical calculation of film effectiveness based on a modified Goldstein-Sellers method (Fig 6.2 b).
3. FE heat-transfer analysis in an enlarged domain (Fig 6.2 c), using the results of steps 1 and 2 as input.

Details of the implementation of this scheme are given in Appendix A. Three coolant mass flow rates, $\dot{m}_c$, are considered and are expressed by the non-dimensional term, $m^* = c_p \dot{m}_c / hA$, where c_p (J/kg/K) is the specific heat capacity, A (m^2) the area subject to external thermal loading, h (W/m^2/K) the external heat transfer coefficient imposed by the external flow. Table 1 gives the prescribed values employed in the CFD model of Fig 6.2 a1.

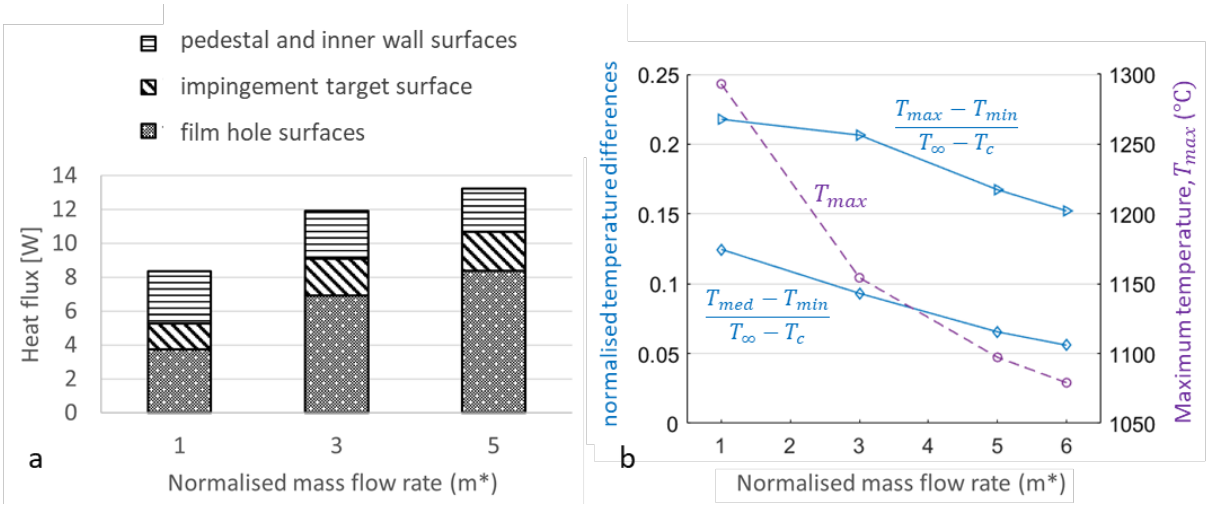


Figure 6.3: Aerothermal results for the unit cell of Fig 6.2 a1 (geometric ratios of t_c/D_{imp} = 2.86 and H/D_{imp} = 4.29). a) Contribution of the following three regions to internal convective cooling (internal heat flux): film hole surfaces, impingement target surface (= inner surface of outer wall) and pedestal and inner wall surfaces, for varying m^*. b) Variation of total normalised thermal difference $T_{max} - T_{min}$ in the system, normalised thermal difference across the pedestal height $T_{med} - T_{min}$ and average maximum temperature T_{max} on the external outer wall surface with coolant mass flow rate, m^*.

m^*	1	3	5	6
min ε	0.35	0.51	0.57	0.60
ΔT[K]	191	182	147	130
$\Delta T_{ped}/\Delta T$	0.59	0.43	0.41	0.40
$\overline{TF}$	0.08	0.10	0.07	0.06
max TF	0.06	0.05	0.02	0.01

m^*		1	3	5
H/D_{imp}	t_c/D_{imp}	$\overline{Nu}$		
0.86	2.86	9.52	24.2	37.6
4.29	2.86	7.93	22.7	36.4
7.14	2.86	7.15	20.4	33.0
4.29	0.57	8.13	23.4	37.8
4.29	1.43	7.99	22.8	36.7
4.29	5.71	7.85	22.6	36.2

Table 6.2: a) Aerothermal output variables for the unit cell of Fig 6.2 a1 (geometric ratios of t_c/D_{imp}= 2.86 and H/D_{imp}= 4.29) for varying non-dimensional mass flow rate, m^*. b) Average Nusselt number on the inner surface of the outer wall (impingement target surface) for each geometric combination and mass flow rate m^*.

6.2.2.2 Full thermal Solution

We first examine the full thermal solution obtained based on the standard unit cell configuration in Fig 6.2 a1 (H/D_{imp} = 4.29 and t_c/D_{imp} = 2.86). Fig 6.3 a shows the contribution of each of the following three regions to internal convective cooling: a) pedestal and inner wall surfaces, b) impingement target surface (= inner surface of outer wall) and c) film hole surfaces. The last of these contributes the most to internal cooling, especially at large coolant flow values, m^*, given the large heat sink offered by the high outer wall porosity. This suggests that although the impingement jet is important, i.e. $\sim$ 20% contribution to internal convective cooling, it can play a secondary role at large m^*. Nevertheless, it is anticipated that for higher external heat fluxes, h, the impingement jet would act as an important heat sink, limiting elevations in wall temperatures. This is based on the relation of the heat transfer coefficient, $h = q/(T_w - T_f)$, and the impingement jet offers a high heat transfer coefficient, thus any elevations in wall temperature will produce a higher heat flux to counter such increased temperatures.

The cooling performance can be assessed based on the film effectiveness parameter, $\eta_f = (T_\infty - T_{aw})/(T_\infty - T_c)$ and/or the cooling effectiveness parameter, $\varepsilon = (T_\infty - T_w)/(T_\infty - T_c)$, where T_∞ is the external free-stream temperature, T_c the coolant temperature, T_{aw} the adiabatic external wall surface temperature and T_w the temperature at a given wall surface; η_f expresses how well the external surface is cooled by the emerging film jets, whereas ε signifies the overall cooling performance considering both internal and external flows and is inversely proportional to the temperature at a given wall surface; the minimum value of ε in the system for each m^*

is given in Table 6.2 a, whereas the temperature profile for the full domain of the transpiration system is shown in Fig 6.2 c. In principle, transpiration occurs when the solid boundary is in thermal equilibrium with the adjacent fluid, but practically this can be thought to occur when they are within 1% of the overall driving temperature. In this way we can construct the transpiration factor, $TF = 1 - \frac{T_w - T_{f,outlet}}{T_\infty - T_c}$, which is the temperature difference between the wall and fluid divided by the temperature difference between the hot (mainstream) and cold (coolant) flows. Table 6.2 a gives the calculated area-averaged, ($\overline{TF}$), and maximum transpiration factor, max TF, associated with the external hot wall surface, in the investigated m^* range. It is found that $\overline{TF} < 0.1$ and that some locations approach the benchmark TF of 0.01; the latter depends on m^* and one may infer that an increase in m^* may reduce the value further. While transpiration cooling has not been theoretically realised across a majority of the domain and operating conditions, it can be argued that the system of high outer wall porosity studied here acts as a bridge between conventional effusion and transpiration cooling.

6.2.2.3 Wall spacing and inner wall thickness effects on internal aerothermal field

To explore how the wall spacing/pedestal height influences the above aerothermal results we firstly use the Nusselt number, $Nu = hD_{imp}/k$, defined here as the ratio of convective to conductive heat transfer at the fluid-solid interface of the impingement target surface. Where h (W/m^2/K) is the (heat transfer coefficient and, h (W/m^2/K), k (W/m/K) the thermal conductivity of the fluid, k (W/m/K) which is temperature dependent according to kinetic theory). Fig 6.4 a provides variations of the Nu contours at the target surface; area-averaged results,($\overline{Nu}$), for different geometric combinations and m^* values are summarised in Table 6.2 b. Wall spacing/pedestal height determines the distance between the impingement jet entry and the target surface, referred to as the target spacing. Reducing this spacing is found to increase the Nu values in Fig 6.4 a, resulting in both a higher maximum Nu at the impingement jet stagnation point and a wider area of elevated heat transfer. As supported by Patil and Vedula [114], the effect is a consequence of: a) the shorter distance travelled by the jet and therefore the fewer opportunities for deterioration of the peak jet velocity, and b) a stronger lateral jet which emerges from the impingement jet stagnation point.

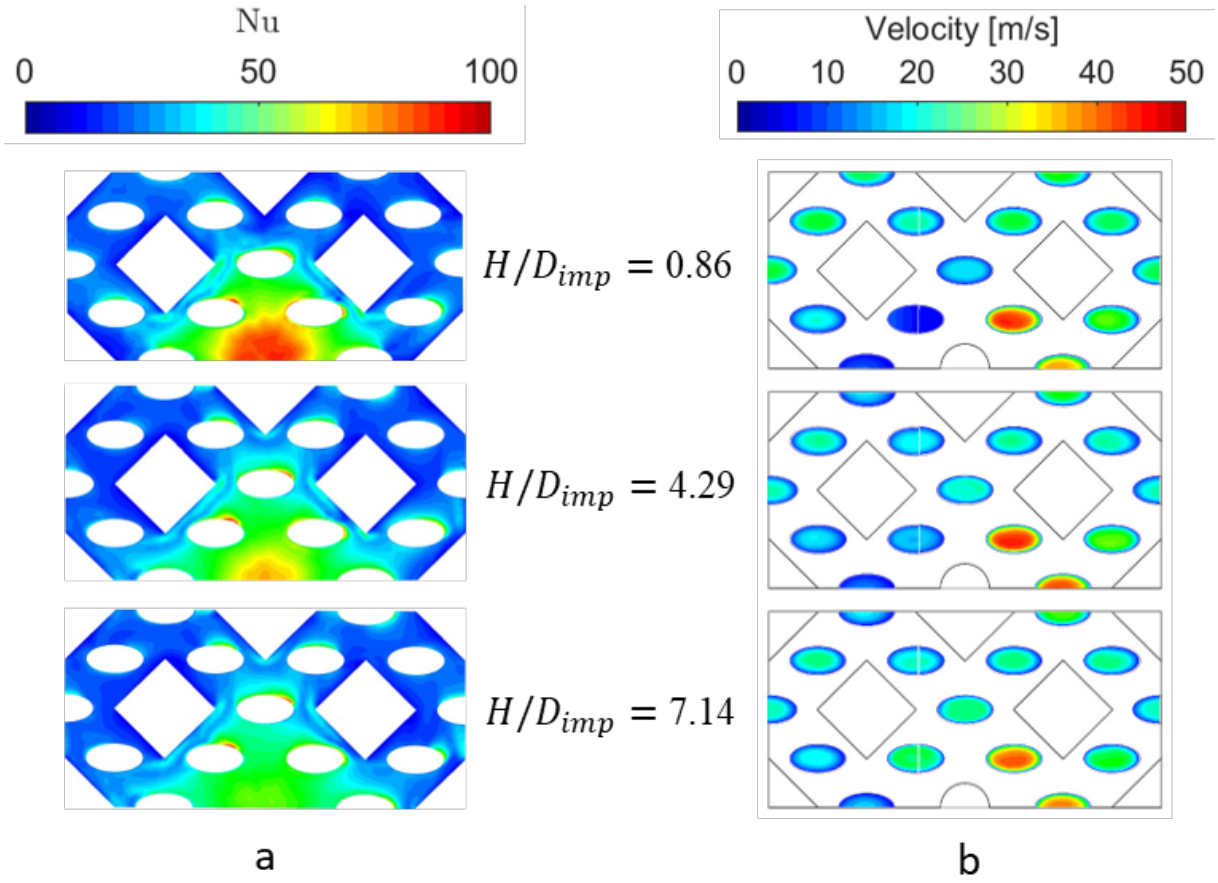


Figure 6.4: a) Comparison of Nusselt number contours at the impingement target surface (inner surface of outer wall) for varying pedestal height ratio, H/D_{imp} (for fixed $t_c/D_{imp} = 2.86$ and $m^* = 3$). b) Velocity contours at film hole exits.

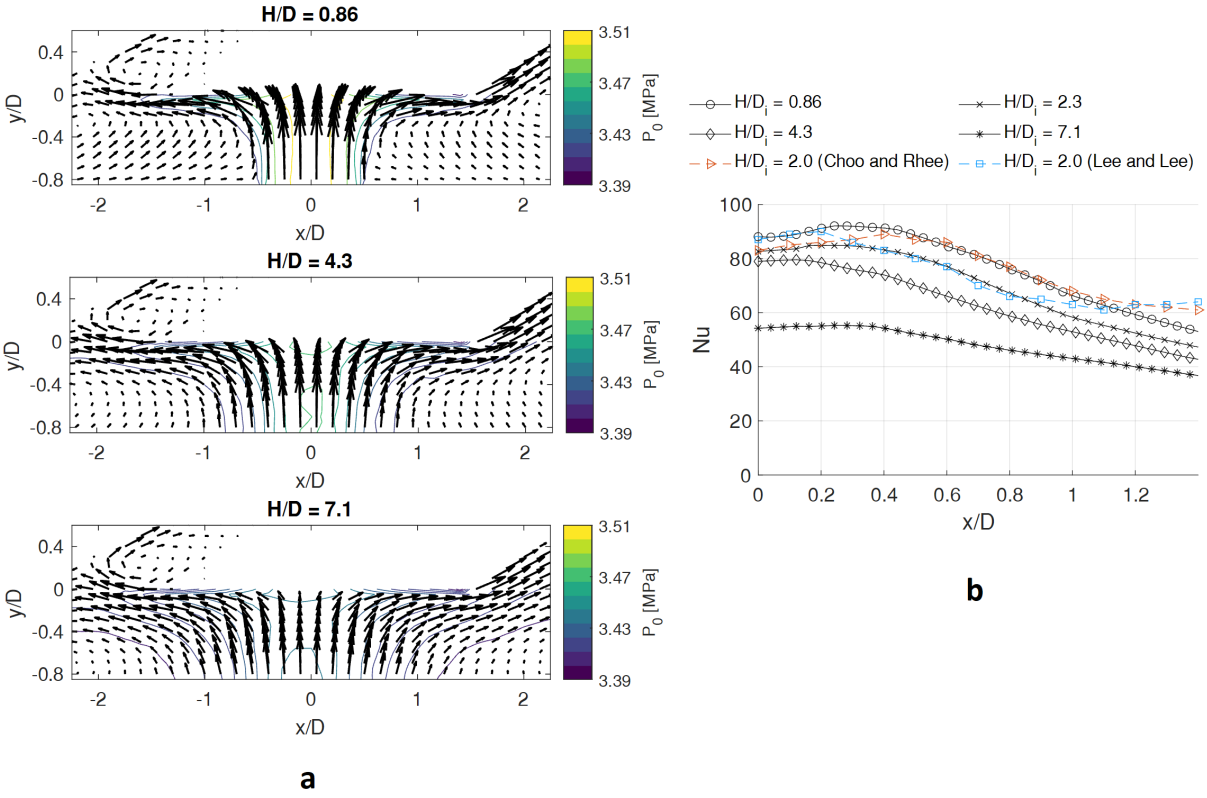


Figure 6.5: a) Velocity vectors and total pressure contours for varying pedestal height ratio, H/D_{imp}, for fixed t_c/D_{imp} = 2.86 and impingement Reynolds number of 10,400 (m^* = 3). The influence of impingement target spacing on the impingement jet was observed with a more defined impingement jet and lateral wall for lower H/D_{imp}. b) Nusselt values on the impingement target surface at y/D_{imp} = 0 plane for varying pedestal height ratio, H/D_{imp}, for fixed t_c/D_{imp} = 2.86 and impingement Reynolds number of 10,400 (m^* = 3). Impingement Nu is plotted for Choo and Rhee (2001) [112] and Lee and Lee (1998) [113] for H/D_{imp} = 2.0 and Re_{imp} of 10,000.

To further understand these assumptions velocity vectors and total pressure contours for three target spacings are displayed in Fig 6.5 a. A deterioration of the peak jet velocity and a widening of the impingement jet was observed for increasing H/D_{imp}. Give that the film holes are located near the impingement jet stagnation region (less than 2 D_{imp}) it is proposed that this proximity exhibits a strong influence over the impingement jet shape and intensity. Consequently, the thermal augmentation of the impingement jet is affected, and shown in Fig 6.5 b. We consider the Nu along a radial line for the impingement target surface for the range of H/D_{imp}, as well as results from literature (Choo and Rhee [112], Lee and Lee [113]). Nu in the stagnation region reduced as H/D_{imp} increased due to the lower impingement and radial wall jet velocity. In agreement with [115] it can be said that the location of effusion holes in relation to impingement jets strongly impacted the heat transfer values. While the results for $H/D_{imp} \sim 2$ appear representative of measurements in literature, especially in the stagnation region, as radial distance increases the values are lower than those in [112] and [113]. However, a direct comparison poses difficulties as results from literature rarely consider impingement jets in such proximity to the film holes as well as such a high ratio of film to impingement holes. Given the numerical difficulties with accurate assessment of the impingement jet Nu as well as geometric differences, the results published here are encouraging, but further study and experimental validation for such geometries should be considered in future work.

Despite the benefits of a narrow wall spacing, H/D_{imp}, on the impingement cooling performance, Fig 6.4 b shows that the distribution of mass flow to the film holes (velocity contours) is adversely impacted, as it becomes increasingly uneven. This is evidenced by the minimum outlet mass flow results plotted in Fig 6.6 a. In the worst scenario, hot gas-ingestion is observable for $H/D_{imp} = 0.86$ and both $m^* = 3$, $m^* = 5$, but positive mass flow is shown for the higher H/D_{imp} cases, with an increase in minimal outlet mass flow. An increase in overall coolant flow reduces the share received by the most deprived film hole, exacerbating the risk of hot-gas ingestion. The discrepancy in coolant flow is explained by the location and orientation of the film hole inlets in relation to the impingement jet stagnation point. For two film holes in close vicinity to this region, there is an inlet with a favourable angle and one with an unfavourable an-

gle compared to the direction of the lateral jet which emerges from the impingement stagnation region, and this can be visualised by the velocity vectors in Fig 6.5 a. In the former case, the lateral jet needs only turn by the film holes angle of inclination, 30 degrees in this case. However, for the lateral jet moving in the opposite direction to the angle of inclination, a direction change of 150 degrees must be made, and flow separation is more likely. At low H/D_{imp} the impingement jet and, in turn, the lateral jet have increased velocity, hence there is less time and space for these flow corrections to be made. Thus, the flow will favour film holes which impose less of an obstacle.

Importantly, Fig 6.6 c indicates that the cooling effectiveness parameter at both the external outer wall surface (dashed lines - $\varepsilon = (T_\infty - T_{max})/(T_\infty - T_c)$) and inner wall surface (solid lines - $\varepsilon = (T_\infty - T_{min})/(T_\infty - T_c)$) increases with H/D_{imp}, particularly at low m^*; in the low H/D_{imp} regime this effect may be partially attributed to the unfavourable effect of poorly fed film holes being stronger than the desirable effect of Nu increasing at the target surface. Since film holes contribute to most of the convective cooling in the type of systems studied here, the detriment of hot-gas ingestion can significantly degrade the overall cooling capability and therefore low H/D_{imp} values should be avoided. This is despite the fact that reducing H/D_imp is shown (Fig 6.6 c) to alleviate the difference in the cooling effectiveness values at the outer and inner walls (compare solid and dashed lines at each m^*), which is proportional to the total temperature difference $T_{max} - T_{min}$ in the system that drives thermal stresses.

In contrast to the wall spacing/pedestal height, the inner wall thickness is found to have a marginal impact on the flow distribution (see Fig 6.6 b) and to not cause any hot gas ingestion; a noticeable effect on flow arises only for the aspect ratio below unity, i.e. t_c/D_{imp}= 0.57. This is consistent with the study by Garimella and Nenaydykh [116] where the impingement hole aspect ratio was observed to have very little influence on Nu above unity, whereas below unity an increase in both stagnation and average Nu was observed. It was argued that the separation bubble does not reattach for low aspect ratio holes and reduces the effective hole diameter, leading to an increased jet velocity to maintain continuity and hence higher heat transfer. Despite these benefits, Fig 6.6 d demonstrates that for the double wall systems considered here the cooling

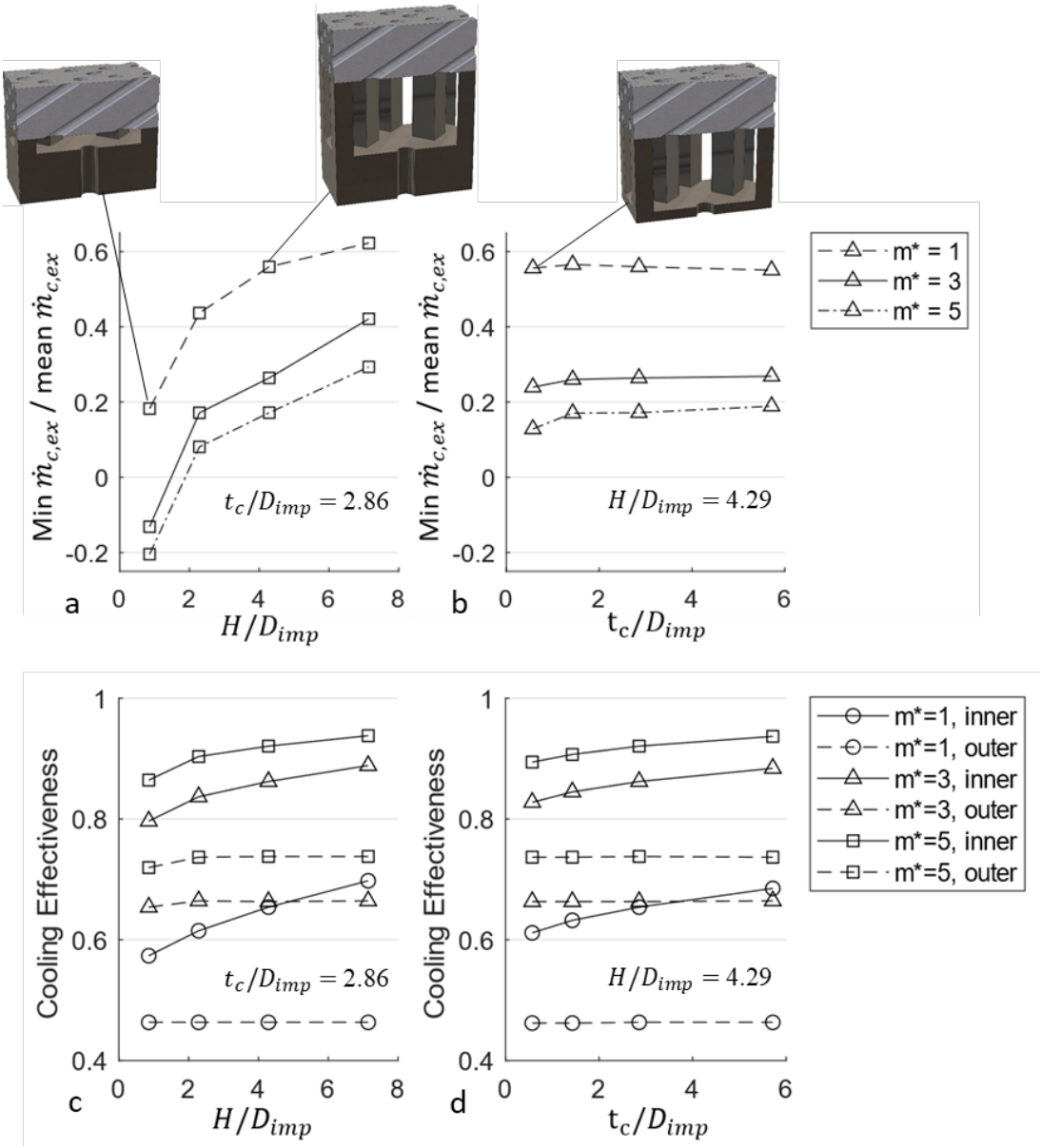


Figure 6.6: a) Minimum coolant mass flow at outlets for varying pedestal height H/D_{imp} ratio and coolant flow m^*. b) Minimum coolant mass flow at outlets for varying inner wall thickness t_c/D_{imp} ratio and coolant flow m^*. Cooling effectiveness parameter at the outer wall and inner wall external surfaces based on internal convection for: c) varying pedestal height H/D_{imp} ratio and coolant flow m^*, and d) varying inner wall thickness t_c/D_{imp} ratio and coolant flow m^*.

effectiveness in the outer wall (solid lines - $\varepsilon = (T_\infty - T_{min})/(T_\infty - T_c)$) increases with t_c/D_{imp}, suggesting that the inner wall has a more significant impact on the cooling effectiveness than the Nu number at the impingement target surface. Similar to the effect of reducing H/D_{imp} in Fig 6.6 c, reducing t_c/D_{imp} in Fig 6.6 d reduces the difference in cooling effectiveness, and thus the temperature difference between the outer and inner walls.

6.2.3 Link between aerothermal and mechanical analysis

6.2.3.1 Overall strategy

Our next step is to investigate the implications of the above aerothermal results on mechanical performance. The ultimate scope of our study is to identify the full range of possible temperature and stress fields, such that an optimal design can be found that meets both aerothermal and mechanical performance requirements. The aerothermal analysis in Section 6.2.2 indicates the degree to which the wall spacing/pedestal height, H, and inner wall thickness, t_c, influence the cooling effectiveness field and therefore the temperature field. The latter influences the thermal stress field and therefore the mechanical performance. In this context, H and t_c have an indirect effect on mechanical performance through their effects on the aerothermal field. A direct effect on mechanical performance is deemed here to occur when thermal stresses vary with geometry without any changes required in the temperature field. This is true here only for t_c, since the nominal thermal stresses in the walls are effectively invariant with H for a fixed temperature field; the latter is attributed to the fact that wall rotations are constrained in turbine blade components [103]. This leaves only the geometric parameter t_c to be varied in the following mechanical analysis in order to characterise its direct effect on the stress field. To highlight the influence of t_c, in this analysis the temperature field is kept fixed.

The indirect effects of H and t_c on the stress field will not be studied explicitly here; this would require a different temperature field to be prescribed in the FE model of Fig 6.1d for each $H - t_c$ combination. A more efficient strategy is to idealise the temperature field such that it can be described by three parameters: the peak temperature in the system T_{max}, the total temperature difference $\Delta T = T_{max} - T_{min}$ across the double walls and the difference $\Delta T_{ped} = T_{med} - T_{min}$

across the pedestal height (see Fig 6.1d). The relationship between ΔT and the values of H, t_c can be evaluated from the cooling effectiveness results in Figs 6.5c-d; the effect of H and t_c on ΔT_{ped} and its importance on thermal stresses is not significant and can be reasonably ignored. A single mechanical FE simulation for a typical temperature field can then determine how stresses scale with ΔT. With this information, any modifications of the temperature field, i.e. of the parameter ΔT, induced by changes of H and/or t_c can be readily translated into changes in stresses. The idealisation of the temperature field has an additional merit. It allows for analytical stress solutions to be generated, which will be used here to understand the role of key parameters in the problem (e.g. wall thickness ratio, crystal orientation, thermoelastic material properties) as well as to interpret the FE results. The validity of idealising the temperature field for the purposes described above was demonstrated in [108, 92], on the basis that high order temperature perturbations play a minor role in determining the thermal stresses. This observation was made for systems of modest outer wall porosity (Fig 6.2.2.1a2) and it is reasonably assumed to also hold for the high porosity systems considered here (Fig 6.2.2.1a1).

6.2.3.2 Using the aerothermal output

We now interpret the temperature field results in the context of mechanical performance and choose a typical fixed temperature field for use in the mechanical analysis. The three temperature field parameters, T_{max}, ΔT and ΔT_{ped} are given as a function of m^* in Fig 6.3b (note: ΔT and ΔT_{ped} are normalised by $T_\infty - T_c$) and Table 6.2a. ΔT is known to be the main thermal quantity that determines the magnitude of the thermal stresses, whereas $\Delta T_{ped} = T_{med} - T_{min}$ has been found to have a second order effect [108, 117]; that is, the membrane stresses dominate over bending stresses in the hot wall as $\Delta T_{ped}/\Delta T$ increases. Although this implies a small increase in tensile stresses in the cool wall, a more significant reduction in compressive stresses in the outer hot wall surface occurs, such that high $\Delta T_{ped}/\Delta T$ can be deemed beneficial to mechanical performance in most cases [117]. In this regard, Table 6.2a implies that a lower m^* is beneficial. However, the variation of $\Delta T_{ped}/\Delta T$ in the m^* range is found to be relatively small and its effect on stresses is generally far less important than the effect of ΔT. In fact, a large m^* is favourable, not only because it reduces ΔT (Table 6.2a) but also because it reduces the peak metal temperature, T_{max}; the latter is important because the elastoplastic properties of Ni-alloys

degrade sharply at temperatures $T < 700°C$.

Based on the above, a representative temperature field for use in the mechanical analysis could correspond to $m^* = 5$, with parameters $T_{max} = 1100°C$, $\Delta T = 147°C$ and $\Delta T_{ped}/\Delta T = 0.41$. However, engine efficiency requirements may pose a limit to the maximum value of m^* that can be used in practice, and it is generally difficult to know a priori the exact value of m^* and corresponding temperature field. Furthermore, our primary aim here is to determine how stresses scale with ΔT in the elastic range, and because of the linear nature of the problem an arbitrary value of ΔT can be used in the mechanical analysis. In this regard, we use a standard set of parameters $T_{max} = 1100°C$, $\Delta T = 100\,°C$ and $\Delta T_{ped}/\Delta T = 0.5$ (i.e. $T_{med} = 1050°C$, $T_{min} = 1000°C$). When evaluating the results of the analysis, the scaling factor ΔT is replaced by the reference thermal stress, $\sigma_T = \kappa \bar{t} \bar{E} \alpha \Delta T/(1-\bar{\nu})$= 318 MPaa, where $\bar{E}$ = 150 GPaa, $\bar{\nu}$ = 0.34 and $\alpha = 2 \times 10^{-5}$ are isotropic CMSX-4 properties for 1050 °C, ΔT= 100 °C, $\bar{t}$ = 0.5 is the ratio of an individual wall thickness over the sum of wall thicknesses and κ = 1.4 is a scaling factor associated with the temperature dependence of thermoelastic properties, α, $\bar{E}$, $\bar{\nu}$ [117].

6.2.4 Mechanical analysis

6.2.4.1 Material Model for CMSX-4 alloy

We consider the thermoelastic properties of the CMSX-4 alloy shown in 6.7. These include an isotropic thermal expansion coefficient, α, which increases with temperature, T, and three independent stiffness constants, C_{11}, C_{12}, C_{44} which decrease with T; each constant decreases in a different manner such that the degree of elastic anisotropy represented by the Zener factor, $A = 2C_{44}/(C_{11} - C_{12})$, increases with T; A is the ratio of shear moduli corresponding to the $\langle 100 \rangle$ and $\langle 110 \rangle$ crystallographic directions [118]. The Young's modulus, $\hat{C}_{11}$, and compliance, $\hat{S}_{11}$, along a direction with cosines, l_1, l_2, l_3 relative to the principal crystal axes [001], [010], [100] (shown in Fig 6.7b) obey the relation $1/\hat{C}_{11} = \hat{S}_{11} = S_{11} + lS_{44}(1-A)$, where S_{11}, S_{44} are compliance constants defined in Appendix B and $l = l_1^2 l_2^2 + l_2^2 l_3^2 + l_3^2 l_1^2$; $l = 0$ along the three cube normal directions $\langle 100 \rangle$, $l = 1/4$ along the six cube face diagonals $\langle 110 \rangle$ and $l = 1/3$ along the four cube diagonals $\langle 111 \rangle$. For Fig 6a this implies that at a typical temperature of

interest, $T \approx 1000°C$, the $\langle 110 \rangle$ and $\langle 111 \rangle$ directions are 1.95 and 2.85 times stiffer than $\langle 100 \rangle$, whereas the volume averaged Young's modulus, $\bar{E}$, is 1.9 times higher than that along $\langle 100 \rangle$. The volume averaged modulus $\bar{E}$ and Poisson's ratio $\bar{\nu}$ are computed in Appendix C and will be used here to represent the case of a polycrystalline CMSX-4 where a large number of grains with different orientations statistically gives an isotropic macroscopic response.

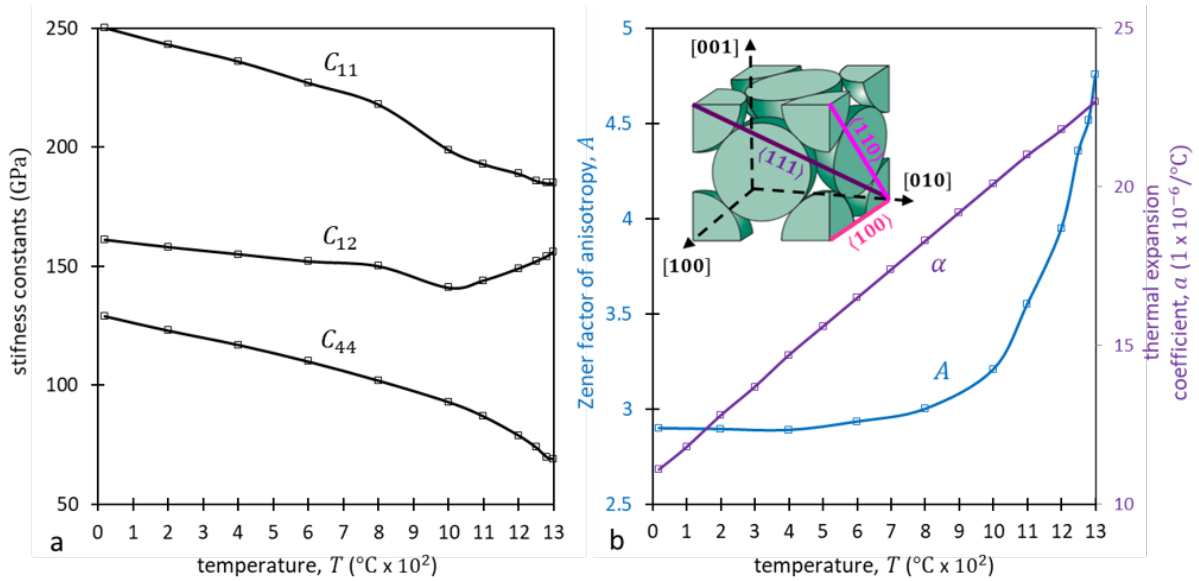


Figure 6.7: Thermoelastic properties of the CMSX-4 alloy. (a) Stiffness constants versus temperature (taken from [119]). (b) Zener factor of anisotropy and coefficient of thermal expansion (taken from [120]).

6.2.4.2 Thermal stresses in a double wall turbine blade

Prior to analysing the detailed stress field in the repeating unit of Fig 6.1d, it is essential to firstly determine stresses in the double wall turbine blade model of Figs 6.1a-b. This allows us to capture anisotropic effects associated with single crystal blades that cannot be captured by a unit cell model with constant curvature, as well as to identify the overall nature of the nominal thermal stresses in the real component and justify the kinematic boundary conditions to be used in a subsequent unit cell analysis. component of interest justify the in repeating A blade length of 60 mm and 1 mm uniform wall thicknesses and wall spacing are used; the blade is supported at the fir-tree region in which zero y-displacements and z-displacements are applied on its lateral surfaces (denoted in blue in Fig 6.1a) and zero x-displacement on its front surface (denoted in red in Fig 6.1a). Pedestals are not modelled discretely but instead their presence is mimicked through enforcing zero relative x, y, z displacements between each node at the inner hot wall

surface and its adjacent node at the inner cool wall surface. We prescribe the temperatures T_{max} = 1100 °C and T_{med} = 1050 °C at the outer and inner surface of the hot wall and T_{min} = 1000 °C at the entire cool wall (temperature field justified in Section 6.2.3.2), in a uniform manner along the streamwise, ξ, and spanwise, z, directions of the blade (see Fig 6.1b). A detailed description of the blade model in Fig 6.1a-b is given in a previous report [108] where thermal, centrifugal (CF) and aerodynamic bending (P) stresses were studied for an isotropic material. Here we explore how thermal stresses occur when the elastic anisotropy of the CMSX-4 alloy comes into play.

The orientation of the principal crystal axes (Fig 6.1c) with respect to the global blade system XYZ (Figs 6.1a-b) is defined by a sequence of three intrinsic rotations of type ZX'Z" [121] by the Euler angles, ϕ, θ, ψ; the angle θ defines the cone illustrated in Fig 6.1b; the transformation matrix between the crystal and blade systems is given in Appendix B. In current manufacturing procedures only θ is controlled, with the target value being θ= 0 ° such that $\langle 100 \rangle$ aligns with the blade axis Z; blades that do not satisfy $\phi \leq 15°$ are rejected. The randomness of ϕ and ψ angles implies that different blades exhibit different mechanical behaviour. This is evident here by comparing the thermal stress field at a representative blade cross-section (15 mm away from the blade root) between the cases of no crystal rotation (Figs 7a-b) and a crystal rotation of ϕ= 45 ° (Figs 7c-d); in Figs 7e-f we also plot results for polycrystalline CMSX-4 where the stresses are higher since the volume averaged $\bar{E}$ and $\bar{\nu}$v properties are used.

Before explaining the orientation effect, it is important to recognize that for the thin wall structures considered here stresses effectively arise only in the wall planes. The cool wall is in pure tension and therefore experiences positive maximum and intermediate principal stress, i.e. $\sigma_1 > 0$ and $\sigma_2 > 0$, ($\sigma_3 \approx 0$), whereas the hot wall is subjected to membrane compression combined with bending such that the in-plane principal stresses are compressive, $\sigma_2 > 0$ and $\sigma_3 < 0$ in its outer fibres and the out of plane principal stress, $\sigma_1 \approx 0$. To best illustrate these characteristics we plot the maximum absolute principal stresses, $\sigma = \max\langle|\sigma_1|,|\sigma_3|\rangle$, in Figs 6.8 a,c,e and intermediate principal stresses, $\sigma = \sigma_2$, in Figs 6.8 b,d,f, and normalise them with respect to the reference thermal stress, σ_T defined in Section 6.2.3. The σ_2 stresses are approx-

imately equal to the stresses along the global blade axis, Z, i.e. $\sigma = \sigma_2 \approx \sigma_z$ in Figs 6.8b,d,f, whereas the maximum absolute principal stresses are approximately equal to the stresses along the blade chord/streamwise, ξ blade direction, i.e. $\sigma = \max\langle|\sigma_1|,|\sigma_3|\rangle \approx \sigma_\xi$ in Figs 6.8 a,c,e. These features apply along almost the entire blade length because a uniform temperature field is prescribed and therefore any variation in the stress field effectively occurs only near the blade root and the blade tip regions.

An effect that occurs regardless of anisotropy is that at the highly curved regions of the blade the σ_ξ stresses are higher than σ_z stresses (see Fig 6.8 e-f); such effects have been explained in [117]. The major effect induced by anisotropy (Figs 6.8 a-d) is that the σ_z stresses lie along the [001] direction (due to $\theta = 0^\circ$) and therefore are much lower than the σ_ξ stresses which are highest in regions where the direction of σ_ξ aligns with the [110] direction (as denoted in Fig 6.8a). This alignment generally occurs at different blade regions for different rotations, ϕ (note that $\phi = \psi$ when $\theta = 0^\circ$), which in combination with the aforementioned curvature effect leads here to a better overall mechanical response in Figs 6.8 c-d for $\phi = 45^\circ$ compared to Figs 6.8 a-b for $\phi = 0^\circ$. In this regard, various authors have looked at optimising the crystal orientation for specific blade geometries based on parametric FE analysis [122, 123, 124]; however, theoretical solution are not available that provide physical insight into the orientation effect for thin wall systems and none of these studies have considered the effect of stress raising features, i.e. holes and pedestals, which are important stress raising features of the double wall transpiration cooling systems considered here. These aspects will be addressed in the next sections.

6.2.4.3 Thermal stress in flat double plates

To aid the development of theoretical solutions for nominal stresses (in the absence of holes and pedestals) we ignore wall curvature effects and utilise the idealised flat unit cell in Fig 1d for a variable crystal orientation. Consider the system xyz which is local to the turbine blade (Figs 6.1 a-b) and global to the unit cell (Fig 6.1d). The kinematic requirement of equal total strains

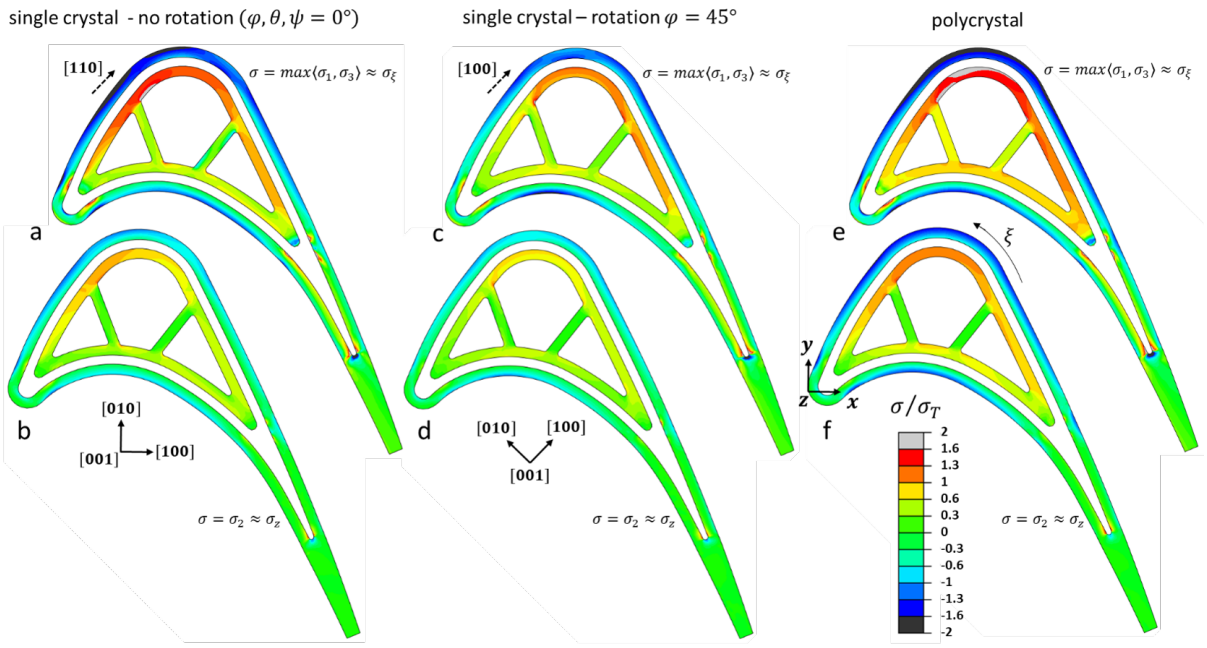


Figure 6.8: Thermal stress fields at the cross-section of the turbine blade model of Fig 6.1b, 15 away from the blade root. (a-b) A single crystal CMSX-4 blade with no crystal rotation with respect to the blade system. (c-d) A crystal rotation of $\phi = 45°$. (e-f) A polycrystalline (isotropic) blade where volume averaged properties of CSMX-4 are used. a,c,e show maximum absolute principal stresses; b,d,f show intermediate principal stresses; all stresses are normalised by the reference stress, σ_T= 318 MPaa.

between the walls in x the direction gives:

$$\frac{s^M_{h\ x}}{t_h}\int_{-\frac{t_c}{2}}^{\frac{t_h}{2}} \hat{S}_{11}(T(y))dy \quad + \frac{s^M_{h\ z}}{t_h}\int_{-\frac{t_c}{2}}^{\frac{t_h}{2}} \hat{S}_{13}(T(y))dy \quad + \frac{1}{t_h}\int_{-\frac{t_h}{2}}^{\frac{t_h}{2}} \alpha(T(y))T(y)dy$$
$$= s_{cx}\,\hat{S}_{11}(T_{min}) \quad + s_{cz}\,\hat{S}_{13}(T_{min}) \quad + aT_{min} \qquad (6.1)$$

The same requirement for the z direction gives:

$$\frac{s^M_{h\ x}}{t_h}\int_{-\frac{t_c}{2}}^{\frac{t_h}{2}} \hat{S}_{31}(T(y))dy \quad + \frac{s^M_{h\ z}}{t_h}\int_{-\frac{t_c}{2}}^{\frac{t_h}{2}} \hat{S}_{33}(T(y))dy \quad + \frac{1}{t_h}\int_{-\frac{t_h}{2}}^{\frac{t_h}{2}} \alpha(T(y))T(y)dy$$
$$= s_{cx}\,\hat{S}_{31}(T_{min}) \quad + s_{cz}\,\hat{S}_{33}(T_{min}) \quad + aT_{min} \qquad (6.2)$$

Equilibrium along x and z respectively gives:

$$s^M_{h\ x}t_h + s_{cx}t_c \ = 0 \qquad (6.3)$$

$$s^M_{h\ z}t_h + s_{cz}t_c = 0 \qquad (6.4)$$

where $s^M_{h\,x}$, $s^M_{h\,z}$ are the nominal membrane thermal stresses in the hot wall along x and z, s_{cx}, s_{cz} are the corresponding cool wall stresses, t_h, t_c are the hot and cool wall thicknesses and the terms $\hat{S}_{ij}$ are components of the compliance matrix $\hat{\mathbf{S}}$ in the xyz system, which is related to the material compliance, $\mathbf{S}$, according to $\hat{\mathbf{S}} = \bar{\mathbf{T}}^T \mathbf{S} \bar{\mathbf{T}}$, where the transformation matrix, $\bar{\mathbf{T}}$, is constructed based on the Euler angles, φ, θ, ψ in Appendix B. Since the temperature, T, varies with position, y, through the thickness of the hot wall, $\hat{S}_{ij}$ and a are both functions of $T(y)$ on the LHS of Eqs 6.1-6.2, whereas on the RHS of Eqs Eqs 6.1-6.2 they have constant values since the cool wall is at uniform temperature, T_{min}. Bending stresses, $s^B_{h\,x}(y)$, $s^B_{h\,z}(y)$, in the hot wall due to the temperature variation $T(y)$ are determined by postulating zero total bending curvatures about z and x axes, which respectively gives:

$$\begin{aligned}
&\frac{M_{hz}}{I}\int_{-\frac{t_h}{2}}^{\frac{t_h}{2}} \hat{S}_{11}(T(y))\, y^2 dy \; + \frac{M_{hx}}{I}\int_{-\frac{t_h}{2}}^{\frac{t_h}{2}} \hat{S}_{13}(T(y))\, y^2 dy \; + \int_{-\frac{t_h}{2}}^{\frac{t_h}{2}} \alpha(T(y))T(y)\, y dy = 0 \quad (a)\\
&\frac{M_{hx}}{I}\int_{-\frac{t_h}{2}}^{\frac{t_h}{2}} \hat{S}_{31}(T(y))\, y^2 dy \; + \frac{M_{hz}}{I}\int_{-\frac{t_h}{2}}^{\frac{t_h}{2}} \hat{S}_{33}(T(y))\, y^2 dy \; + \int_{-\frac{t_h}{2}}^{\frac{t_h}{2}} \alpha(T(y))T(y)\, y dy = 0 \quad (b)
\end{aligned} \tag{6.5}$$

where $I = {t_h}^3/12$ is the second moment of area per unit length and M_{hx}, M_{hz} are the bending moments about x and z, such that $s^B_{h\,x}(y) = M_{hz}y/I$ and $s^B_{h\,z}(y) = M_{hx}y/I$. By superimposing a uniform centrifugal z-stress, p_{CF}, the resulting nominal stresses are:

$$\begin{aligned}
\sigma_{hx}(y) = s^M_{h\,x} + s^B_{h\,x}(y) \quad \text{and} \quad \sigma_{hz}(y) = s^M_{h\,z} + s^B_{h\,z}(y) + p_{CF} \quad (a)\\
\sigma_{cx} = s_{cx} \quad \text{and} \quad \sigma_{cz} = s_{cz} + p_{CF} \quad (b)
\end{aligned} \tag{6.6}$$

We now utilise Eqs 6.1-6.6 to reveal the effect of crystal orientation on the compressive nominal stress magnitude at the external surface of the hot wall, $\sigma_{hx}(y = -t_h/2)$ and $\sigma_{hz}(y = -t_h/2)$, for the full range of Euler angles φ, θ, ψ. We consider the same temperature field used in Section 6.2.4.2 with $T_{max} = 1100°$C, $T_{med} = 1050°$C and $T_{min} = 1000°$C. The results are illustrated in Fig 6.9 in terms of absolute values normalised by the reference thermal stress, σ_T= 318 MPaa. First, we recognise that for $\theta = 0°$ the φ rotation is equivalent to the ψ rotation; in this case, the entire

range of behaviour can be studied by varying $\varphi or \psi$ between 0° and 45° and the x-stresses and z-stresses can only align with the 100 or 110 crystal axes. For $\theta > 0°$ the effect of orientation becomes more complex. The z-stresses (aligned with Z blade axis in Fig 6.1b), generally take small values for low θ (see Fig 6.9), since in this range the stresses act approximately along the compliant 001 crystal axis; note however that even for $\theta = 0°$ the z-stresses slightly increase when x-stresses increase, as the two components are coupled by Hooke's law (Eqs 6.1-6.2). It appears that the worst scenario in terms of z-stresses in the turbine blade is when $\theta = 45°$ (see Fig 6.9) because these are a maximum for many combinations of φ and ψ due to alignment of the stiff 111 crystal direction with the z direction.

These results justify the use of a maximum permissible value of $\theta = 15°$ by the current manufacturing practise. Additional FE simulations for this extreme ($\theta = 15°$) using the blade model in Fig 6.1b show that the results in Figs 6.8 a-b are not significantly modified. Conclusively, our design problem here is mainly concerned with orientation effects associated with the variation of φ between 0° and 45° and this variation will be our main consideration in the following FE analysis of stresses at features.

6.2.4.4 Thermal and centrifugal stresses in a DWTC system

We now study local stresses at holes and pedestals in Fig 6.1d for a wide range of practical thermal-centrifugal load combinations. We firstly need to acknowledge that centrifugal (CF) stresses, p_{CF}, generally vary along the spanwise Z blade axis between zero at the tip of a blade to a maximum value at the root. As a result, for the purposes of this study we will use a fixed temperature field and vary p_{CF}. In particular, we apply the same temperatures uniformly along the walls used in Section 6.2.4.2 ($T_{max} = 1100°$C, $T_{med} = 1050°$C, $T_{min} = 1000°$C - see Fig 6.1d) and vary p_{CF} in the range 0 – 300 MPaa, such that p_{CF}/σ_T ranges from 0 to ∼1 (σ_T= 318 MPaa); the validity of using the idealised temperature field of Fig 6.1d in which temperatures do not vary along the wall planes has been demonstrated in [108]. Here p_{CF} is the nominal CF stress carried by the gross wall sections and is introduced in Fig 6.1d in the form of an equivalent uniform traction $p_{CF\,net}$ ($< p_{CF}$) at the $\bar{z}$= 1 plane, throughout the reduced/net sections of the walls. The calculation of $p_{CF\,net}$ based on turbine rotational speed (rpm), material density and transpiration cooling geometry is provided in Appendix D. In terms of displacement bound-

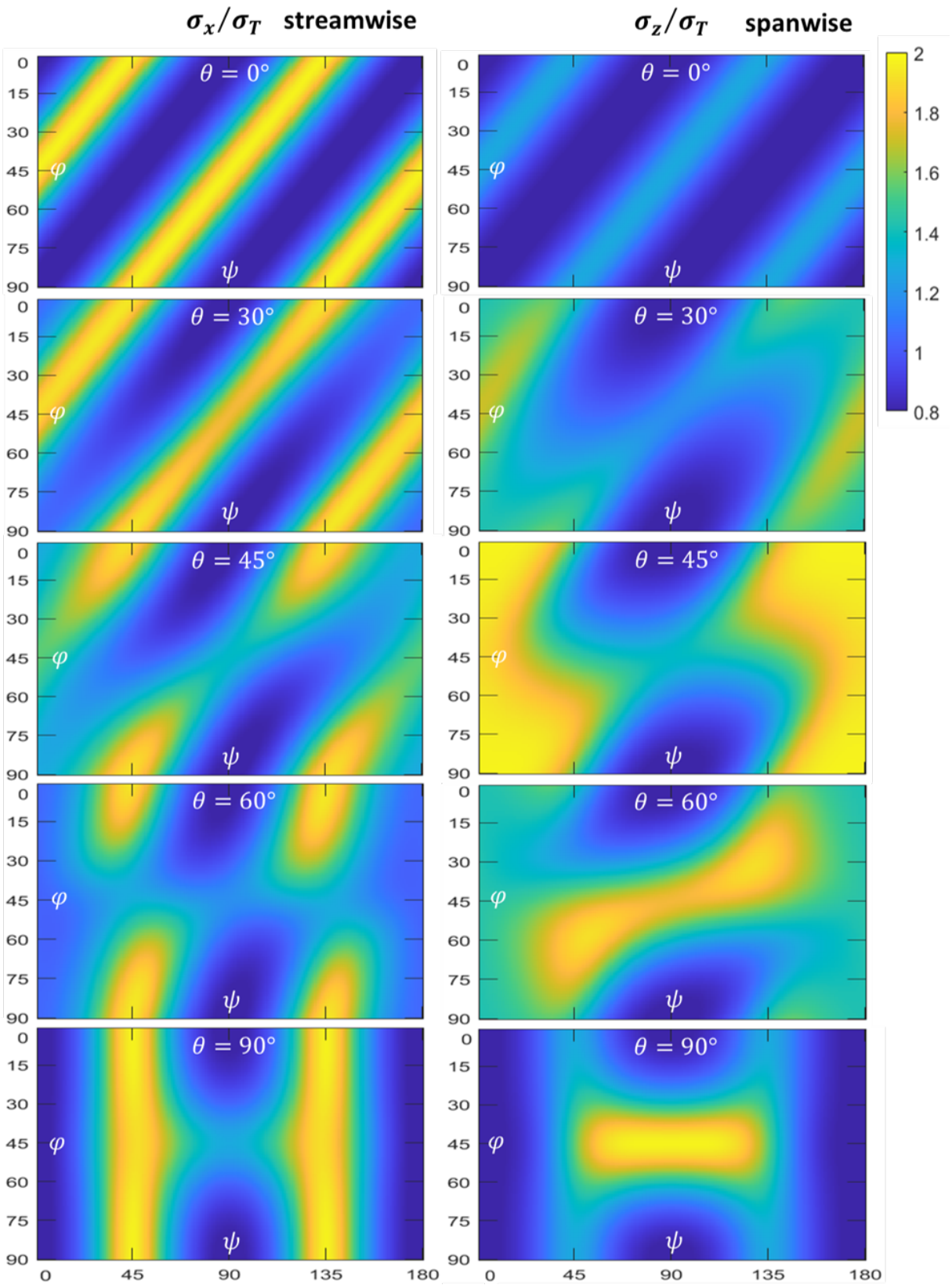


Figure 6.9: Variation of the magnitude of the nominal compressive thermal stress at the outer fibre of the hot wall along the x and z directions in the system of Fig 6.1d, with respect to the crystal rotation (Euler) angles, ϕ, θ, ψ. Stresses are computed theoretically through Eqs 1-3 (p_{CF}= 0) and are normalised over the reference thermal stress, σ_T= 318 MPaa; x and z correspond to the streamwise and spanwise directions of the blade in Fig 6.1b.

ary conditions, we apply zero z-displacements at the $\bar{z}$= 0 plane, common z-displacement for all nodes at $\bar{z}$= 1 and periodic conditions at the pair of $\bar{x}$= 0, $\bar{x}$= 1 planes; note that here $\bar{z}$= 0 and $\bar{z}$= 1 are symmetry planes because the crystal is rotated only about the φ axis (see Fig 6.1d).

Our results are summarised in Figs 6.10-6.11. Firstly, for a typical combination of $\varphi = 45°$ and p_{CF}= 225 MPaa in Figs 6.10a-c we indicate that the resulting $max\langle\sigma_1, |\sigma_3|\rangle$ stress field (Fig 6.10c) is given by superposition of the thermal (Fig 6.10a) and CF (Fig 6.10b) stress fields. The detailed distribution of stress at features for the same thermal-CF loading combination is illustrated in Figs 6.10a-f in terms of maximum absolute resolved shear stress, $max\langle|\boldsymbol{\tau}_{\mathbf{rss}}|\rangle$, amongst the 12 octahedral slip systems $\{111\}110$ of the FCC lattice, with the $\boldsymbol{\tau}_{\mathbf{rss}}$ vector (12x1) given by Schmid's law as $\boldsymbol{\tau}_{\mathbf{rss}} = \boldsymbol{\sigma} : (\mathbf{s} \otimes \mathbf{n})$, where $\boldsymbol{\sigma}$ is the stress tensor (3x3) in the crystal system and $\mathbf{s}$, $\mathbf{n}$ are the matrices (12x3) containing unit vectors normal to the slip planes and unit vectors in the direction of slip, respectively. By taking the peak value $max\langle|\boldsymbol{\tau}_{\mathbf{rss}}|\rangle$ at each feature and normalising it by the range of the critically resolved shear stress during cycling between the hot and cold temperatures, $\Delta\tau_{crss} = \tau_{crssT} + \tau_{crss0}$, we construct the plots in Figs 6.11a1-c1, where the ratio $\frac{max\langle|\boldsymbol{\tau}_{\mathbf{rss}}|\rangle}{\Delta\tau_{crss}}$ indicates the degree by which local reversed plastic straining would occur in practice, which provides a measure of the likelihood of the development of fatigue damage; the calculation of $\Delta\tau_{crss}$ based on the critical resolved shear stress at high temperature, τ_{crssT} (full thermal loading) and at room temperature, τ_{crss0} (zero loading) is provided in Appendix E.

From a practical perspective, conclusions about fatigue performance may be drawn based on Figs 6.11a1-c1 alone. The following effects are observed:

(a) A thinner cool wall (t_c/t_h= 0.5) reduces film hole stresses at the cost of increasing stresses at internal features, i.e. impingement hole and pedestal.

(b) Hole stresses are higher for $\varphi = 45°$ compared to $\varphi = 0°$ (Figs 6.11a1-b1) whereas slightly the opposite is shown for the pedestal stresses (Fig 6.11c1).

(c) CF loading generally increases stresses at internal features (Figs 6.11b1-c1) whereas film hole stresses (Fig 6.11a1) initially reduce in the low p_{CF} regime and then increase in the high p_{CF} regime.

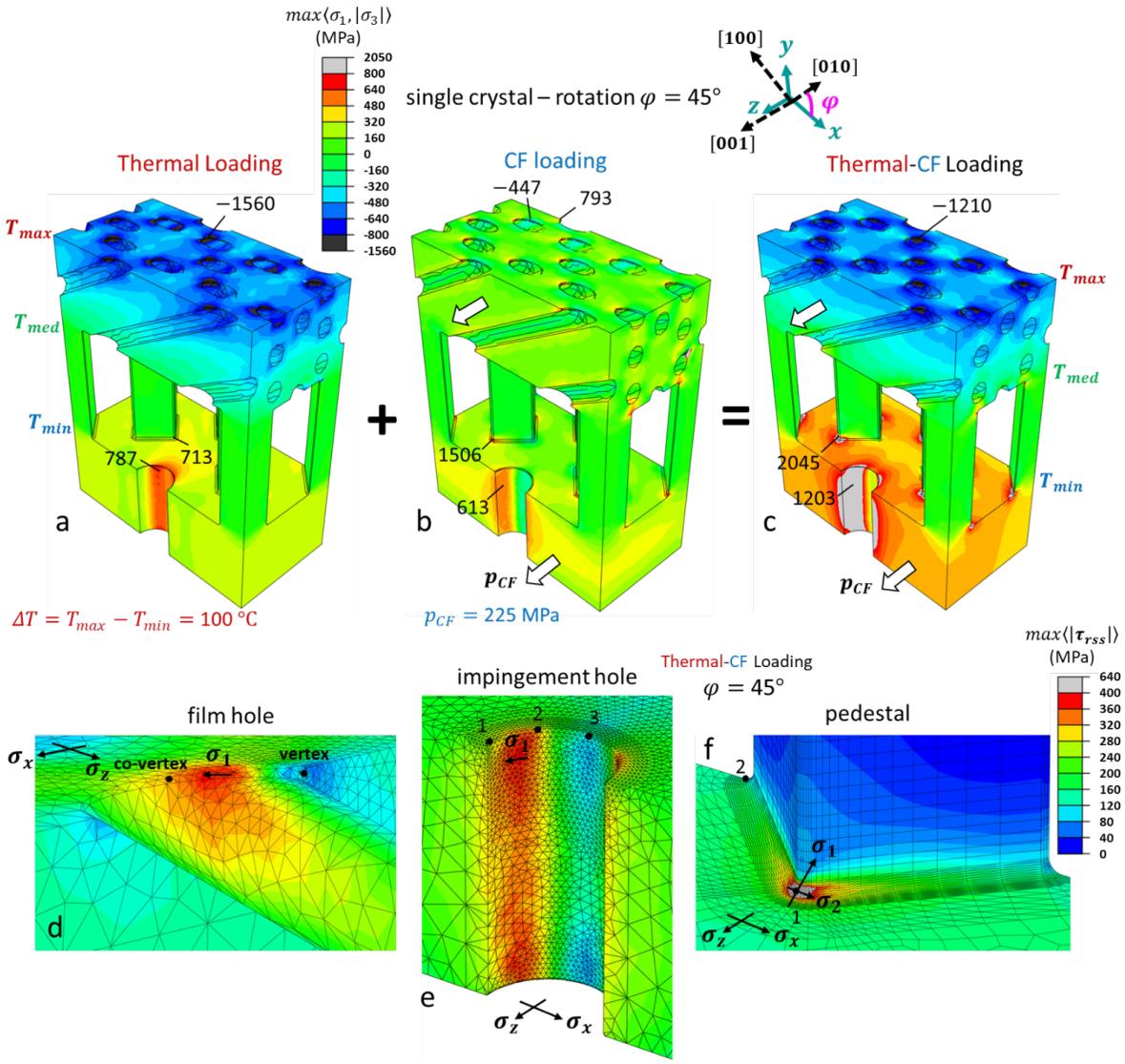


Figure 6.10: Mechanical analysis results for the model in Fig 6.1d with a crystal rotation of ϕ=45 °. a) Stress field for pure thermal loading for the model in Fig 6.1d with a crystal rotation of ϕ=45 °. b) Stress field for pure centrifugal loading. c) Stress field for combined loading. d) Stresses at the outer rim of the film hole for combined loading. e) Stresses at the impingement hole for combined loading. f) Stresses at the inner pedestal fillet for combined loading. In a-c the absolute max principal stress is plotted, whereas in d-f the max absolute resolved shear stress is plotted.

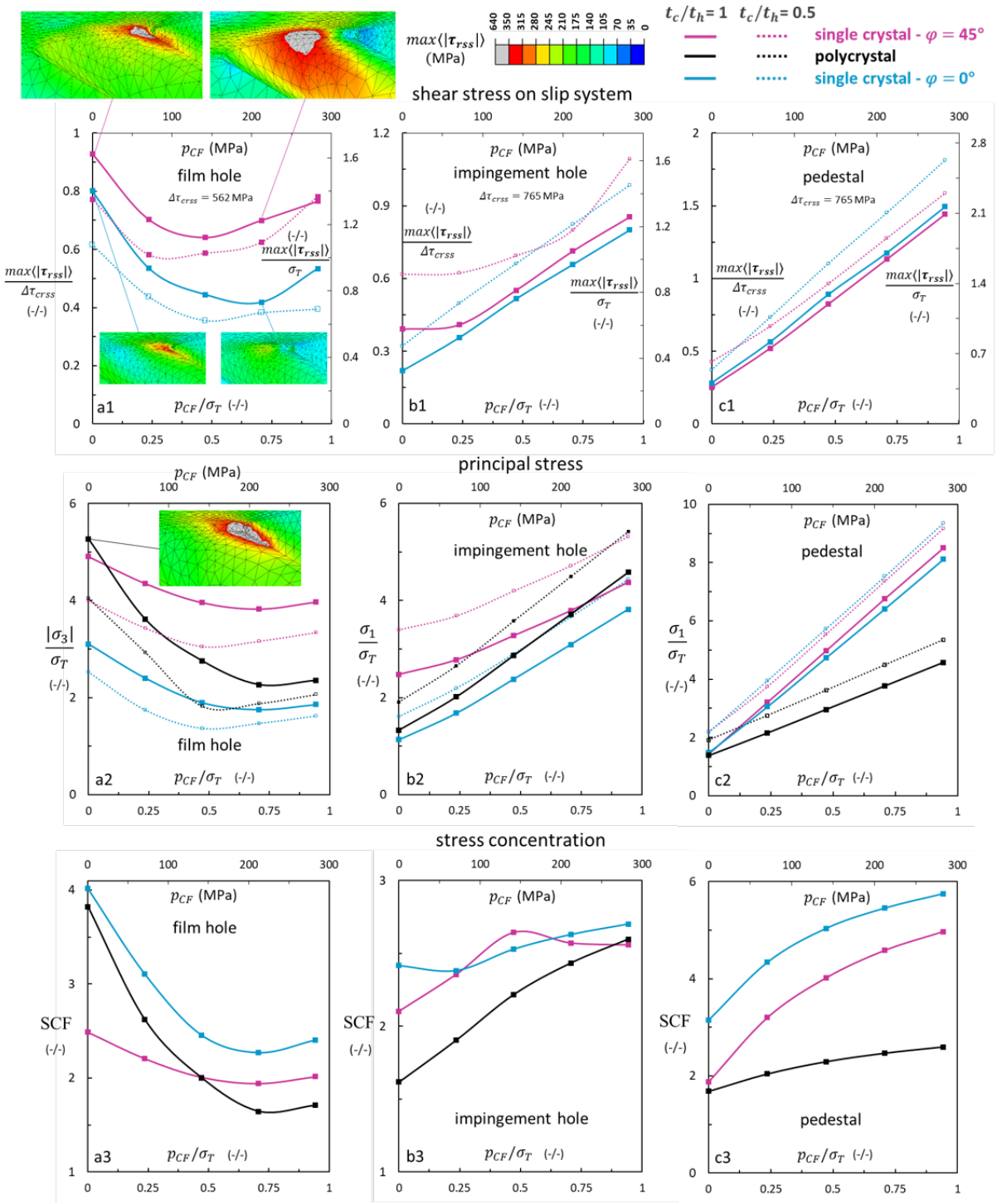


Figure 6.11: Variation of stress quantities (vertical axes) with respect to centrifugal stress p_{CF} and centrifugal-thermal loading ratio, p_{CF}/σ_T, (two horizontal axes on each graph); two wall thickness ratios, t_c/t_h, and two single crystal orientation angles, ϕ, are considered, along with the case of a polycrystal. In a1-c1 the normalised values of max absolute resolved shear stress (RSS) are plotted for critical locations at the film hole, impingement hole and pedestal. For the same critical locations, a2-c2 plot the normalised values of the principal stress with max magnitude, $|\sigma_3|$ or σ_1, whereas a3-c3 plot the stress concentration factor (SCF) as defined by Eqs 4a-c.

In order to interpret these effects we can consider that $max\langle|\tau_{\mathbf{rss}}|\rangle$ scales with the peak compressive stress magnitude, $|\sigma_3|$, at the film hole and the peak tensile stress, σ_1, at the impingement hole and the pedestal. Both $|\sigma_3|$ and σ_1 are found to: a) occur at approximately the same location at each feature as the peak value of $max\langle|\tau_{\mathbf{rss}}|\rangle$ (not shown), and b) to vary in a similar manner with respect to the p_{CF}/σ_T and t_c/t_h ratios as well as the rotation, φ. We also note that the elastic stress state at the locations of the peak stress at the holes is effectively uniaxial and involves a principal stress in the x-z plane which is tangent to the circumference of the rim of each hole, i.e. $\sigma_1, \sigma_2 \approx 0$ at the film hole (compression) and $\sigma_2, \sigma_3 \approx 0$ at the impingement hole (tension). In contrast, the pedestal fillet experiences a biaxial state as the σ_1 component (which is transversely tangent to the fillet in Fig 6.10f) is accompanied by a σ_2 component which is circumferentially tangent to the filleted corner. All the above suggest that the $max\langle|\tau_{\mathbf{rss}}|\rangle$ results can be interpreted based on the $|\sigma_3|$ behaviour at the film hole and the σ_1 behaviour at the impingement hole and pedestal.

In order to fully explain the effects described in A, B and C, we note that $|\sigma_3|$ and σ_1 can be expressed as:

$$\begin{aligned} \text{film hole:} \quad & |\sigma_3| = |\sigma_{hx}(y=-t_h/2)| \bullet SCF_{film} \quad (a) \\ \text{impingement hole:} \quad & \sigma_1 = max\langle\sigma_{cx},\sigma_{cz}\rangle \bullet SCF_{imp} \quad (b) \\ \text{pedestal:} \quad & \sigma_1 = \sigma_{cz} \bullet SCF_{ped} \quad (c) \end{aligned} \tag{6.7}$$

where σ_{cx}, σ_{cz} are the nominal cool wall stresses and $\sigma_{hx}(y=-t_h/2)$ is the nominal stress at the outer surface of the hot wall (all determined theoretically in Section 6.2.4.3) and SCF represents the stress concentration factor, which is determined from the FE simulations and is plotted in Fig 6.11. Each term in Eqs 6.7a-c accounts for global effects that apply to both single crystals and polycrystals, as well as anisotropic effects that apply only for a single crystal and scale with the Zener factor, A. The global effects related to the nominal stresses are:

(a) The σ_z/σ_x ratio increases with p_{CF}/σ_T in the cool wall and decreases in the hot wall (σ_x is independent of p_{CF}/σ_T).

(b) A lower t_c/t_h ratio reduces both $|\sigma_x|$ and $|\sigma_z|$ in the hot wall at the cost of increasing the corresponding nominal stresses in the cool wall; this explains the effect observed in all the Figs 6.11a1-c1 and 6.11a2-c2 described in A.

The anisotropic effect for the nominal stresses is that the rotation, φ, decreases $sigma_z/\sigma_x$ in both walls by increasing $|\sigma_x|$; this is because σ_x aligns with the compliant 100 direction for $\varphi = 0^\circ$ and with the stiff 110 direction for $\varphi = 45^\circ$, whereas $|\sigma_z|$ here always aligns with 100. The increase of $|\sigma_x|$ is the major contributor to the effect observed in Figs 6.11a1-b1 and Figs 6.11a2-b2 described in B with regards to hole stresses.

The global effects related to SCF that are insensitive to the degree of anisotropy are:

1. For an equibiaxial stress field, i.e. σ_z/σ_x= 1, the SCF is maximum at the vertex of the elliptical rim of the film hole in the x-z plane (Fig 6.10d) and minimum at the co-vertex, whereas SCF is uniform along the circular rim of the impingement hole.

2. The increase of σ_z/σ_x in the cool wall due to increasing p_{CF}/σ_T, increases the maximum SCF at the pedestal filleted corner (see Fig 6.11c3) and the impingement hole (see Fig 6.11b3) at which the critical location moves to point 1 shown in Fig 6.10e; this explains the effect observed in Figs 6.11b1-c1 and 6.11b2-c2 described in C with regards to the impingement hole and pedestal. In contrast, the decrease of σ_z/σ_x with increasing p_{CF}/σ_T in the hot wall reduces the SCF at the vertex of the film hole and increases the SCF at the co-vertex, i.e. the location of the maximum SCF departs from the vertex and moves towards the co-vertex (see contours attached in Fig 6.11a1); this results in a large reduction of the SCF at the critical location as p_{CF}/σ_T increases (see Fig 6.11a3), followed by an increase of SCF at large p_{CF}/σ_T values. This phenomenon explains the effect observed in Figs 6.11a1 and 6.11a2 with regards to the film hole described in C.

The anisotropic effect with regards to the SCF is that the SCF increases at locations where the principal stress direction aligns with secondary crystallographic directions. For example, when $\varphi = 0^\circ$ the σ_1 stress along the impingement hole circumference aligns with the 100 crystal axes at points 1, 3 and with 110 (the stiffest direction) at point 2 (see Fig 6.10e); as a result for p_{CF}/σ_T= 0 the maximum SCF occurs at point 2 and is higher than the SCF corresponding to

a polycrystal material (shown in Fig 6.11b3), by a degree which depends on the Zener factor, A. When, $\varphi = 45°$, σ_1 aligns with 100 at point 1, with 110 at point 3 and with 111 at point 2 (points denoted in Fig 6.11e); therefore the maximum SCF occurs again at point 2, followed by a lower value at a point 3 and an even lower one at point 1. The same effects apply at the film hole with the difference here being that, due to the ellipticity and inclination, the location of the maximum SCF tends to be near the vertex; nevertheless, we generally find that even when $\varphi = 0°$ and $p_{CF}/\sigma_T = 0$, the higher stiffness along 110 causes the location of the maximum SCF to slightly depart from the vertex, where it occurs for a polycrystal (compare contours between Figs 6.11a1 and Fig 6.11a2). Regarding the pedestal, the σ_1 stress in Fig 6.10f aligns with 110 and 111 for $\varphi = 0°$ and $\varphi = 45°$, respectively; despite this, the SCF in Fig 6.11c3 is lower for $\varphi = 45°$, which is attributed to the significantly lower value of σ_z/σ_x [108].

6.2.5 Evaluation of results

We now evaluate all our results and discuss their significance. A key highlight is that a DWTC system with large outer wall porosity (large film hole density) provides a high cooling effectiveness at moderate mass flow rates, allowing for theoretical transpiration cooling to be approached. In particular, a high porosity enhances convective cooling along the film hole surfaces, gives the component effective cooling near the external surface and reduces the temperature difference between the outer and inner wall. The outer wall porosity of 19.2% in the geometry analysed here (Fig 6.2 a1) leads to total thermal differences across the two walls in the range 190–130 °C, which is a significant advancement when compared to values of 270 °C reported previously [108] for a system with an outer wall porosity of 10% (Fig 6.2 a2). By also considering that thermal stresses are driven by these thermal differences and that the presence of film holes reduces the apparent elastic stiffness of the outer wall, we can argue that a high porosity simultaneously offers substantial improvements in mechanical performance. However, there remain aspects requiring further consideration, such as the impact of film hole density and coolant mass flow rate on aerodynamic penalty [125] and engine efficiency [54, 126] and potential fatigue cracking events due to crystallographic slip caused by narrow spacing between film holes [127, 128]. Contrary to these former reports, the current study shows that a close proximity of film holes does not cause elevated shear stresses at the ligament sections between

holes, which may be due to the fact that previous papers only considered transverse film holes and uniform uniaxial loading. Despite our results encouraging the use of high film hole density, they only account for an elastic material response, suggesting that further validation is required in the elasto-plastic-creep regime. This will be explored more fully in a future publication.

We should recognise here that the above structural performance benefits of high outer wall porosity are considered to arise by the reduction of thermal stresses alone, on the basis that in double wall blades these stresses dominate over mechanical stresses induced by centrifugal and/or aerodynamic loading [108, 117]. However, based on the current film hole arrangement, when the outer wall porosity is as high as 19.2% (Fig 6.2a1) the nominal centrifugal stress can increase by a factor of 2.73 due to a drastic reduction in the net cross section of the walls in the streamwise direction of the blade (explained in Appendix D); the factor reduces to only 1.45 for a porosity of 10% (Fig 6.2a2). Thus, for an engine operating at 12000 rpm and for the geometric parameters of Table 1, we predict (using the scheme in Appendix D) that the root of the blade will experience a nominal centrifugal stress of 310 MPaa with a net-section stress of 847 MPaa for 19.2% porosity (Fig 6.2a1) and a net-section stress of only 450 MPaa for 10% porosity (Fig 6.2a2). These values can be overly conservative, in that traditional blade designs involve an increasing wall thickness towards the blade root [129], but concerns arise regarding the integrity of the high porosity system at high engine speeds. Locally, fatigue is a major concern since the net stress will be scaled further by a large stress concentration factor at the hole and pedestal features. Globally, high mechanical stresses can activate ratchetting mechanisms (incremental plastic collapse of the whole structure within a small number of cycles), especially for the out-of-phase thermomechanical cycling typically experienced in turbine blades [130]. Another potential global failure mechanism is the continuous accumulation of tensile creep deformation during the high temperature stage of each loading cycle. All the above suggest that high outer wall porosity systems can drastically reduce thermal stresses but at the detriment of elevated mechanical stresses which can give rise to additional failure modes in addition to fatigue. These mechanical stresses, however, can be mitigated by using alternative film hole arrangements that reduce the net wall section in the streamwise direction.

An additional characteristic of the high outer wall porosity DWTC system considered here is that the impingement jet becomes a secondary cooling mechanism, providing the system with redundancies. As an example, particle blockage may be induced by volcanic ash [64] or dust [131] reducing the film effectiveness as well as internal convective cooling of an individual film hole. However, this could be partially compensated by nearby film holes which will have a greater share of mass flow, elevating their contribution to film and convective cooling. Furthermore, any increase in metal temperatures may be limited by the impingement jet and other internal surfaces, i.e. pedestals. These features become increasingly important as small film hole diameters have increased susceptibility to blockage from external deposition. Further research should look to understand the likelihood of blockage and how impactful such events would be.

In terms of internal cooling features, a key highlight of our results is that despite a reduction of wall spacing/pedestal height promotes impingement cooling and reduces the outer-inner wall thermal difference at low coolant flow rates, it has a negative influence on the coolant flow distribution to the film holes and significantly enhances the risk of hot gas ingestion. This must be avoided as the internal surfaces would not be protected by a thermal barrier coating and therefore would be susceptible to oxidation and thermal fatigue. It is also worth considering that in this study a constant external pressure was applied to the outlets, whereas in reality a pressure gradient would be present on the external blade surface. A positive pressure gradient from leading to trailing film hole will further reduce the mass flow to the leading film holes and is likely to exasperate the poor flow distribution. Consequently, we argue that the reduction of outer-inner wall thermal difference associated with short pedestals is outweighed by the risk of hot-gas ingestion, and thus the pedestals should generally be of sufficient length in practice to prevent ingestion. Future research may look into identifying the minimum wall spacing/pedestal height for which hot-gas ingestion is avoided, given a film hole arrangement.

It is emphasised here again that given a temperature field the pedestal height does not influence thermal stresses, as explained in [103] based on the kinematics of a turbine blade; it can only influence aerodynamic bending stresses but these are much smaller than thermal stresses, par-

ticularly in double wall turbine blades [108]. This implies that from a mechanical point of view, pedestal height is a secondary design variable. The wall thickness ratio, on the other hand, has a drastic influence on the thermal stress field and is the most significant design variable when it comes to structural integrity, along with the geometry of the film holes (inclination, shape). Our results show that varying the inner wall thickness for a constant outer wall thickness has a small influence on the aerothermal field, suggesting that designers can consider this to be a flexible constraint. Our results for an anisotropic material are consistent with previous recommendations based on isotropic materials, in that the inner wall thickness should be minimised to reduce thermal stresses at the film holes where the largest potential for fatigue cracking is displayed [109]. It is important, nevertheless, to determine the lower threshold for such a reduction given the inevitable increase of tensile thermal stresses at the impingement hole and pedestal fillet. In particular, we have shown here that a low inner wall thickness combined with severe centrifugal loading (along with thermal loading) can lead to severe tensile stresses and therefore reverse plasticity in a pedestal with a very sharp fillet (radius 30 μm); however, this represents an extreme stress concentration case and is deliberately used here in order to study the implications of poor manufacturing. In practise, a larger fillet radius is expected to result in a drastically lower stress concentration [103], giving enough room for reducing the inner wall thickness for the purpose of improving the fatigue performance at the film holes. An elasto-plastic-creep FE analysis will help verify this argument.

We have not explored film hole geometry effects in this study, but we have identified an important anisotropic effect of relevance to the relation between hole shape and fatigue. We have shown that the critical stress at the vicinity of a hole has the tendency to occur at the location where the principal stress direction aligns with the stiffest crystallographic direction. As a result, the critical location for fatigue changes significantly depending on the biaxial wall nominal stress ratio, i.e. the thermal-centrifugal load combination, especially along a non-circular hole rim, e.g. the elliptical rim of the currently used film holes. This makes it difficult for a designer to know the exact critical location without performing FE analysis for the particular loading combination of interest. In a previous study [110] we recommended reducing the degree of ellipticity of the film hole rim (the intersection between an inclined cylinder and the plane of the

wall) in order to reduce stress concentration at the vertex (at the cost of increasing stress concentration at the co-vertex); however, this concerned pure thermal loading and isotropic elasticity where the critical fatigue location always lies at the elliptical vertex. In practise, the new results here suggest that ellipticity should not be reduced in cases of high centrifugal loading because the highest stresses occur at the elliptical co-vertex rather than the vertex. This implies that the optimal film hole shape may vary along the length of the turbine blade, i.e. between a circular rim near the blade tip (zero centrifugal stresses) and an increasingly elliptical rim towards the blade root (maximum centrifugal stresses). It should be acknowledged, however, that modifying the film hole shape for optimal fatigue performance will generally require considerations not only of the elastic anisotropy but also the creep-plastic anisotropy of the material [132].

6.2.6 Conclusions

In this paper a computational methodology for the aerothermal and mechanical design of double wall transpiration cooled (DWTC) systems for gas turbine blades and a range of high temperature thin walled components has been presented.

We find that systems of high film hole density (high wall porosity) result in a better cooling efficiency and thermal stress performance compared to previously studied DWTC systems of modest outer wall porosity. However, depending on the film hole arrangement they can result in an elevation of mechanical stresses arising from centrifugal loading due to a reduction in the net wall section. In particular, cooling effectiveness values of over 0.8 were observed on the external hot surface and in some places theoretical transpiration was achieved. Such systems represent a clear advance in the development of efficient cooling systems for turbine blades, although further research on blockage, pressure margin and flow migration are required.

In terms of geometric effects, we find that connecting the two walls with short pedestals enhances the internal impingement cooling but at a higher risk of hot gas ingestion; it is therefore suggested that the pedestals should be short, but long enough to avoid such effects. The inner wall thickness, on the other hand, is shown to have less impact on the aerothermal response, giving designers the freedom to reduce inner wall thickness for the scope of reducing thermal stresses in the more critical outer wall, thus improving the mechanical performance at the film holes.

The stress concentration at the film hole, impingement hole and pedestal fillets is influenced by several effects that can either be termed global and independent of the anisotropic properties of the material or depend on the anisotropic nature of the material response. Anisotropy increases significantly the difficulty in predicting the critical hot spot stress location at the film holes, adding complexity to the task of optimising film hole shape for optimal fatigue performance. Crystal orientation is shown to have little influence on pedestal stresses as opposed to impingement hole stresses and especially film hole stresses, which show a strong influence.

Despite the principal axis of single crystal gas turbine blades being in alignment with the compliant ⟨100⟩ crystallographic direction, it is highlighted that local stresses at features, e.g. holes and pedestals, will inevitably occur along the stiffer, secondary crystallographic directions, e.g. ⟨⟨110⟩ and ⟨111⟩.

The methodology and results presented in this paper aim to facilitate the implementation of the DWTC technology in turbomachinery and other high temperature applications.

Acknoledgements

The work was supported by EPSRC programme grant EP/P000878/1, with further support from Rolls-Royce PLC. Dr Alex Murray is acknowledged for useful discussions on the aerothermal aspects and Dr Nicolo Grilli for useful discussions on crystal anisotropy

Appendix A. Details on aerothermal analysis steps

A1. Internal CDF analysis

The important outputs of the CFD analysis are the coolant velocity, v_f, and temperature at each film hole exit, $T_{f,outlet}$. An unstructured mesh is used with fifteen prism layers along fluid-solid interfaces with an overall height of 0.1 mm and a growth rate of 1.2, to keep the non-dimensional wall height, $y^+ \leq 1$. The solver is pressure-based and uses the realizable $k-\varepsilon$ turbulence model, with enhanced wall function and thermal effects enabled. Air is treated as an ideal gas for the fluid domain with thermal conductivity and viscosity evaluated by kinetic theory and the Sutherland method, respectively. The role of radiative heat flux has not been considered in the present study, since the emphasis here is placed on understanding the role of internal features on the aerothermal and mechanical performance based on a fixed heat load. We can therefore reasonably assume here that the magnitude of the heat load i.e. whether radiation heat flux is combined with convective heat flux, will not alter our conclusions. It can be also noted that in the study by Li et al. [133], the radiative error, i.e. the ratio of external radiative heat flux compared to the total heat flux applied onto the hot wall (q_{rad}/q_{tot}) for pure air was between 5 and 10 % for a temperature ratio, T_∞/T_c, in the range 1.75 – 2; in this study T_∞/T_c =

1.8 and therefore the error can be assumed to be small.

A2. Modified Goldstein-Sellers method

Goldstein's [26] empirical formulation of film effectiveness, $\breve{\eta}_{f,i}$, concerns a single film jet and provides the shape and strength of heat protection as a function of the blowing ratio, M, i.e. $\breve{\eta}_{f,i} = \breve{\eta}_{f,i}(M,\xi,\zeta)$ where ξ, ζ are streamwise and spanwise positions with respect to the film hole. Firstly, the coolant exit velocity at each hole, v_f (provided by CFD) and the blowing ratio, M are passed into the modified Goldstein equation [26]:

$$\breve{\eta}_{f_i}(M,\xi,\zeta) = \frac{M v_{film} D_{film}}{8\alpha_t \left(\frac{\xi}{D_{film}} + \xi_{film}\right)} \exp\left[-\left(\frac{\zeta}{c_1}\right)^{c_2}\right] \tag{6.8}$$

The turbulent diffusivity α_t and variable ζ_{decay} are dependent on M, and values for these are based on experimental and correlation data (Murray et al. [10]. and Baldauf et al. [98]). The referenced studies were also used to find the variables influencing the spanwise decay and shape, c_1 and c_2, which are dependent on M, ξ. The coolant temperature at the film hole exit, T_f (provided by CFD) along with $\breve{\eta}_{f,i}(M,\xi,\zeta)$ are then used in:

$$\eta_{f,i}(\xi,\eta) = \breve{\eta}_{f,i}(M,\xi,\zeta)\frac{T_\infty - T_f}{T_\infty - T_c} \tag{6.9}$$

The film effectiveness in an array of cooling holes where interactions of film jets come into play is then found by Sellers' superposition equation [78]:

$$\eta_f(x,y) = 1 - \prod_{i=1}^{n}\left(1 - \eta_{f,i}(x,y)\right) \tag{6.10}$$

where the local positions ξ,ζ are transformed into global positions x,y. The adiabatic temperature field is finally determined by:

$$\eta_f(x,y) = \frac{T_\infty - T_{aw}(x,y)}{T_\infty - T_c} \tag{6.11}$$

In this way the aerothermal field output from a repeating unit-cell can be extended to the enlarged domain shown in Fig 6.2 c.

A3. FE heat transfer analysis

The full domain use seven repeating unit-cells attached to an upstream and downstream flange section and is solved in ANSYS Mechanical using results from the CFD as well as the empirically found film effectiveness. Wall temperatures and heat fluxes are exported from the unit-cell CFD to a Matlab program to determine the surface heat transfer coefficients, h , based upon wall temperature, T_w, inlet coolant temperature, T_c, and the wall heat flux, q, through the relation $h = q/(T_w - T_c)$. These values are extended from a single unit-cell to the unit-cell repeating area and exported as boundary conditions into ANSYS Mechanical alongside T_{aw} and h for the hot-side surface calculated by the film effectiveness methodology. The film effectiveness applied here is assumed to be the middle cell of three unit-cells in the spanwise direction. As such, the film superposition has lateral influence from adjacent unit-cells. The upstream and downstream plate extents are assumed to be perfectly insulated. Internal walls outside the repeating blocks are given the area-average of the CFD results for that component feature. As an example, the pedestals would take the area-averaged heat transfer coefficient observed in the unit-cell as calculated by $h = q/(T_w - T_c)$. Finally, with all inputs provided, the FEA solver calculates the temperature field for all solid surfaces throughout the domain.

This method represents a numerically efficient scheme for solving complex internal cooling geometries, but the fluid and solid domains are inherently decoupled. This occurs in two ways, firstly the films are not modelled in the CFD and therefore there is no external cooling effect. Secondly, in the FEA the internal fluid and wall temperatures are decoupled. In the first instance the film effectiveness is underestimated as T_f will be higher from the unit-cell CFD than if films were applied. In the second instance the internal heat transfer will have an associated error given that in the FEA the film effectiveness is applied but not in the unit-cell domain. Although the flow field is not likely to be significantly altered due to changes in wall temperature and therefore the calculated heat transfer coefficients should be representative. These differences were studied in [89] where it was highlighted that in situations with high film effectiveness an under prediction of the cooling effectiveness occurs, compared to a fully coupled methodology.

Appendix B. Transformation from crystal system to global system

The relationships between the three elastic moduli and three compliance constants are:

$$S_{11} = \frac{C_{11}+C_{12}}{(C_{11}-C_{12})(C_{11}+2C_{12})},\ S_{12} = -\frac{C_{12}}{(C_{11}-C_{12})(C_{11}+2C_{12})},\ S_{44} = \frac{1}{C_{44}} \quad (B1)$$

The compliance matrix is:

$$\mathbf{S} = \begin{bmatrix} S_{11} & S_{12} & S_{12} & 0 & 0 & 0 \\ S_{12} & S_{11} & S_{12} & 0 & 0 & 0 \\ S_{12} & S_{12} & S_{11} & 0 & 0 & 0 \\ 0 & 0 & 0 & S_{44} & 0 & 0 \\ 0 & 0 & 0 & 0 & S_{44} & 0 \\ 0 & 0 & 0 & 0 & 0 & S_{44} \end{bmatrix} \quad (B2)$$

The transformation from the crystal system to the blade system based on the sequence of φ, θ, ψ rotations is given by the matrix:

$$\mathbf{T} = \begin{bmatrix} cos\varphi & -sin\varphi & 0 \\ sin\varphi & cos\varphi & 0 \\ 0 & 0 & 1 \end{bmatrix} \bullet \begin{bmatrix} 1 & 0 & 0 \\ 0 & cos\theta & -sin\theta \\ 0 & sin\theta & cos\theta \end{bmatrix} \bullet \begin{bmatrix} cos\psi & -sin\psi & 0 \\ sin\psi & cos\psi & 0 \\ 0 & 0 & 1 \end{bmatrix} \quad (B3)$$

For column vector operations, **T** must be expanded into:

$$\bar{\mathbf{T}} = \begin{bmatrix} {T_{11}}^2 & {T_{12}}^2 & {T_{13}}^2 & 2T_{12}T_{13} & 2T_{11}T_{13} & 2T_{11}T_{12} \\ {T_{21}}^2 & {T_{22}}^2 & {T_{23}}^2 & 2T_{22}T_{23} & 2T_{21}T_{23} & 2T_{21}T_{22} \\ {T_{31}}^2 & {T_{32}}^2 & {T_{33}}^2 & 2T_{32}T_{33} & 2T_{31}T_{33} & 2T_{31}T_{32} \\ T_{21}T_{31} & T_{22}T_{32} & T_{23}T_{33} & T_{22}T_{33}+T_{23}T_{32} & T_{21}T_{33}+T_{23}T_{31} & T_{21}T_{32}+T_{22}T_{31} \\ T_{11}T_{31} & T_{12}T_{32} & T_{13}T_{33} & T_{12}T_{33}+T_{13}T_{32} & T_{11}T_{33}+T_{13}T_{31} & T_{11}T_{32}+T_{12}T_{31} \\ T_{11}T_{21} & T_{12}T_{22} & T_{13}T_{23} & T_{12}T_{23}+T_{13}T_{22} & T_{11}T_{23}+T_{13}T_{21} & T_{11}T_{22}+T_{12}T_{21} \end{bmatrix} \quad (B4)$$

where T_{ij} are the components of **T** computed from Eq B3.

Appendix C. Volume averaged elastic properties for a polycrystal

Voigt proposed that the shear modulus of a polycrystalline material can be found by averaging the stress expressions for a given strain over all possible directions in a single crystal, whereas Reuss proposed that the relations expressing strain for a given stress should be averaged, giving the following results:

$$\bar{G}_{Voigt} = \frac{C_{11} - C_{12} + 3C_{44}}{5} \qquad (C1)$$

$$\bar{G}_{Reuss} = \frac{5C_{44}\left(C_{11} - C_{12}\right)}{4C_{44} + 3\left(C_{11} - C_{12}\right)} \qquad (C2)$$

where $\bar{G}_{Voigt}$ and $\bar{G}_{Reuss}$ overpredict and underpredict the true shear modulus as they assume uniform strain and uniform stress through the polycrystal, respectively. Hill showed that the reality lies between the above extremes, such that the true modulus is very closely approximated by the average, $\bar{G}_{Hills} = \left(\bar{G}_{Voigt} + \bar{G}_{Reuss}\right)$. By using $\bar{G}_{Hill}$ and the Bulk modulus, $B = \left(C_{11} + 2C_{12}\right)/3$, the volume averaged Poisson's ratio and Young's modulus are then computed by:

$$\bar{\nu} = \frac{3B - 2\bar{G}_{Hill}}{2\left(3B + \bar{G}_{Hill}\right)} \qquad (C3)$$

$$\bar{E} = 2G(1 + \bar{\nu}) \qquad (C4)$$

Appendix D. Calculation of net centrifugal stress $p_{CF\,net}$

We adopt the calculation scheme previously described in [108]. This involves an initial calculation of the centrifugal (CF) stress, $p_{CF} = \left(\rho + \rho^*\right)\omega^2 \widetilde{L}_x$, carried by the gross cross section of the walls, where ρ is the material density (kg/m^3), ω is the turbine rotational speed (rad/s) and $\widetilde{L}_x = L_x\left(R_{tip} - 0.5L_x\right)$ is a function of the distance, L_x (mm), between the blade tip and the blade location of interest as well as the distance, R_{tip} (mm), between the blade tip and the engine axis; ρ^* (kg/m^3) is an 'equivalent' density determined by $\rho^*\omega^2\widetilde{L}_x = \left(F_{ped} - F_{holes}\right)/S$, which can increase or decrease p_{CF} (MPa) depending on whether the centrifugal (CF) force added by the total inertia of pedestals, F_{ped}, (from the blade tip to the blade location of interest) is larger or smaller than the CF force deduced by the total volume of holes, F_{holes} (from the blade tip to the blade location of interest); $S = s\left(t_h + t_c\right)$ denotes the gross section of the walls (mm^2)

for a unit cell length, s (mm), along the x axis (Fig 6.1d). In Fig 6.1d there exist four planes where pedestals are repeated (pedestal centreline distance along z axis is here equal to the unit cell width w) and one plane where pedestals are repeated every $2w$ in order to accommodate the impingement hole. This gives [108]:

$$F_{ped} = \rho\ \omega^2 V_{ped} \left\{ 4\frac{L_x}{w}\left[R_{tip} + 0.5\left(w - L_x\right)\right] + \frac{L_x}{2w}\left[R_{tip} + 0.5\left(2w - L_x\right)\right] \right\} \qquad (D1)$$

Impingement holes are repeated every $2w$ in a single plane of Fig 6.1d, whereas an equivalent of four film holes is repeated every w, and another four film holes every $0.5w$, giving [108]:

$$\begin{aligned} F_{holes} = {} & \rho\ \omega^2 V_{imp} \frac{L_x}{2w}\left[R_{tip} + 0.5\left(2w - L_x\right)\right] \\ & + 4\ \rho\ \omega^2 V_{film} \left\{ \frac{L_x}{w}\left[R_{tip} + 0.5\left(w - L_x\right)\right] + \frac{L_x}{0.5w}\left[R_{tip} + 0.5\left(0.5w - L_x\right)\right] \right\} \end{aligned} \qquad (D2)$$

Pedestal, impingement hole and film hole volumes are respectively given by $V_{ped} = H{D_{ped}}^2$, $V_{imp} = 0.25\pi t_c {D_{imp}}^2$ and $V_{film} = 0.25\pi t_h {D_{film}}^2 / cos^2\gamma (\gamma = \pi/3 rad)$. The cross sections removed by the presence of impingement and film holes at the $\bar{z} =$ 1 plane are $S_{imp} = D_{imp} t_c$ and $S_{film} = D_{film} t_h / cos^2\gamma$, such that the net centrifugal stress applied as a boundary where load is prescribed in the FE model is $p_{CF\,net} = p_{CF} S / \left(S - S_{imp} - 2S_{film}\right)$. Note that there exist two planes in Fig 1d in which a section equivalent to four film holes is removed, such that the maximum net stress is $p_{CF\,netMax} = p_{CF} S / \left(S - S_{imp} - 4S_{film}\right)$. If $F_{walls} = \rho\omega^2 \widetilde{L}_x S$ is the CF force associated with the inertia of the walls, then for Fig 6.1 d (or Fig 6.2 a1) and the dimensions given in Table 6.1 we get $F_{ped}/F_{walls} \approx 0.22$ and $F_{holes}/F_{ped} \approx 0.92$, implying that the total inertia of pedestals acts to increase p_{CF} by 22% but due to the high density of film holes 92% of this increase is cancelled. In contrast, the system studied previously in [108] and shown here in Fig 6.2 a2 ($D_{film} = D_{imp} = D_{ped} = t_h = t_c =$ 1 mm, s= 8 mm, w= 4 mm) corresponds to $F_{ped}/F_{walls} \approx 0.048$ and $F_{holes}/F_{ped} \approx 0.72$. The key difference is that the system in Fig 6.2 a2 gives $p_{CF\,netMax} = p_{CF\,net} = 1.45 p_{CF}$ whereas Fig 6.2 a1 gives $p_{CF\,netMax} = 2.73 p_{CF}$.

Appendix E. Calculation of material yield stress range $\Delta\tau_{\mathbf{crss}}$

We consider the monotonic stress-strain experimental data obtained by Allan for CMSX-4 [134] for a macroscopic strain rate of 10^{-4}/s. We assume here that plasticity is driven only by the 12 octahedral slip systems $\{111\}\langle 110\rangle$ and that the yield strength is rate independent and pressure independent i.e. equal between tension and compression. Given that the Schmid factor associated with $\{111\}\langle 110\rangle$ slip is small for macroscopic loading along the $\langle 111\rangle$ direction and that in most cases stresses at holes and pedestals occur near the $\langle 110\rangle$ direction, we calculate the critical resolved shear stress range, $\Delta\tau_{crss}$, based on the macroscopic yield stress data for $\langle 110\rangle$ oriented crystals [134]. By taking the average data between compression and tension, the room temperature yield strength used here is $\sigma_{y\langle 110\rangle}$= 1100 MPaa; multiplying by the Schmid factor of 0.4082 gives the room temperature critical resolved shear stress, τ_{crss0}= 450 MPaa. The strength decreases to $\sigma_{y\langle 110\rangle}$= 700 MPaa at 1000 °C and $\sigma_{y\langle 110\rangle}$= 440 MPaa at 1100 °C, which respectively correspond to the temperatures at the internal features (impingement hole and inner pedestal fillet) and external features (film hole) at full loading; this implies critical resolved shear stresses of τ_{crssT}= 286 MPaa and τ_{crssT}= 180 MPaa at internal and external features at high temperature and yield stress ranges of $\Delta\tau_{crss}$= 736 MPaa and $\Delta\tau_{crss}$= 630 MPaa, respectively.

6.3 Further Investigation

The importance of the outer and inner wall spacing alongside the film hole proximity to the impingement jet stagnation point were investigated for a specified highly porous geometry. A further geometric variation was considered to assess how changes to the film hole proximity may impact these findings. The HS2 (T1) domain studied in Chapter 8 was used as a point of comparison to the study in the above journal paper. A brief overview of the domain is presented and the results of the study, which used the same methodology as detailed in Section 6.2.2.1, are discussed.

6.3.1 Domain

The geometry of interest had a hole diameter double that of the previous study with the same non-dimensional spacing. Additonanlly the impingement jets had double the spacing, but with a larger diameter to maintain the same jet velocity at a given flow rate. Therefore the ratio of film holes to impingement holes is maintained, however an important difference is that for HS2 (T1) no film holes are located in direct proximity to the impingement jet stagnation region. Four pedestal heights and three innerskin thicknesses were chose to represent a wide range to assess the impact on the aerothermal characteristics. Geometry parameters are tabulated in Table 6.3 and annotated in Figure 6.12, and variation in pedestal height visualised in Figure 6.13.

D_f	0.4 mm
D_i	0.5 mm
L_p	0.5 mm
L/D_f	10
S_f	3.5 D_f
S_i	11.2 D_i
S_p	2.8 L_p
α	30 °
t_o	2.5 D_f

Variable H_p				
H_p/D_i	0.6	1.6	3.0	5.0
t_i/D_i	2.86			

Variable t_i			
t_i/D_i	1.0	2.0	4.0
H_p/D_i	3.0		

Table 6.3: Geometric parameters

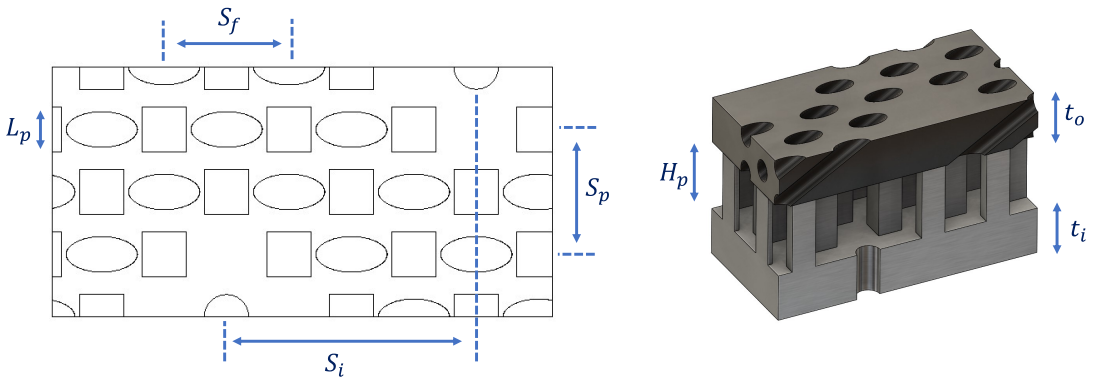


Figure 6.12: Annotated schematic of HS2 (T1)

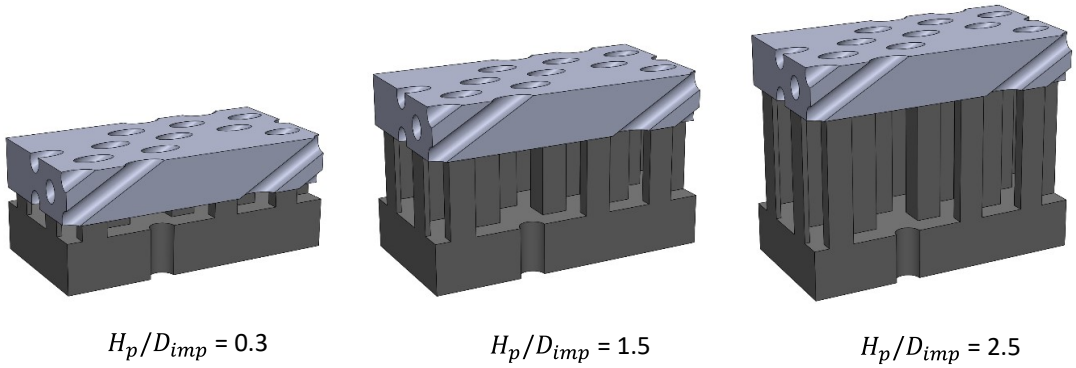


Figure 6.13: Visualisation of the variation in pedestal height for the HS2 (T1) unit-cell.

6.3.2 Results

Mass flow variation between film holes was only moderately observed through the domain. To quantify this finding Figure 6.14 displays the ratio of the minimum mass flow rate of the film holes to the mean mass flow rate, $\frac{min(\dot{m}_{c,ex})}{max(\dot{m}_{c,ex})}$ for both the variation in H_{ped} and t_i. The pedestal height had an moderate influence on the minimum mass flow. For $H_{ped}/D_{imp} \leq 1.6$, $\frac{min(\dot{m}_{c,ex})}{max(\dot{m}_{c,ex})} \approx 0.6$, while for $H_{ped}/D_{imp} \geq 3.0$ a more even distribution was observed with a ratio greater than 0.8. Therefore it can be expected that a reduction in the pedestal height has a detrimental impact on the mass flow distribution to film holes, however hot-gas ingestion is not a concern on these flow conditions, and the levels of variation are not overly-concerning. In contrast, changes in the innerskin thickness, $1.0 \geq t_i/D_{imp} \leq 4.0$, had no noticeable influence on the flow distribution to film holes.

Influence on the impingement and radial jet is shown in Figure 6.16 by velocity vectors overlaid on pressure contours for each geometric configuration. The left column corresponds to increas-

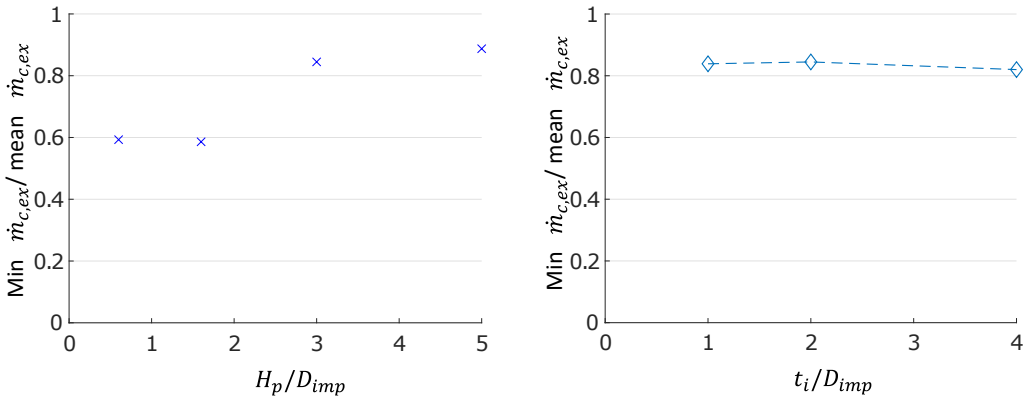


Figure 6.14: Influence of H_p and t_i on the minimum mass flow ratio to any film hole. H_p had a mild influence on the mass flow distribution, while t_i had no significant impact.

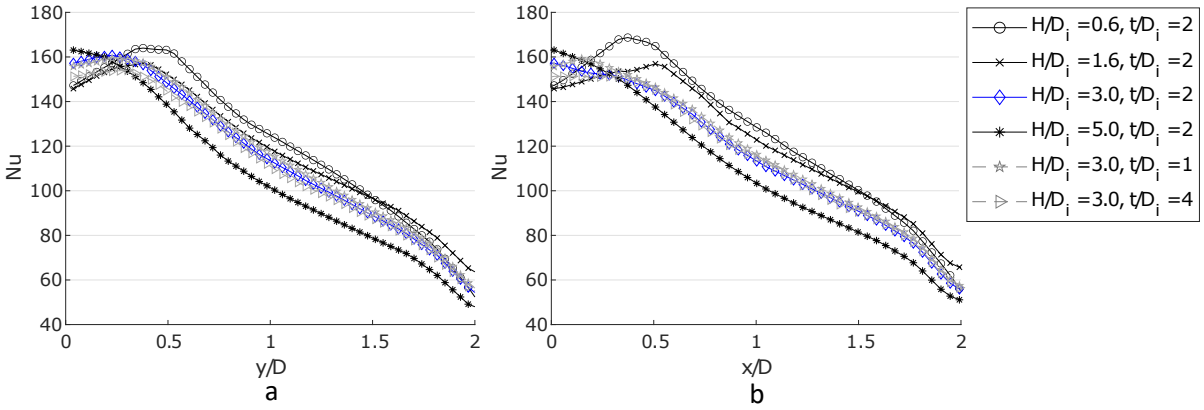


Figure 6.15: Nusselt number at the impingement target surface for: a) y=0 plane b) x=0 plane. For a flow condition of $Re_{imp} = 2.4 \times 10^4$.

ing pedestal height, while the right-hand column is increasing innerskin thickness. For the former a widening radial jet is observed as well as a less pronounced radial jet. Consequently the peak velocity of the impingement jet near the stagnation region is significantly lower for larger pedestal heights. In contrast, from these plots it is difficult to observe any differences as a consequence of changing innerskin thickness.

To confirm these findings and assess thermal impacts, target surface Nu in two radial directions, the planes of $y/D_{imp} = 0$ and $x/D_{imp} = 0$, are given in Figures 6.15 a and b, respectively. In general high heat transfer occurs at the stagnation zone, and this decreases as the flow travels radially outward due to a thickening boundary layer. The influence of innerskin thickness on the impingement heat transfer is made by comparing the two grey lines alongside the blue line. The differences here are minimal. On the other hand, variations can be observed for

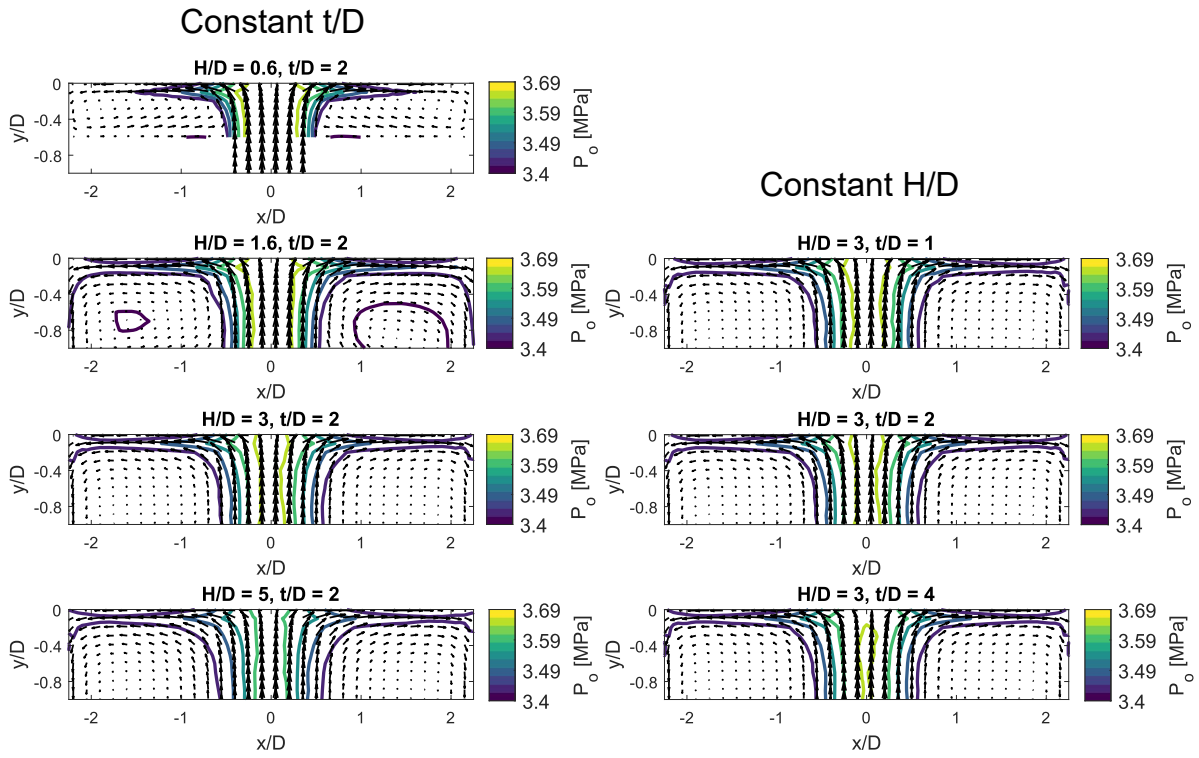


Figure 6.16: Velocity vectors and static pressure contours for a) variable pedestals heights (H_{ped}/D_{imp}) at constant innerskin thickness (t_i/D_{imp}), and b) variable $t_i/Dimp$ at constant H_{ped}/D_{imp}. At a fixed impingement Reynolds number of 2.4×10^4.

changes in pedestal height, as would be expected given the previously mentioned alterations to the impingement jet structure. The baseline geometry corresponding to $H_p/D_{imp} = 3.0$ and $t_i/D_{imp} = 2.0$ had the maximum Nusselt number near the centre of the jet stagnation region, and this is also true for a larger pedestal height, $H_p/Dimp = 5.0$. For the larger pedestal height heat transfer is lower for both radial lines, apart from an elevation within y/D_{imp} and x/D_{imp} < 0.25. In contrast, for a reduction in H_p, Nu is elevated for $x/D_{imp} > 0.3$ with the stagnation peak occurring at $x/D = 0.4$ and $x/D = 0.6$ for H_p/D_{imp} = 0.6 and 1.6 respectively. These findings are similar to those of Choo and Rhee (2001) [112] where a stagnation region peak was observed for H/D of 0.33 and 1.0.

6.4 Summary

Reducing mechanical stresses in a turbine blade is crucial for longevity and reliability of turbine blades. Two geometric parameters, pedestal height and innerskin thickness, were considered in two DWTC designs with high outerskin porosity. It was observed that for double-wall configurations with a ratio of film to impingement holes greater than unity the flow distribution can be significantly altered by the internal structure. A reduction in pedestal height enhanced the internal impingement cooling but increased the variation in mass flow to film holes. For the two geometries analysed, geometry T2 exhibited such large flow variations that reversed flow to some outlets was suspected, indicating the significant risk of hot-gas ingestion. For T1, the reduced proximity of film holes in relation to the impingement jet diminished this effect, but variation in the mass flow between film holes remained, although with reduced magnitude. The innerskin thickness, and therefore the impingement hole aspect ratio, was varied and in both cases there was no significant impact on the flow variation or overall heat transfer.

Given that the pedestal height influences the aerodynamic bending stresses rather than the thermal stresses, and that the former is much lower than the latter, this should be considered a secondary design variable to avoid negative affects to the aerothermal field. On the other hand, the innerskin thickness can be treated as a more flexible constraint, and minimisation of this parameter can reduced thermal stresses.

Statement of Authorship for joint/multi-authored papers for PGR thesis

To appear at the end of each thesis chapter submitted as an article/paper

The statement shall describe the candidate's and co-authors' independent research contributions in the thesis publications. For each publication there should exist a complete statement that is to be filled out and signed by the candidate and supervisor **(only required where there isn't already a statement of contribution within the paper itself).**

Title of Paper	Coupled Aerothermal-Mechanical Analysis in Single Crystal Double Wall Transpiration Cooled Gas Turbine Blades with a Large Film Hole Density.
Publication Status	□Published □ ~~Accepted for Publication~~ □~~Submitted for Publication~~ □~~Unpublished and unsubmitted work written in a manuscript style~~
Publication Details	Courtis, Matthew and Skamniotis, Christos and Cocks, Alan and Ireland, Peter, "*Coupled Aerothermal-Mechanical Analysis in Single Crystal Double Wall Transpiration Cooled Gas Turbine Blades with a Large Film Hole Density*.", Applied Thermal Engineering, 2022, 119329, ISSN 1359-4311. https://dx.doi.org/10.2139/ssrn.4102556

Student Confirmation

Student Name:	Matthew Courtis		
Contribution to the Paper	Thermal work undertaken and analyzed by Matthew Courtis and Stress Analysis by Christos Skamniotis. Details: Section 6.2.2 performing of all numerical work, analysis of results and writing relating to thermal analysis. Shared writing of the introduction 6.2.1 and Evaluation of results 6.2.5 and Conclusions 6.2.6.		
Signature 		Date	07/07/23

Supervisor Confirmation

By signing the Statement of Authorship, you are certifying that the candidate made a substantial contribution to the publication, and that the description described above is accurate.

Supervisor name and title: Peter Ireland, Head of the Oxford Thermofluids Institute		
Supervisor comments		
Signature: 	Date	24/07/2023

This completed form should be included in the thesis, at the end of the relevant chapter.

7 Evaluation of Numerical Methods

7.1 Overview

A preliminary numerical evaluation of the overall cooling performance of two double-wall configurations was made assessing the impact of increased outerskin porosity using the decoupled unit-cell method. And detailing the output of the numerical results. The first main update to this method is then considered in Section 7.3 where the influence of modelling film-hole inclination is discussed. Section 7.4 evaluates a comparison of the numerical methods outlined in Chapter 4 in terms of computational demand, overall film and cooling performance as well as differences in mass flow distribution. Lastly, a comparison to experimental results is made.

7.2 Preliminary Numerical Study

7.2.1 Unit-Block Results

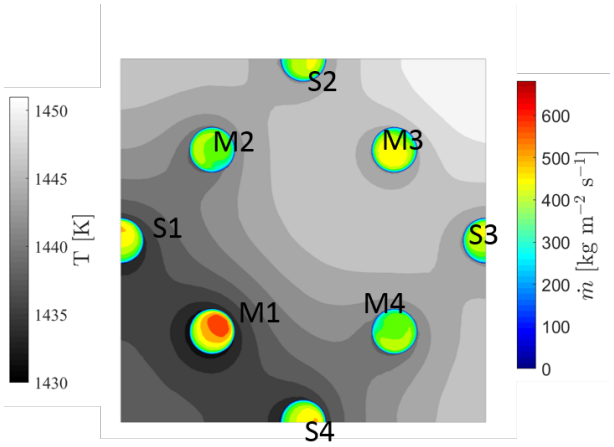


Figure 7.1: Variation of mass flow through film holes (engine conditions), with temperature contours of the film skin

Figure 7.1 illustrates a variation in blowing ratio for the film-holes in the unit-block arrangement. Since too large a blowing ratio could cause jet lift-off and degrade the film effectiveness, or too low would reduce the cooling capacity, the importance of this variation was considered. The film hole closest to the impingement jet (M1) had the highest coolant mass flow, while the lowest two holes were M2 and M4. It was found that for engine conditions the ratio of least to maximum coolant mass flow ($\dot{m}_{min}/\dot{m}_{M1}$) through a cooling hole was 0.67 - this was also observed at rig conditions, a ratio of 0.66.

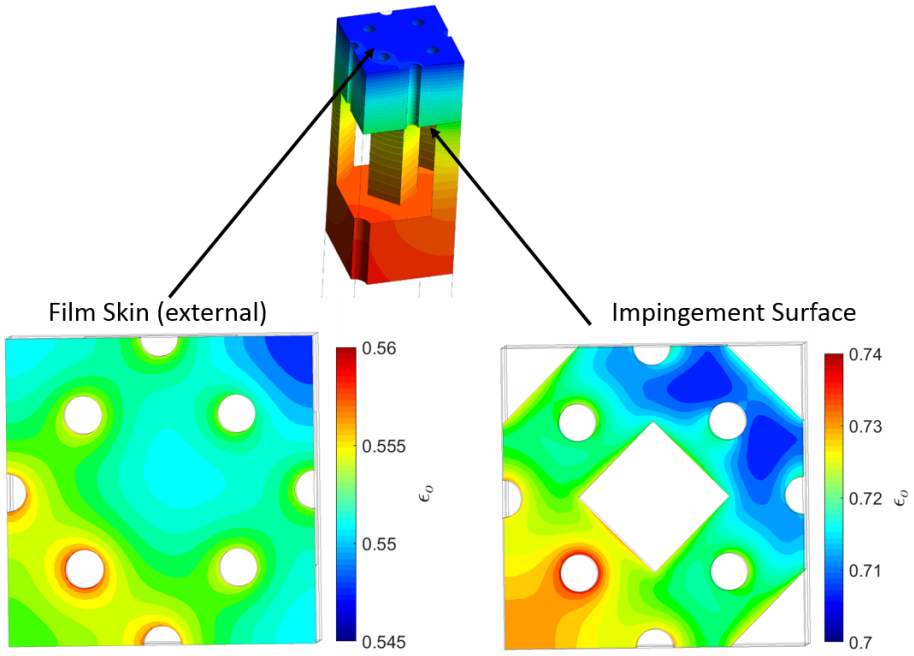


Figure 7.2: Overall Cooling Effectiveness for the film skin (left) and impingement surface (right). Engine conditions.

Cooling effectiveness contours due to internal convection are shown in Figure 7.2. The impingement jet had an impact on the temperature distribution on the inner surface of the outer skin. The result was a higher overall cooling effectiveness where the impingement jet stagnates on the impingement wall. The highest values were observed by the hole in closest proximity to the jet (M1), a consequence of the wall jet which forms and accelerates towards the film cooling hole. Another consequence of the impingement jet is creating a variation in the coolant mass flow through film holes, as previously discussed.

The overall effectiveness varied on the film skin, as would be expected for a double-skinned

system using impingement jets. The cooling effectiveness, without taking into account the film, was greater than 0.545 across the entire film skin surface. The region where this was highest was in close proximity to the three holes closest to the impingement jet. Two main factors are responsible for this. Firstly, the larger coolant mass flow through these holes in comparison to the others results in a more convective cooling within the holes. Secondly, the cooling enhancement of the impingement jet.

Despite the variations in mass flow between film holes, the levels of variation of ε_o is only small and no significant adverse affects were observed in the film or overall cooling effectiveness. The importance of this variation is inhibited by the lower mass flow of coolant passing through any individual hole compared to previous effusion geometries.

7.2.2 Full Solution

A comparison of the overall cooling performance contours for the external surface for TD1 and D6 is shown in Figure 7.3. The result is that of a repeating unit-block domain with flanges in both cases and based on the coolant mass flow required for a D6 blowing ratio of 0.36 at experimental rig conditions. The results highlight a higher cooling effectiveness for TD1 across the extent of the domain. Areas of distinct thermal protection as a consequence of individual films are less obvious for TD1, which can be interpreted as a more uniform coverage, a result of a lower pitch between cooling holes, S_x and S_z. Moreover, a distinct benefit is enhanced upstream cooling performance. While the coolant holes start in the same stream-wise location, the proximity of adjacent cooling holes in both the stream- and span-wise direction helps to promote a more even thermal distribution within the external skin and the building of a covering film layer. However, a large portion of this benefit is gained from the increased downstream cooling performance, as conduction through the material dampens upstream thermal attack.

Averaged cooling effectiveness is plotted in Figures 7.4a and 7.4b which correspond to stream- and span-wise averaged values. The former provides further evidence of a more uniform temperature distribution across the domain. Away from the edges, approximately $30\,\text{mm} < z < 150\,\text{mm}$, the averaged stream-wise ε_o is reasonably flat, with only a small variation between

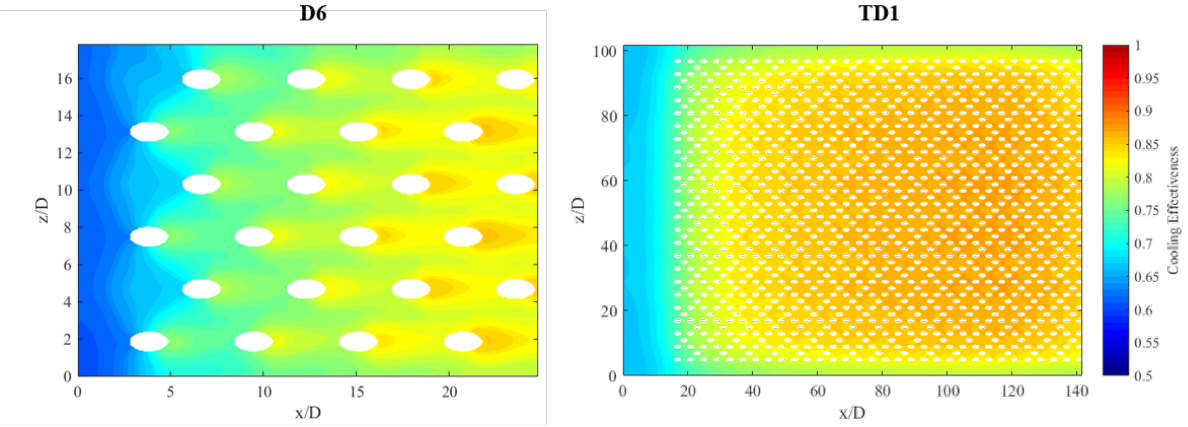
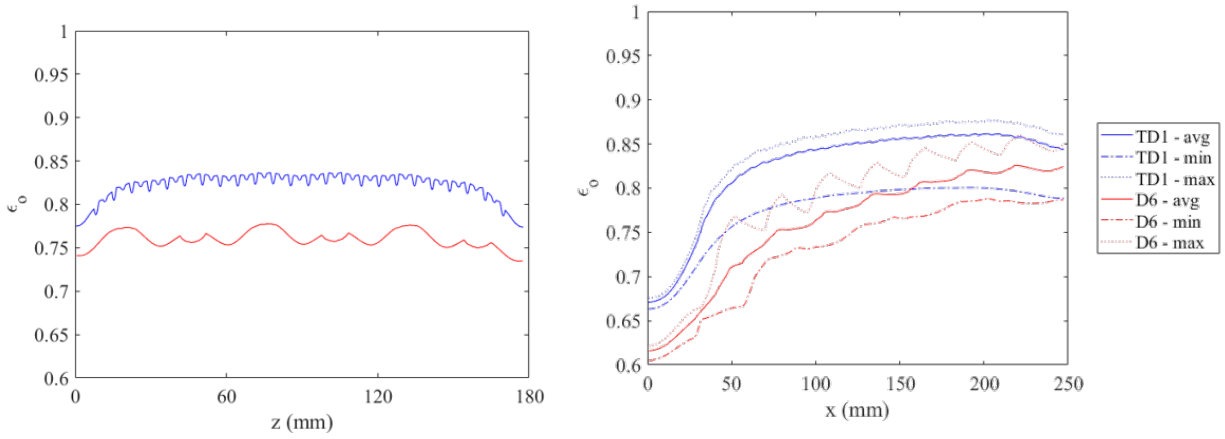


Figure 7.3: Overall Cooling Effectiveness Contours for D6 and TD1



(a) Stream-wise average

(b) Span-wise average - with minimum and maximum values

Figure 7.4: Average Cooling Effectiveness for the External Skin of TD1 vs D6

columns of films. This contrasts with D6 which varies by about 0.4 in the same region. The averaged stream-wise ε_o clearly illustrates the overall improvement of cooling performance for TD1, as the minimum, average and maximum values are raised throughout. This difference begins at the leading edge and is compounded after the first several cooling rows. However, the distribution for TD1 begins to plateau after approximately 14 cooling rows ($\approx$ 100mm), while the D6 design continues to benefit with subsequent distance. At the trailing edge of the flat plate the span-wise averaged values become comparable, in fact the minimum is equal between the two designs, although the maximum and average are still higher for TD1.

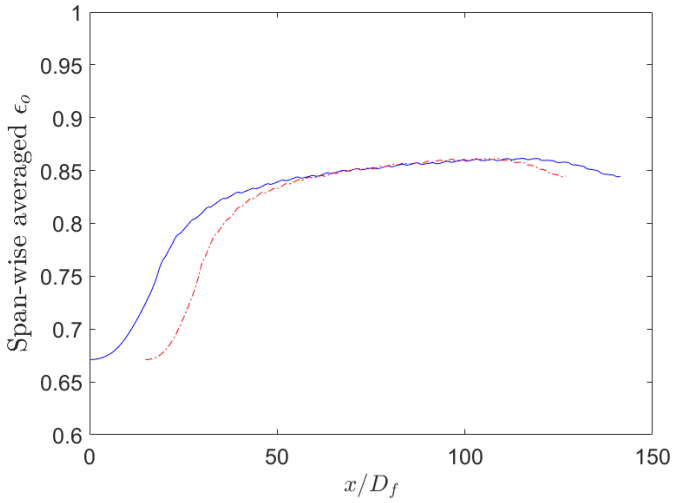


Figure 7.5: Reduction in span-wise averaged cooling effectiveness with the modelling of a flange

7.2.3 Full Test Piece Considerations

Expanding to the full domain from each unit block provides a framework for comparison (numerically) between designs of differing geometries and conditions. However, any experimental comparison must be done carefully. Physically the domains will differ due to the presence of a finite edge on all four sides, and this results in areas which will have no film cooling and reduced convective cooling, through the holes and internally. To provide some correction for this, the geometry used in ANSYS Mechanical has been investigated with and without the flange. Modelling of the flange is achieved in the following way. Exterior side-surfaces of the test-piece have adiabatic boundary conditions imposed. This is a consequence of contact with the internal insulation, which has a low thermal conductivity. Internal surfaces forming the edges of the domain, and any features outside the repeating block domain, are provided with the average pedestal heat transfer coefficient from the unit-block CFD. Both the repeating-unitblock and flange-inclusive model for the film surface were modelled for the TD1 geometry at experimental rig conditions and span-wise averaged overall cooling effectiveness for the film surface are illustrated in Figure 7.5. The cooling performance is altered with the addition of the flange. This is a consequence of conduction of temperatures at the flange propagating to the unit-blocked area, and so simply comparing the correct domain area between experimental and numerical may not be sufficient, without the correct assumptions to consider the domain as a whole.

7.3 Hole Inclination

Preliminary studies modelled film holes in the unit-block methods normal without any inclination angle. This was done to take advantage of the symmetry boundary condition in the CFD solver. Firstly, the discharge coefficient will change due to aspect ratio of the film holes and changes to flow structure especially at the sharp edge of the film inlet. As a consequence, the pressure drop for a given flow rate will change, and Byerley [88] demonstrated that the discharge coefficient can change between 0-30%. Secondly, in the CFD results the internal heat transfer will be underestimated due to a reduction in the internal film-hole wetted area, see Figure 7.6. While this can be compensated by interpolating the heat transfer coefficient onto the inclined holes, the internal increase in coolant temperature will be underestimated. Consequently, the film effectiveness will be an over-prediction. For high porous designs where the film effectiveness can account for a significant portion of the overall cooling, this may be unacceptable. Lastly, for a high number of film holes, these inevitably become in close proximity to the impingement jets and the orientation of the holes in relation to the lateral jet which emerges on the internal surface of the outerskin plays a crucial role in the amount of mass flow which enters the film hole. This is explored further in Chapter 8. Consequently, it was deemed important to model the inclination of the film holes using a periodic boundary in the unit-cell methods.

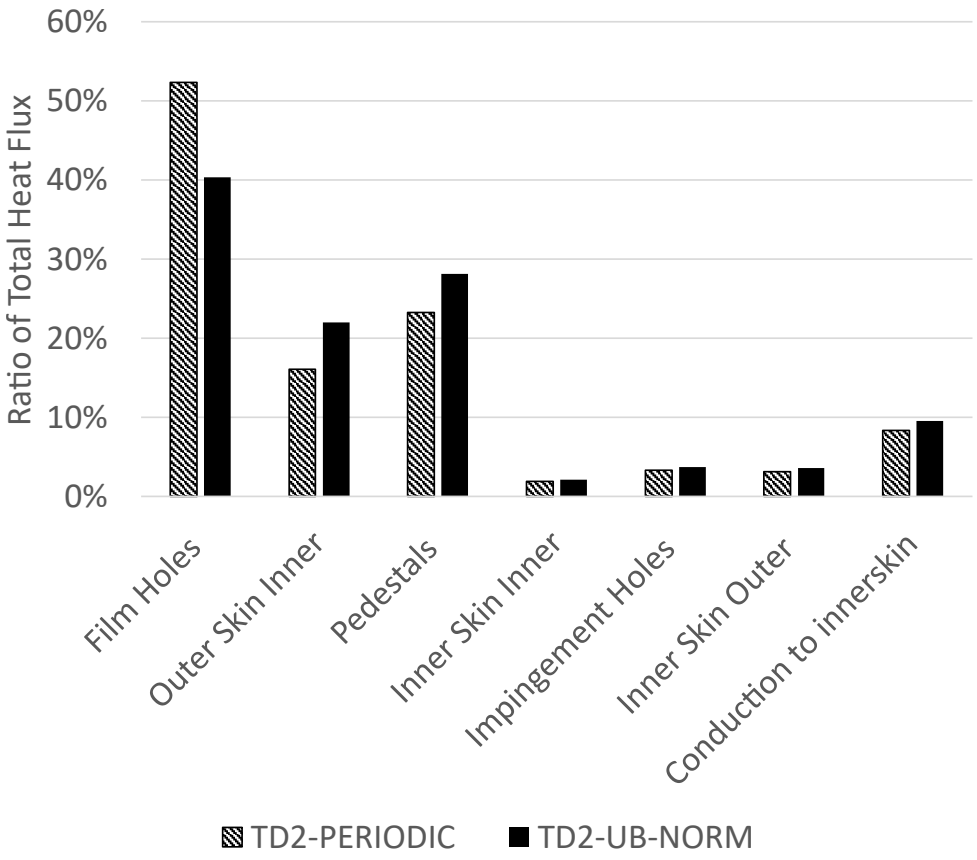


Figure 7.6: Impact of inclination angle of film holes on internal component share of the heat flux - TD2 configuration (T2) at mass flow rate of $m^* \sim 3.5$

7.4 Model comparison

The use of each numerical methods was made for three coolant mass flow rates, $m^* = 3.4$, 4.8 and 6.9, and three configurations of interest, E2 (D6), T1 (HS2) and T2 (TD2). The exception was T2 was not modelled using the full streamwise domain (SSD method) to avoid overly expensive computation times. Additionally the SSD method was conducted using both a constant external pressure (P_∞) as well as one representative of the rig setup, where $P_\infty = f(x)$. This was done using pressure tappings at five locations in the streamwise direction, and the resulting pressure relation could be applied as outlet boundary conditions in the CFD.

Firstly, an assessment of the computational time of each method was for the computational time was made in terms of CPU core hours required for the CFD solve, see Table 7.1. Evaluation of the film effectiveness from these results was significantly shorter and similarly for the computation required in ANSYS steady state. And therefore their contribution was not considered here. The decoupled unit-cell method required less than 10 hours for E2 and T1, and over 20 hours for T2 given the large number of film holes and small film diameter requiring a finer mesh. Moving from the decoupled-unit block method to a multi-cell approach (semi-decoupled unit-cell method) doubled the CFD expense required for all three configurations. For the semi-decoupled streamwise domain, the increase over the DUC method was over 9 times for E1 and over 12 times for T1. Given this increase, one can assume that for T2 the SSD method may require well in excess of 300 core hours. In comparison to all these methods, the low-order model provides an estimate for the cooling performance on the order or seconds, however, it is worth remembering that its reliance on heat transfer coefficients from CFD for the inner-outer wall and the pedestal surfaces.

Cost in CPU core hours				
		E2	T1	T2
Low Order Model	LOM	$\ll 1$	$\ll 1$	$\ll 1$
Decoupled Unit Cell	DUC	8.0	8.9	22.2
Semi-decoupled Unit Cell	SUC	16.0	17.8	44.4
Semi-decoupled Streamwise Domain	SSD	77.8	111.1	

Table 7.1: Estimated cost of each numerical method in CPU core hours. Estimated as the solution time multiplied by the number of cores.

Area-average outerskin-outer film effectiveness, $\overline{\overline{\eta_f}}$

	E2			T1			T2		
m^*	3.4	4.8	6.9	3.4	4.8	6.9	3.4	4.8	6.9
DUC	0.124	0.181	0.242	0.202	0.287	0.382	0.283	0.388	0.485
SUC	0.125	0.182	0.245	0.202	0.288	0.384	0.298	0.406	0.506
SSD, P_∞	0.123	0.181	0.241	0.208	0.294	0.391			
SSD, $P_\infty = f(x)$	0.102	0.166	0.234	0.178	0.277	0.381			

Table 7.2: Film effectiveness comparison between modelling methods

Area-average outerskin-outer cooling effectivenes, $\overline{\overline{\varepsilon_o}}$

	E2			T1			T2		
m^*	3.4	4.8	6.9	3.4	4.8	6.9	3.4	4.8	6.9
LOM	0.625	0.687	0.738	0.687	0.751	0.807	0.768	0.832	0.878
DUC	0.646	0.712	0.763	0.686	0.759	0.808	0.748	0.811	0.848
SUC	0.646	0.715	0.764	0.697	0.761	0.810	0.754	0.816	0.860
SSD, P_∞	0.659	0.724	0.772	0.700	0.764	0.812			
SSD, $P_\infty = f(x)$	0.653	0.720	0.770	0.691	0.760	0.810			

Table 7.3: Cooling effectiveness comparison between modelling methods

Before considering the impact of modelling methods on film effectiveness, it is first important to understand how these models differ in calculation of the films. As discussed in Chapter 4 the DUC method will underestimate the film effectiveness as no external protection was added in the CFD and therefore film hole exit temperatures are overestimated. Moreover, in both unit-cell methods, constant mass flow was assumed for each unit-cell, which was not necessarily the case once modelling the full stream-wise domain. In Table 7.2 this was realised by lower film effectiveness observed for each configuration between the DUC and SUC methods, and this difference increased as one increased the mass flow rate. The dependence on mass flow rate was unsurprising as the difference in outlet temperature was further exasperated by the strengthening films associated with added coolant flow. Another striking feature is the reduction in film effectiveness for the SSD method once a variable external pressure is applied. This was likely a consequence of coolant migrating towards the downstream film holes where the pressure gradient is more favourable. This feature will be discussed in more detail in Section 7.5.

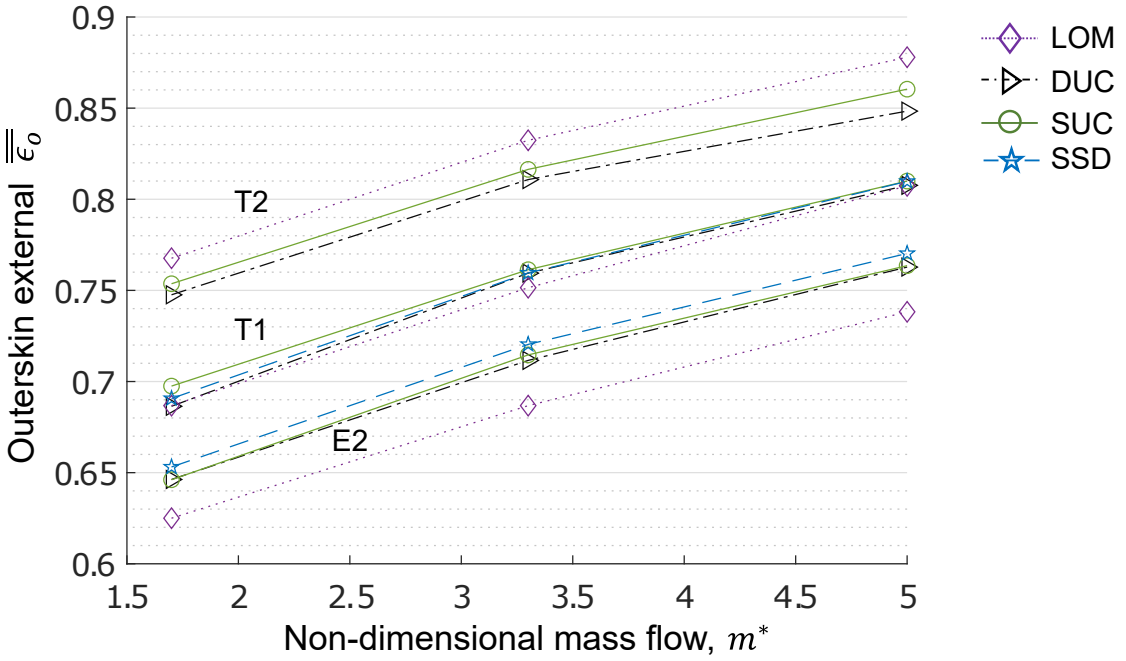


Figure 7.7: Comparison of the area-averaged cooling effectiveness on the film-side wall between the four numerical methods. E2, T1 and T2 configurations were evaluated at three mass flow rates. The SSD method shown here includes a variable external pressure.

Tabulated results for the outer hot-wall can be found in Table 7.3. Here the generalisation can be made, with perhaps the exception of LOM, that there is only small differences in the overall cooling between the numerical methods and the conditions tested. For clarity, these values have been plotted in Figure 7.7, and the SSD results correspond to those where an external pressure gradient has been applied. One can observe that the differences between CFD methods is small and no significant change with non-dimensional mass flow rate. These results are encouraging with regards towards using the DUC method, considering the reduced computational expense in terms of both solver time and memory. Another interesting feature is the comparison of the CFD methods in relation to using a low-order thermal model. For the least porous geometry, E2, the LOM under-predicted the cooling performance for all three mass flow condition, by approximately 0.02. For T1, the results were less than for CFD, but in general there was little between them. Finally, for T2 the LOM results were higher than the CFD. While it is uncertain the exact nature of these differences, the empricial correlations used for the impingement jet does not consider nearby obstacles or film outlets in such proximity, and results from Chapter 6 highlighted the complex nature between impingement jets and internal features. Additionally, the Dittus-Boelter relation may not fully capture the convection between the film hole and in-

ternal coolant flow, given separation which occurs at acute angles of film holes for a jet moving in the opposing direction to the hole inclination. Therefore, especially for T2, this simple correlation may be unrepresentative. Despite this, the LOM reasonably captured the trends of all three configurations.

7.5 Pressure gradient

To assess the impact of the application of an external pressure gradient, the cumulative sum of the fraction of coolant mass consumed was plotted across the streamwise direction for E2 and T1 in Figures 7.8 and Figures 7.9 respectively. In each figure the results from the constant external pressure are plotted as well as those for variable pressure at each of the three coolant flow rates. As the streamwise direction begins with the leading edge hole, the mass fraction starts above 0, but this is more noticeable for E2 due to the large film hole sizes and more moderate spacing between them. Unsurprisingly, for constant P_∞ the mass fraction is split evenly across the domain for both E2 and T1. However, the introduction of $P_\infty = f(x)$ results coolant favouring the downstream film holes, as a consequence of a more favourable pressure gradient across the external wall at these locations. This can be quantified as the ratio of external pressure difference, from the most upstream to downstream film holes, to internal cavity pressure.

$$\frac{P_{\infty,1} - P_{\infty,n}}{P_{c,int}} \tag{7.1}$$

The largest difference between cumulative mass fraction occurs at approximately the middle of the plate in both E2 and T1, and for all mass flow rates. Additionally, in both situations the largest difference is just over 10% of total coolant mass for $m^* = 3.4$. However, with increasing mass flow rate, the bias in distribution of coolant flow reduces. This can be explained by increasing internal cavity pressure with coolant mass flow, $P_{c,int}$. As this value increase, for a fixed external pressure, the ratio expressed above decreases, resulting in less of a driving force to push coolant towards the downstream films. In this way, at high coolant flows this bias will be less of a problem, but for low coolant flows this could lead to quite problematic results where low performing films near the leading edge are further weakened by the mass imbalance. Impact of this behaviour on the film effectiveness has been capture in Figure 7.10 where the spanwise-

average film effectiveness is displayed for both configurations and boundary conditions and all three mass flow rates. Similarly, it is most obvious for low m^* that the leading edge films are deprived of some coolant, resulting in worse films. While the downstream films will benefit from this increase in mass fraction and in fact benefits are observed downstream of the final film row. However, despite this equalisation of mass fraction, due to the nature of film superposition, the downstream benefit may be outweighed by the poor initial film performance and this is reflected by the tabulated results shown previously in Table 7.2. However, as the coolant mass increases the influence of constant and variable pressure on film effectiveness are reduced, and barely noticeable for $m^* = 6.9$. In general the influence of external pressure gradient was relatively inconsequential on the film effectiveness and overall cooling for flat configurations. However, it is worth considering that with the introduction of a larger pressure gradient (curvature) and lower relative the mass flows rates, the consequence on film effectiveness may be more serious.

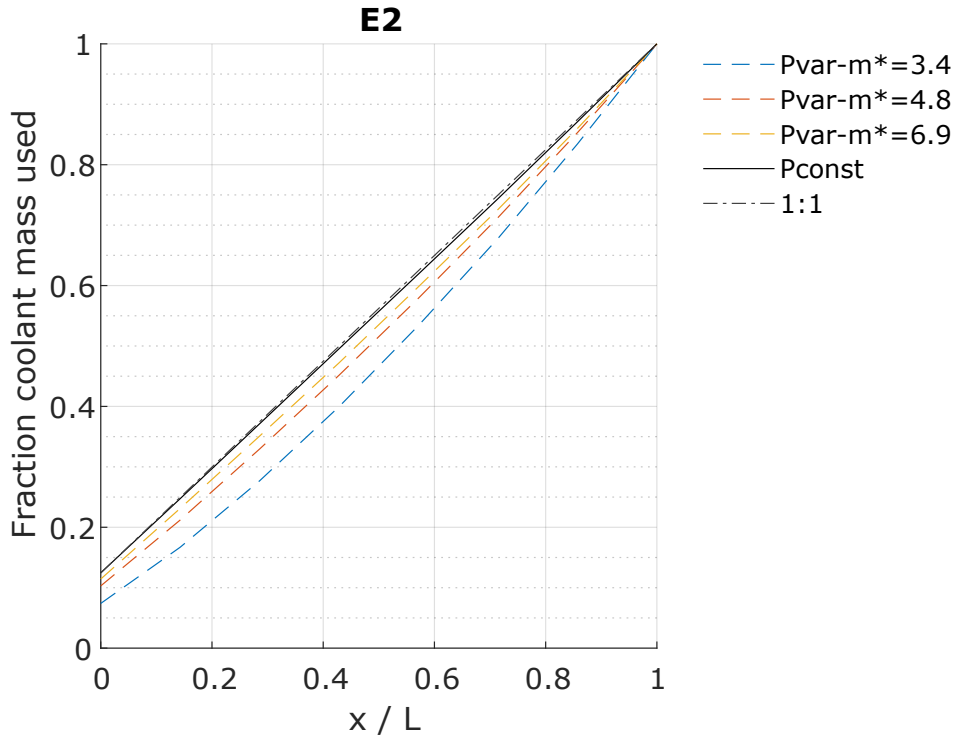


Figure 7.8: Cumulative mass fraction with distance downstream of the leading film hole for E2 under constant or variable external pressure.

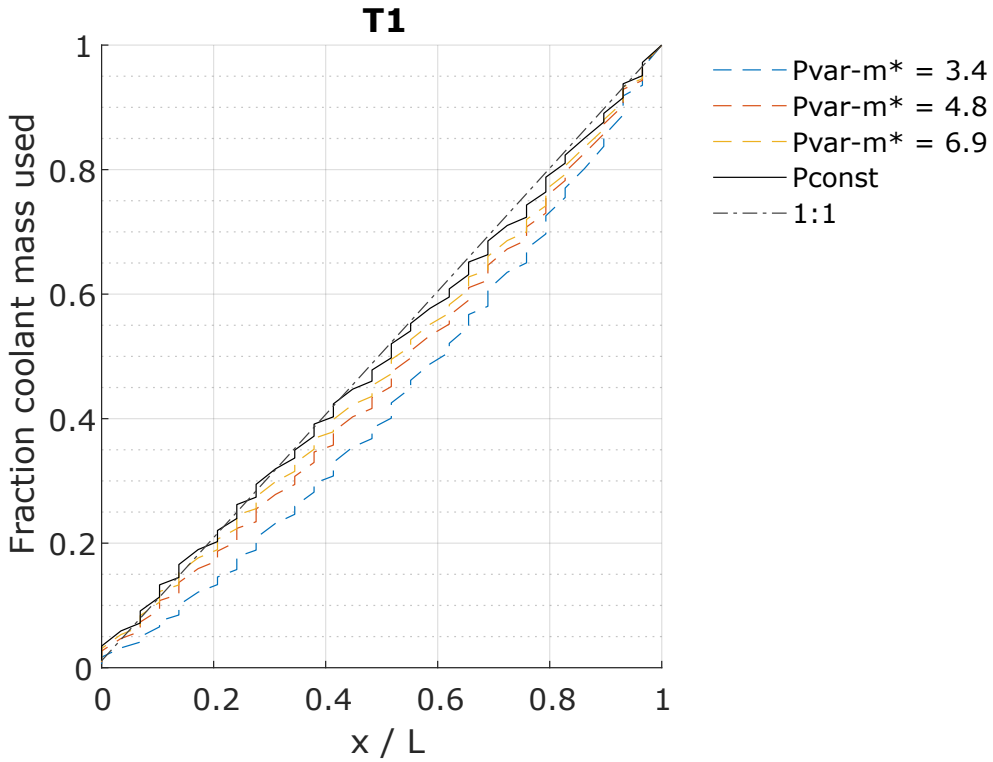


Figure 7.9: Cumulative mass fraction with distance downstream of the leading film hole for T1 under constant or variable external pressure.

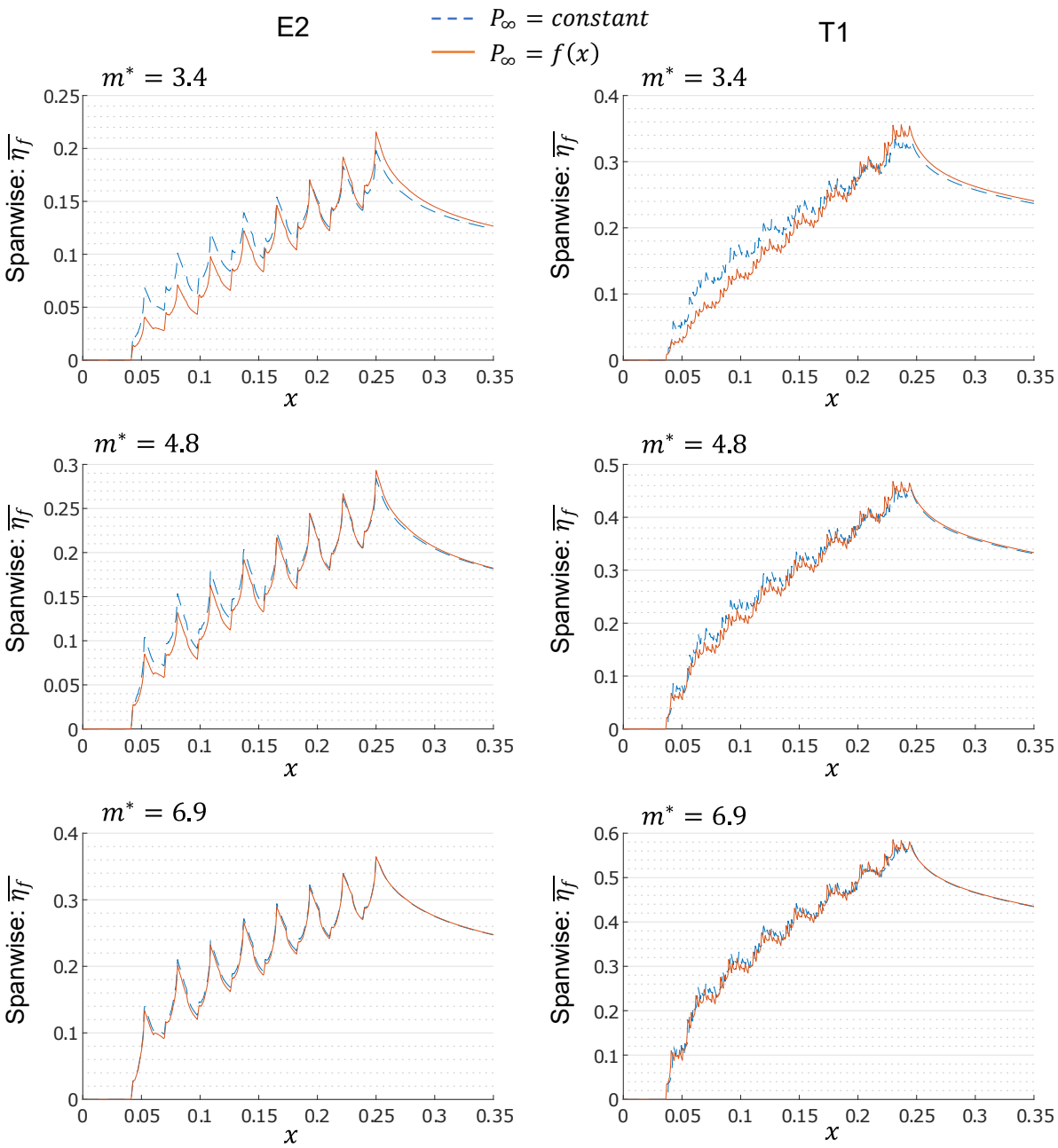


Figure 7.10: Spanwise-average film effectiveness using a constant and variable external mainstream pressure. E2 and T1 configurations were investigated using a full streamwise domain with outlet conditions on the film-holes.

7.6 Experimental comparison

A comparison of the decoupled unit-cell method was made to experimental results for the three geometries. The area-averaged outerskin-external cooling effectiveness across the range of mass flow rates is illustrated in Figure 7.11. In addition, curves of the theoretical internal convective effectiveness are displayed. The cooling effectiveness of an isothermal blade with uniform external heating can be expressed by equation 7.2.

$$\varepsilon_o = \frac{m^* \eta_c}{1 + m^* \eta_c} \tag{7.2}$$

As a consequence these configurations can be compared to a purely internally cooled double-wall at varying convective efficiencies.

The numerical method did a good job of capturing both the relative differences between configurations as well as their behaviour with mass flow rate. These results provide confidence in the ability to quickly assess the cooling performance of flat-plate geometries, despite the simplifications and assumed boundary conditions. In addition to this, these results provide encouragement in that higher outerskin porosity can reduce the mean external wall temperature. While further analysis will be covered in Chapter 8, it is worth noting that T2 had cooling effectiveness values in excess of an internally cooled blade with theoretical convective efficiency of 1.

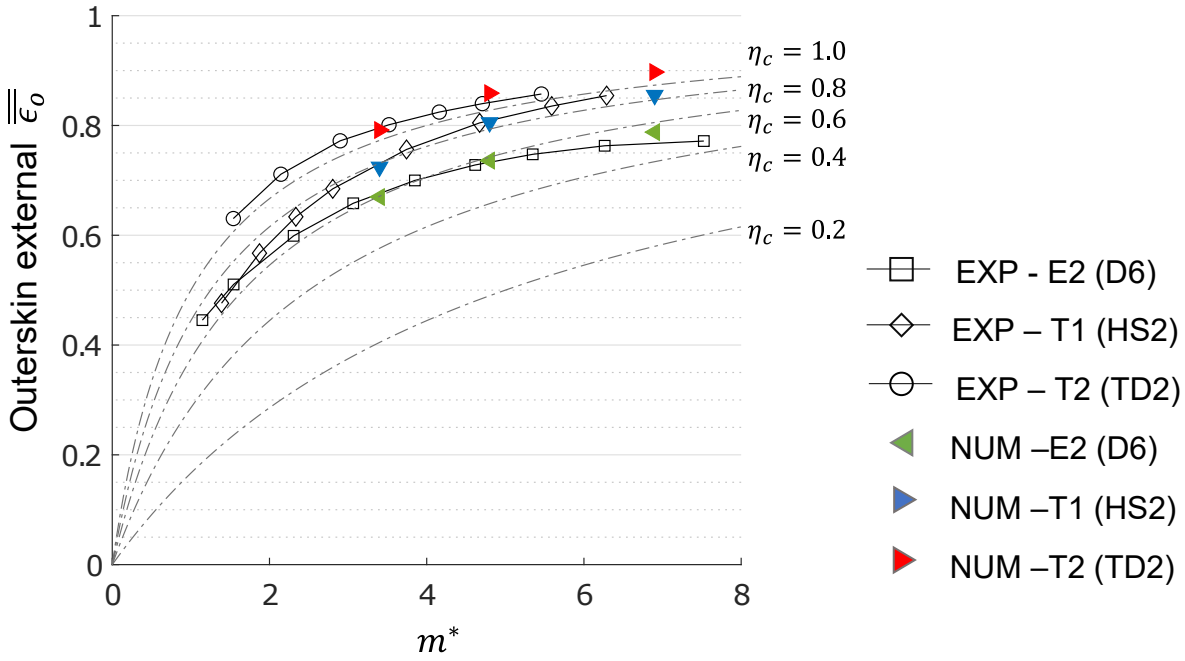


Figure 7.11: Area-averaged outerskin cooling effectiveness vs mass flow rate for three geometries of interest: E2, T1 and T2. Results from the decoupled unit-cell method (DUC) are displayed against experimental results and theoretical constant convective efficiency (η_c) curves.

7.7 Summary

Model choice is an important consideration and is dependent on the geometry and flow characteristics being investigated. As porosity increases streamwise pressure gradients become increasingly significant on mass flow distribution, and hence unit-block type models reduce in the accuracy of behaviour. Furthermore, the use of a simple de-coupling method underestimates film protection. Moving toward larger domain sizes will help capture these features but there is an associated computational cost that increases with domain size, and can be a factor of 10 of more depending on the area of interest. However, the comparison of these methods suggests that the use of a decoupled unit-cell method adequately captures the overall cooling performance and can save significant computational cost.

While for flat plate configurations the external pressure gradient only had a small influence on the results observed here, the introduction of curvature may result in much larger deviations. Despite these limitations, given the computational savings without modelling external flow, and the difficulty in accurately capturing the heat transfer and aerodynamics of film jets in a cross-flow, a separate internal CFD and empirically found external boundary condition still provides an invaluable tool for assessment of complex cooling arrangements.

8 Evaluation of Outerskin Porosity

8.1 Overview

In pursuit of transpiration cooling we look to further understand how differences in outerskin porosity influence the aerothermal characteristics of double wall turbine blades. Given the potential benefits of film holes in close proximity as highlighted in Chapter 5, assessment of the overall thermal performance was required. Two geometries with outerskin porosity of 20% were compared to variations previously studied by Murray in [85] with porosity of less than 10%. A numerical evaluation is made in which four configurations are compared in terms of internal cooling characteristics, film protection and finally the overall thermal performance. Aerodynamic challenges are also considered to understand the feasibility of such designs. This work was presented at the ASME Turbo Expo 2022 in Rotterdam. To supplement the findings from this paper, experimental results are provided and highlight key features of highly porous geometries which represent a step towards transpiration cooling.

8.2 ASME 2022 paper

Proceedings of ASME Turbo Expo 2022
Turbomachinery Technical Conference & Exposition
GT2022
June 13-17, 2022, Rotterdam, The Netherlands

Influence of Porosity on Double-Walled Effusion-Cooled Systems for Gas Turbine Blades

Matthew Courtis, Peter Ireland

Oxford Thermofluids Institute

Department of Engineering Science

University of Oxford

Oxford, OX1 3PJ, United Kingdom

Abstract

Double wall effusion cooling (DWEC) systems for gas turbine blades utilise two skins connected by pedestals and take advantage of cooling benefits provided by impingement jets and film holes. The latter exhausts coolant externally onto the blade surface forming a protective layer against the high external heat loads, which can be enhanced via the beneficial influence of adjacent films. Consequently, increasingly porous outerskins are being considered in order to provide greater thermal protection and/or reduce the required coolant mass consumption. To realise such systems, further research must understand how the internal aerothermal field is affected by high porosity.

A semi-decoupled unit-cell computational fluid dynamics (CFD) method is applied to a range of DWEC systems to understand overall cooling effectiveness as well as internal characteristics. A comparison of internal convection highlights a shift in the breakdown of cooling performance, due to the large changes in wetted surface area of the outerskin. For low porosity, most of the internal cooling occurs through the jet impingement on the internal outerskin wall, while the addition of more film holes provides an increasingly greater proportion of convective heat

transfer. On the external surface, porosity increased film effectiveness due to film superposition, provided a more uniform film coverage, and reduced the likelihood of jet-lift-off.

Coupling the benefits of internal cooling and film effectiveness resulted in a reduction of mean metal temperature, peak temperature and temperature gradient between the outer and inner walls. Criteria reflecting the main drivers for thermal fatigue. Despite these benefits, for the most porous DWEC configuration a variation in mass flow between film holes was observed, and in some cases the risk of hot gas ingestion was evident. DWEC components would benefit from further understanding of the susceptibility to blockage, the pressure margin limits and the extent of flow migration.

8.2.1 Introduction

Gas turbine blades are subject to high thermal loads from the combustor with temperatures that can exceed the metal softening point. The desire for such high turbine inlet temperature derives from the enhancement of overall engine efficiency and thus to maintain suitable life cycles of critical engine components, protective systems are required. These can be broadly grouped as: internal cooling, external cooling and thermal barrier coating.

The first two techniques require coolant flow to be bled from upstream compressor stages and exhaust from the turbine blade via a mixture of internal passages, pedestals, ribs, impingement jets or film holes. However, the use of any coolant comes with an associated cycle efficiency penalty and potential for aerodynamic losses. Consequently, reducing the amount of mass flow used while maintaining suitable metal temperatures requires further advancement in turbine cooling systems.

Developments in turbine cooling were summarised by Krewinkel [5] and indicate the move from discrete film hole cooling toward effusion and transpiration-like cooling, which is driven by increased efficiency with porosity [6]. Effusion cooling is established by many rows of film holes, while transpiration cooling is associated with the use of porous materials. While manufacturing constraints have kept the latter from being realised, the evolution of additive manufacturing en-

ables the design of novel and small-scale internal structures [7]. Despite this, further research is required to address associated problems, such as blockage [8, 9], risk of hot-gas ingestion [10] and high computational demand [11].

In recent years double-wall effusion cooling (DWEC) systems have been of interest [135, 136] and a typical DWEC system is illustrated in Fig.8.1 which displays a cut-through of the solid with fluid velocity vectors overlaid. Coolant enters the configuration through openings in the innerskin called impingement holes (D), which form a coolant jet that moves toward the target surface, the outerskin-inner surface (B), where it loses velocity and begins to turn. This is known as the stagnation region and will move radially outwards as a lateral jet along the wall. The impingement jet acts as an efficient mechanism for enhancement of heat transfer and is often used in leading edge cooling [17]. The coolant will be driven towards the film holes, but structures can form between skins, and the internal surface area provided by pedestals (C) can increase the heat transfer. As the coolant moves out through the film holes (A), further heat will be transferred between the outerskin and fluid before emerging onto the external surface as a protective film jet.

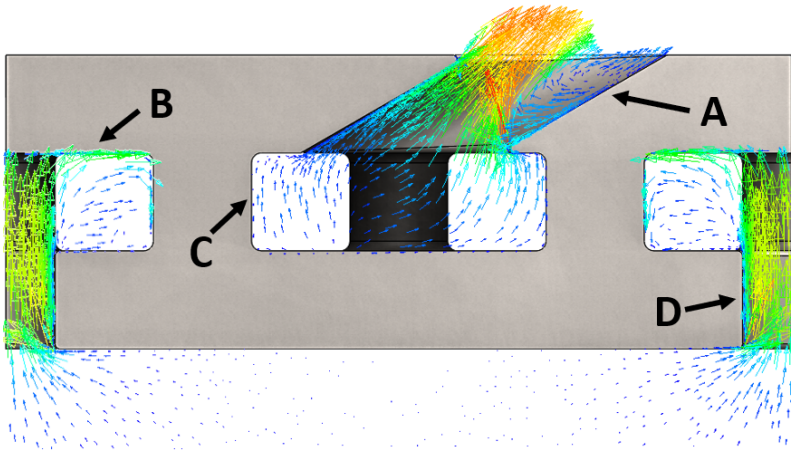


Figure 8.1: Visualisation of flow through a typical DWEC system. The following components are identified: A) film holes, B) outerskin-inner wall, C) pedestals, D) impingement holes.

Coolant jets with low momentum relative to the mainstream flow form films which are well attached to the external surface and act as a buffer between the external hot flow and the turbine blade wall. However, as the momentum ratio increases this jet may lift off the blade surface, reducing it's ability to provide a protective layer [26, 137]. A key determinant for this condition

is the blowing ratio, M, defined as the ratio of the product of density and velocity between the film hole jet and mainstream flow.

$$M = \frac{\rho_c V_c}{\rho_\infty V_\infty} \tag{8.1}$$

In an effort to stay away from lift-off, the porosity on the outer surface can be increased, reducing the film jet velocity V_c and therefore M. High porosity is achieved by low film hole spacing which was shown by Sellers [78] to promote film hole interaction resulting in positive superposition of films. In this way, porosity over 20% can lead to high film effectiveness and protection which extends in the streamwise direction well after the final film hole [100].

In addition to good film protection, high outer-wall porosity provides an increase in the internal wetted area which can promote high internal convective heat transfer. In fact, for a given film hole spacing to diameter ratio (S_f/D_f), a reduction in film hole diameter may provide an increase in the cooling effectiveness [138]. In this way, outerskin porosity can influence both the internal and external cooling mechanisms.

Computational fluid dynamics (CFD) methods are extensively used to understand the fluid flow and heat transfer within a turbine blade, but accurate and robust solutions for complex flows represent a fundamental challenge. Dewan et al. [139] highlighted the particular problems of using Reynolds-Averaged Navier-Stokes (RANS) models to capture impingement jet heat transfer, due to the complexity of the flow in the stagnation region, involvement of arbitrary coefficients and poor performance of the wall functions in the stagnation and wall jet regions. Modelling of the coolant films provides an additional challenge as well as ensuring mesh convergence. While accurately capturing individual holes is possible at a moderate computational cost [140], larger coolant hole arrays will substantially increase that cost. Moreover, RANS models can struggle to accurately predict mixing and lateral spread of films [141]. Nevertheless, CFD is a powerful tool and careful implementation can be used to expand our understanding of aerothermal problems.

Further investigation of porosity effects on DWEC configurations is required for timely imple-

mentation of transpiration-like systems in industry. This study used a decoupled conjugate numerical method to model four geometries with similar internal structures but varying outerskin porosity. Both internal convection and film effectiveness were evaluated and used to calculate the overall effectiveness, as well as an evaluation of the importance of outerskin porosity.

8.2.2 Geometric Domain

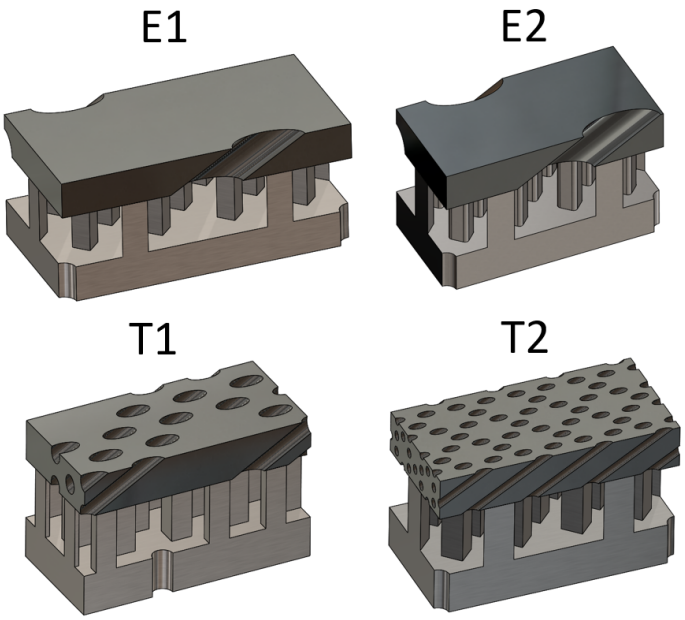


Figure 8.2: Renderings of the four unit-cell domains.

	E1	**E2**	**T1**	**T2**
D_f [mm]	1	1	0.4	0.2
D_{imp} [mm]	0.7	0.5	0.5	0.5
H_i/D_{imp}	1.43	2	2	2
H_o/D_f	1	1	2.5	5
S_f/D_f	8	5.64	3.5	3.5
S_{imp}/D_{imp}	11.4	11.3	11.3	11.3
H_p/D_{imp}	2.14	3	3	3
A_w/A_{in}	3.3	4.4	6.2	7.9
ϕ_g	0.049	0.099	0.192	0.192

Table 8.1: Geometric parameters for the repeating unti-cell domains.

Four DWEC variations with common internal features were constructed as flat plates (248 mm x 178 mm) and the repeating unit-cell domains are displayed in Fig. 8.2 with associated dimensions in Table 8.1.

$$\phi_g = 1 - \frac{A_{o-o}}{A_{in}} \tag{8.2}$$

Characterisation of these geometries can be made by the geometric porosity described in equation 8.2, where A_{o-o} is the outerskin-outer surface area. Based on this definition, ϕ_g is directly related to the film hole spacing, S_f/D_f. Another important parameter to consider is the ratio of internal wetted area to inlet area, A_w/A_in, which captures the internal cooling potential.

E1 and E2 are representative of current effusion type designs previously studied [87, 54] with ϕ_g of approximately 5% and 10% respectively. These both have a film hole diameter of 1 mm but the former has a larger film and impingement hole spacing, and because of the larger unit-cell size, the impingement hole diameter was increased in order to maintain the same impingement jet velocity at a fixed mass flow rate per unit area.

T1 and T2 are a move towards more transpiration-like geometries with higher porosity, ϕ_g = 19.2%. T1 has a film hole diameter of 0.4 mm and in order to accommodate film hole spacing, pedestals had to be rotated by 45°, otherwise the internals are the same as E2. T2 also copied the internal structure of E2 but introduced smaller film holes with a diameter of 0.2 mm, while keeping the same film hole spacing as T1. And therefore the same geometric porosity as T1, resulting in more holes per unit area and consequently an increase in convective area. Lastly, for T1 and T2, any film hole situated directly above an impingement jet hole was removed.

8.2.3 Numerical Model

A decoupled method was applied to evaluate the overall cooling performance, utilising internal CFD of a representative unit-cell alongside an empirical calculation of the external film effectiveness. These were both used as inputs into a three-dimensional Fourier law solver to determine wall temperatures of an enlarged domain. This method was successfully demonstrated previously [87], although in the current study film holes are modelled with inclination. An adjustment to the film effectiveness model was also made, and was shown to have good agreement with experimental data [2]. A schematic of the procedure is shown in Fig.8.3, and further detail of each step provided in subsequent sections of this paper.

Assessment of aerothermal performance was made at three coolant flow rates which are ex-

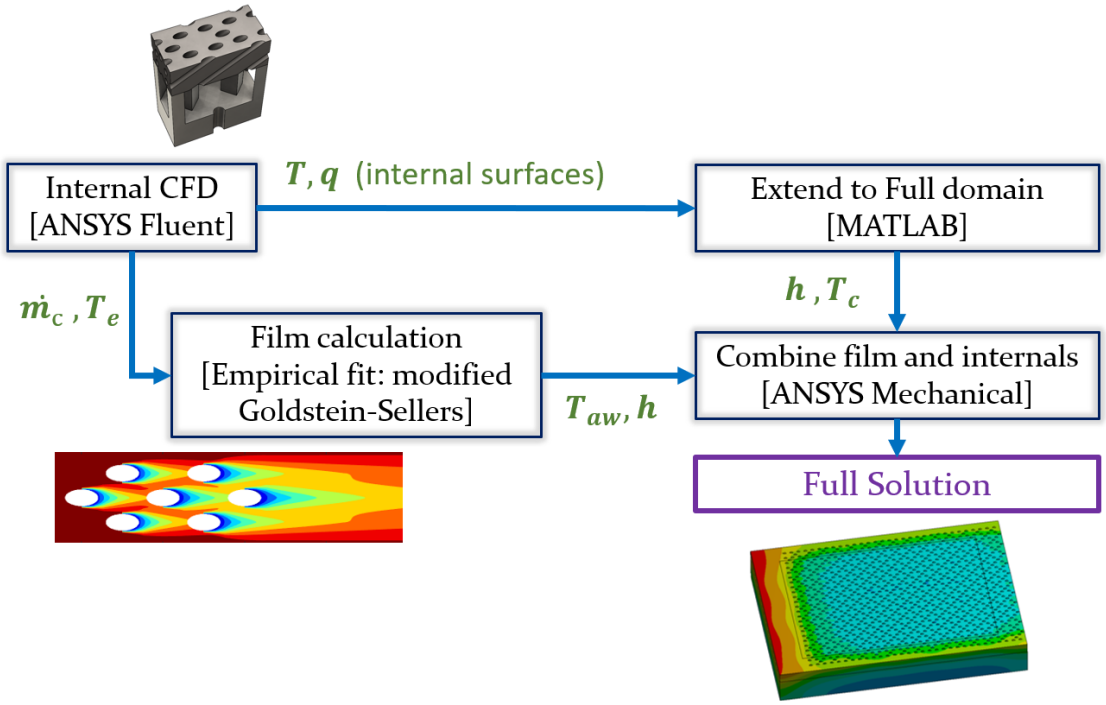


Figure 8.3: Schematic demonstrating implementation of decoupled method

pressed by a non-dimensional coolant mass flow rate

$$m^* = \frac{c_p \dot{m}_c}{Ah} \tag{8.3}$$

Here c_p is the specific heat capacity, $\dot{m}_c$ the mass flow rate of the coolant, A is the area subject to external thermal loading and h (W/m^2/K) is the external heat transfer coefficient due to mainstream flow. This provides a metric to compare between different cooling schemes.

Internal Computational Model

T_c	1000	K
m^*	1.7, 3.3, 5.5	-
$\dot{m}_c/A_{in}$	12.5, 25, 37.5	kg/s/m^2
T_∞	1870	K
h	7500	W/m^2/K
P_∞	3.4	MPa

Table 8.2: Boundary conditions applied to CFD domain.

An unstructured mesh was constructed in *ANSYS Mesher* with fifteen prism layers along fluid-solid interfaces with an overall height of 0.01 mm and a growth rate of 1.2, to keep non-dimensional wall height, $y^+ \leq 1$. The solver method used in *ANSYS Fluent* was pressure-based

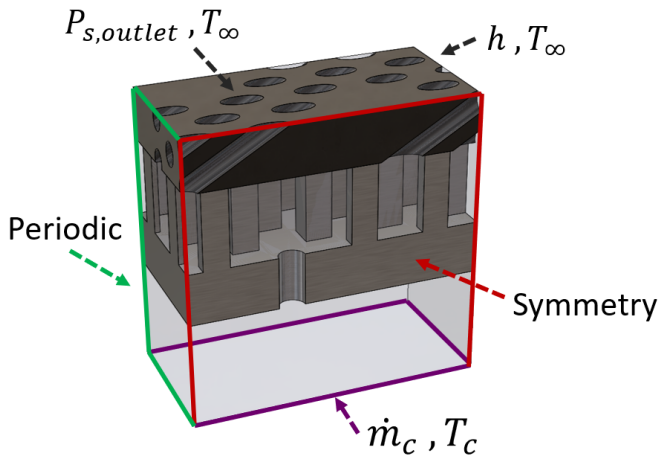


Figure 8.4: Implementation of boundary conditions in CFD solver and representation of the fluid and solid domain for T1.

using the realizable $k-\varepsilon$ turbulence model with enhanced wall function and thermal effects enabled. Air was treated as an ideal gas for the fluid domain with thermal conductivity and viscosity evaluated by kinetic theory and Sutherland method, respectively. The solid domain used temperature dependent properties in [142] of the nickel superalloy CMSX-4 for density, thermal conductivity and specific heat capacity.

Each unit-cell was subject to the same boundary conditions of mass flow at inlet (per unit area), constant pressure outlets at film hole exhausts, heat flux at external wall as defined by a heat transfer coefficient and driving temperature, symmetry for fluid spanwise extents, periodic interfaces for streamwise front and back faces and symmetry for solid spanwise extents. An example of the domain with boundary conditions highlighted is shown in Fig. 8.4 with values applied in Table 8.2.

We must accept some limitations on the overall accuracy of the CFD given the associated problems with RANS models to accurately capture the thermal augmentation at the impingement jet stagnation point as well as that of the lateral wall jet. However, using a Realizable approach over the standard $k-\varepsilon$ should provide some improvement [17] and moderate accuracy was deemed appropriate to analyse broad trends between geometric variations.

Film Effectiveness Model

To avoid explicitly solving the external flow field and incurring high computational costs films were modelled using an empirical correlation first proposed by Goldstein [26], which models the decay of a film in both the streamwise (x) and spanwise (y) directions. A modified variation of this correlation is expressed in Equation 8.4 and shown to be appropriate by Murray et al. [10] and Courtis et al. [2].

$$\eta_f = \frac{MV_\infty D}{8\alpha_t \left(x/D + x_{decay}\right)} \exp\left(-\left(\frac{y}{c_1}\right)^{c_2}\right) \tag{8.4}$$

Experimental data of the film effectiveness for a single hole at a range of blowing ratios (M) was used to find the turbulent thermal diffusivity α_t and x_{decay}, which describes the decay in film effectiveness along the centre-line with streamwise distance. The spanwise distance constant, c_1 and spanwise shaping constant, c_2, are variables dependent on both M and x. Each film hole is subject to the modified Goldstein equation independently to find $\hat{\eta}_f$, and together with the film hole exit temperature, T_f, used in Equation 8.5 to compute the film effectiveness accounting for differences in T_f between film holes.

$$\eta_{f,j}(x,y) = \hat{\eta}_{f,j}(x,y)\frac{T_\infty - T_f}{T_\infty - T_c} \tag{8.5}$$

In practice M can be found from the mass flow and temperature at film hole outlets from the CFD, along with the external flow conditions: T_∞, P_∞, V_∞.

A superposition method proposed by Sellers [78] was used to capture the interaction between films. This represents an important distinction for some of the geometries investigated in this study due to the proximity of adjacent holes compared to typical cooling arrangements. Each film is taken to be independent, where downstream layers can be considered to operate with a free-stream temperature as influenced by the preceding film, and can be described by Equation 8.6 and visualised by Fig.8.5.

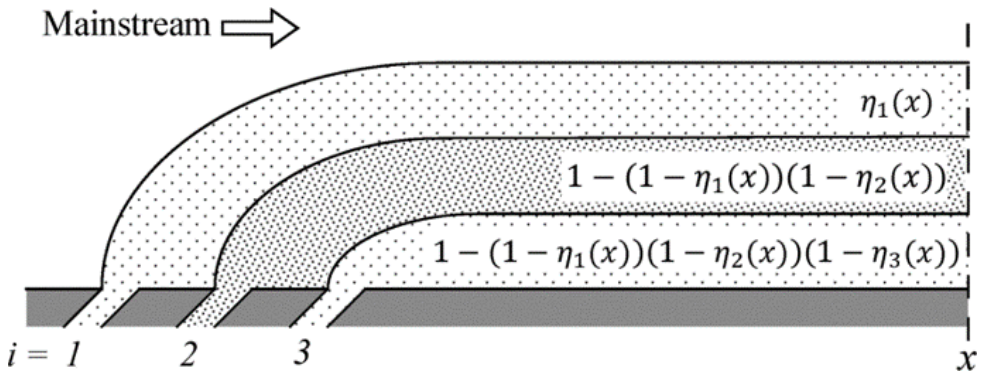


Figure 8.5: Illustration of the streamwise development of films using Sellers [90]

$$\eta_f(x,y) = 1 - \prod_{j=1}^{n} \left(1 - \eta_{f,j}(x,y)\right) \tag{8.6}$$

The film effectiveness and therefore adiabatic wall temperature for each film is calculated across the entire domain, and each global point (x,y) calculated with Sellers. Therefore the superposition of films will be accounted for across the entire domain and thus the adiabatic temperature can be determined at any point by:

$$\eta_f(x,y) = \frac{T_\infty - T_{aw}(x,y)}{T_\infty - T_c} \tag{8.7}$$

Coupling of Internal and External Thermal Fields

CFD internal wall temperatures T_w and heat flux q for the unit-cell were exported and expanded to make up the entire repeating cell domain. The heat transfer coefficient was calculated from these two parameters using the following equation

$$h = \frac{q}{T_w - T_{ref}} \tag{8.8}$$

Where T_{ref} was set as the inlet coolant temperature. The internal heat transfer coefficient (h) and coolant temperature (T_c) alongside the external wall temperature corresponding to the calculated film effectiveness ($n_f(x,y)$) were provided as inputs to *ANSYS Mechanical* for calculation of the overall thermal field. Outside of the repeating unit-cell domain, each component was prescribed the area-averaged value corresponding to that in the CFD solution, and the external side walls were treated as adiabatic walls. Refer to FIG. 8.3 for a visualisation of this process.

8.2.4 Results

Results shall be discussed in three parts as evaluated by the numerical method: internal features, film effectiveness and overall cooling. An overview of external film effectiveness and cooling effectiveness are tabulated in Table 8.5 and 8.6 for each geometry and condition. These can be found in Appendix 8.2.6.

Internal Features

Internal cooling of the geometries was compared using results from the CFD of the internal unit-cell. Convective heat flux for categorised internal features is shown for each geometry at $m^* = 3.3$ in Fig. 8.6. For comparison between unit-cells the heat flux per inlet unit area is normalised by the inlet area for T2:

$$q_n = q/(A_{in}/A_{in,T2}) \tag{8.9}$$

The internal convective area is positively influential on the overall heat flux sunk by the geometry, however, what is striking is the manner in which this is achieved. The majority of heat transfer for E1 and E2 occurs on the outerskin-inner surface, a result of the enhancement to heat flux caused by both the impingement and lateral jet on this surface. Conversely, the majority of cooling shifts to the internal film hole surface area for T1 and even more so for T2. Quantitatively q_n contributed by the film hole walls shifts from 6.4 to 33.5 [W/(m^2/m^2)] for E2 and T2 respectively, whereas the outerskin-inner surface falls from 19.4 to 8.0 [W/(m^2/m^2)]. Given the identical internal design of T2 and E2, the change in amount of impingement cooling observed is not a consequence of changes to the impingement jet itself, but the difference in outerskin temperature. The outerskin-inner mean temperature for T2 at $m^* = 3.3$ is 120 K less than that of E2 and consequently a lower heat flux for the same impingement Nusselt number was observed. As such the impingement jet may still offer more cooling potential at a given mass flow rate if further thermal loading is applied. And the more porous configurations (T1 and T2) offer redundancy in the cooling system as the impingement jet acts as a secondary cooling mechanism.

While mass flow distribution to the film holes for geometries with equal numbers of film and

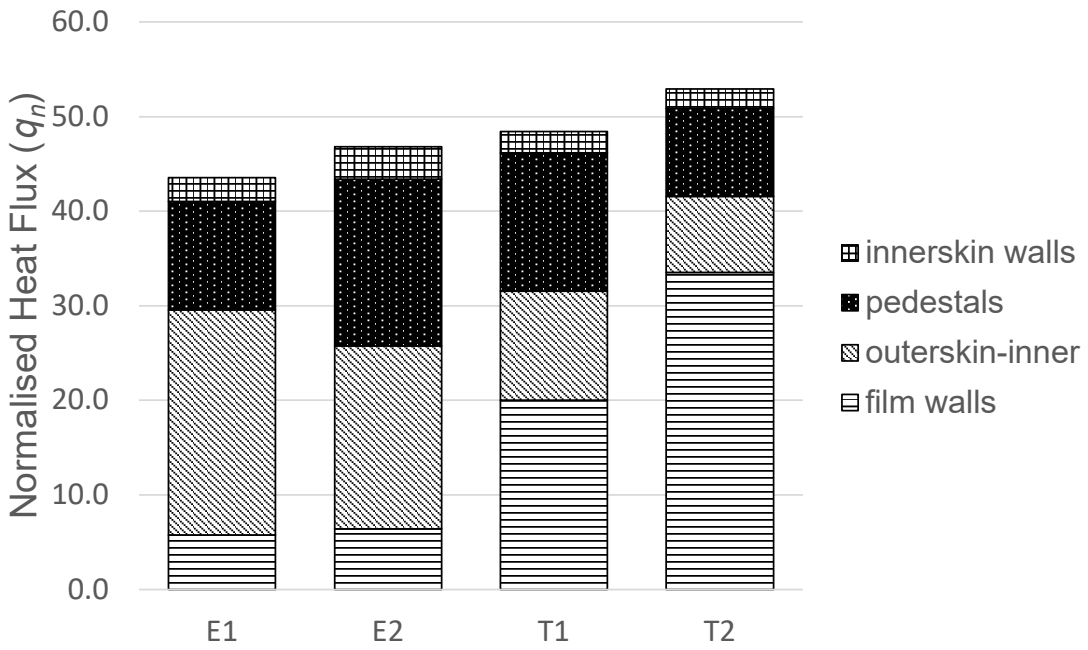


Figure 8.6: Magnitude of heat flux generated for each internal feature, m^* = 3.3. Cooling shifts from majority of the impingement jet (outerskin-inner surface) to the film hole internal area as internal film hole surface area increases.

impingement holes were approximately equal, T1 and T2 demonstrated variable flow distributions as observed in Fig.8.7. These findings are consistent with [143] where variation in coolant flow between film holes was heightened as the ratio between the porosity of the outer- and inner- skins (ϕ_o/ϕ_i) increased. In this case, near the impingement jet there was an outlet with a much higher mass fraction of flow and an outlet with reduced mass fraction. This is caused by the hole inclination angle and the two relative paths coolant must take in order to exhaust from each hole respectively. In the design of T1, film holes in close proximity to the impingement hole were removed, resulting in less variability in mass flow. For the remaining film inlets, the pedestals act as dampeners against large variations in coolant migration.

T2 demonstrates a more extreme variation in mass flow in which film holes directly upstream of the impingement jet are largely deprived of coolant. This is observed further by the velocity vectors for a cut-plane of the symmetry face for T2 in Fig.8.8. In the case of the film hole downstream of the impingement jet (the plot on the right), the lateral jet along the outerskin-inner wall has a turning angle of 30°. On the other hand, the upstream film hole imposes a turning of 150° which results in detachment from the wall surface and a separation bubble forms. A larger proportion of the flow will not make this turn and rather migrate toward other outlets. To

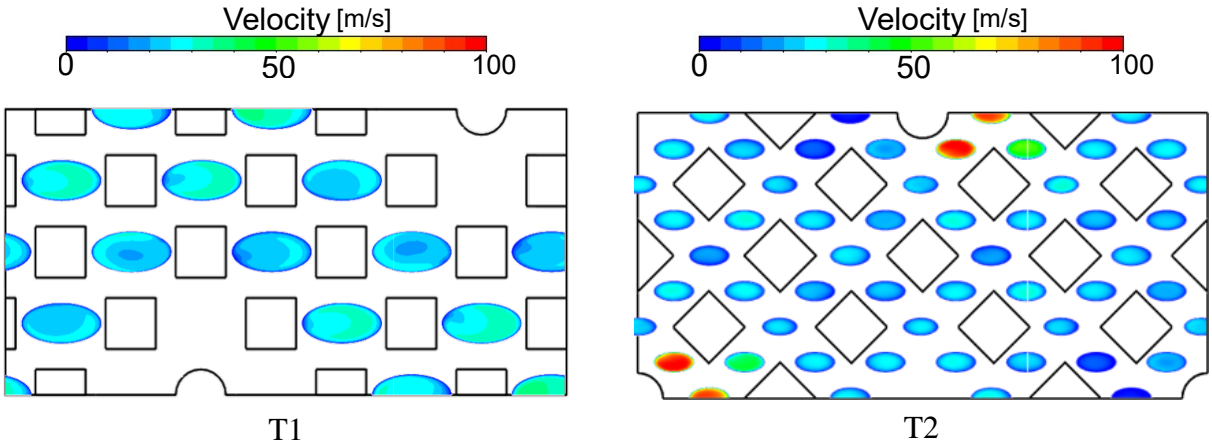


Figure 8.7: Film outlet distribution for T1 and T2. Velocity contours are displayed for each film hole outlet at the relative inlet position compared to the impingement holes and pedestals

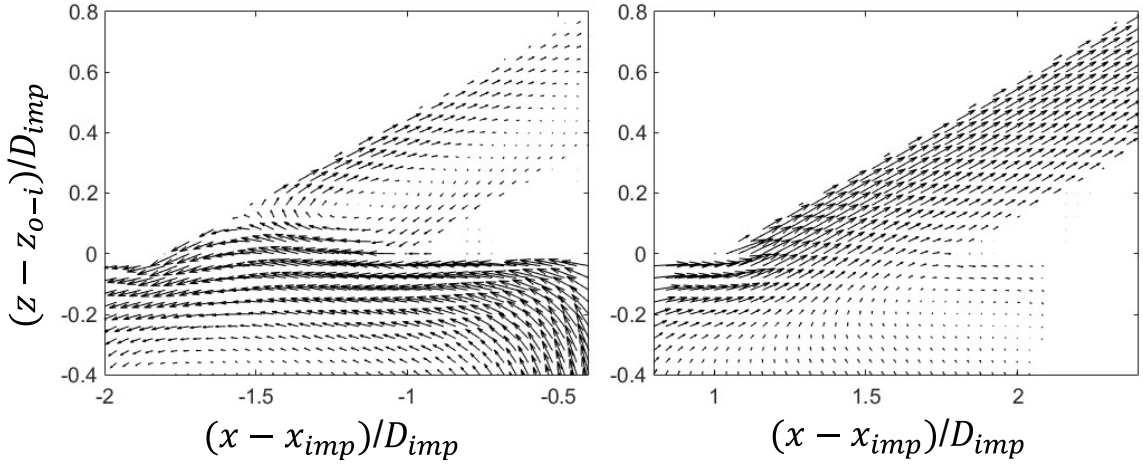


Figure 8.8: Velocity vectors for two film holes in close proximity to the impingement jet (T2). The left plot is the upstream film hole which has a poor mass flow fraction. The right hand plot is the downstream film hole which is overly compensated with coolant

alleviate this problem, removal of film holes at the cost of porosity could be made.

Further evaluation of the flow through the double-wall was made using the backflow pressure margin (BFM) which can be expressed as the ratio of the pressure drop and the exit static pressure.

$$BFM = \Delta P / P_{\infty} \tag{8.10}$$

This quantity serves as an indicator of positive flow of coolant through the blade. In this study, the BFM was found for both the film holes and across the entire double-wall and how these values change with mass flow are shown in FIG. 8.9. There was minimal difference in the

pressure margin across the entire double-wall between E2, T1 an T2, a consequence of the impingement process incurring the majority of the pressure drop and all three designs having the same impingement hole properties. Across the film holes the BFM reduced as ϕ_g of the outerskin increased, resulting in values lower than 1% for T1 and T2. This suggest increased susceptibility to hot-gas ingestion, where external high temperature flow enters into a film hole and may promote oxidation on surfaces which have no thermal barrier coating applied.

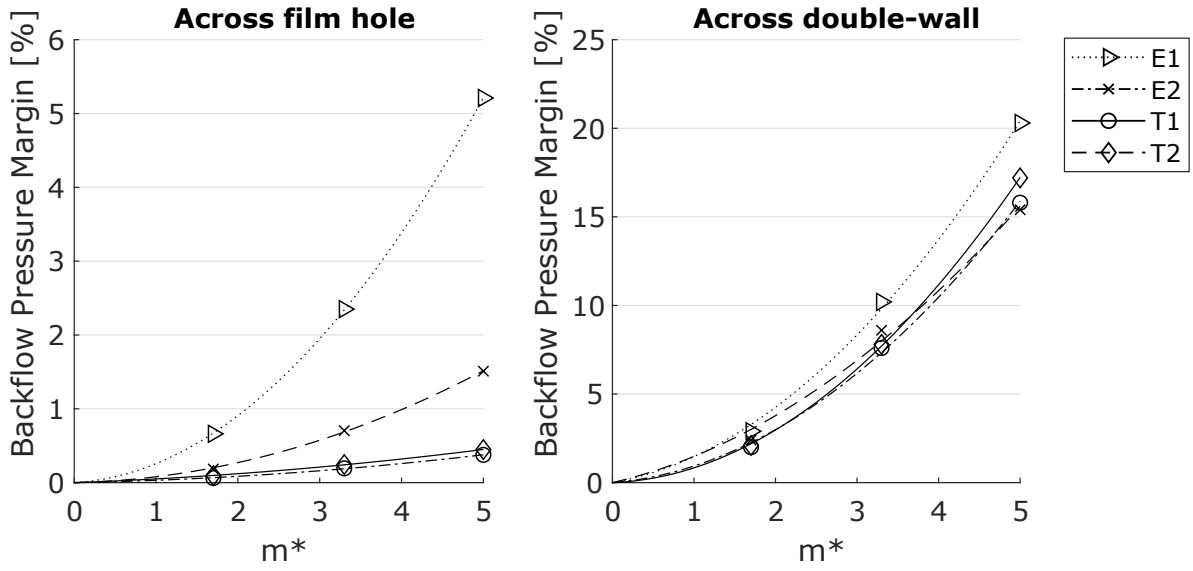


Figure 8.9: Backflow pressure margin (BFM). The BFM was calculated across both the film holes and double-wall, on the left and right plots respectively.

In this study a constant pressure was applied to the domain outlets, whereas in practice the presence of a pressure gradient would exist in the streamwise direction. On the suction surface especially, upstream film holes would be exposed to a higher static pressure, which ultimately may result in a skew of local film BFM throughout the unit-cell, and an even greater impact for the entire domain. As a worse case scenario, hot-gas ingestion may result and small film holes may be more susceptible to particle blockage by ash or dust. It has been shown [64, 144] that that an increase in metal temperatures was associated with an increase in blockage of volcanic ash and dust respectively, resulting in a positive feedback loop, inciting more blockage. Hence, any localised temperature rises could compound to much more global consequences. Another area for concern is that in the two aforementioned studies a large hole inclination angle with respect to the coolant flow direction had a higher rate of particle blockage. Unfortunately this corresponds to the film holes observed in this study to have the minimal mass flow rates, leaving

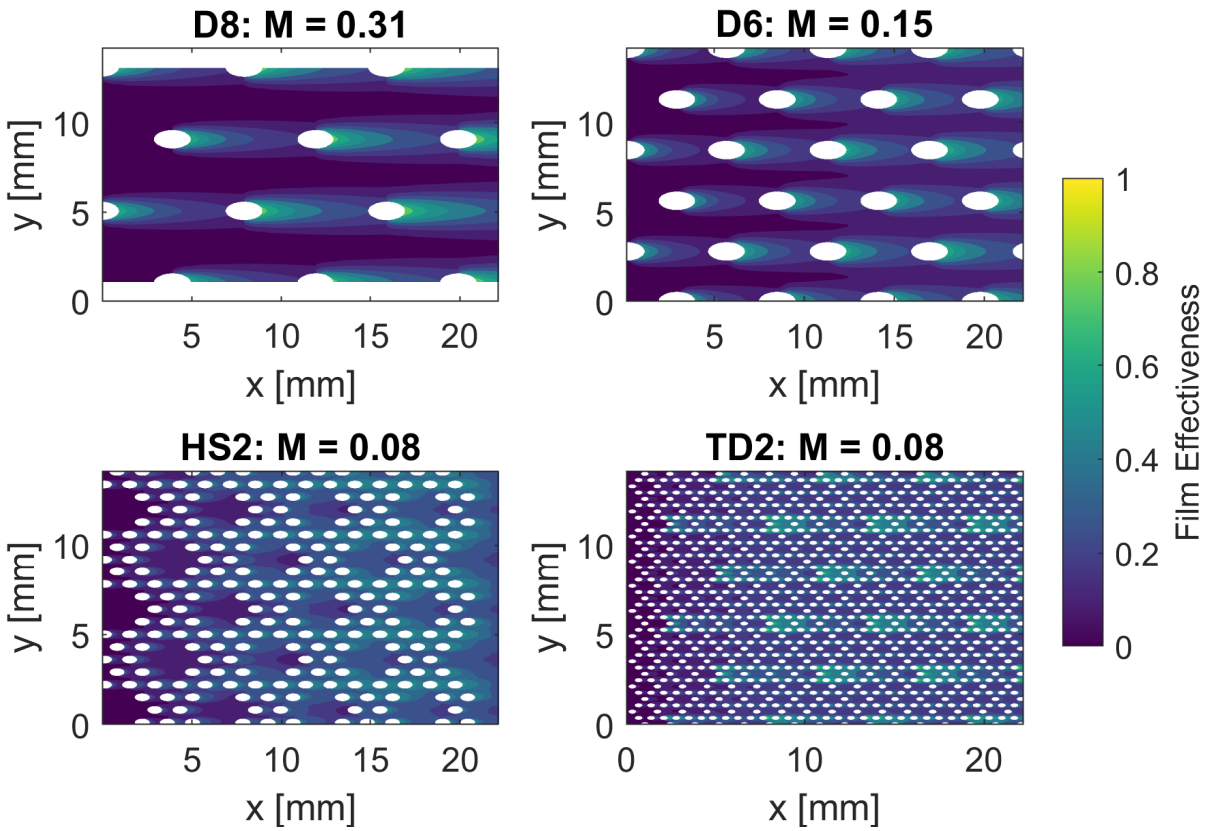


Figure 8.10: Film effectiveness contours for $m^* = 1.7$

them particularly vulnerable.

Despite the variation in outlet flow, the impact on internal cooling is minimal given the proximity of nearby film holes, and thus any imbalance of coolant distribution tends to be inconsequential to the overall cooling effectiveness. Additionally, given that the film hole with least mass flow was situated nearby the impingement jet, this is already in a region of high convective cooling. The large potential for cooling present in the outerskin acts to provide a more effective cooling system, and relatively high cooling effectiveness values at the outerskin can be realised even before the consideration of film effectiveness.

Film Effectiveness

Empirically calculated film effectiveness contours are displayed in Fig. 8.10 and Fig. 8.11. Two mass flow rates (m^* = 1.7 and 5.0) are displayed for each geometry, and the mean blowing ratio (M) at each condition displayed above the relevant plot. Areas with no or minimal film cooling, known as hot streaks, were evident for E1 and E2, but reduced for T1 and T2 once a lasting

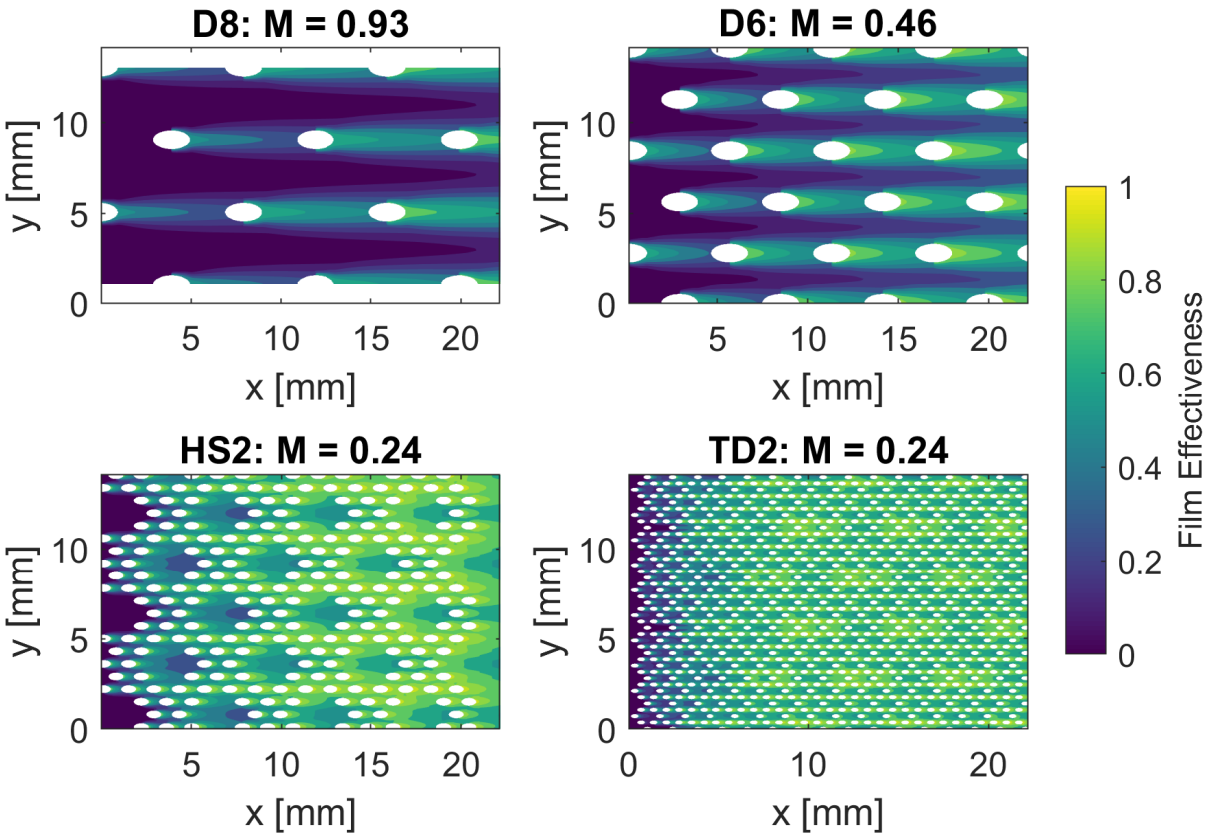


Figure 8.11: Film effectiveness contours for $m^* = 5.0$.

film was established. This is a result of the proximity of film holes in the spanwise direction (y) which enables interaction between adjacent film holes, whereas for more moderate spacing the film hole columns are not able to influence one another. For $m^* = 5.0$ the coverage is relatively uniform for T1 and T2 in the spanwise direction, with film effectiveness building up through superposition in the streamwise direction (x). However at the low mass flow rate of $m^* = 1.7$ variation in mass flow between film holes is evident, resulting in hot streaks. Despite this, the coverage of film protection is more uniform than that of E1 and E2.

Spanwise-averaged film effectiveness at $m^* = 5.0$ was calculated for each geometry and illustrated in Fig. 8.12. Both T2 and T1 reach a saturated film effectiveness of approximately 0.7 and 0.75 respectively. T2 reaches this in approximately 8.5 mm which corresponds to 12 film hole rows and T1 reaches this after about 16 mm (11 rows). This indicates a benefit of smaller film hole diameter, as more film rows are required for a given distance and therefore more superposition. Additionally, we have a reduced streamwise distance with no film cooling. However, this comes at the cost of variable mass flow distribution and the associated problems previously

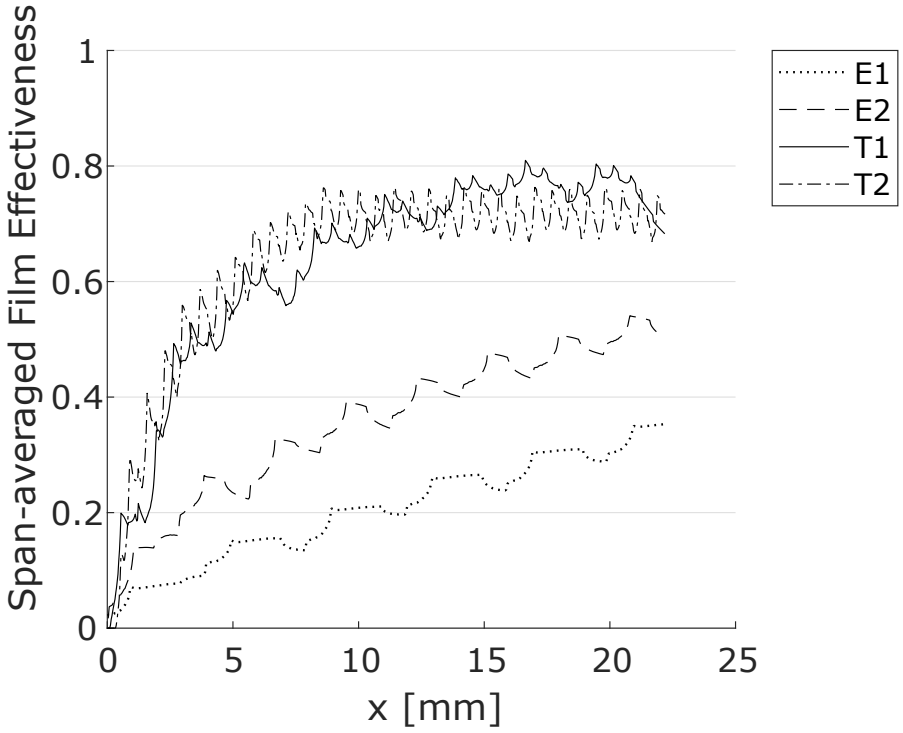


Figure 8.12: Span-averaged film effectiveness for $m^* = 5.0$. Geometries with higher outerskin porosity exhibit elevated film effectiveness for the same mass flow rate.

mentioned, and in practice could have the problem observed by Wambersie et al. [100], where a similar hole diameter (0.5 mm at 2.3x engine scale) had hot gas ingestion and consequently no film protection for the first several rows.

E1 and E2 had reduced protection throughout the domain, and did not reach a plateau in film saturation. For E1, jet lift-off occurred given the worse performance of individual films compared to E2. Consequently, we have realised the benefits of superposition between adjacent rows which ultimately provides a more uniform and elevated film coverage.

Overall Cooling

Assessment of the thermal performance was captured through a parameter known as the cooling effectiveness, ε. Defined in Equation 8.11 as the ratio of temperature difference between the mainstream flow and solid surface to that of the driving temperature.

$$\varepsilon = \frac{T_\infty - T_w}{T_\infty - T_c} \tag{8.11}$$

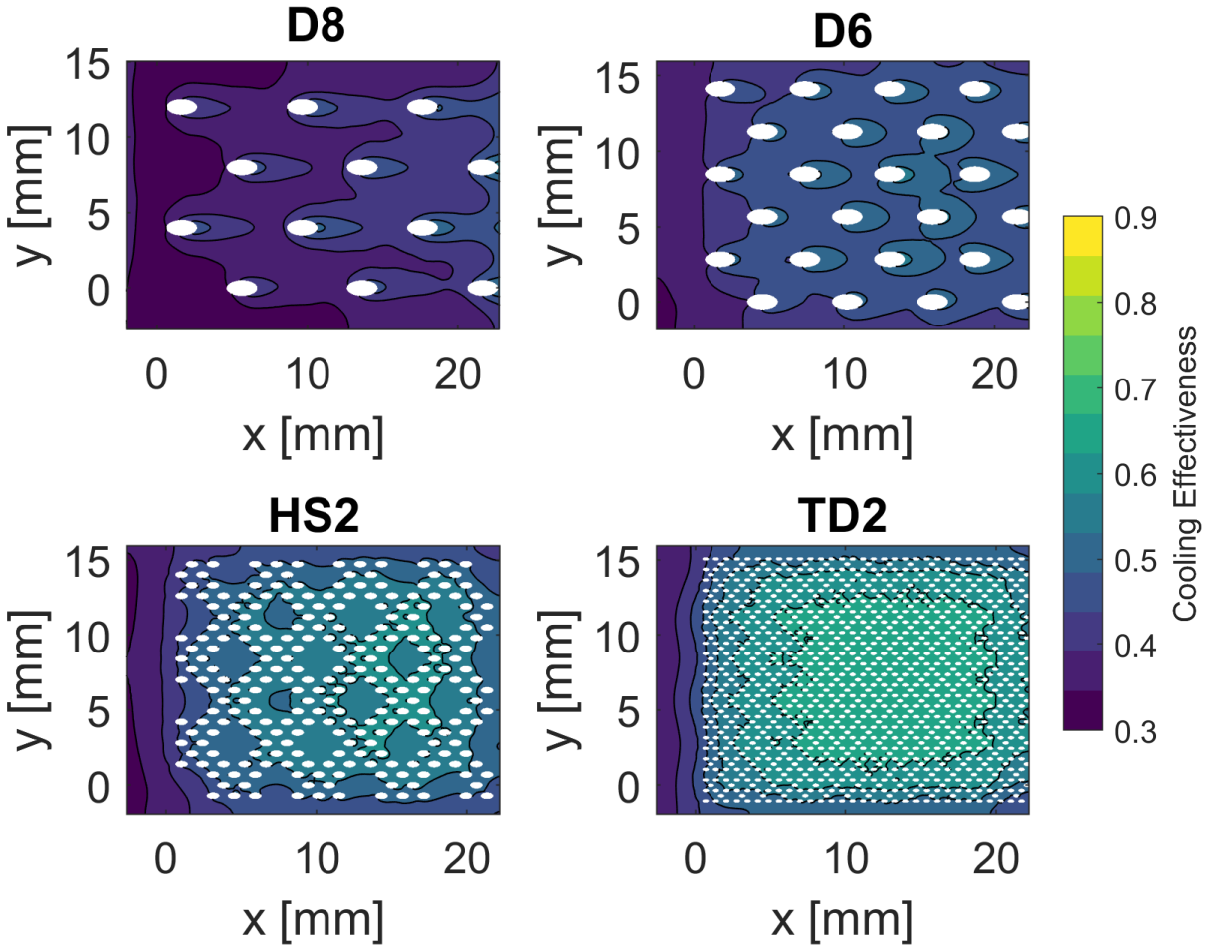


Figure 8.13: Cooling effectiveness contours at $m^* = 1.7$

Cooling effectiveness throughout the domain was calculated for each geometry at $m^* = 1.7, 3.3, 5.0$ and results for the external outerskin surface displayed by contours in Fig. 8.13 and Fig. 8.14. In both contour sets a benefit to thermal protection offered by T1 and T2 over the other two geometries was observed. Both have a faster increase in ε with steamwise distance as well as an elevated peak ε. Additionally, thermal protection is more uniform in the spanwise direction, with some variation as a result of impingement cooling, disparity in coolant flow between film holes and gaps between film hole locations.

Area-averaged cooling effectiveness ($\bar{\varepsilon}$) are displayed in Fig.8.15. As would be expected the inner and outer effectiveness increased with added coolant mass flow, with diminishing returns for an increase in m^*. T2 displayed a higher $\bar{\varepsilon}$ of 0.22 and 0.125 compared to E1 and E2 respectively for the outerskin surface. For a driving temperature of 870K this corresponds to a range of 100 K to 200 K benefit to mean temperatures. Another feature presented here is that

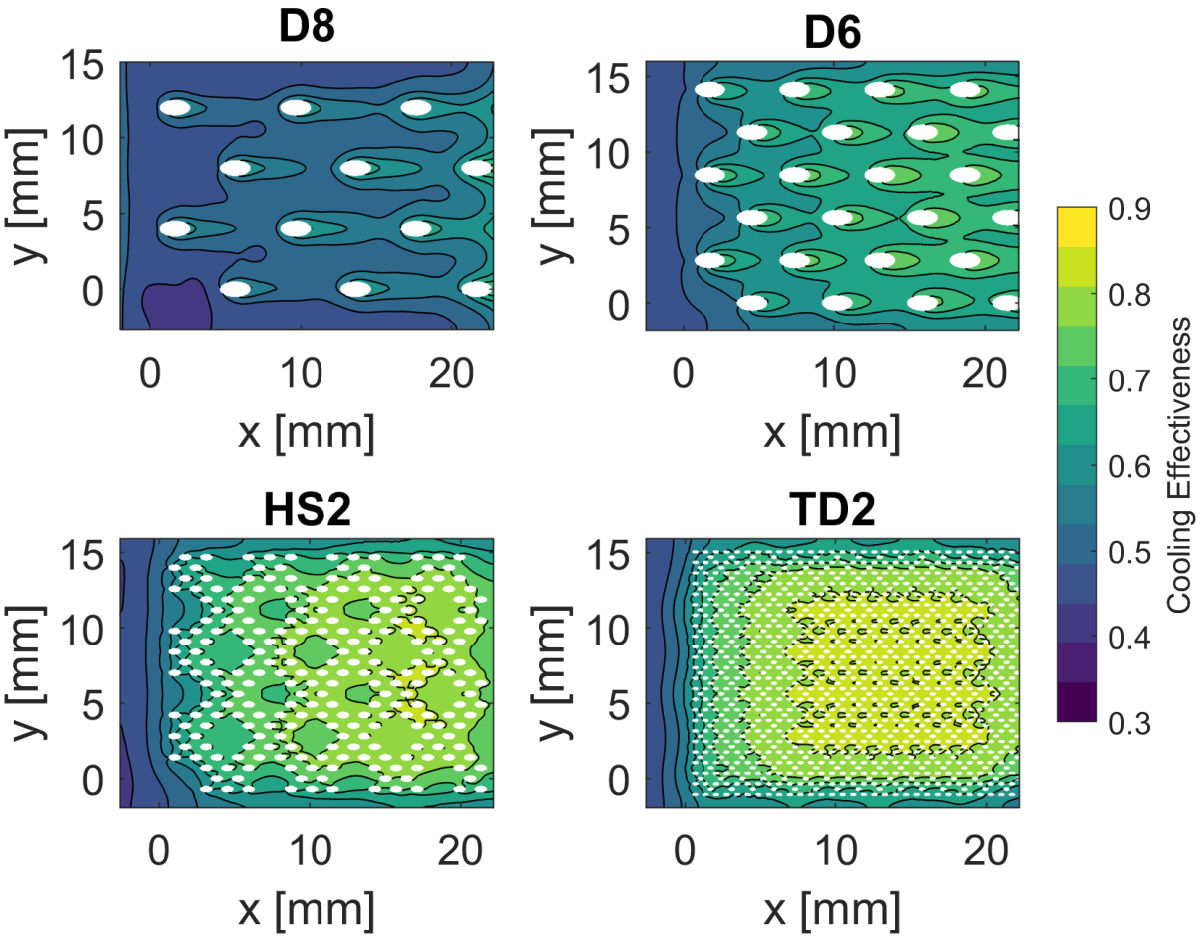


Figure 8.14: Cooling effectiveness contours at $m^* = 5.0$

with added mass flow, the benefits of T2 compared to T1 start to diminish, as both geometries appear asymptotic towards similar values. However, both exhibit expected asymptotes higher than E2 which additionally sits above E1.

m^*	1.7	3.3	5.0
E1	0.24	0.27	0.29
E2	0.27	0.27	0.26
T1	0.25	0.23	0.21
T2	0.21	0.19	0.17

Table 8.3: Overall effectiveness difference between the outer and inner exterior surfaces, $\bar{\varepsilon}_{ov,o} - \bar{\varepsilon}_{ov,i}$. The temperature gradient between skins can be reduced with increased outerskin porosity.

A reduction in temperature gradient was observed through the double wall geometry for more transpiration-like configurations. This can be inferred by the difference in the inner (dashed line) and outer (solid line) surface for each geometry. These have been tabulated in Table 8.3, where T2 had the lowest temperature gradient throughout the range of mass flows.

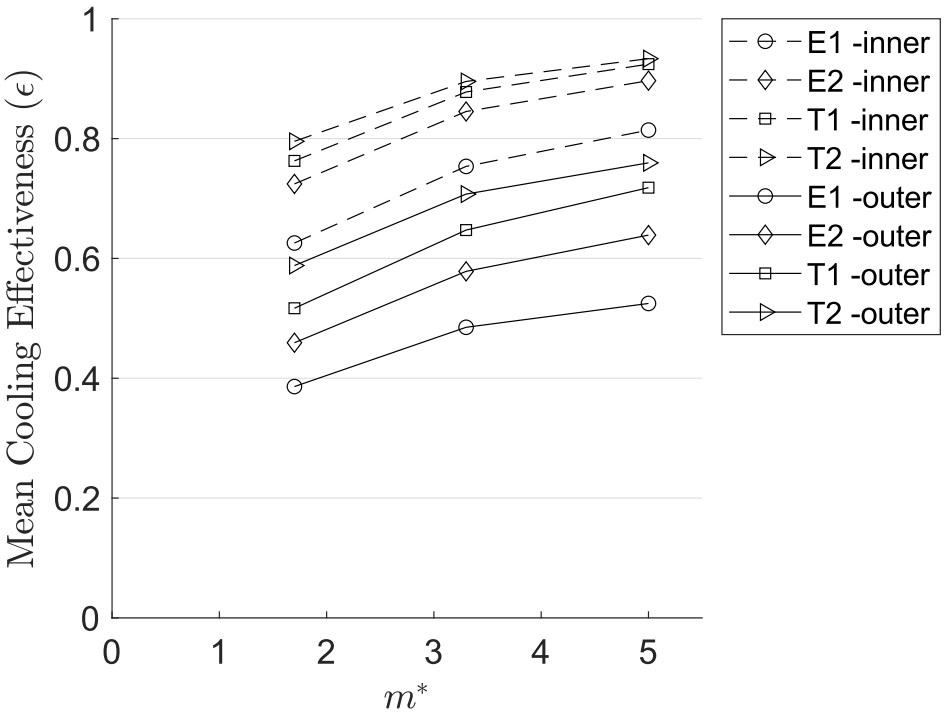


Figure 8.15: Inner and outer mean overall-effectiveness. The two geometries with 20% geometric porosity (T1 and T2) displayed elevated cooling effectiveness for both surfaces across the range of coolant mass flows.

A large proportion of the cooling potential has been shifted towards the outer-external surface, resulting in the outerskin being cooled more effectively, and high temperatures do not persist as far radially into the blade. While this also decreases temperatures in the innerskin, this relation is not linear. For both T2 and T1, added mass flow reduces this temperature gradient, while it appears insensitive for E2 and the converse trend for E1. For a designer this is encouraging as three main drivers of thermal stress (peak temperature, mean temperature and temperature gradient) can be minimised through increased outerskin porosity and the introduction of added coolant.

While we have discussed the benefit of elevated protection at a fixed mass flow rate, an equally useful implementation would be to reduce the coolant required for adequate protection, benefiting overall engine-cycle efficiency. A simple linear interpolation of the equivalent m^* required for T2 to meet the cooling effectiveness of E2 at $m^* = 3.3$ equates to a m^*_{eq} of 2.46. Hence, reducing the required coolant mass flow rate by approximately 25%.

Reduction in film hole diameter between T1 and T2 provided increased internal surface area,

promoting further increase to the overall cooling performance and can be quantified by the difference in $\bar{\varepsilon}$ on the outerskin exterior surface which was 0.08 0.07 and 0.05 at m^* = 1.7, 3.3 and 5.0 respectively. These are significant increases in cooling performance, however, the added risk of hot-gas ingestion and hole blockage must be considered by a designer before implementation.

	Area-Averaged TF			Minimum TF		
m^*	1.7	3.3	5.0	1.7	3.3	5.0
E1	0.36	0.36	0.36	0.19	0.14	0.13
E2	0.26	0.24	0.22	0.16	0.11	0.09
T1	0.22	0.17	0.13	0.15	0.08	0.04
T2	0.17	0.11	0.09	0.11	0.04	0.035

Table 8.4: Transpiration Factor for the outerskin external surface for the repeating unit-cell area. Here the area-average as well as minimum values are tabulated.

Given our ambitions for transpiration cooling systems an assessment of how close we are was made. Theoretical transpiration cooling is achieved once the solid and coolant fluid have reached equilibrium, but a practical definition could be made as a temperatures difference of 1% or lower compared to the driving temperature difference. A transpiration factor is presented here as

$$TF = \frac{T_w - T_c}{T_\infty - T_{c,in}} \tag{8.12}$$

Tabulated data for the outerskin external surface TF are given in Table 8.4, where in this instance T_c is the average outlet temperature $\bar{T}_f$. The area considered was the region of the unit-block domain ($x > 0$, $0 < y < nS_{y,j}$) to exclude the influence of the unprotected upstream and side flanges.

E1 and E2 are far from transpiration even at the highest mass flow rate investigated with the external hot surface at an area-averaged value of 36% and 22% respectively. Even the high porosity of T1 only had a TF of 13%, although the minimum value is 4.0%. T2 exhibited an area-averaged TF of 17 %, 11% and 9% and the minimum TF achieved across the geometry was 11%, 4.0% and 3.5% respectively. These results demonstrate that T2 is not drastically far from an idealised transpiration cooled system for mass flow rates above $m^* = 3.3$, as well as across significant portions of the T1 domain.

8.2.5 Summary

A decoupled conjugate method was applied to double-walled cooling systems using computational fluid dynamics for the internal aerothermal field and an empirical correlation for external thermal loads. Outerskin porosity was investigated to assess the impact on both cooling performance and internal flow structure. Internal cooling shifts from being mainly dependent on the impingement jet (for outerskin porosity lower than 10%) to the internal surface area of film holes (for outerskin porosity near 20%). While theoretical transpiration was not realised for the geometries studied, the most effective geometry (T2) may be deemed to be transpiration-like with differences in solid and fluid temperatures of less than 10%.

High outerskin porosity configurations exhibited variable outlet mass flow which would appear to be dependent on the film to impingement hole ratio, and the proximity of the film hole inlets to the impingement-jet stagnation region. Further research is required to assess the impact of flow migration for highly porous systems, and the effect external pressure gradients imposed by the suction and pressure surface will have on the distribution of coolant as well as susceptibility to hot-gas ingestion.

In general, an increase in outerskin porosity provided the following benefits:

1. More uniform and elevated film effectiveness protection on the external blade surface.
2. Reduction in the maximum and mean temperature on the external surfaces as well as enhanced overall cooling performance throughout the double wall structure.
3. Reduction in the thermal gradient between outer and inner skins.

Exploration into the highlighted benefits and further knowledge of associated issues will help to facility the integration of transpiration-like DWEC configurations into real-engine turbine blade design.

8.2.6 Tabulated Results

	Area-Averaged η_f			Max η_f		
m^*	1.7	3.3	5.0	1.7	3.3	5.0
E1	0.17	0.19	0.20	0.78	0.74	0.76
E2	0.20	0.32	0.35	0.69	0.86	0.86
T1	0.27	0.51	0.63	0.56	0.89	0.96
T2	0.29	0.51	0.63	0.83	0.93	0.97

Table 8.5: Film Effectiveness: area-averaged and maximum results

	Area-Averaged ε_o			Minimum ε_o		
m^*	1.7	3.3	5.0	1.7	3.3	5.0
E1	0.39	0.49	0.53	0.31	0.39	0.44
E2	0.48	0.61	0.67	0.36	0.45	0.49
T1	0.55	0.70	0.77	0.38	0.46	0.50
T2	0.64	0.77	0.82	0.44	0.53	0.58

Table 8.6: Cooling effectiveness on the outerskin outer surface: area-averaged and minimum results

8.3 Experimental Results

T2 and T1 configurations were tested in the facility described in Section 5.3.2.3 using two brazed metal plates and monitored on both sides by two IR cameras. The results of film cooled wall are displayed as cooling effectiveness contour plots in Figures 8.16 and 8.17 respectively and can be compared to results of E2 by Murray [85] in Figure 8.18. T2 exhibits high cooling effectiveness with values of 0.9 and over at $m^* \geq 5.46$. In general, across the coolant flow rate investigated, the variation in cooling effectiveness in the spanwise direction was low, less than 0.1. And reasonable levels of protection above 0.6 were observed even at low m^*. These high levels of protection were a consequence of high internal surface area leading to high internal convection as well as the benefits of film superposition alongside the film proximity removing areas where hot-streaks can develop. For T1, similarly high levels of protection occurred as well as low variation in the ε_o in the spanwise direction, but the absolute levels for T1 were lower than that of T2, especially at low m^*. As an example, comparison of the bottom-left ($m^* = 2.94$) plot in 8.17 and the middle-left ($m^* = 2.90$) in Figure 8.16 highlights the elevated cooling effectiveness for T2 compared to T1. The latter offers less internal surface area compared to T2, but at twice the Reynolds number as a consequence of a larger film diameter. However, given the relation for internal convection as expressed by the Dittus-Boelter equation, $Nu \propto Re^{0}.8$, and that T2 has twice the internal film-hole wetted area, it would be expected for T1 to have lower internal convective cooling. The CFD displayed this behaviour in Section 8.2.4 Figure 8.6.

In contrast to T1 and T2, the less porous geometry of E2 had visible variation in the cooling effectiveness in the spanwise direction. This was a consequence of the discrete film behaviour and hot-streaks for moderately spaced film holes, and the reduction of film hole proximity to one another concentrates the internal convective cooling at these same locations. Moreover, not only was the highest levels of cooling protection not reached, but the most upstream visible region experienced much lower protection, which was likely a combination of the hot-streak behaviour and lower internal convective cooling. As a consequence the peak temperature is higher for E2 in comparison to T1 and T2. For all three configurations presented here there was no visible influence of the impingement jet cooling on the external wall. This was a consequence

of a relatively large number of impingement jets, reducing the spacing internally between locations with minimal convective cooling and a reduced jet Reynolds number resulting in a lower peak internal Nusselt number. Additionally, especially for the case of E2, the locations without impingement cooling are where the film hole is located. For T1 and T2, the number and coverage of film holes lends itself to more uniform temperature distributions.

The impingement-side contours are shown in Figures 8.19, 8.20 and 8.21, for T2, T1 and E2 respectively. T2 exhibited high cooling effectiveness which was asymmetric with elevated values on the downstream half, but there was a reduction as one moves towards the downstream edge. This would be expected as there was no internal cooling present along the flange regions of the double-wall configuration, but the build-up of film effectiveness reduces the external heat load downstream from the leading edge. In contrast, for T1, the reduction in cooling effectiveness near the downstream flange was less apparent than T2. And the peak cooling effectiveness region occurred further downstream being around the final impingement row for T1, compared to the penultimate row for T2. The only difference in internal features was the orientation of the pedestals, but this would not explain the differences highlighted here. The suspected cause may be that the cooling effectiveness on the film-side surface is more biased downstream for T1, compared to T2, which in turn shifts the location of the peak for the impingement-side. For E2, this location was more similar to T2, the penultimate impingement row. However, E2 had a lower cooling performance compared to either T1 and T2. Given the similarity of internal features and previously discussed inferior film-side protection, this comes as no surprise.

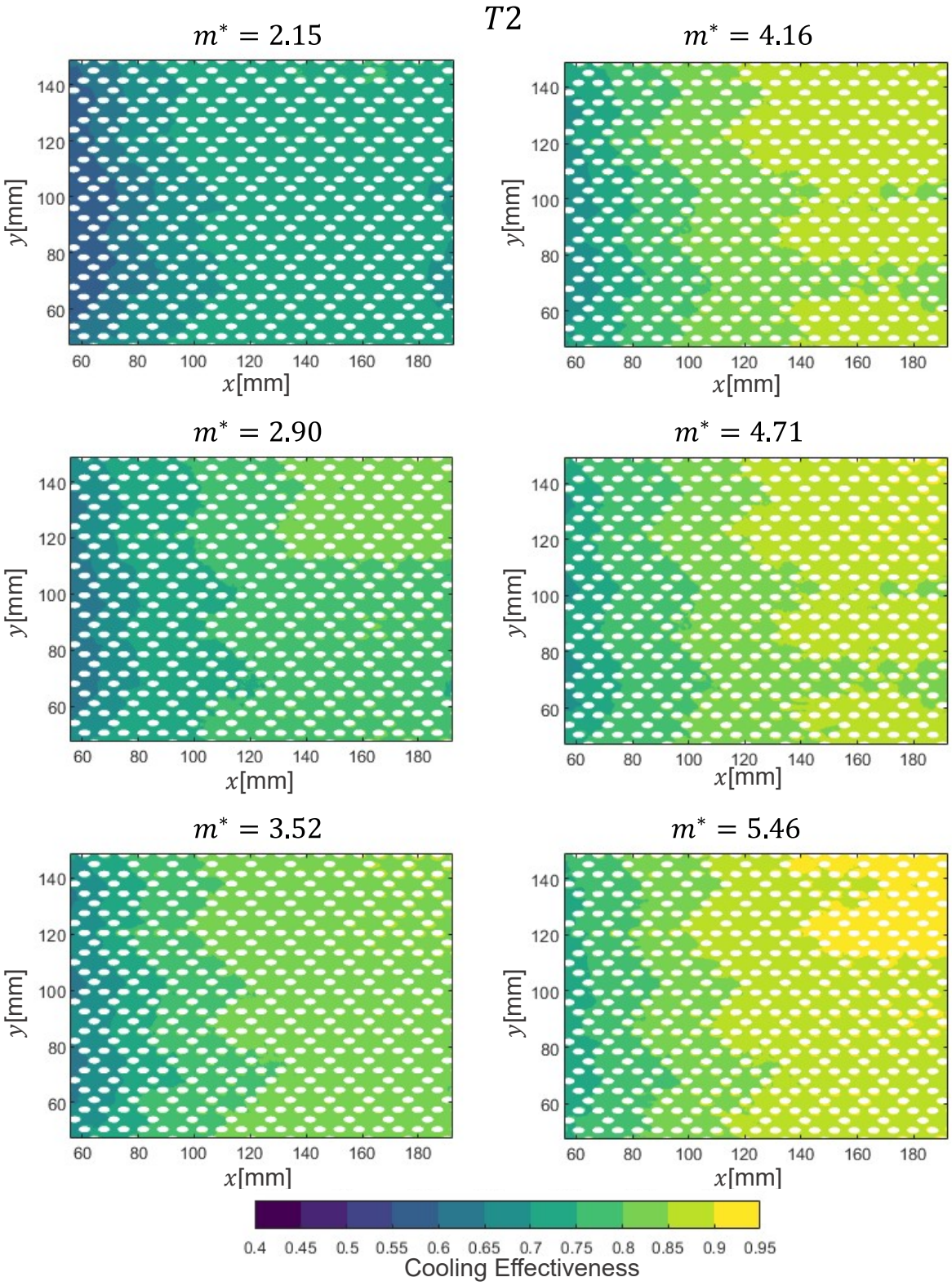


Figure 8.16: IR external cooling effectiveness on the outerskin-outer surface (film cooled wall).

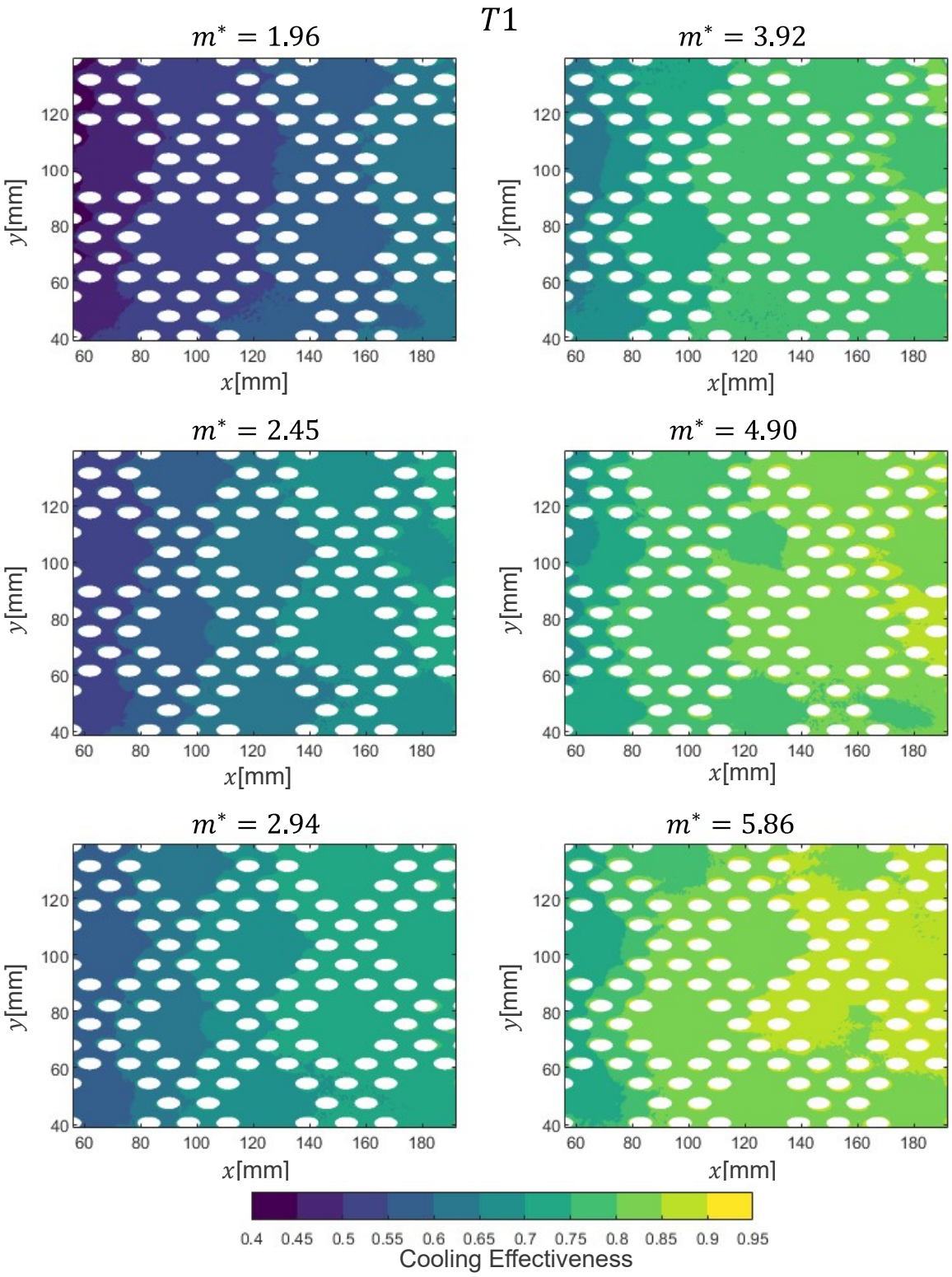


Figure 8.17: IR external cooling effectiveness on the outerskin-outer surface (film cooled wall).

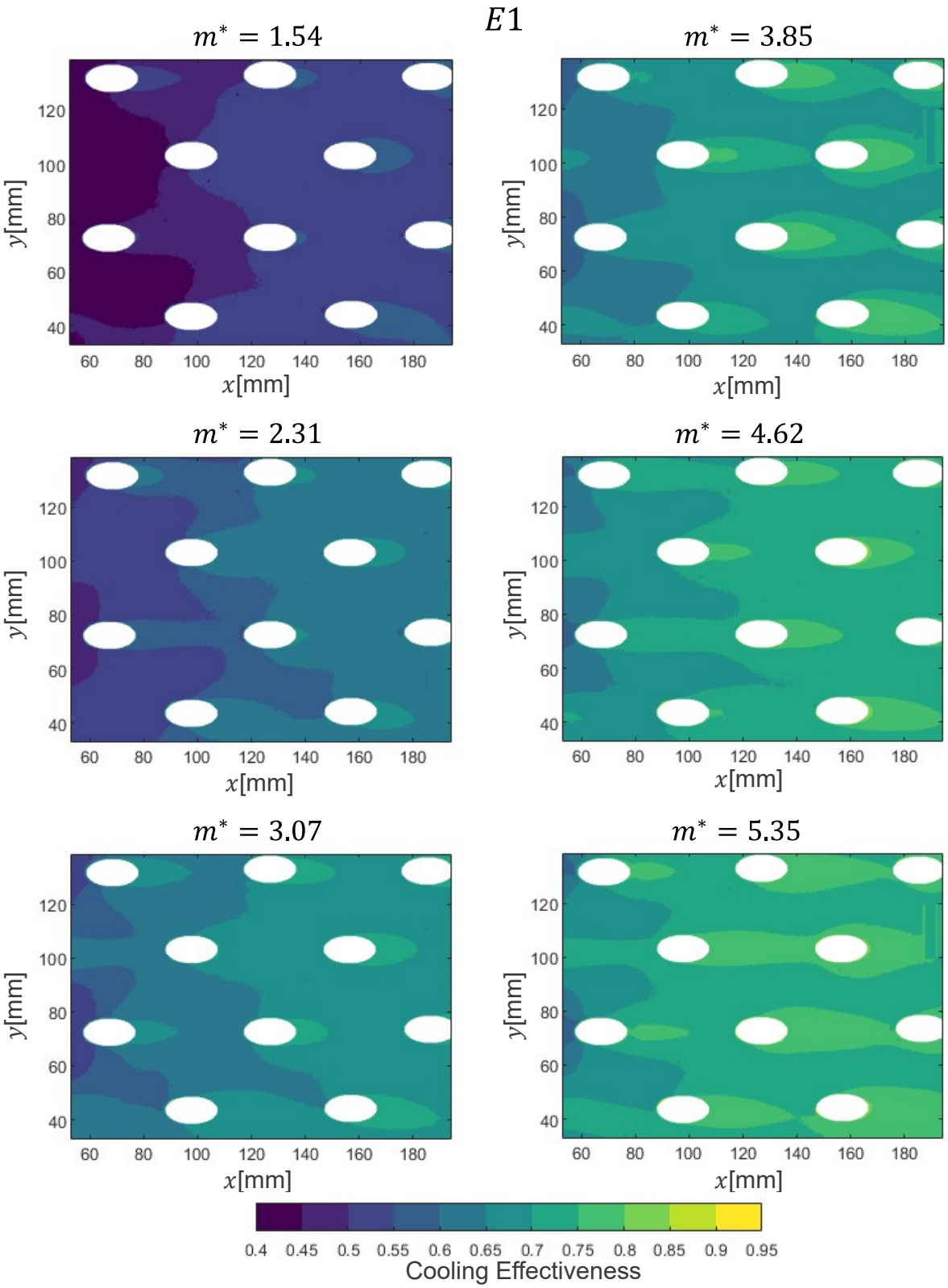


Figure 8.18: IR external cooling effectiveness on the outerskin-outer surface (film cooled wall).

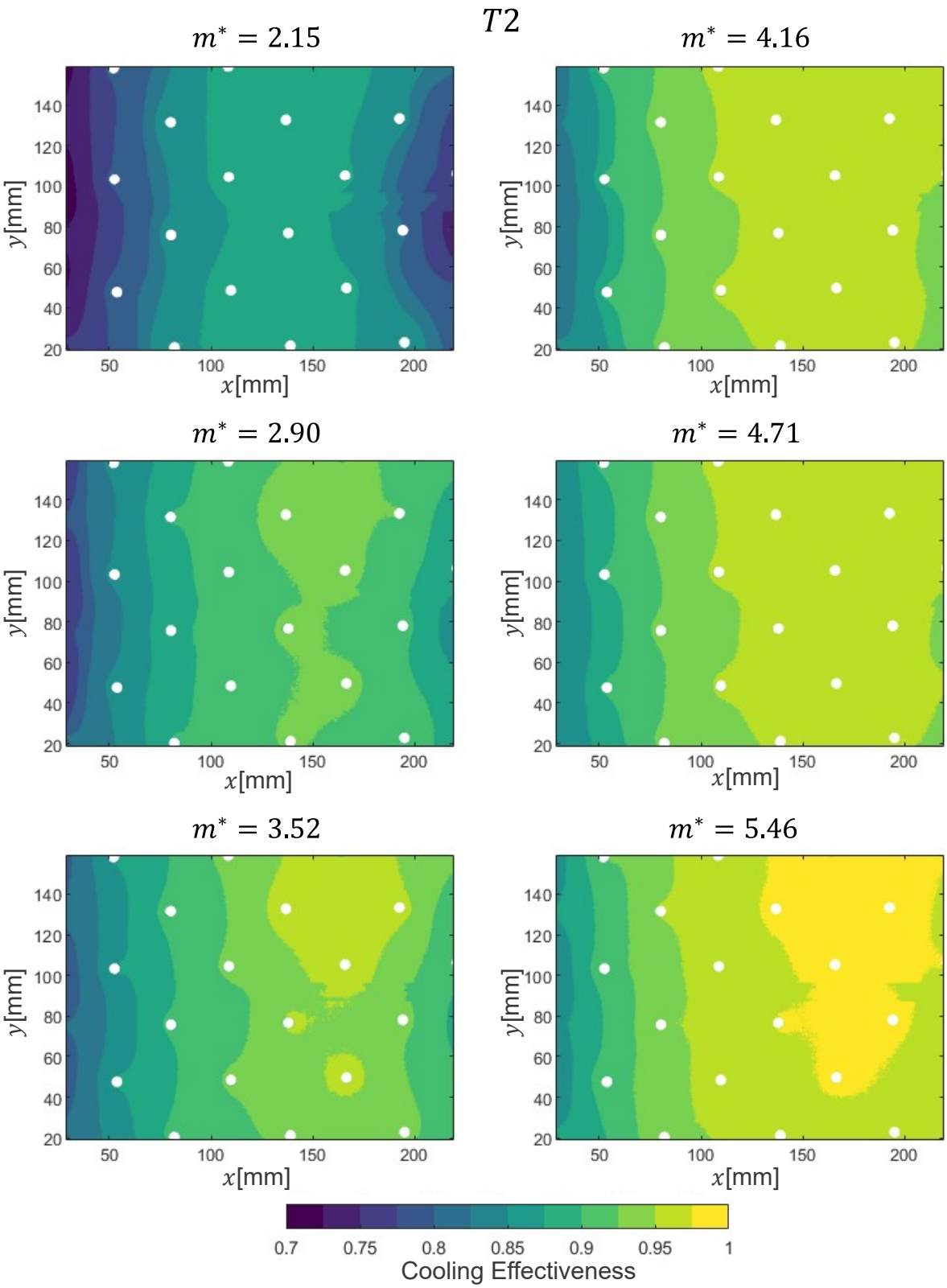


Figure 8.19: IR external cooling effectiveness on the innerskin-inner (impingement wall).

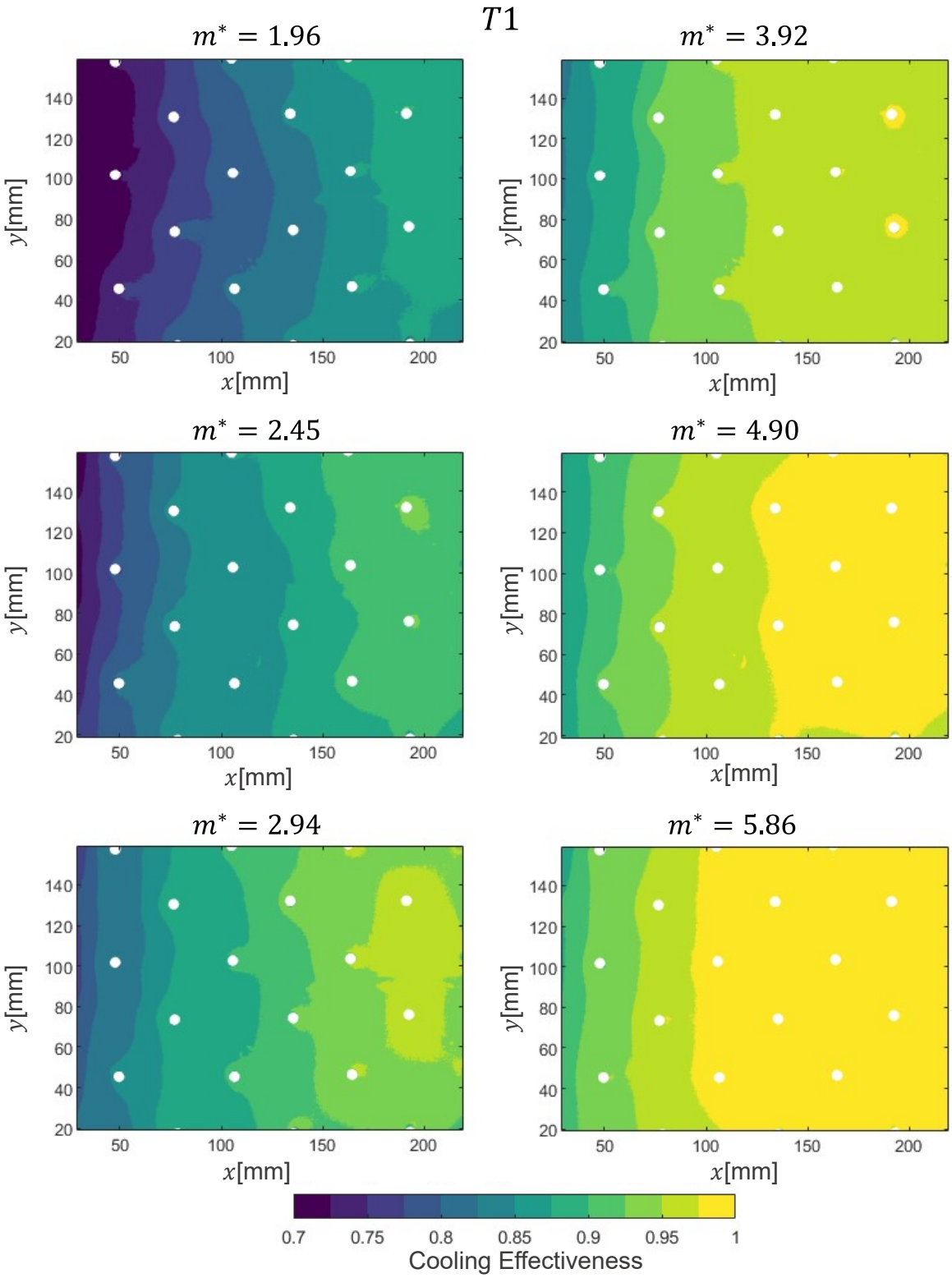


Figure 8.20: IR external cooling effectiveness on the innerskin-inner (impingement wall).

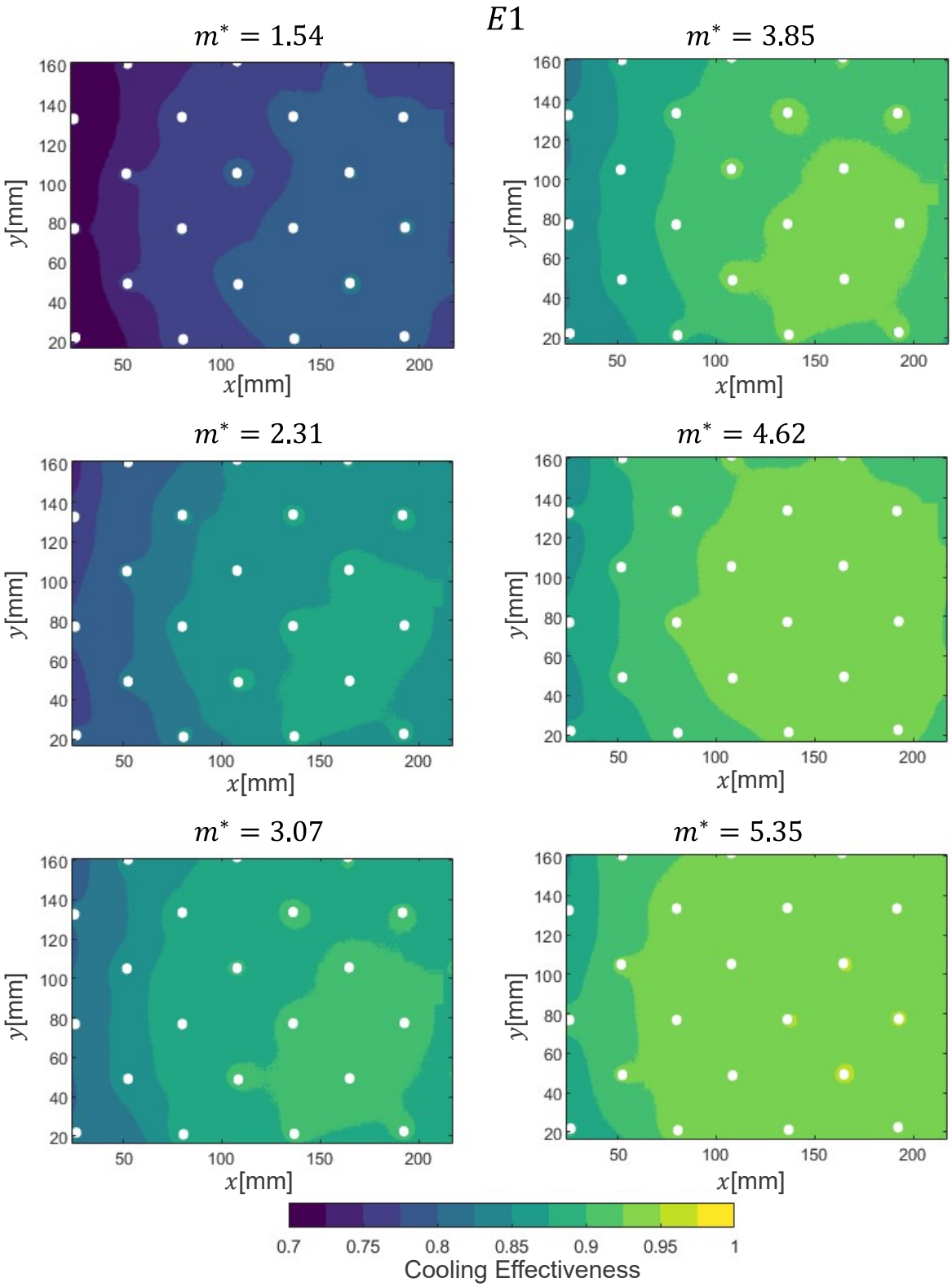


Figure 8.21: IR external cooling effectiveness on the innerskin-inner (impingement wall).

The area-average of the cooling performance of each configuration at each coolant flow rate is shown in Figures 8.22 and 8.23 for the film-side and impingement-side respectively. E1, T1 and T2 results are plotted alongside all the DWEC results by Murray [85]. The most striking feature for the film-side results is the increased protection provided by T2 over T1 and E2. Additionally, in comparison to the best performing geometry investigated by Murray, TD2 raised the area-average η_o by between 0.05 and 0.1 in the range $1.5 < m^* < 5.5$. For operating conditions of $T_\infty = 2000\,\text{K}$ and $T_c = 1000\,\text{K}$ this represents a reduction between 50 K and 100 K, providing a reduction in the likelihood of material creep. For T1, mid-range and higher mass flow rates ($m^* > 3$) provide elevated protection compared to Murray's configurations and it approaches the levels of T2. However, at low coolant rates, $m^* < 3$, T2 had lower effectiveness levels compared to Murray's best configuration, and for $m^* < 1.5$ didn't perform as well as E2. Given the similar levels of film protection offered by T1 and T2, the internal cooling becomes the driving force for these differences, where T2 has elevated internal cooling due to the increased film-hole wetted-area. At low flow rates, and therefore small blowing ratios, the internal cooling dominates the performance, which realises the difference between T1 and T2. The lower internal convective cooling does not make-up the difference due to poor film cooling as compared to E2 where the blowing ratios are less than lift-off and operating effectively. As coolant increases the films being to operate more effectively and with superior superposition and internal wetted area, T2 provides elevated protection compared to Murray's designs. As coolant is increased further the film protection starts to dominate cooling behaviour and therefore the difference in overall cooling performance between T1 and T2 is reduced.

For the impingement-side, the difference between the E2, T1 and T2 is relatively low, < 0.05. T1 demonstrated the highest values at the high flow rates, but given the high levels of cooling performance the realised surface temperatures would not be a concern for normal operation and hence all can be assumed adequate.

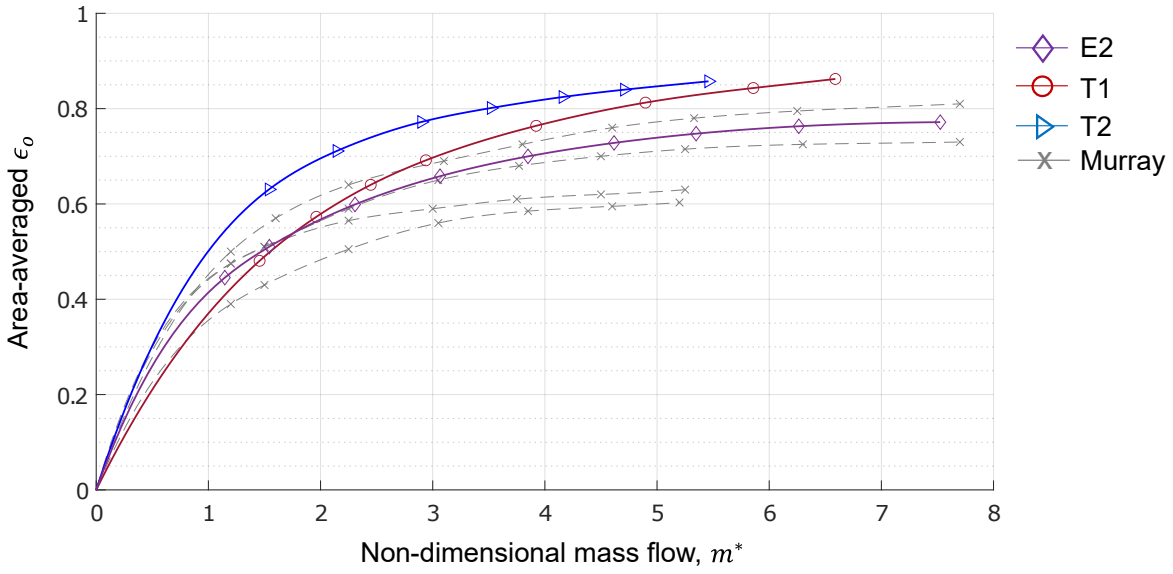


Figure 8.22: IR mean external cooling effectiveness on the outerskin-outer surface (film-cooled wall) for variable porosity configurations, as well as experimental DWEC configurations by Murray [85].

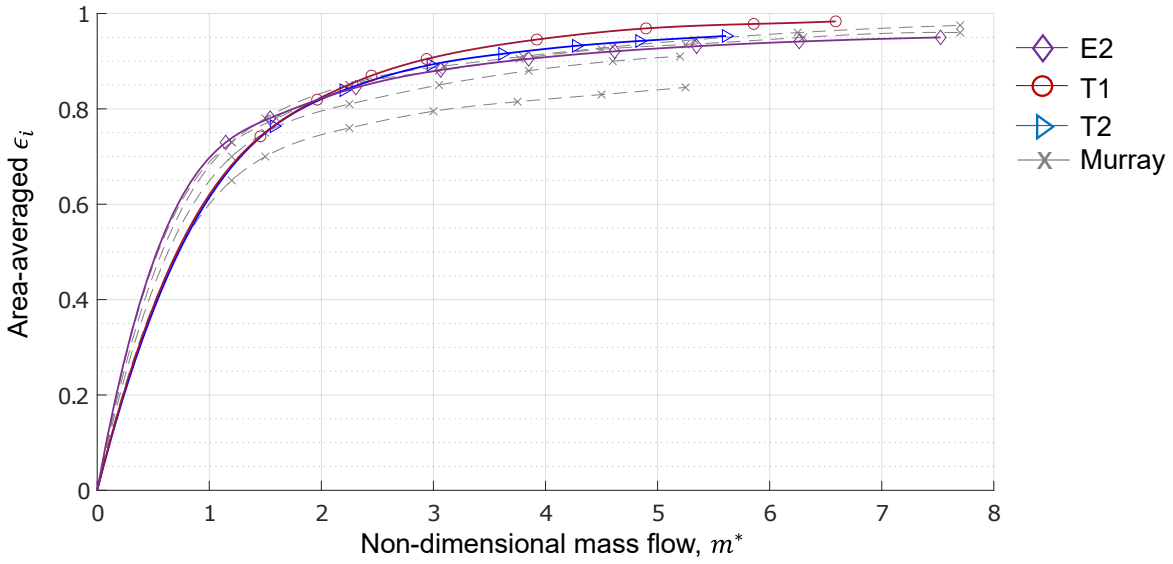


Figure 8.23: IR mean external cooling effectiveness on the innerskin-outer surface (impingement wall) for variable porosity configurations, as well as experimental DWEC configurations by Murray [85].

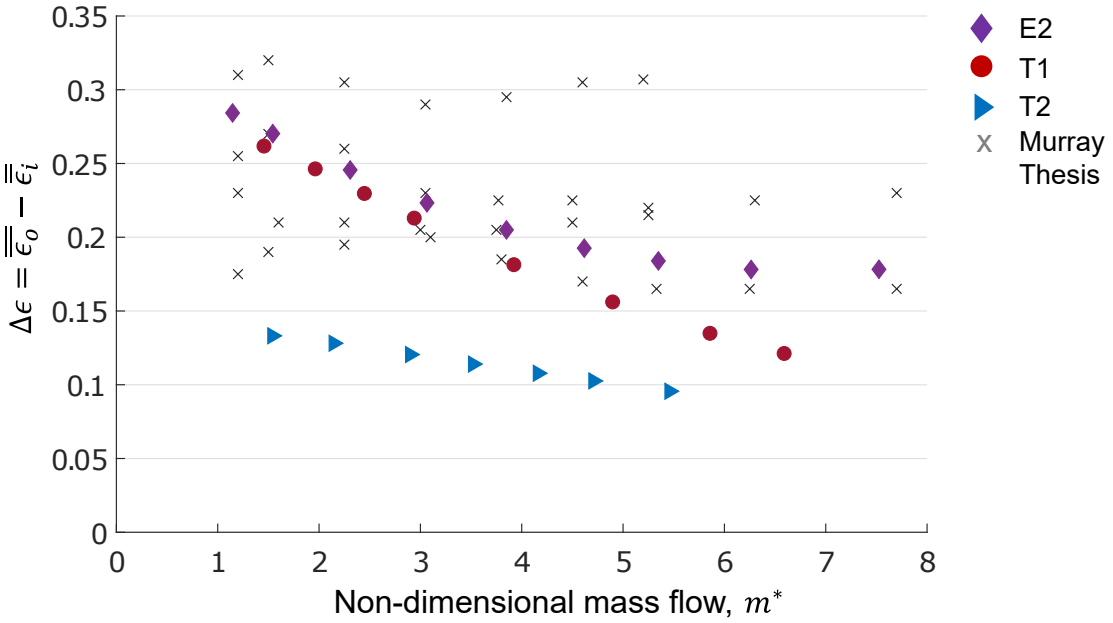


Figure 8.24: Thermal gradient between inner- and outer- surfaces for E1, T1 and T2 and configurations from Murray [85].

As discussed in Section 8.2, the numerical results found that the T2 configuration reduces the thermal gradient between the external and internal skins, ultimately helping to reduce failure by low cycle fatigue. To further evaluate these findings the mean thermal driving force was plotted against the non-dimensional mass flow rate for each configuration in Figure 8.24. The thermal driving force was found as the difference between the area-averaged film-side and impingement-side cooling effectiveness:

$$\Delta\varepsilon = \overline{\overline{\varepsilon_o}} - \overline{\overline{\varepsilon_i}} \tag{8.13}$$

For E2, T1 and T2, and increase in the coolant mass flow reduced the thermal gradient between the walls, as the temperatures on the film-side wall reduces faster than that of the impingement-side wall. For E2 the reduction in thermal gradient decays with rising mass flow rate, while T1 and T2 experiences behaviour which can be approximated as linear. As a consequence, despite similar $\Delta\varepsilon$ at low m^* for E2 and T1, at the higher flow rates the latter had a reduced thermal gradient. T2 experienced the lowest thermal gradient, across the range of flow rates investigated, and the gap between it and T1 and E2 was largest at low mass flow rates. T2 also outperformed all the configurations investigated by Murray. This is an important finding, as we can confirm that T2 provides a superior thermal performance in relation to peak temperatures, mean temperatures and the thermal gradient between walls.

8.4 Summary

A numerical method and experimental tests investigated the behaviour of double-walled configurations to attain the importance of porosity on the overall cooling performance. The assessment of peak temperature, mean temperature and thermal gradient was made. The numerical results found the following:

1. Outerskin porosity provides a more uniform protection on the external blade surface.

2. Outerskin porosity can reduce the peak temperature and mean temperatures of the external hot-side wall, which will promote longer in-service life of a turbine blade.

3. Outerskin porosity can reduced thermal gradients between outer- and inner- walls, which reduces the associated thermal stresses.

4. Increase in the ratio of number of film to impingement holes can result in variable coolant distribution between film holes, and in a worst case be a source of hot-gas ingestion.

Experimental results confirmed these findings in relation to thermal protection. It is recommended that further research is required to assess the impact of these configuration in engine-like blade geometries. This will help understand how these benefits can be translated to the different blade regions (leading edge, suction surface and pressure surface) and how to tackle potential problems of variable coolant distribution and hot-gas ingestion.

9 Concluding Remarks

This thesis documents an investigation into the benefits associated with highly porous film cooling and its implementation in a double-wall system. Efficiently cooled systems can be achieved further motivation for further development of densely-packed effusion arrays and a key step towards transpiration cooling. Provided here is a summary of the highlights of this thesis and suggestions for further work to progress turbine cooling technology.

9.1 Summary of the film effectiveness work

A modified Goldstein-Sellers film superposition method was employed to characterise the behaviour of dense film arrays, and shown to predict the behaviour of film superposition relatively well, but did not completely account for lateral mixing compared to experimental results. The spanwise spacing has a profound impact on the superposition of film cooling promoting high film effectiveness and full lateral coverage. Variable mass distribution to film holes was observed for highly-packed film-arrays, highlighting the need for considered implementation to avoid hot-gas ingestion.

9.2 Summary of the double-wall work

The innerskin thickness and the spacing between the inner- and outer- skin (pedestal height) were varied to assess the impact on the aerothermal field, as a reduction in both parameters can help manage the stresses in a turbine blade. It was found that systems of high film hole density result in a better cooling efficiency and thermal stress performance compared to previously studied systems of modest outer wall porosity. In terms of geometric effects, we find that connecting the two walls with short pedestals enhances the internal impingement cooling but at

a higher risk of hot gas ingestion; it is therefore suggested that the pedestals should be short, but long enough to avoid such effects. The inner wall thickness, on the other hand, is shown to have less impact on the aerothermal response, giving designers the freedom to reduce inner wall thickness for the scope of reducing thermal stresses in the more critical outer wall, thus improving the mechanical performance at the film holes.

9.3 Summary of the numerical evaluations work

Four numerical method variations were used to assess the cooling performance of double-wall system:

- LOM - low order model
- DUC - de-coupled unit-cell
- SUC - semi-coupled unit-cell
- SSD - semi-coupled streamwise (internal) domain

Using the film effectiveness prediction from the previously used Goldstein-Sellers superposition method and internal CFD, apart from the case of the low order model which utilised empirical correlations. The use of a simple decoupled method (DUC) underestimates film protection, while moving toward larger domain sizes (SUC and SSD) will help capture these features. But there is an associated computational cost that increases with domain size. The comparison of these methods suggests that the use of a decoupled unit-cell method adequately captures the overall cooling performance.

9.4 Summary of outerskin porosity in a double-wall configuration

A decoupled conjugate method was applied to double-walled cooling systems using computational fluid dynamics for the internal aerothermal field and an empirical correlation for external thermal loads. Outerskin porosity was investigated to assess the impact on both cooling performance and internal flow structure. It was shown that internal cooling shifts from being mainly

dependent on the impingement jet to the internal film-hole surface area. And using an outer surface porosity of 20% leads to cooling which can be described as transpiration-like in nature, i.e. less than 10% in the difference of the solid and coolant fluid. Further to this, experimental tests using metal double-wall configurations with a range in outerskin porosity were conducted. An increase in the outerskin porosity was shown to provide the following benefits:

- More uniform and elevated film effectiveness protection on the external blade surface.
- Reduction in the maximum and mean temperature on the external surfaces as well as enhanced overall cooling performance throughout the double wall structure.
- Reduction in the thermal gradient between outer and inner skins.

9.5 Suggestions for Further Work

Below are suggestions are further developments to the work presented here.

- Further experimental research to assess the nature of superposition in highly packed film arrays is required to confirm the lateral spread at low blowing ratios and further develop empirical predictive methods for film cooling. Moreover, employing further parameters such as hole aspect ratio, compound angle and hole shape will provide a more complete understanding on how best to incorporate small diameter (<0.4 mm engine scale) film hole arrays into turbine blades.
- To the authors knowledge there is sparse literature on the aerodynamic and thermal boundary layer for highly dense film cooling arrays. Further experimental should investigate the impact that the hole spacing, angle and other parameters have on this, to provide a more fundamental understanding on why enhanced film cooling is created as well as the implications on the aerodynamic performance of a turbine blade. This could be implemented using a traverse system at several streamwise locations at and downstream of the film-hole array. A cold and/or hot wire anemometry technique could be utilised.
- The experimental facility here only considered the external outer and inner walls of the test piece. However, internal geometric variation and porosity impacts the flow features

and heat transfer properties of the impingement jet and internal cross-flow. A facility which is able to assess the internals would provide further insight into the enhancements of highly porous double-wall configurations. For example double-wall pieces and thermodynamic liquid crystals may capture the associated internal heat transfer augmentation.

- Understanding the consequences of highly porous double wall designs in more engine representative conditions, especially considering the non-steady behaviour for turbine blades in a engine compared to the steady state considered in the experimental and numerical work shown here. For example, an investigation on the influence of transient pressure fields on high density film hole arrays or porous blocks. Furthermore more studies for representative curvature are required to clarify the extent of film effectiveness enhancement.

- The work here highlighted that high outerskin to innerskin porosity can result in variation in the mass flow delivered to film holes and increase the risk of hot-gas ingestion. Further work is required to assess the influence of turbine blade characteristics on this behaviour, such as blade curvature and film array location. This may help engineers design flow management systems which may be required for highly porous turbine blades.

Bibliography

[1] L. S. Langston, "Crossflows in a Turbine Cascade Passage," *Journal of Engineering for Power*, vol. 102, pp. 866–874, 10 1980.

[2] M. Courtis, A. Murray, B. Coulton, P. Ireland, and I. Mayo, "Influence of Spanwise and Streamwise Film Hole Spacing on Adiabatic Film Effectiveness for Effusion-Cooled Gas Turbine Blades," *International Journal of Turbomachinery, Propulsion and Power 2021, Vol. 6, Page 37*, vol. 6, p. 37, 8 2021.

[3] "Rolls-Royce UltraFan. Date accessed: 18/04/2023 https://www.rolls-royce.com/innovation/ultrafan.aspx."

[4] T. J. Carter, "Common failures in gas turbine blades," *Engineering Failure Analysis*, vol. 12, pp. 237–247, 4 2005.

[5] R. Krewinkel, "A review of gas turbine effusion cooling studies," *International Journal of Heat and Mass Transfer*, vol. 66, pp. 706–722, 11 2013.

[6] A. V. Murray, P. T. Ireland, and A. J. Rawlinson, "An Integrated Conjugate Computational Approach for Evaluating the Aerothermal and Thermomechanical Performance of Double-Wall Effusion Cooled Systems," *Proceedings of ASME Turbo Expo 2017: Turbomachinery Technical Conference and Exposition. GT2017-64711*, pp. 1–12, 6 2017.

[7] W. E. Frazier, "Metal additive manufacturing: A review," *Journal of Materials Engineering and Performance*, vol. 23, pp. 1917–1928, 4 2014.

[8] L. Yang, Z. Min, S. N. Parbat, and M. K. Chyu, "Effect of Pore Blockage on Transpiration Cooling With Additive Manufacturable Perforate Holes," in *Volume 2D: Turbomachinery*, p. V02DT47A004, ASME, 6 2018.

[9] B. Varney, B. Barker, J. P. Bons, T. Wolff, and P. Gnanaselvam, "Fine Particulate Deposition in an Effusion Plate Geometry," 6 2019.

[10] A. Murray, P. Ireland, T. Wong, S. Tang, and A. Rawlinson, "High Resolution Experimental and Computational Methods for Modelling Multiple Row Effusion Cooling Performance," *International Journal of Turbomachinery, Propulsion and Power*, vol. 3, p. 4, 1 2018.

[11] P. Kalghatgi and S. Acharya, "Modal analysis of inclined film cooling jet flow," *Journal of Turbomachinery*, vol. 136, 8 2014.

[12] Research Councils UK, "Transpiration Cooling Systems for Jet Engine Turbines and Hypersonic Flight," 2018.

[13] R. G. Eckert and J. B. Esgar, "Survey of advantages and problems associated with transpiration cooling and film cooling of gas-turbine blades," *NACA-RM-E50K15*, 1951.

[14] L. Battisti, R. Fedrizzi, and G. Cerri, "Novel Technology for Gas Turbine Blade Effusion Cooling," *Proceedings of GT2006 ASME Turbo Expo 2006: Power for Land, Sea and Air GT2006-90516*, 2006.

[15] M. Courtis, C. Skamniotis, A. Cocks, and P. Ireland, "Coupled aerothermal-mechanical analysis in single crystal double wall transpiration cooled gas turbine blades with a large film hole density," *Applied Thermal Engineering*, p. 119329, 10 2022.

[16] J.-C. Han and S. Ekkad, "Recent Development in Turbine Blade Film Cooling," *International Journal of Rotating Machinery*, vol. 7, no. 1, pp. 21–40, 2001.

[17] N. Zuckerman and N. Lior, "Jet Impingement Heat Transfer: Physics, Correlations, and Numerical Modeling," in *ADVANCES IN HEAT TRANSFER VOL. 39* (G. A. Greene, J. P. Hartnett†, A. Bar-Cohen, and Y. I. Cho, eds.), vol. 39 of *Advances in Heat Transfer*, pp. 565 – 631, Elsevier, 2006.

[18] J. H. Horlock, D. T. Watson, and T. V. Jones, "Limitations on Gas Turbine Performance Imposed by Large Turbine Cooling Flows," *Journal of Engineering for Gas Turbines and Power*, vol. 123, p. 487, 7 2001.

[19] A. K. Sinha, D. G. Bogard, and M. E. Crawford, "Film-cooling effectiveness downstream of a single row of holes with variable density ratio," *Journal of Turbomachinery*, vol. 113, pp. 442–449, 7 1991.

[20] J. B. Anderson, E. J. Boyd, and D. G. Bogard, "Experimental investigation of coolant-to-mainstream scaling parameters with cylindrical and shaped film cooling holes," in *Proceedings of the ASME Turbo Expo*, vol. 5B, American Society of Mechanical Engineers (ASME), 2015.

[21] C. R. B. Day, M. L. G. Oldfield, and G. D. Lock, "The Influence of Film Cooling on the Efficiency of an Annular Nozzle Guide Vane Cascade," 6 1997.

[22] Margason R J, "Fifty years of jet in cross flow research," in *In AGARD*, 11 1993.

[23] E. Sakai and T. Takahashi, "Numerical Study on Effects of Density Ratio on Film Cooling Flow Structure and Film Cooling Effectiveness," *Proceedings of the ASME Turbo Expo*, vol. 5A-2017, 8 2017.

[24] S. H. Smith and M. G. Mungal, "Mixing, structure and scaling of the jet in crossflow," *J. Fluid Mech*, vol. 357, pp. 83–122, 1998.

[25] E. R. G. Eckert and J. N. B. Livingood, "Comparison of effectiveness of convection-, transpiration-, and film-cooling methods with air as coolant," tech. rep., 1954.

[26] R. J. Goldstein, "Film Cooling," *Advances in Heat Transfer*, vol. 7, pp. 321–379, 1 1971.

[27] S. V. Ekkad, J. C. Han, and H. Du, "Detailed Film Cooling Measurements on a Cylindrical Leading Edge Model: Effect of Free-Stream Turbulence and Coolant Density," *Journal of Turbomachinery*, vol. 120, pp. 799–807, 10 1998.

[28] C. Wang, J. Zhang, and J. Zhou, "Optimization of a fan-shaped hole to improve film cooling performance by RBF neural network and genetic algorithm," *Aerospace Science and Technology*, vol. 58, pp. 18–25, 11 2016.

[29] T. Holt, P. Ireland, and K. Self, "Film Cooling Effectiveness Downstream of Optimised Cross Corrugated Slot Geometry with Exit Shaping," 2017.

[30] G. E. Andrews, I. M. Khalifa, A. A. Asere, and F. Bazdidi-Tehrani, "Full coverage effusion film cooling with inclined holes," *Proc. ASME*, 1995.

[31] J. Yao, J. Xu, K. Zhang, J. Lei, and L. M. Wright, "Effect of density ratio on film-cooling effectiveness distribution and its uniformity for several hole geometries on a flat plate," *Journal of Turbomachinery*, vol. 141, no. 5, pp. 1–10, 2019.

[32] S. Haydt and S. Lynch, "Flowfield of a shaped film cooling hole over a range of compound angles," in *Proceedings of the ASME Turbo Expo*, vol. 5C-2018, American Society of Mechanical Engineers (ASME), 8 2018.

[33] W. Li, X. Lu, X. Li, J. Ren, and H. Jiang, "High resolution measurements of film cooling performance of simple and compound angle cylindrical holes with varying hole length-to-diameter ratio - Part I: Adiabatic film effectiveness," *International Journal of Thermal Sciences*, vol. 124, pp. 146–161, 2 2018.

[34] M. Gritsch, A. Schulz, and S. Wittig, "Adiabatic Wall Effectiveness Measurements of Film-Cooling Holes With Expanded Exits," *Journal of Turbomachinery*, vol. 120, p. 549, 7 1998.

[35] D. A. Fletcher, "Internal cooling of turbine blades : the matrix cooling method," 1997.

[36] H. Wu, H. Cheng, Y. Li, C. Rong, and S. Ding, "Effects of side hole position and blowing ratio on sister hole film cooling performance in a flat plate," *Applied Thermal Engineering*, vol. 93, pp. 718–730, 1 2016.

[37] J. D. Heidmann and S. Ekkad, "A Novel Anti-Vortex Turbine Film Cooling Hole Concept," *Proceedings of the ASME Turbo Expo*, vol. 4 PART A, pp. 487–496, 3 2009.

[38] K. Kusterer, A. Elyas, D. Bohn, T. Sugimoto, and R. Tanaka, "Double-jet film-cooling for highly efficient film-cooling with low blowing ratios," in *Proceedings of the ASME Turbo Expo*, vol. 4, pp. 23–34, American Society of Mechanical Engineers Digital Collection, 8 2008.

[39] S. G. Schwarz, R. J. Goldstein, and E. R. G. Eckert, "The Influence of Curvature on Film Cooling Performance," in *ASME 1990 International Gas Turbine and Aeroengine Congress and Exposition*, 6 1990.

[40] R. J. Goldstein, E. R. G. Eckert, H. D. Chiang, and E. Elovic, "Effect of Surface Roughness on Film Cooling Performance," *Journal of Engineering for Gas Turbines and Power*, vol. 107, pp. 111–116, 1 1985.

[41] D. L. Schmidt, B. Sen, and D. G. Bogard, "Effects of Surface Roughness on Film Cooling," in *ASME 1996 International Gas Turbine and Aeroengine Congress and Exhibition*, 6 1996.

[42] F. E. Ames, "Aspects of Vane Film Cooling With High Turbulence: Part I—Heat Transfer," *Journal of Turbomachinery*, vol. 120, pp. 768–776, 10 1998.

[43] D. L. Schmidt and D. G. Bogard, "Effects of Free-Stream Turbulence and Surface Roughness on Film Cooling," in *ASME 1996 International Gas Turbine and Aeroengine Congress and Exhibition*, 6 1996.

[44] N. W. Foster and D. Lampard, "The Flow and Film Cooling Effectiveness Following Injection through a Row of Holes," *Journal of Engineering for Power*, vol. 102, pp. 584–588, 7 1980.

[45] G. E. Andrews, A. A. Asere, M. C. Mkpadi, and A. Tirmahi, "Transpiration Cooling Contribution of Film Cooling to the Overall Cooling Effectiveness," *ASME 1986 International Gas Turbine Conference*, 1986.

[46] Y. Jiang, L. Capone, P. Ireland, and E. Romero, "A detailed study of the interaction between two rows of cooling holes," in *Proceedings of the ASME Turbo Expo*, vol. 5A-2017, American Society of Mechanical Engineers (ASME), 8 2017.

[47] R. O. Hickel, E. L. Warren, and A. Kaufman, "Experimental investigation of the flow, oxidation, cooling, and thermal-fatigue characteristics of a laminated porous sheet material," *National Aeronautics and Space Administration*, 3 1972.

[48] General Electric, "GE Rolls-Royce F136 Program History & Engine Details," 2004.

[49] A. H. Lefebvre and D. R. Ballal, *Gas Turbine Combustion: Alternative Fuels and Emissions, Third Edition*. Taylor & Francis, 2010.

[50] G. Andrews, M. Gupta, and M. Mkpadi, "Full Coverage Discrete Hole Film Cooling: Cooling Effectiveness," *International Journal of Turbo and Jet Engines*, vol. 2, 1 1985.

[51] H. H. Cho, D. H. Rhee, and R. J. Goldstein, "Effects of Hole Arrangements on Local Heat/Mass Transfer for Impingement/Effusion Cooling With Small Hole Spacing," *Journal of Turbomachinery*, vol. 130, p. 041003, 10 2008.

[52] R. Krewinkel, *Numerical investigation of influences from manufacturing and operation on effusion cooling and its application to gas turbine blades*. PhD thesis, RWTH Aachen University, 2012.

[53] A. V. Murray, P. T. Ireland, and E. Romero, "Development of a steady-state experimental facility for the analysis of double-wall effusion cooling geometries," *Journal of Turbomachinery*, vol. 141, 4 2019.

[54] G. C. Ngetich, P. T. Ireland, A. V. Murray, and E. Romero, "A 3D Conjugate Approach For Anaysing A Double-Walled Effusion-Cooled Turbine Blade," *ASME Turbo Expo 2018*, 2018.

[55] W. Li, X. Lu, X. Li, J. Ren, and H. Jiang, "On improving full-coverage effusion cooling efficiency by varying cooling arrangements and wall thickness in double wall cooling application," *Journal of Heat Transfer*, vol. 141, 4 2019.

[56] M. Miller, G. Natsui, M. Ricklick, J. Kapat, and R. Schilp, "Heat Transfer in a Coupled Impingement-Effusion Cooling System," *Volume 5B: Heat Transfer*, 2014.

[57] T. Langener, "A Contribution to Transpiration Cooling for Aerospace Applications Using CMC Walls," p. 141, 2011.

[58] J. Polezhaev, "Transpiration cooling for blades of high temperatures gas turbine," *Energy Conversion and Management*, 1997.

[59] S. Schweikert, J. von Wolfersdorf, M. Selzer, and H. Hald, "Experimental Investigation on Velocity and Temperature Distributions of Turbulent Cross Flows over Transpiration Cooled C/C-Wall Segments," 2013.

[60] A. Laganelli, "A comparison between film cooling and transpiration cooling systems in high speed flow," in *Proceedings ofthe AlAA 8th Aerospace Sciences Meeting, New York, NY. AIAA 1970-153*, (Reston, Virigina), American Institute of Aeronautics and Astronautics, 1 1970.

[61] J. Wang, J. Messner, and H. Stetter, "An Experimental Investigation on Transpiration Cooling Part II: Comparison of Cooling Methods and Media," *The International Journal of Rotating Machinery*, 2002.

[62] F. J. Bayley, "Performance and Design of Transpiration-Cooled Turbine Blading," in *Volume 1B: General*, p. V01BT02A022, ASME, 4 1978.

[63] D. G. Bogard and K. A. Thole, "Gas turbine film cooling," *Journal of Propulsion and Power*, vol. 22, pp. 249–270, 5 2006.

[64] S. Wylie, A. Bucknell, P. Forsyth, M. McGilvray, and D. R. Gillespie, "Reduction in flow parameter resulting from volcanic ash deposition in engine representative cooling passages," *Journal of Turbomachinery*, vol. 139, 3 2017.

[65] M. Grayburn, "British Airways Boeing 747-236 Volcanic Cloud Encounter on the 24 June 1982—Investigation Report," tech. rep., Rolls-Royce, 1983.

[66] G. Huang, Y. Zhu, Z. Liao, and P. X. Jiang, "Experimental investigation of self-pumping internal transpiration cooling," *International Journal of Heat and Mass Transfer*, 2018.

[67] L. Yang, W. Chen, and M. K. Chyu, "A convolution modeling method for pore plugging impact on transpiration cooling configurations perforated by straight holes," *International Journal of Heat and Mass Transfer*, 2018.

[68] M. Arai and T. Suidzu, "Porous ceramic coating for transpiration cooling of gas turbine blade," 2013.

[69] "Middle East aviation services market growth continues | Boeing Services."

[70] J. Basley, K. Gouder, and J. F. Morrison, "Mixing of an effusion film within a turbulent boundary layer," *9th EUROPEAN CONFERENCE FOR AERONAUTICS AND SPACE SCIENCES (EUCASS)*, 2022.

[71] P. T. Ireland and T. V. Jones, "Liquid crystal measurements of heat transfer and surface shear stress," *Measurement Science and Technology*, vol. 11, pp. 969–986, 7 2000.

[72] G. Caciolli, B. Facchini, A. Picchi, and L. Tarchi, "Comparison between PSP and TLC steady state techniques for adiabatic effectiveness measurement on a multiperforated plate," *Experimental Thermal and Fluid Science*, vol. 48, pp. 122–133, 7 2013.

[73] E. Schmidt, "Verdunstung und warmeugergang," *Gesundheits-Ingenieur*, vol. 29, pp. 525–529, 1929.

[74] W. Nusselt, "Wärmeübergang, Diffusion und Verdunstung," *ZAMM - Zeitschrift für Angewandte Mathematik und Mechanik*, vol. 10, no. 2, pp. 105–121, 1930.

[75] P. Renze, W. Schro\"{o}der, and M. Meinke, "Large-Eddy Simulation of Interacting Film Cooling Jets," in *Volume 3: Heat Transfer, Parts A and B*, pp. 81–90, ASME, 1 2009.

[76] W. Jessen, M. Konopka, and W. Schr\"{o}der, "Particle-Image Velocimetry Measurements of Film Cooling in an Adverse Pressure Gradient Flow," in *Volume 4: Heat Transfer, Parts A and B*, pp. 1459–1470, ASME, 10 2010.

[77] Y. Jiang, A. Murray, P. Ireland, and L. Di Mare, "Coolant jets interaction in effusion cooling system: experimental and numerical study," American Society of Mechanical Engineers, 2019.

[78] J. P. Sellers, "Gaseous Film Cooling With Multiple Injection Stations," *AIAA Journal*, vol. 1, pp. 2154–2156, 9 1963.

[79] Z. Wang, P. Yan, H. Huang, and W. Han, "Coupled BEM and FDM Conjugate Analysis of a Three-Dimensional Air-Cooled Turbine Vane," in *Volume 3: Heat Transfer, Parts A and B*, pp. 21–30, ASME, 2009.

[80] S. Amaral, T. Verstraete, R. Van den Braembussche, and T. Arts, "Design and Optimization of the Internal Cooling Channels of a High Pressure Turbine Blade—Part I: Methodology," *Journal of Turbomachinery*, vol. 132, p. 021013, 4 2010.

[81] A. Bonini, A. Andreini, C. Carcasci, B. Facchini, A. Ciani, and L. Innocenti, "Conjugate Heat Transfer Calculations on GT Rotor Blade for Industrial Applications: Part I—Equivalent Internal Fluid Network Setup and Procedure Description," in *Volume 4: Heat Transfer, Parts A and B*, p. 669, ASME, 6 2012.

[82] A. Andreini, A. Bonini, R. Da Soghe, B. Facchini, A. Ciani, and L. Innocenti, "Conjugate Heat Transfer Calculations on GT Rotor Blade for Industrial Applications: Part II—Improvement of External Flow Modeling," in *Volume 4: Heat Transfer, Parts A and B*, p. 681, ASME, 6 2012.

[83] B. Kirollos and T. Povey, "An Energy-Based Method for Predicting the Additive Effect of Multiple Film Cooling Rows," *Journal of Engineering for Gas Turbines and Power*, vol. 137, p. 122608, 12 2015.

[84] N. E. Holgate, "Novel leading edge film cooling experiments and geometries," 2019.

[85] A. V. Murray, *Advanced gas turbine cooling: double-wall turbine cooling technologies in turbine NGV/blade applications*. PhD thesis, University of Oxford, 2019.

[86] FLIR, "LWIR Science-Grade Camera: FLIR A655sc: 16-1683-INS-A655sc Datasheet," 2018.

[87] A. V. Murray, P. T. Ireland, and E. Romero, "Experimental and Computational Methods for the Evaluation of Double-Wall, Effusion Cooling Systems," *Journal of Turbomachinery*, vol. 142, no. 11, 2020.

[88] A. R. Byerley, *Heat Transfer Near th Entrance to a Film Cooling Hole in a Gas Turbine Blade*. PhD thesis, University of Oxford, 1989.

[89] B. Coulton, A. V. Murray, and P. T. Ireland, "A Computation Approach to Aerothermal Analysis of Complex Internal Turbine Cooling Geometries," *Proceedings of ASME Turbo Expo 2022 Turbomachinery Technical Conference and Exposition*, 2022.

[90] M. Thomas and T. Povey, "A novel scalar tracking method for optimising film cooling systems," *Proceedings of the Institution of Mechanical Engineers, Part A: Journal of Power and Energy*, vol. 230, pp. 3–15, 2 2016.

[91] A. V. Murray, P. T. Ireland, and E. Romero, "An Experimentally Validated Low-Order Model of the Thermal Response of Double-Wall Effusion Cooling Systems for High-Pressure Turbine Blades," *Journal of Turbomachinery*, vol. 143, 11 2021.

[92] E. Elmukashfi, A. V. Murray, P. T. Ireland, and A. C. Cocks, "Analysis of the thermomechanical stresses in double-wall effusion cooled systems," *Journal of Turbomachinery*, vol. 142, 5 2020.

[93] R. J. Goldstein and A. I. Behbahani, "Impingement of a circular jet with and without cross flow," *International Journal of Heat and Mass Transfer*, vol. 25, pp. 1377–1382, 9 1982.

[94] D. R. Gillespie and P. T. Ireland, *Intricate internal cooling systems for gas turbine blading*. PhD thesis, University of Oxford, c1998, 1998.

[95] N. Rogers, Z. Ren, W. Buzzard, B. Sweeney, N. Tinker, P. Ligrani, K. Hollingsworth, F. Liberatore, R. Patel, S. Ho, and H.-K. Moon, "Effects of Double Wall Cooling Configuration and Conditions on Performance of Full-Coverage Effusion Cooling," *Journal of Turbomachinery*, vol. 139, p. 051009, 6 2017.

[96] K. M. Bernhard Gustafsson and T. Gunnar Johansson, "An experimental study of surface temperature distribution on effusion-cooled plates," *Journal of Engineering for Gas Turbines and Power*, vol. 123, pp. 308–316, 1 2001.

[97] J. F. Muska, R. W. Fish, and M. Suo, "The Additive nature of film cooling from rows of holes," *Journal of Engineering for Gas Turbines and Power*, vol. 98, pp. 457–463, 10 1976.

[98] S. Baldauf, A. Schulz, and S. Wittig, "High resolution measurements of local effectiveness by discrete hole film cooling," in *Proceedings of the ASME Turbo Expo*, vol. 3, American Society of Mechanical Engineers (ASME), 12 1999.

[99] E. Lutum and B. V. Johnson, "Influence of the Hole Length-to-Diameter Ratio on Film Cooling With Cylindrical Holes," *Journal of Turbomachinery*, vol. 121, p. 209, 4 1999.

[100] A. Wambersie, H. Wong, P. Ireland, and I. Mayo, "Experiments of Transpiration Cooling Inspired Panel Cooling on a Turbine Blade Yielding Film Effectiveness Levels over 95%," *International Journal of Turbomachinery, Propulsion and Power 2021, Vol. 6, Page 16*, vol. 6, p. 16, 6 2021.

[101] M. Courtis, A. V. Murray, P. Ireland, and I. Mayo, "Influence of Spanwise- and Streamwise- Film Hole Spacing on Adiabatic Film Effectiveness for Gas Turbine Blades," *Proceedings of 14th European Conference on Turbomachinery Fluid dynamics & Thermodynamics*, pp. 1–14, 2021.

[102] N. M. El-Hady and A. K. Verma, "Instability of compressible boundary layers along curved walls with suction or cooling," *https://doi.org/10.2514/3.8369*, vol. 22, pp. 206–213, 5 2012.

[103] C. G. Skamniotis and A. C. Cocks, "2D and 3D thermoelastic phenomena in double wall transpiration cooling systems for gas turbine blades and hypersonic flight," *Aerospace Science and Technology*, p. 106610, 2 2021.

[104] M. Courtis, C. Skamniotis, A. Cocks, and P. Ireland, "Coupled aerothermal-mechanical analysis in single crystal double wall transpiration cooled gas turbine blades with a large film hole density," *Applied Thermal Engineering*, p. 119329, 2022.

[105] Reed R.C., "The superalloys: fundamentals and applications," *Cambridge university press*, 2008.

[106] M. Kim, D. H. Shin, J. S. Kim, B. J. Lee, and J. Lee, "Experimental investigation of effusion and transpiration air cooling for single turbine blade," *Applied Thermal Engineering*, vol. 182, p. 116156, 1 2021.

[107] F. Satta and G. Tanda, "Effect of discrete-hole arrangement on film-cooling effectiveness for the endwall of a turbine blade cascade," *Applied Thermal Engineering*, vol. 91, pp. 507–514, 12 2015.

[108] C. Skamniotis, M. Courtis, and A. C. Cocks, "Multiscale analysis of thermomechanical stresses in double wall transpiration cooling systems for gas turbine blades," *International Journal of Mechanical Sciences*, vol. 207, p. 106657, 10 2021.

[109] C. Skamniotis and A. C. Cocks, "Creep-plasticity-fatigue calculations in the design of porous double layers for new transpiration cooling systems," *International Journal of Fatigue*, vol. 151, 10 2021.

[110] C. Skamniotis and A. C. Cocks, "Designing against severe stresses at compound cooling holes of double wall transpiration cooled engine components," *Aerospace Science and Technology*, vol. 116, p. 106856, 9 2021.

[111] R. Kumar, V. S. Kumar, M. M. Butt, N. A. Sheikh, S. A. Khan, and A. Afzal, "Thermo-mechanical analysis and estimation of turbine blade tip clearance of a small gas turbine engine under transient operating conditions," *Applied Thermal Engineering*, vol. 179, 10 2020.

[112] H. H. Cho and D. H. Rhee, "Local Heat/Mass Transfer Measurement on the Effusion Plate in Impingement/Effusion Cooling Systems," *Journal of Turbomachinery*, vol. 123, pp. 601–608, 7 2001.

[113] J. H. Lee and S. J. Lee, "Turbulent Heat Transfer Characteristics in a Stagnation Region of Axi-Symmetric Jet Impingement," *International Heat Transfer Conference 11*, pp. 433–438, 5 1998.

[114] V. S. Patil and R. P. Vedula, "Local heat transfer for jet impingement onto a concave surface including injection nozzle length to diameter and curvature ratio effects," *Experimental Thermal and Fluid Science*, vol. 92, pp. 375–389, 4 2018.

[115] A. Andreini, L. Cocchi, B. Facchini, L. Mazzei, and A. Picchi, "Experimental and numerical investigation on the role of holes arrangement on the heat transfer in impingement/effusion cooling schemes," *International Journal of Heat and Mass Transfer*, vol. 127, pp. 645–659, 12 2018.

[116] S. V. Garimella and B. Nenaydykh, "Nozzle-geometry effects in liquid jet impingement heat transfer," *International Journal of Heat and Mass Transfer*, vol. 39, pp. 2915–2923, 9 1996.

[117] C. Skamniotis and A. C. Cocks, "Thermal and centrifugal stresses in curved double wall transpiration cooled components with temperature dependent thermoelastic properties," *International Journal of Solids and Structures*, vol. 234-235, p. 111273, 1 2022.

[118] K. M. Knowles and P. R. Howie, "The Directional Dependence of Elastic Stiffness and Compliance Shear Coefficients and Shear Moduli in Cubic Materials," *Journal of Elasticity*, vol. 120, pp. 87–108, 6 2015.

[119] A. Epishin, B. Fedelich, M. Finn, G. Künecke, B. Rehmer, G. Nolze, C. Leistner, N. Petrushin, and I. Svetlov, "Investigation of Elastic Properties of the Single-Crystal Nickel-Base Superalloy CMSX-4 in the Temperature Interval between Room Temperature and 1300 °C," *Crystals 2021, Vol. 11, Page 152*, vol. 11, p. 152, 2 2021.

[120] D. Dye, K. T. Conlon, P. D. Lee, R. B. Rogge, and R. C. Reed, "Welding of single crystal Superalloy CMSX-4: Experiments and Modeling," *Superalloys 2004 (Tenth International Symposium)*, 2004.

[121] M. W. R. Savage, "The Influence of Crystal Orientation on the Elastic Stresses of a Single Crystal Nickel-Based Turbine Blade," *Journal of Engineering for Gas Turbines and Power*, vol. 134, 1 2012.

[122] X. Zhang, H. Gao, K. Yu, Z. Wen, Y. Zhao, and Z. Yue, "Crystal orientation effect and multi-fidelity optimization of a solid single crystal superalloy turbine blade," *Computational Materials Science*, vol. 149, pp. 84–90, 6 2018.

[123] M. Segersäll, D. Leidermark, and J. J. Moverare, "Influence of crystal orientation on the thermomechanical fatigue behaviour in a single-crystal superalloy," *Materials Science and Engineering: A*, vol. 623, pp. 68–77, 1 2015.

[124] N. Hou, W. Gou, Z. Wen, and Z. Yue, "The influence of crystal orientations on fatigue life of single crystal cooled turbine blade," *Materials Science and Engineering: A*, vol. 492, pp. 413–418, 9 2008.

[125] W. He, Q. Deng, W. Zhou, T. Gao, and Z. Feng, "Film cooling and aerodynamic performances of a turbine nozzle guide vane with trenched cooling holes," *Applied Thermal Engineering*, vol. 150, pp. 150–163, 3 2019.

[126] J. Liu, X. Lin, X. Zhang, and B. An, "Investigation on cooling effectiveness and aerodynamic loss of a turbine cascade with film cooling," *Journal of Thermal Science*, vol. 25, pp. 50–59, 2 2016.

[127] J. Wang, J. Liang, Z. Wen, Y. Yang, and Z. Yue, "The inter-hole interference on creep deformation behavior of nickel-based single crystal specimen with film-cooling holes," *International Journal of Mechanical Sciences*, vol. 163, p. 105090, 11 2019.

[128] Z. X. Wen, J. W. Liang, C. Y. Liu, H. Q. Pei, S. F. Wen, and Z. F. Yue, "Prediction method for creep life of thin-wall specimen with film cooling holes in Ni-based single-crystal superalloy," *International Journal of Mechanical Sciences*, vol. 141, pp. 276–289, 6 2018.

[129] D. H. Thulin R.D. and I. Singer, "Energy efficient engine high-pressure turbine detailed design report," 1982.

[130] O. Kauss, H. Tsybenko, K. Naumenko, S. Hütter, and M. Krüger, "Structural analysis of gas turbine blades made of Mo-Si-B under transient thermo-mechanical loads," *Computational Materials Science*, vol. 165, pp. 129–136, 7 2019.

[131] T. M. Cory, K. A. Thole, K. L. Kirsch, R. Lundgreen, R. Prenter, and S. Kramer, "Impact of Dust Feed on Capture Efficiency and Deposition Patterns in a Double-Walled Liner," *Proceedings of the ASME Turbo Expo*, vol. 2D-2019, 11 2019.

[132] A. Ma, D. Dye, and R. C. Reed, "A model for the creep deformation behaviour of single-crystal superalloy CMSX-4," *Acta Materialia*, vol. 56, pp. 1657–1670, 5 2008.

[133] H. Li, M. Wang, and R. You, "Impact of radiative heat flux on turbine blade heat transfer in high temperature environments," *Applied Thermal Engineering*, vol. 212, p. 118505, 7 2022.

[134] C. Allan, *Plasticity of nickel base single crystal superalloys*. PhD thesis, Massachusetts Institute of Technology, 1995.

[135] Y. Rao, Y. Liu, and C. Wan, "Multiple-jet impingement heat transfer in double-wall cooling structures with pin fins and effusion holes," *International Journal of Thermal Sciences*, 2018.

[136] S. H. Kim, K. H. Ahn, J. S. Park, E. Y. Jung, K. Y. Hwang, and H. H. Cho, "Local heat and mass transfer measurements for multi-layered impingement/effusion cooling: Effects of pin spacing on the impingement and effusion plate," *International Journal of Heat and Mass Transfer*, 2017.

[137] J. C. Han and A. P. Rallabandi, "Turbine Blade Film Cooling Using PSP Technique," *Frontiers in Heat and Mass Transfer*, vol. 1, no. 1, 2010.

[138] Z. Huang, Y.-B. Xiong, Y.-Q. Liu, P.-X. Jiang, and Y.-H. Zhu, "Experimental investigation of full-coverage effusion cooling through perforated flat plates," *Applied Thermal Engineering*, vol. 76, pp. 76–85, 2 2015.

[139] A. Dewan, R. Dutta, and B. Srinivasan, "Recent trends in computation of turbulent jet impingement heat transfer," *Heat Transfer Engineering*, vol. 33, no. 4-5, pp. 447–460, 2012.

[140] Y. Jiang, A. Murray, L. d. Mare, and P. Ireland, "Mesh sensitivity of RANS simulations on film cooling flow," *International Journal of Heat and Mass Transfer*, vol. 182, 2021.

[141] F. B. Jones, D. W. Fox, and D. G. Bogard, "Evaluating the Usefulness of RANS in Film Cooling," *Proceedings of the ASME Turbo Expo*, vol. 5A-2019, 11 2019.

[142] K. C. Mills, *Recommended values of thermophysical properties for selected commercial alloys*. Woodhead Publishing, 2002.

[143] M. v. d. Noort and P. Ireland, "A Low Order Flow Network Model for Double-Wall Effusion Cooling Systems," *International Journal of Turbomachinery, Propulsion and Power 2022, Vol. 7, Page 5*, vol. 7, p. 5, 2 2022.

[144] B. Varney, B. Barker, J. Bons, P. Gnanaselvam, and T. Wolff, "Fine Particulate Deposition in an Effusion Plate Geometry," *Journal of Turbomachinery*, vol. 143, 1 2021.